GDAŃSK UNIVERSITY OF TECHNOLOGY

The author of the doctoral dissertation: Maciej Kaczmarczyk
Scientific discipline: mechanical engineering

DOCTORAL DISSERTATION

Title of doctoral dissertation: Effectiveness of waterjet propulsors in underwater vehicle propulsion

Title of doctoral dissertation (in Polish): Efektywność wodnych pędników odrzutowych w napędach pojazdów głębinowych.

Supervisor signature	Second supervisor Signature
dr hab. inż. Lech Rowiński, prof. PG	<Title, degree, first name and surname>
Auxiliary supervisor signature	Cosupervisor signature
<Title, degree, first name and surname>	<Title, degree, first name and surname>

Gdańsk, 2025

GDAŃSK UNIVERSITY OF TECHNOLOGY

STATEMENT

The author of the doctoral dissertation: Maciej Kaczmarczyk

I, the undersigned, declare that I am aware that in accordance with the provisions of Art. 27 (1) and (2) of the Act of 4th February 1994 on Copyright and Related Rights (Journal of Laws of 2021, item 1062), the university may use my doctoral dissertation entitled:

"Effectiveness of waterjet propulsors in underwater vehicle propulsion"

for scientific or didactic purposes.[1]

Gdańsk,…… ……

signature of the PhD student

Aware of criminal liability for violations of the Act of 4th February 1994 on Copyright and Related Rights and disciplinary actions set out in the Law on Higher Education and Science (Journal of Laws 2021, item 478), as well as civil liability, I declare, that the submitted doctoral dissertation is my own work.

I declare, that the submitted doctoral dissertation is my own work performed under and in cooperation with the supervision of dr hab. inż. Lech Rowiński, prof. PG.

This submitted doctoral dissertation has never before been the basis of an official procedure associated with the awarding of a PhD degree.

All the information contained in the above thesis which is derived from written and electronic sources is documented in a list of relevant literature in accordance with Art. 34 of the Copyright and Related Rights Act.

I confirm that this doctoral dissertation is identical to the attached electronic version.

Gdańsk,…… ……

signature of the PhD student

I, the undersigned, agree to include an electronic version of the above doctoral dissertation in the open, institutional, digital repository of Gdańsk University of Technology.

Gdańsk,…… ……

signature of the PhD student

*delete where appropriate

[1] Art 27. 1. Educational institutions and entities referred to in art. 7 sec. 1 points 1, 2 and 4–8 of the Act of 20 July 2018 – Law on Higher Education and Science, may use the disseminated works in the original and in translation for the purposes of illustrating the content provided for didactic purposes or in order to conduct research activities, and to reproduce for this purpose disseminated minor works or fragments of larger works.
2. If the works are made available to the public in such a way that everyone can have access to them at the place and time selected by them, as referred to in para. 1, is allowed only for a limited group of people learning, teaching or conducting research, identified by the entities listed in paragraph 1.

GDAŃSK UNIVERSITY OF TECHNOLOGY

DESCRIPTION OF DOCTORAL DISSERTATION

The Author of the doctoral dissertation: Maciej Kaczmarczyk

Title of doctoral dissertation: Effectiveness of waterjet propulsors in underwater vehicle propulsion

Title of doctoral dissertation in Polish: Efektywność wodnych pędników odrzutowych w napędach pojazdów głębinowych

Language of doctoral dissertation: English

Supervisor: dr hab. inż. Lech Rowiński, prof. PG

Date of doctoral defense:

Keywords of doctoral dissertation in Polish: napęd strugowodny, CFD, hydromechanika, ROV, pojazd podwodny

Keywords of doctoral dissertation in English: waterjet propulsion, CFD, hydromechanics, ROV, underwater vehicle

Summary of doctoral dissertation in Polish:

Podstawowym celem pracy było określenie przydatności wybranych metod półempirycznych oraz algorytmów numerycznych do szczegółowej analizy zjawisk zachodzących wewnątrz poszczególnych elementów pędnika strugowodnego oraz określenie efektywności tych metod do wyznaczania parametrów geometrycznych pędnika strugowodnego służącego do napędu niewielkiego pojazdu podwodnego. Dotychczas analizowany pojazd napędzany był standardowymi śrubami osłoniętymi prostą kratką, która, co prawda zapewniała skuteczną ochronę pracujących śrub, jednak mocno zwiększała opór pojazdu. W poniższej dysertacji przeanalizowano, a następnie przebadano pracę trzech różnych pędników strugowodnych oraz napędu śrubowego w dwóch konfiguracjach. Analiza objęła obliczenia analityczne, numeryczne oraz badania eksperymentalne w laboratorium i w warunkach odpowiadających warunkom rzeczywistym. Już na etapie rozważań analitycznych pędnik strugowodny pokazał, iż może być skutecznym zamiennikiem standardowych śrub osłoniętych kratką. Niższa sprawność pędnika strugowodnego względem standardowych śrub rekompensowana jest mniejszym oporem pojazdu, natomiast kanał pędnika strugowodnego zapewnia bardzo dobrą osłonę pracującego wirnika. Następnie badania rzeczywiste pojazdu potwierdziły skuteczność metod analityczno-empirycznych oraz numerycznej w projektowaniu niestandardowych pędników strugowodnych do nietypowych zastosowań.

Summary of doctoral dissertation in English:

The main aim of this work was to determine usefulness of selected semi-empirical and numerical algorithms for detailed analysis of phenomena occurring in different components of waterjet propulsion, as well as defining effectiveness of these methods in defining geometrical parameters of waterjet propulsion for small size underwater vehicle. The vehicle used in this analysis, so far, was driven by standard propellers covered with

simple mesh guard. It provided good protection for operating screws, but at the same time increased vehicle's total drag significantly. In this dissertation have been analyzed theoretically and then investigated empirically three different waterjet drives and standard propellers in two configurations. Analysis covered analytical calculations, numerical simulations, laboratory experiments and real-world tests. The waterjet propulsion showed it can be successful replacement for standard screws right at the initial, analytical considerations stage. The waterjet propulsion's lower overall efficiency – comparing to standard propellers – was compensated with lower vehicle's total drag. What is more, waterjet's tunnel delivers very good protection for operating rotor. Furthermore, real vehicle's tests have proved effectiveness of both analytical-empirical as well as numerical methods in designing outsized waterjet drives for non-standard use.

This page was left blank deliberately.

Table of contents

Nomenclature

GREEK SYMBOLS

α	tunnel axis curvature angle [deg]
δ_1	pipe diameter decrease angle [°]
δ_2	pipe diameter increase angle [°]
δ_3	pipe axis divergence angle [°]
δ_D	diffuser flare angle [°]
δ_C	confuser (outlet nozzle) flare angle [°]
δ	boundary layer thickness [m]
δ_L	laminar boundary layer thickness [m]
δ_T	turbulent boundary layer thickness [m]
ζ	non-dimensional fluid flow energy loss coefficient [-]
ζ_l	non-dimensional linear fluid flow energy loss coefficient [-]
ζ_1	non-dimensional linear fluid flow energy loss coefficient (diffuser) [-]
ζ_2	non-dimensional linear fluid flow energy loss coefficient (diffuser bend) [-]
ζ_3	non-dimensional linear fluid flow energy loss coefficient (confuser) [-]
ζ_4	non-dimensional linear fluid flow energy loss coefficient (hydraulic head) [-]
ζ_{P0}	propeller's coefficient of excellence [-]
ζ_T	propeller's load factor [-]
η_{WJ}	propulsion drive efficiency [-]
η_{WJ}^o	tunnel drive efficiency [-]
η_p	pump efficiency [-]
λ	linear drag friction coefficient [-]
μ	velocity index [-]
ν	water kinematic viscosity coefficient [m^2/s]
ρ	fluid density [kg/m^3]
σ_v	cavitation number [-]
σ_{vi}	cavitation number for cavitation inception [-]
χ	flow cross-section areas coefficient [-]

LATINA SYMBOLS

A	pipe cross-section area [m^2]
A_1	cross-section area at point 1 [m^2]
A_2	cross-section area at point 2 [m^2]
A_{D1}	diffuser cross-section area (inlet) [m^2]
A_{D2}	diffuser cross-section area (outlet) [m^2]
A_{C1}	confuser (outlet nozzle) cross-section area (inlet) [m^2]
A_{C2}	confuser (outlet nozzle) cross-section area (outlet) [m^2]
c_1	inlet absolute velocity [m/s]
c_2	outlet absolute velocity [m/s]
C_b	Bondeman's coefficient (propeller's static thrust coefficient) [-]

C_k	von Karman's coefficient (propeller's yield coefficient) [-]
c_{pm}	average water velocity in the pump [m/s]
c_∞	water free stream velocity [m/s]
d	pipe hydraulic diameter [m]
d_1	pipe hydraulic diameter at point 1 [m]
d_2	pipe hydraulic diameter at point 2 [m]
D	rotor / pump / propeller diameter [m]
D_{out}	outlet nozzle diameter [m]
D_{PR}	pipe hydraulic diameter (rotor area) [m]
e	pipe relative roughness [-]
F_u	waterjet thrust force [N]
F_{umax}	waterjet maximum thrust force [N]
g	standard Earth gravity [m/s^2]
h	water depth [m]
H	waterjet propulsor / pump hydraulic head [m]
h_l	flow losses (linear) [m]
h_o	flow losses (local / obstacle) [m]
h_s	summary flow losses [m]
i	simplified flow losses coefficient [-]
I_{total}	total current [A]
k	pipe absolute roughness [m]
l	pipe length [m]
l_C	confuser (outlet nozzle) length [m]
L	vehicle’s length [m]
m	mass flow rate [kg/s]
M	torque [Nm]
n	propeller / rotor / engine revolutions [rpm]
n_{sQ}	pump kinematic speed index [rpm]
N_d	power delivered to the propeller [W]
N_p	pump power [W]
N_{Loss1}	power losses at diffuser [W]
N_{Loss2}	power losses at diffuser bend [W]
N_{Loss3}	power losses at confuser [W]
N_{Loss4}	power losses at hydraulic head [W]
N_{Loss}	summary power losses [W]
N_u	pump effective power [W]
N_{out}	outlet jet stream power [W]
p	the absolute ambient pressure (total pressure) [Pa]
p_p	pressure at considered point [Pa]
p_{atm}	atmospheric pressure [Pa]
p_H	pump hydraulic pressure [Pa]
p_v	vapour pressure [Pa]
P	power delivered to propeller / propulsor [W]
P_{total}	total power (energy) [W] / [Wh]

Q	pump mass flow rate [kg/s]
r	pipe radius [m]
R	tunnel curvature radius / pipe bend radius [m]
R_e	Reynolds number [-]
$R_{e\ cr}$	critical Reynolds number [-]
s	pipe porosity depth [m]
$S_{L\ cr}$	maximum length of laminar boundary layer [m]
S_L	laminar boundary layer length [m]
S_{PROP}	propeller's cross-section area [m^2]
S_T	turbulent boundary layer length [m]
S_{S_vel}	nondimensional specific suction velocity [-]
T	thrust force [N]
t	time [s]
u	vehicle's velocity [m/s]
U_∞	fluid free stream velocity [m/s]
U_i	critical fluid free stream velocity (cavitation inception) [m/s]
U_{total}	total voltage [V]
v	fluid / vehicle velocity [m/s]
v_1	fluid velocity at point 1 [m/s]
v_2	fluid velocity at point 2 [m/s]
v_C	fluid velocity at vena contracta [m/s]
w	momentum wake fraction [-]
w_1	relative fluid velocity at propulsion inlet [m/s]
w_2	relative fluid velocity at propulsion outlet [m/s]
w_{D1}	fluid velocity at diffuser inlet [m/s]
w_{D2}	fluid velocity at diffuser outlet [m/s]
w_{C1}	fluid velocity at confuser (outlet nozzle) inlet [m/s]
w_{C2}	fluid velocity at confuser (outlet nozzle) outlet [m/s]

OTHERS

CFD	Computational Fluid Dynamics
DNS	Direct Numerical Simulation
DVL	Doppler Velocity Log
FSI	Fluid Structure Interaction
FVM	Finite Volume Method
LES	Large Eddy Simulation
RANS	Reynolds-averaged Navier – Stokes equations
S	Starting point for boundary layer development
SP	Standard propellers
SP+G	Standard propellers with propellers' guard
SST	Shear Stress Transport
U	transition point between laminar and turbulent boundary layer area
T	Turbulent boundary layer area

WJ29G	Graupner's waterjet drive (29 [mm] rotor diameter)
WJ39G	Graupner's waterjet drive (39 [mm] rotor diameter)
WJ49G	Graupner's waterjet drive (49 [mm] rotor diameter)
WJ50	Newly designed waterjet drive (50 [mm] rotor diameter)

1 Objective of this work

The objective of this work is to determine usefulness of selected semi-empirical and numerical algorithms for:

— detailed analysis of phenomena occurring in different components of operating waterjet propulsion
— definition (optimization) of geometrical parameters of waterjet propulsion in order to achieve high efficiency in operating conditions specific for small size underwater vehicle.

2 Thesis

Right at the beginning of this work it was assumed that it was possible to optimize geometrical parameters of waterjet propulsion with a use of computational fluid dynamics. However, to prove this thesis high accuracy of numerical calculations of investigated phenomena is required.

The thesis – that it is possible to achieve comparable propulsion efficiency for waterjet propulsion and reference drive – is utilitarian. The reference drive is a standard propeller propulsion of underwater vehicle in precisely specified configuration.

3 Introduction

3.1 Propulsion systems of submersible vehicles

3.1.1 Propulsors and propellers

"A ***propulsor*** is a mechanical device that gives propulsion to a vehicle. The word is commonly used in the marine vernacular, and implies a mechanical assembly that is more complicated than a propeller. The Kort nozzle and pump-jet are examples.

An example propulsor is shown in the accompanying picture. It has a shroud, which cuts down on blade-tip cavitation and radiated noise. It also has a rotor element and a stator. The stator concentrates the thrust in axial direction and reduces energy wasted in the tangential flow (therefore eliminating torque on the hull). The number of blades in the rotor & stator will typically be equal to two different prime numbers to avoid standing waves. The blades in the rotor or the stator may be angled to further reduce noise. The physical design and layout are very much similar to a single stage axial-flow compressor." [1]

Figure 3.1: The example of a propulsor [2]

"A ***propeller*** is a type of fan that transmits power by converting rotational motion into thrust. A pressure difference is produced between the forward and rear surfaces of the airfoil-shaped blade, and a fluid (such as air or water) is accelerated behind the blade. Propeller dynamics can be modelled by both Bernoulli's principle and Newton's third law. A marine propeller is sometimes colloquially known as a *screw propeller* or *screw*." [3]

Figure 3.2: The example of a propeller [4]

3.1.2 Underwater vehicles

A torpedo may be defined as the very first independent, self-propelled, unmanned submersible vehicle back in the 1900. However, it took about another half of a century to develop Remotely Operated Vehicle in its present form. Numerous of their examples can be easily found in the Internet. Therefore, only a brief overview through contemporary solutions of the most popular vehicles including remotely operated (ROV), autonomous vehicles (AUV) and diver propulsion Vehicles (DPV) is presented in this chapter.

Looking back – let us say the last twenty years – we can observe rapid technological development that opened many new possibilities. One of them is an opportunity to substitute a human operator by a machine in most of underwater works. Moreover, remotely operated vehicle either enables a difficult task to be completed or in many cases makes it easier and cheaper to perform. They may vary in shape, size and functionality, but what they have in common is their propulsion system based on traditional propellers. Putting aside other sources of potential problems, this seems to be the gravest one from operator's point of view. Regardless any protection used, propellers are in hazard of being damaged by obstacles floating in the water. It is important for small vehicles operating in restricted areas such as docks, lakes, pipes, sewage systems, rivers etc. especially. Even a small thing can account for serious mechanical damages. It can hamper work schedule, complicate task and in an extreme situation can lead to loss of a vehicle. It can also generate substantial financial losses. Therefore, regardless of who operates the vehicle and what type of work performs, it is crucial to develop reliable device that secures safe work.

Obviously, any drive failure is unacceptable and the number of unpleasant experiences gained in practice forced designers to search for a new, alternate solution. Bare and ducted propellers, which have been used so far proved to be still vulnerable. Having been developed, propellers' guards improved their safety record significantly, but at the same time decreased efficiency seriously.

The pictures below represent common vehicles in the particular categories.

Figure 3.3: The first ROV used by British Royal Navy to recover torpedoes and mines. [5]

Figure 3.4: A contemporary ROV with ducted propellers additionally equipped with protection grills. [6]

The small, miniature ROV in the pictures below is a good example of both smart design (the way that propellers are protected) and dangerous environment it operates in (e.g., sewage systems, flood channels etc.).

A 

B 

Figure 3.5: The example small ROV used in sewage system maintenance – A [7] B [8].

A 

B 

C 

Figure 3.6: An example AUVs – A [9] B [10] C [11].

A 

B 

Figure 3.7: An example DPVs – A [12] B [13].

Regardless the size and destination of the vehicles we can see the designers took special care of the propellers. With some exceptions of the torpedoes and torpedo-like ones, all of the rest host more or less complex protectors and covers. In particular situations, it took an extreme form (e.g., Figure 3.5 or Figure 3.7 A). Such solutions have negative influence on propulsion's efficiency obviously. Moreover, they limit the range and time of operation for the ones powered by the batteries (AUVs and DPVs).

An alternative solution to this is a use of a waterjet propulsion. Its smaller and compact design makes it less vulnerable to mechanical damages from anything floating in the water as well as such drive system is less prone to sucking-in tether, ropes, strings or any other debris while operating backwards.

The waterjet propulsors are utilized for the following reasons:

— reduction in propeller size for the same thrust
— reduction in thrust variation due to vessel's velocity changes
— protection of rotating elements against mechanical damage
— isolation of rotating components in order to avoid human and animal injuries
— protection of bottom of shallow water channels against scouring by a screw type propeller
— improvement of vessel's manoeuvrability

3.1.3 Waterjet propulsions

History of the waterjet propulsor is relatively short. "The Italian inventor Secondo Campini showed the first functioning man-made pump-jet engine in Venice in 1931." [14] However, the first person to build commercial product was New Zealand inventor Sir William Hamilton in 1954.

The literature dealing with waterjet propulsions of marine vehicles is as comprehensive as that devoted to standard screw propellers both opened and ducted. Propulsors are usually developed as complete sets by commercial companies. Such drive kits are composed of mechanically strong structures forming the flow duct and protecting all active components that define performance of the propulsor. Detailed data, however, are considered to be intellectual property of respective designers. In spite of this restrictions the community of naval architects and marine engineers shares the information to feasible extent. Very important role in knowledge exchange plays Waterjet Group of ITTC that tries to normalize description, nomenclature and tests of the phenomena in waterjet propulsor.

3.1.4 Basic idea of a waterjet propulsor

The waterjet propulsor can be considered as an extension of the shrouded or ducted propeller sometimes known as screw propeller operating in the Kort nozzle. The simplest form of the waterjet propulsion is a pump jet shown in the Figure 3.8. The specific feature of such device is a fluid velocity decrease between the inlet and the rotor inside the duct. Lower velocity results in higher pressure that improves propeller's (rotor's) operating conditions.

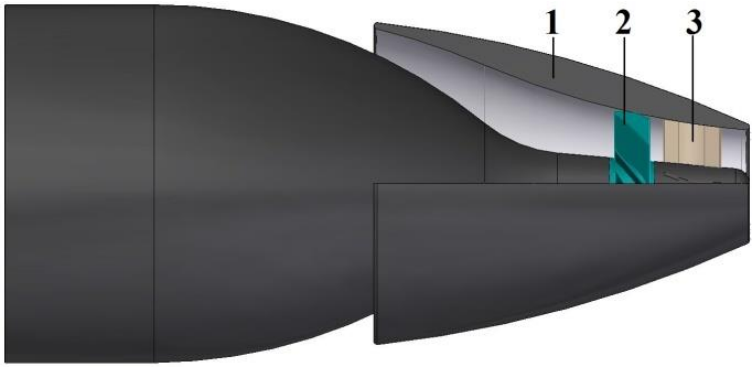

Figure 3.8: The cross section of an exemplary pump jet propulsor. 1 – duct, 2 – rotor, 3 – stator.

This kind of a design has found its use in submarines and torpedoes (Figure 3.10). In addition to its high efficiency, it also generates noticeably less noise in comparison to standard bare propeller [15]. The pump jets are also utilised in the outboard motors.

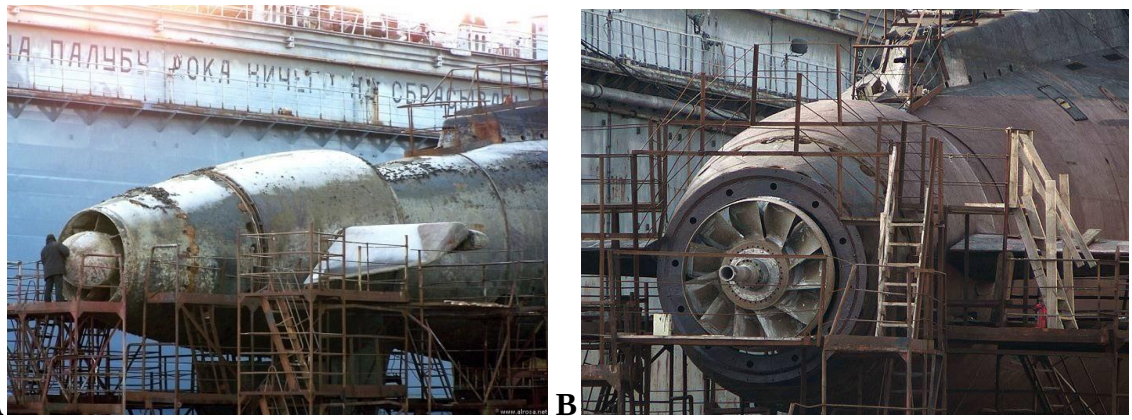

A **B**

Figure 3.9: The exemplary pump jet propulsion: Russian submarine Alrosa A [16] B [17].

Figure 3.10: The exemplary pump jet propulsion: torpedo [18].

[19] In general, waterjet propulsor's design and principle of operation are similar to very popular in use air jet engines. The main differences are:

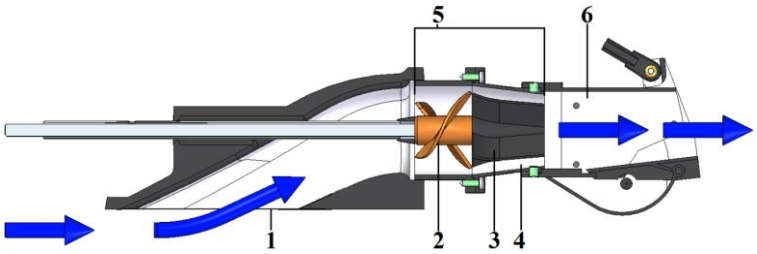

Figure 3.11: Longitudinal section-view of an exemplary waterjet propulsor. Description: 1 – inlet, 2 – rotor, 3 – stator, 4 – outlet nozzle, 5 – pump, 6 – steering nozzle and reversing bucket; the blue arrows – impellent flow direction (water).

Although basic principle in operating is the same for every jet drive, different waterjet propulsion systems can be designed in various ways. There are many combinations of different inlet areas, tunnel shapes as well as outlet nozzles and steering buckets. What characterises them though, is interaction between propulsion and hull – very important correlation greatly influencing propulsion overall efficiency.

As the Figure 3.11 shows, waterjet propulsion can be divided into three main components, which are as follows:

— inlet
— tunnel
— pump – regarded as rotor or rotor-stator pair
— outlet nozzle – often outlet nozzle hosts stator
— steering bucket

The water flow phenomenon inside the waterjet propulsion is complicated and in practice it is impossible to monitor every region of a device properly and precisely. To overcome this, computational simulations (CFD) can be used. They are very useful in visualising flow behaviour inside the tunnel, pump and outlet nozzle.

The very comprehensive general description of the WJ can be found in "Final Report and Recommendations to the 23rd ITTC" [20].

The very basic approach bases on pressure jump expected to be delivered by designed pump [21], [22]. This model is regarded as relatively solid – it simplifies simulations, lowers model mesh count and shortens calculations time. However, it comes with higher risk of error. E.g., as presented by Ricardo Broglia et. al. [23] simulations' errors can be significant and reach about 15%. Or in other words, in this case circulation trial can end up more that ship's length further than it should.

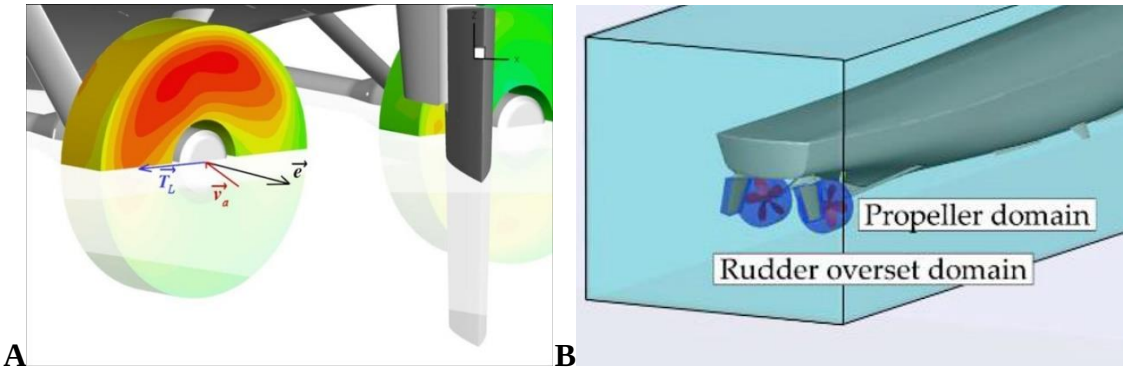

Figure 3.12: Examples of rotor modelling in CFD simulations: A – body-force model; simplification with a use of rotating cylinder (sometimes it can be swirling disc) representing rotor [23]; B – virtual model of investigated rotor [24]. The same modelling scheme applies to waterjet drives.

Nonetheless, with some experience, knowledge and skills in using CFD very good results can be obtained with both methods. Yong Zhang et al. [25] achieved very good corelation

between multiple reference frame model (MRF), sliding mesh model and body-force model. Despite some disparities in velocity fields (cross-section area at station 3 – rotor's inlet, see Figure 6.1), table data look impressive.

Fr	MRF $(1-w_M)$	BFM $(1-w_B)$	$(1-w)$ Error $(=\frac{(1-w_B)-(1-w_M)}{1-w_M})$	MRF C_{mM}	BFM C_{mB}	C_m Error$(=\frac{C_{mB}-C_{mM}}{C_{mM}})$
0.300	0.8467	0.8465	−0.02%	0.8711	0.8710	−0.01%
0.400	0.8521	0.8511	−0.12%	0.8768	0.8763	−0.06%
0.500	0.8569	0.8543	−0.30%	0.8817	0.8794	−0.26%
0.542	0.8555	0.8512	−0.50%	0.8808	0.8762	−0.52%

Figure 3.13: Simulations' results and different models' comparison. Where MRF stands for multiple reference model and BFM stands for body-force model (rotating cylinder). [25]

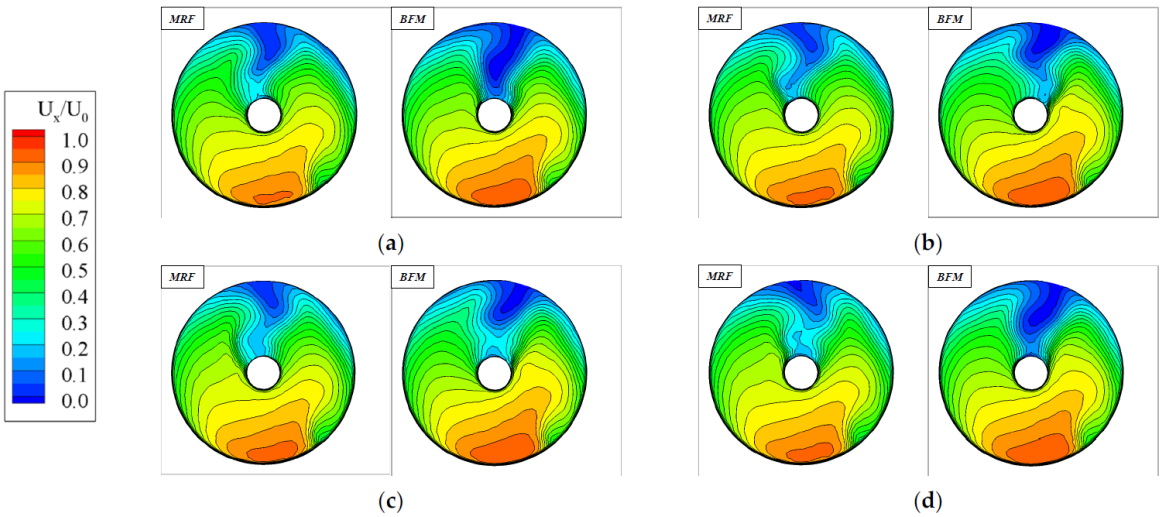

Figure 16. Comparison of non-dimensional axial velocity distribution of the MRF model and body-force model (BFM) at station 3. (**a**) Fr = 0.3; (**b**) Fr = 0.4; (**c**) Fr = 0.5; (**d**) Fr = 0.542.

Figure 3.14: Velocity fields comparison for different modelling methods. [25]

Very important matter that has to be bared in mind while performing simulations predicting waterjet propulsion performance is an interaction between waterjet drive and ship's (vehicle's) hull. Detailed investigation, based on simple-shaped bare hull equipped with single waterjet units was done by Arash Eslamdoost in his licentiate thesis [26] and then analysed in more details in his doctoral dissertation [27].

The experimental investigation, performed on scale-model was done by Tom van Terwisga [28].

Jie Gong and his research team analysed flow around a hull with transom aft equipped with four waterjets. Subsequently, simulations' results were compared with scale-model tests performed in a towing tank [29].

Similar investigation was done by Lei Zhang et al. This time however, it was trimaran with main hull equipped with three waterjet propulsors. Overall, the researchers achieved good convergence between CFD simulations and a flow tank – especially in hull resistance and waterjet thrust measurements [30].

3.1.5 Inlet – flash and ram intake for waterjet propulsors

The impellent inlet characteristics are:

— *flush intake:* standard design in waterjet drives, where the impellent inlet velocity magnitude is smaller than the vehicle pace (it is caused by flow direction changes) (Figure 3.15 A)
— *ram (scoop):* in waterjet propulsions uncommon in use because of its protruding elements (Figure 3.15 B), however a standard solution for jet planes

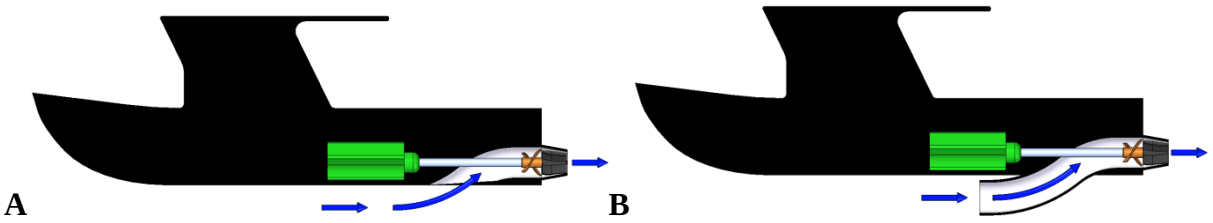

Figure 3.15: Graphical illustration of waterjet flush (A) and ram (scoop) (B) intake.

The shape and size of waterjet inlet is a matter of discussion. There is no one, fixed solution and optimal form and dimensions depend on operating point and hull shape for particular case. The Specialist Committee on Validation of Waterjet Test Procedures in its "Final Report and Recommendations to the 23rd ITTC" [20] recommend inlet in rectangular shape. However, Tom van Terswiga [28] and Scherer et al. [31] claim to achieve results converging within 0.5% for different inlet shapes but with roughly similar proportions – rectangular inlet length had 1.3x inlet width, whereas elliptical one had 1.5x inlet width.

In terms of inlet size, according to 23rd ITTC recommendations [20], previous investigations delivered only about 1% differences in ultimate outcomes for intake capture area variation of 20%.

Contrary to the studies above, Weixuan Jiao et al. [32] proved significant influence of inlet area shape on overall waterjet drive performance. According to their investigation inlet velocity ratio – determined by form and size of an inlet for the same operating conditions – in most cases should include between 0.78 and 0.96. It should provide good balance between high efficiency and low cavitation risk.

In order to improve inflow into the waterjet tunnel even further, vortex generators can be implemented. As Lewis Manunga and Ian Huntsman investigation has shown, it can improve inflow up to 28%. However, it is very important to place generators properly and their location depends on expected operating conditions [33].

3.1.6 Tunnel

The tunnel transports impellent into and out of the pump. Its shape determines pressure and velocity distribution in the propulsion and has direct influence on pump and drive performance.

Figure 3.16: The exemplary shapes of waterjet drive tunnels – sources: A [34], B [35], C [36].

[37] According to the investigation done by Xionghuan Chen et.al. tunnel length has rather minor importance in terms of overall waterjet propulsion efficiency. The utmost difference between outcomes is about 3% (see the Figure 3.18).

The inlet length in this analysis was defined as a straight section of the tunnel (see the Figure 3.17 below).

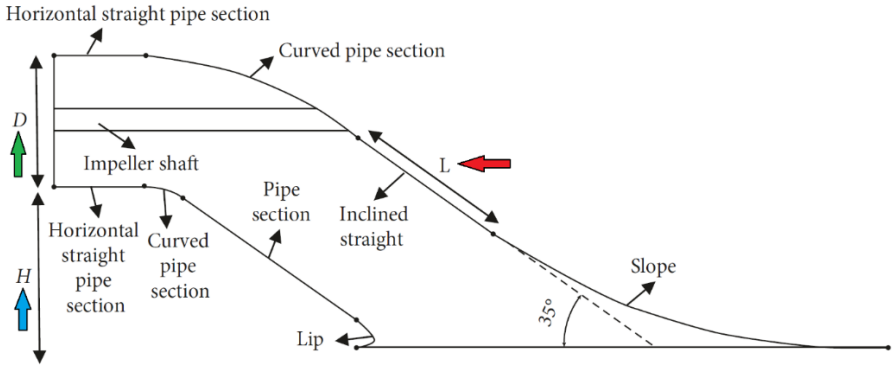

Figure 3.17: The schematic diagram of analysed waterjet propulsor. "L" represents investigated tunnel inlet length, "D" constant tunnel diameter and "H" stands for tunnel height and changes proportionally to length changes. [37]

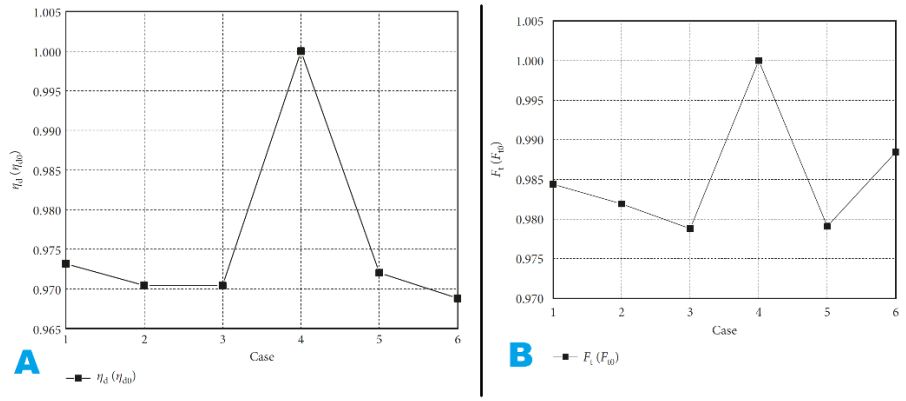

Figure 3.18: The simulation results for six different length of the inlet duct. A – waterjet efficiency, B – waterjet thrust force. [37]

3.1.7 Pump

Generally, this section might be regarded as a standard pump – that is a pair of rotor and stator – hence, because of extensive bibliography available, there is no need of detailed description here. In most cases, it is diagonal or axial pump. However, in case of outboard motors, it might be a helicoidal one. Outboard waterjet centrifugal pumps are supplied by a combination of scoop and flush type intake (see the Figure 3.15). Such drives are perfect for shallow-water boats because of its low draught – contrary to outboard motors with standard screw propellers jet drives demand draught just below vessel bottom. Moreover, it is less prone to many mechanical damages.

In some cases, utilisation of axial pump can be preferred as they tend to have smaller diameter, occupy smaller volume and can be fitted into slender aft [38].

The pump itself, as mentioned earlier, can be modeled in three different ways:

— Rotating disc or cylinder representing operating rotor [21], [22], [23]
— Multiple reference model (MRF) or sliding mesh model [24], [39], [40], [41]
— Interpenetrating mesh model – very specyfic modelling, where solid, meshed body is put inside analysed domain. Uncommon in use because of difficulties in boundary layer solution.

Jinxin Wu et al. [42] proposed interesting solution – an external jet stream injected perpendiculary into the tunnel somewhere between station 4 and 5 (see the Figure 6.1).

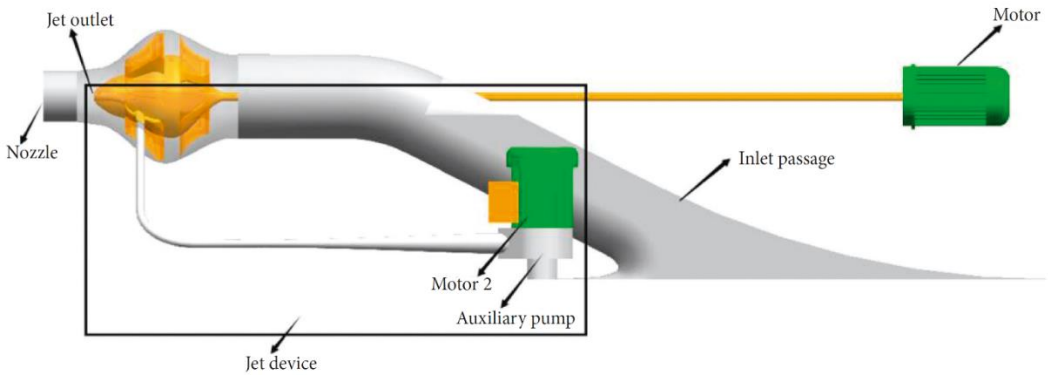

Figure 3.19: Visualization of the idea proposed by Jinxin Wu et al. [42]

3.1.8 Jet stream direction control – outlet nozzle and steering bucket

STEERING NOZZLE – (with an exception of outboard motors mentioned above) outlet nozzle can be ended with steering device. This very clever mechanism allows manoeuvring on limited area easily and precisely. It also gives a possibility to turnarounds, side movements, reversal and backward movements without requirement of motor revolutions direction change. Below, in the pictures Figure 3.21 and Figure 3.22 the different combinations of steering device settings are shown. Longitudinal cross sections visualise flow through the nozzle and arrows in the Figure 3.23 represent particular forces and moments during each manoeuvre.

Figure 3.20: The exemplary waterjet drive steering nozzles – sources: A [43], B [44], C [45].

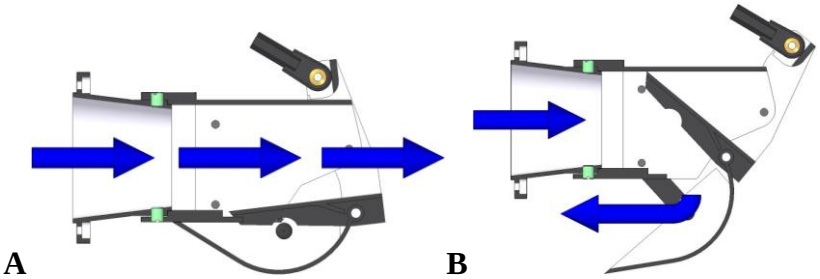

Figure 3.21: Flow through waterjet steering-reversing nozzle: A – FORWARD, B – BACKWARD.

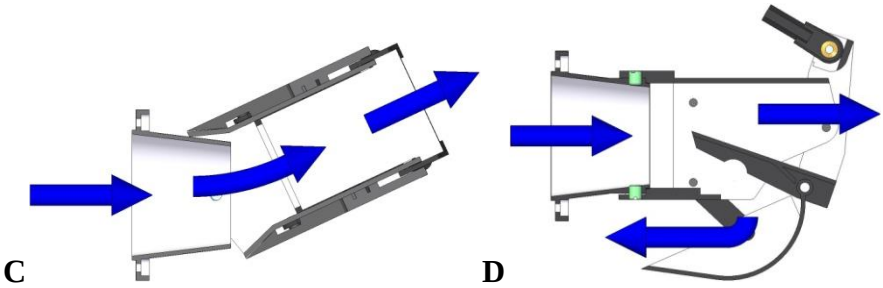

Figure 3.22: Flow through waterjet steering-reversing nozzle: C – TURN, D – STOP.

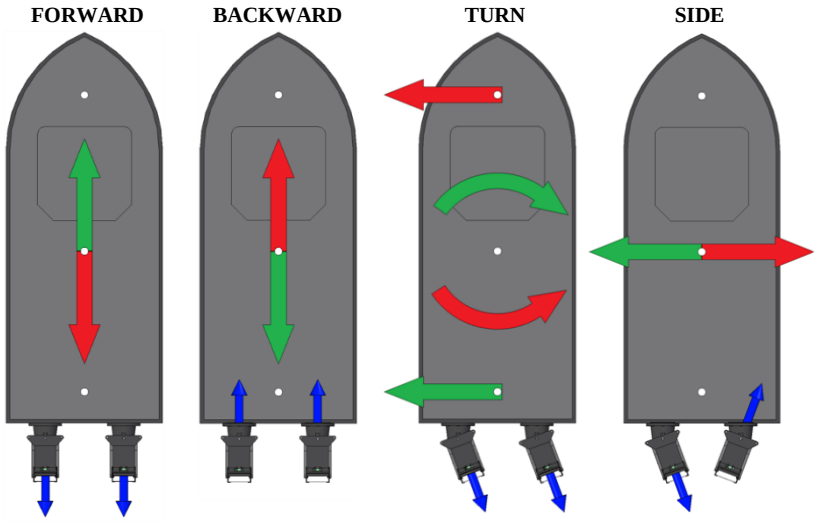

Figure 3.23: Waterjet steering nozzle positions for different movement directions. The green arrows indicate vehicle movement directions, the blue arrows show thrust force directions and the red arrows represent thrust resultant forces. Curved arrows stand for moments generated by corresponding forces.

3.2 Waterjet drive for variable operating conditions

The propulsion design is always optimised for one particular operating point. Any other operating conditions compromise drive's performance. However, naval engineers tried to develop design with much wider scope. In the case of standard screw propellers, it resulted in variable blades' angle. The waterjet propulsor is more complex with much more components. All these elements have to cooperate at the same time and any interference into this structure influences the efficiency at different rate. Therefore, potential optimisation, theoretically, opens significantly more possibilities than the one for standard propellers. In practice, there are three elements that geometry can be variable and moveable:

— tunnel inlet area
— rotor's blades pitch
— outlet nozzle / reversing bucket

The good example of such device is waterjet drive from *Intelli Jet Marine Inc*. The designer introduced unique at three mentioned areas:

— sliding plate at the propulsion intake (red in the Figure 3.24) allowing to alter inlet area
— controllable pitch impeller (green in the Figure 3.24) to adapt rotor's blades settings to particular revolution speed
— peculiar, rectangular outlet nozzle (blue in the Figure 3.24) capable of expanding or narrowing the outlet area in order to control propulsor's thrust

The proper change of the settings of all these three elements, according to the inventor, widens propulsor's operating window and allows maintaining high performance.

Although it is difficult to give precise numbers, the table below compares and contrasts different types of propulsions – the higher digit the better. The table contains selected quotes from the product official web site.

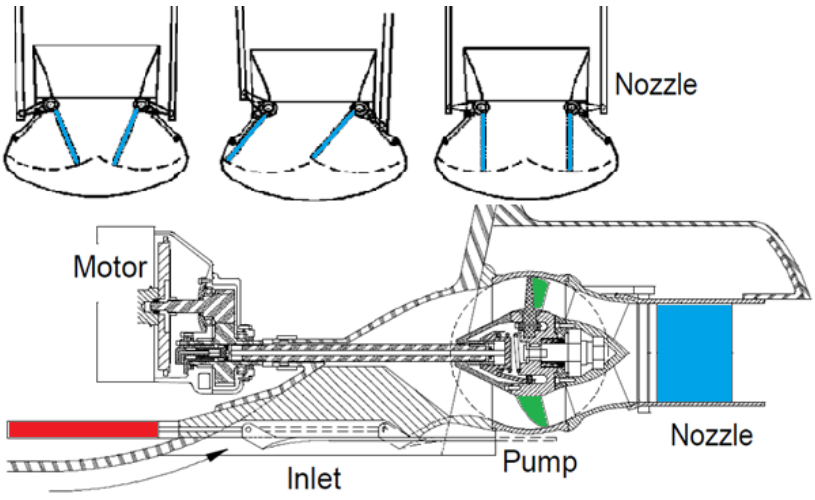

Figure 3.24: The *Intelli Jet* drive scheme with highlighted key elements (based on [46]).

Figure 3.25: The Intelli Jet. [46]

Table 3.1: The comparison of different propulsion types (based on [46]).

no.	feature	screw propeller	podded propeller	constant geometry waterjet	variable geometry waterjet
1	efficiency	4	4	3	4
2	low noise operation	4	4	4	5
3	thrust at various velocities	5	5	4	5
4	acceleration	5	5	3	5
5	manoeuvrability	3	4	2	5
6	safety of operation	3	3	5	5
7	obstruction (size)	3	4	5	5

3.3 Further information

Further, detailed studies of the phenomena appearing inside waterjet propulsors can be found in various doctorate theses, analysis and research rapports such as: “Marine Waterjet Propulsion” [47], First International Symposium on Marine Propulsors in Trondheim [48], “Comparison of waterjet performance in tracked vehicles by impeller diameter” [49], “Numerical and Experimental Evaluation of Waterjet Propelled Delft Catamarans” [50], “Waterjet propulsion system tested in a wind tunnel and compared with numerical simulation” [51], “Numerical Analysis of a Waterjet Propulsion System” [52], “Study of a jet-propulsion method for an underwater vehicle” [53], “Experimental investigation into the performance of the axial-flow-type water jet according to the variation of impeller tip clearance” [54], “ROV with waterjet propulsion” [55], “Pressure distribution and losses in a waterjet propulsion system” [56], “measurements of basic performance for waterjet propulsion system in water tunnel” [57], “CFD and submerged waterjets” [58] et al.

The first steps in preliminary design can be done with a use of work of: professor Wiesław Próchnicki [19] and Kourosh Koushan [59].

The very basic information, but essential in designing and developing waterjet drive can be found in books dealing with the topic “Submersible vehicles. Construction and equipment” [60], “Ship theory” [61], “Hydrodynamics of High-Speed Maritime Vehicles” [62].

4 Object of investigation

4.1 Overall characteristic of the GLUPTAK system

The remotely operated GLUPTAK type vehicle was selected for considerations presented in this work. The GLUPTAK is a small, torpedo like underwater vehicle, powered by internal source of energy. It is used to identify and destroy naval mines by means of the bow mounted shaped charge. The vehicle is able to reach the target up to 400 meters away from a launch point. It is capable of operating in adverse environmental conditions of sea current up to 2.0 [m/s] with maximum velocity of 1.0 [m/s] (relative to sea bottom). This requires vehicle velocity of 3.0 [m/s] relative to the water. In such current conditions, the mission task must be accomplished in just 11 minutes. The two restraining factors here are:

— limited energy capacity of the internal battery pack
— available length of the optical cable utilized to control the vehicle.

For this reason, efficiency of the propulsion system of the vehicle needs to be as high as possible. In addition, the shaped charge used as destruction device is directional and requires precise aiming. This imposes demand of high manoeuvrability of the vehicle itself and the two-axis mounted articulated warhead of the shaped charge.

In horizontal plane, the GLUPTAK vehicle is propelled by means of 4 screw propellers. The fifth propeller, built into the vehicle's hull, is used to control its vertical movement. It was placed at the centre of the vertical drag of the vehicle to minimise tilting during ascent and descent.

Figure 4.1: The GLUPTAK vehicle in its basic configuration – side view.

The horizontal propellers are arranged in X configuration as show in the picture below. Additionally, axes of the propeller shafts are inclined 7 degrees relatively to the longitudinal axis of the vehicle. Such inclination angle is high enough to double the turning moment generated by the propellers.

Figure 4.2: The GLUPTAK vehicle with propellers with a mesh-guard configuration – stern view. Arrangement of four screw propeller set. Directivity of the propellers is colour-coded to avoid mistakes during assembly.

While the vehicle is moving forward, the left pair of the propellers rotates anticlockwise and the right pair rotates clockwise. This solution helps to stabilise the vehicle and reduce rolling moment acting on the vehicle. The rolling moment is caused by torque of the propellers and speed changes of the motors due to inertia of the rotating components. To facilitate manoeuvrability of the vehicle the speed of each propeller is linearly controlled at the range ± 3200 [rpm].

The specific operating conditions of the GLUPTAK vehicle defines requirement regarding its motion capabilities. Two basic modes of operation are considered:

— operation in still water: water current velocity < 0.5 [m/s]
— operation in water current: water current velocity 0.5 ÷ 2.0 [m/s].

Given the maximum turning moment generated by the two pairs the horizontal thrusters working in opposite directions, the highest water current velocity allowing the operator to manoeuvre the vehicle is 0.5 [m/s]. Above this current velocity, the vehicle is only capable of running forward against the current. It can still be inclined from the current line a few degrees in any direction by means of the differentiating of the propellers speed.

In still, calm water, the GLUPTAK vehicle is able to manoeuvre quite well. However, reversing of the horizontal thrusters is to be avoided due to the danger of mechanical destruction of the tether (control fibre).

The propellers of the GLUPTAK vehicle are three-blade Wageningen series propellers of 0.3 surface coefficient and P/D=0.635, designed to operate with optimum performance in forward direction and the design parameters are:

Table 4.1: The GLUPTAK vehicle's screw propeller parameters.

no.	parameter	symbol	unit	value
1	speed	n	[rps]	49
2	advance coefficient	J	[-]	0.49
3	thrust coefficient	K_T	[-]	0.0975
4	thrust	T	[N]	23.0
5	torque coefficient	K_Q	[-]	0.0125
6	torque	Q	[Nm]	0.3
7	efficiency	η	[%]	60.6

The screw geometry was calculated using basic formulas [61] and corrected for real operating conditions using experimental evaluation. The propeller's K_T, K_Q and η characteristics are presented in the chart below (Figure 4.3):

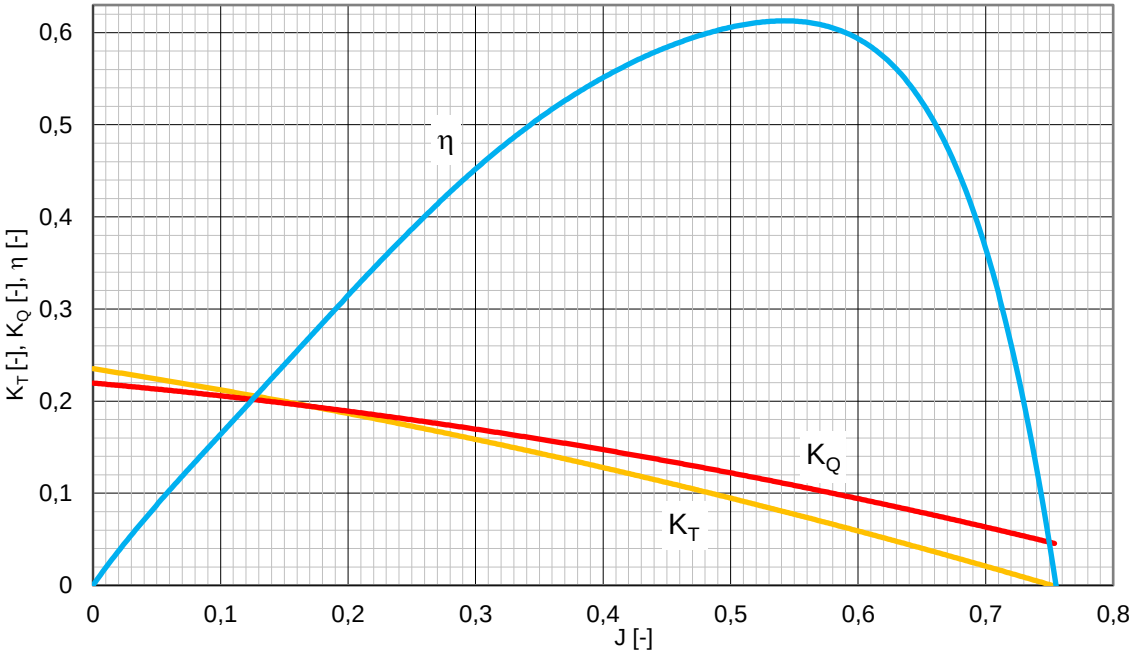

Figure 4.3: The K_T and K_Q coefficients as well as η of the PG-100 propeller designed for cruising speed of 3.0 [m/s].

The propulsion system based on the screw propellers proved to be effective in assumed conditions. However, the propellers are vulnerable to numerous mechanical damages. They are in danger of sucking in plenty of different debris floating underwater (such as seaweeds, ropes, plastic bags, its own tether etc.). An example of such an incident is shown in the Figure 4.4. It proves that relatively thick (3.0 [mm] in diameter) and Kevlar reinforced cable can be easily sucked into the propellers and damaged. The problem is even more serious in case of bare optical cable which is just 0.25 [mm] thick.

Figure 4.4: The tether entangled in one of the propellers of the GLUPTAK vehicle.

To reduce the threats and improve handling capability other arrangements of the propulsion system were considered. A kind of mesh-guard was developed as the simplest solution to this problem. Its effectiveness was proved during series of experiments. It was not perfect but worked to acceptable extent. However, introduction of the guard has increased vehicle's drag by 35% approximately. Such a significant increase of the drag is critically negative factor for the vehicle supplied by internal and limited source of energy. Considering the guard to be a part of the propulsion system, the total efficiency of the propulsion system is 40%, whereas the arrangement without the guard has the efficiency at 60% level.

4.2 Drag force of the GLUPTAK vehicle

The external hull of the GLUPTAK vehicle is composed of the spherical bow, the cylindrical middle section and the conical stern section. The conical section contains propulsion main mechanical components:

- electric motors
- propulsion shafts
- propellers (in standard configuration)
- waterjet tunnels with built-in stators (in waterjet drive configuration)
- rotors (in waterjet drive configuration)

The drag forces of the GLUPTAK vehicle in different configurations are shown in the chart below (Figure 4.5).

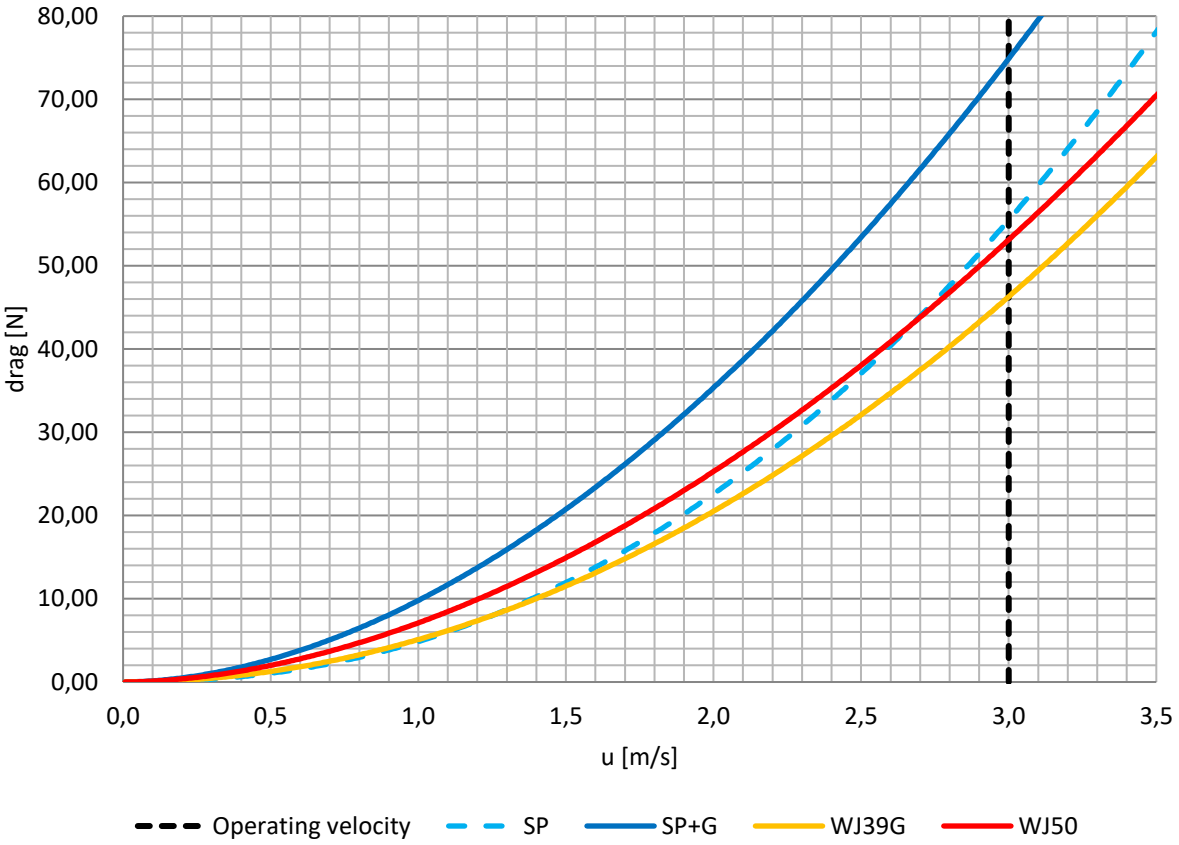

Figure 4.5: Drag curves of the GLUPTAK vehicle in different configurations.

The notations used in the description refer to: *SP* – screw propellers; *SP+G* – screw propellers with mesh-guard; WJ39G – Graupner's waterjet drive (39 [mm] rotor diameter); WJ50 – newly designed waterjet drive (50 [mm] rotor diameter).

Table 4.2: Drag, power consumption and performance comparison for selected vehicle's configurations for vehicle's velocity 3.0 [m/s].

no.	propulsion type	R_{TOTAL} [N]	$T_{per\ propeller}$ [N]	n [rpm]	η	N_d [W]
1	SP	53.5	13.38	2400	57.0%	75
2	SP+G	75.0	18.75	2700	57.0%	110
3	WJ39G	46.0	11.50	5800	17.4%	200
4	WJ50	52.0	13.00	5700	25.5%	135

4.3 Toward development of the waterjet propulsion

Among available solutions for the GLUPTAK vehicle, the waterjet propulsors seemed to be the most promising as the screw propellers replacement. Especially that the protection-grill is obligatory due to tether safety reason. However, because of vehicle's rather small dimensions and low speed, low performance of this arrangement was expected. It also required detailed study regarding its geometry and operating parameters. This work is devoted to study the efficiency of the waterjet propulsors operating in forward direction (without reverse). It means

maximum forward velocity of 3.0 [m/s], that assures operation at water current as fast as 2.0 [m/s] with minimum vehicle's velocity relatively to the sea bottom of 1.0 [m/s].

5 Theoretical performance of the waterjet propulsor

5.1 Power of waterjet propulsion

The thrust force is generated by the jet stream ejected out of the outlet nozzle at the station 6 (see the Table 6.1). It is a product of mass flow rate and difference of absolute velocities at propulsion outlet and inlet.

$$F_u = m \cdot (c_2 - c_1) \quad [N]$$

5.1

The absolute inlet velocity c_1 is:

$$c_1 = w_1 - u \quad \left[\frac{m}{s}\right]$$

5.2

Whereas the absolute outlet velocity c_2 equals to the difference between relative outlet velocity and vessel velocity:

$$c_2 = w_2 - u \quad \left[\frac{m}{s}\right]$$

5.3

Therefore, substitution 5.2 and 5.3 to 5.1 – and simplifying by assumption that tunnel relative inlet velocity w_1 is equal to vehicle's velocity u – results in thrust force of working jet propulsor:

$$F_u = m \cdot (w_2 - u) \quad [N]$$

5.4

The greatest thrust force value available is generated for zero forward speed, which means high jet thrust force at vehicle start.

$$F_u|_{u=0} = m \cdot w_2 = F[N]_{umax}$$

5.5

Effective propulsion power is a product of thrust and vessel velocity:

$$N_u = F_u \cdot u = m \cdot (w_2 - u) \cdot u \quad [W]$$

5.6

The power of the outlet jet stream is described by equation:

$$N_{out} = m \cdot \frac{c_2^2}{2} = m \cdot \frac{(w_2 - u)^2}{2} \quad [W]$$

5.7

The pump power required to supply the propulsor is described by power balance equation:

$$N_p \cdot \eta_p = N_u + N_{out} + N_{Loss} \quad [W]$$

5.8

5.2 Efficiency of waterjet propulsion

[19] Waterjet propulsion drive efficiency is determined by effective power to pump power ratio:

$$\eta_{WJ} \stackrel{\text{def}}{=} \frac{N_u}{N_p} \quad [-]$$

5.9

Therefore, it takes the form:

$$\eta_{WJ} = \frac{N_u \cdot \eta_p}{N_u + N_{out} + N_{Loss}} \quad [-]$$

5.10

Propulsion drive efficiency could also be written as a product:

$$\eta_{WJ} = \eta_{WJ}^o \cdot \eta_p \quad [-]$$

5.11

Thus, for $\eta_p = 1$ and after simple transformation, tunnel drive efficiency takes the form:

$$\eta_{WJ}^o = \frac{N_u}{N_u + N_{out} + N_{Loss}} \quad [-]$$

5.12

Additionally, introducing non-dimensional velocity index

$$\mu = \frac{u}{w_2} \quad [-]$$

5.13

And transforming equation 5.12 it is possible to write it in following form:

$$\eta_{WJ}^o = \frac{2 \cdot (1 - \mu) \cdot \mu}{1 - \mu^2 + 2 \cdot \frac{N_{Loss}}{m \cdot w_2^2}} = \frac{2 \cdot (1 - \mu) \cdot \mu}{1 - \mu^2 \cdot \left(1 - 2 \cdot \frac{N_{Loss}}{m \cdot u^2}\right)} \quad [-]$$

5.14

Graphical representation of this relationship is presented in the Figure 5.1.

For summary energy of different losses in the propulsor as described by relation:

$$\sum \zeta = 2 \cdot \frac{N_{Loss}}{m \cdot u^2} \quad [-]$$

5.15

It is possible do determine drive efficiency as a function of non-dimensional velocity index and energy losses:

$$\eta^o_{WJ} = \eta^o_{WJ}\left(\mu, \sum \zeta\right)$$

5.16

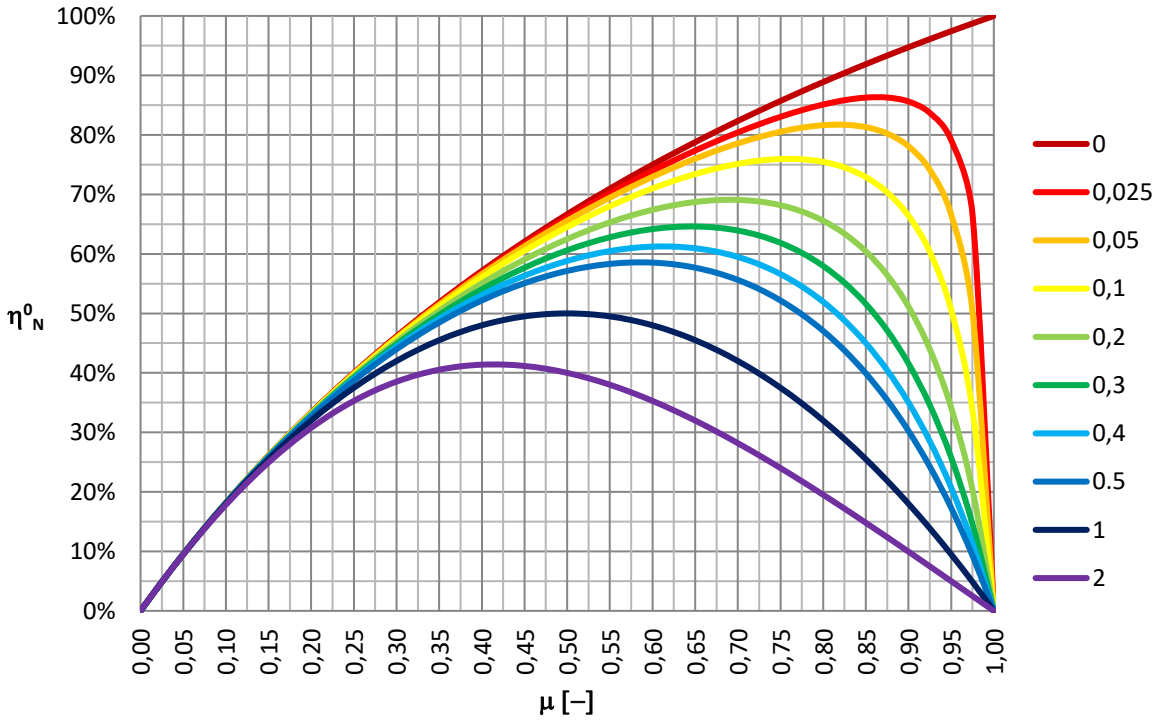

Figure 5.1: Theoretical efficiency of waterjet propulsion $\eta^0_{WJ} = \eta^0_{WJ}(\mu, \sum \zeta)$ for $\eta_p = 1$.

Whereas condition:

$$\frac{d\eta^o_{WJ}}{d\mu} = 0$$

5.17

Allows determining optimum non-dimensional velocity index:

$$\mu_{opt} = \frac{1}{1 + \sqrt{\sum \zeta}} \quad [-]$$

5.18

As well as maximum efficiency of considered propulsion:

$$\eta^0_{WJ\,max} = \eta^0_{WJ}(\mu_{opt}) = \frac{1}{1+\sqrt{\sum \zeta}} \quad [-]$$

5.19

Waterjet drive efficiency can also be obtained from ratio of two velocities: jet outlet velocity w_2 and vehicle's velocity u as a function of non-dimensional fluid flow energy loss coefficient ζ – as indicated in the Figure 5.2.

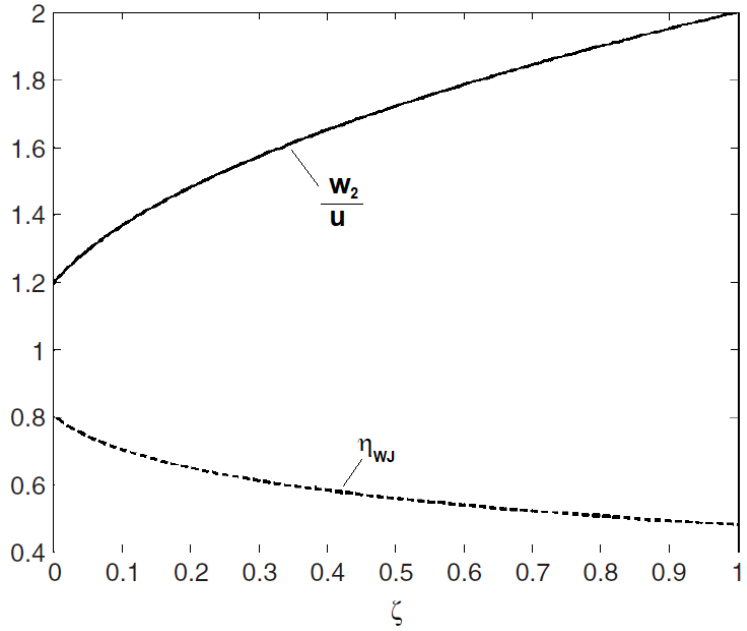

Figure 5.2: Waterjet efficiency as a function of energy loss coefficient and corresponding values of jet outlet velocity to vehicle's velocity ratio. [62]

6 Semi-empirical description of the waterjet propulsor

Two different methods were used to describe energy losses in the waterjet propulsor tunnel:

— the general method describing the flow through the pipe
— Albert Fliegner's method (directly related to waterjet drive)

6.1 Characteristic points of waterjet propulsion

Characteristic points were used in waterjet description and indicated in the Figure 6.1. These points are also measurement points and in accordance with 23rd ITTC guidelines [20] are as follows (Table 6.1):

Table 6.1: Waterjet propulsor's station points according to 23rd ITTC guidelines.

station no.	location
0	free, undisturbed stream far ahead of the vehicle; the point is set far enough from the propulsion inlet that it has no influence over the flow
1	inlet point of tangency (according to 21st ITTC form 1996; later changed into point 1a)
1a	the new location for the inlet point; the distance between points 1 and 1a is equal to inlet width – it is assumed that this is the last point, where there is no interaction between undisturbed flow outside the propulsion (around the vessel hull) and the tunnel inlet
2	inlet throat – the point where the inlet cross section area is measured (A_{D1}) as well as inlet velocity $w_1=w_{D1}$
3	pump face – the point that determines the diffuser inlet and where the diffuser inlet velocity is measured
4	internal pump point – the measurement point set between rotor and stator (the confusor inlet)
5	pump exit – the point set at the confusor outlet (pump exit), where the propulsion relative outlet velocity is measured
6	outlet nozzle point – might not exist and might be merged with point 5 if the outlet nozzle ends at the same point as the stator
7	the vena contracta point (distance from the nozzle depends on outflow velocity)

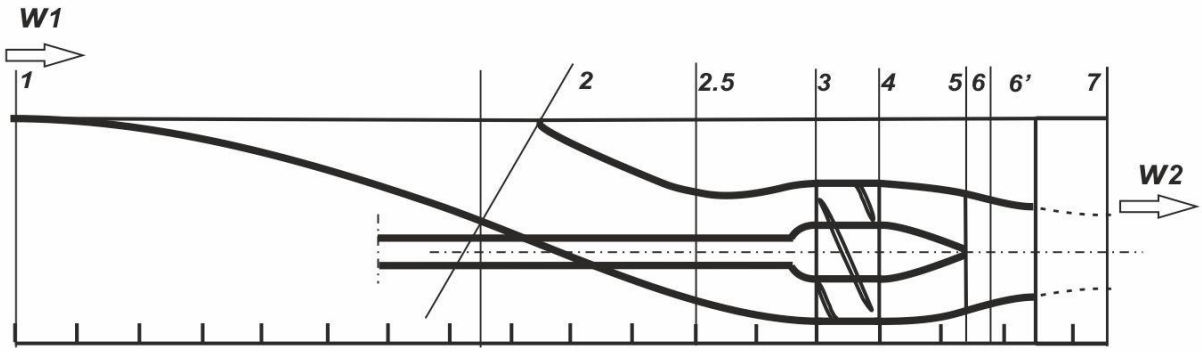

Figure 6.1: The layout of the characteristic points (stations) and velocity symbols for a waterjet drive.

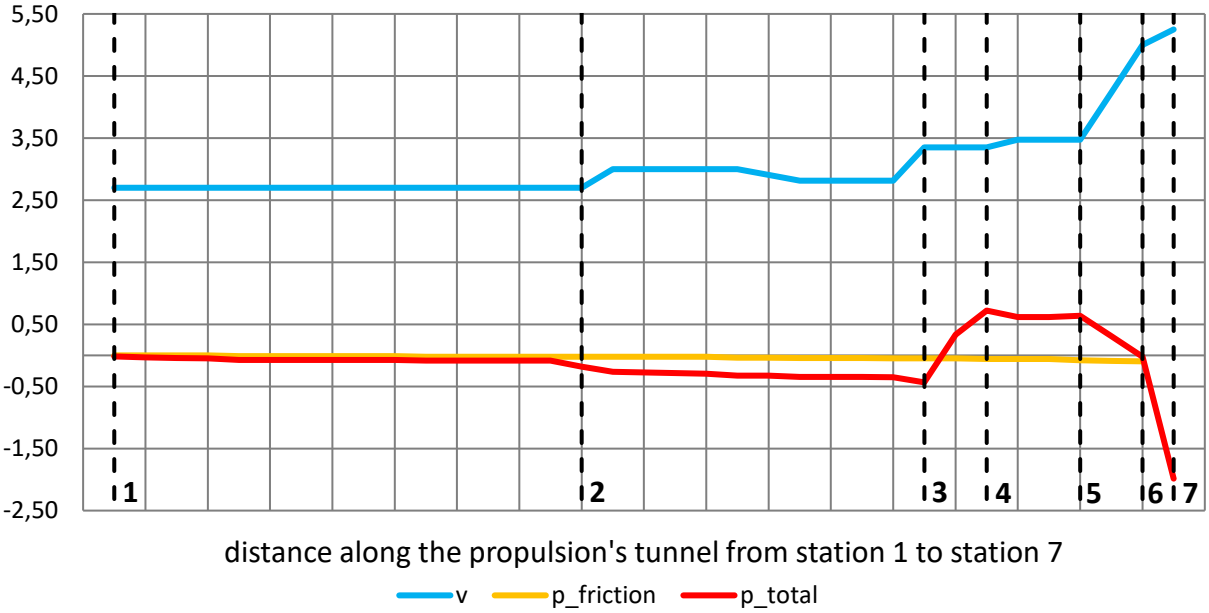

Figure 6.2: Pressure and velocity distribution throughout the waterjet tunnel.

Notation:

v – velocity inside the propulsion tunnel [m/s]

p_friction – pressure loss due to friction [mH_2O]

p_total – total pressure inside the tunnel [mH_2O]

6.2 Elements of the waterjet flow duct

The station points listed in the previous subsection give the possibility to divide the waterjet propulsor into sections (elements). Each of these elements affects the summary flow losses in the propulsor's duct at different rate and their estimation is crucial for the design process. The elements refer to particular parts of the propulsor's geometry.

The flow losses estimation for each element delivers the design guidelines for the designer. It allows for control of the flow inside the propulsor's tunnel in order to meet the requirements for specific operating point with maximum efficiency.

Table 6.2: The waterjet duct elements described using the station points.

no.	element of the waterjet duct	limiting stations
1	undisturbed flow far ahead of the vehicle	0 – 1a
2	area in front of the inlet influencing flow (boundary layer)	1a – 1
3	flow duct (the tunnel) as source of the friction losses	1 – 5
4	the inlet	1
5	the inlet bend	1 – 2
6	the tunnel bend	2 – 3
7	the diffuser	3 – 4
8	the pump	3 – 5
9	the outlet nozzle (confusor)	4 – 5
10	the nozzle end	5 – 6
11	distance to the vena contracta point	6 – 7

6.3 Semi empirical models describing the tunnel losses

The analyses of phenomena in the fluid flow are performed in order to determine the losses mainly. They are expressed by pressure (head) losses and energy (power) losses.

[63] The general theory of flow through the closed pipes divides the pressure losses in into two main elements:

— the losses generated by fluid viscosity and pipe wall roughness (so called linear or friction losses)
— the losses generated by local disturbances in the flow such as changes of the tunnel geometry (so called local losses)

Therefore, sum of flow losses expressed by pressure drops in fluid flowing through a closed pipe is as follows:

$$h_S = \sum h_l + \sum h_o \quad [m]$$

6.1

Traditionally pressure changes in flow through pipes are expressed in meters of water [m] (hydraulic head), that corresponds to pressures generated by pumps expressed in the same units.

The general equation describing flow energy (head) losses is Weisbach's formula:

$$h_{l()} = \zeta_{()} \cdot \frac{v^2}{2 \cdot g} \quad [m]$$

6.2

The ζ coefficient is the loss coefficient depending on local geometry of the pipe such as diameter reduction or expansion, pipe bend, protection grill etc.

The loss coefficient can also be used to express power loss:

$$N_{l0} = \zeta_0 \cdot \frac{m \cdot v^2}{2} \quad [W]$$

6.3

6.4 General model of the tunnel losses

During more than 100 years of research several formulas were developed by researchers for modelling of the fluid flow in the pipe-like structures. Well supported models and formulas were selected in this work to allow basic calculations. It was also decided to utilize the one-dimensional Bernoulli Equation, which uniquely relates velocity and pressure if the usually used simplifying assumptions are valid. In this work, main focus was put on losses in flow phenomenon and coefficients related with it. To determine these coefficients there are various methods available and a few selected are presented below.

Since in considered case energy is conserved along the streamline, the Bernoulli Equation expressed as 6.4 is adopted. Using the equation, we see that increasing the velocity of the flow will reduce the pressure, decreasing the velocity will increase the pressure.

$$p_p + \frac{\rho \cdot v^2}{2} + \rho \cdot g \cdot h = constant$$

6.4

Where p_p is pressure at considered point, $\frac{\rho \cdot v^2}{2}$ represents dynamic pressure and $\rho \cdot g \cdot h$ stands for hydraulic head.

The flow can be laminar or turbulent, but – given considered case – the turbulent one is the dominant force.

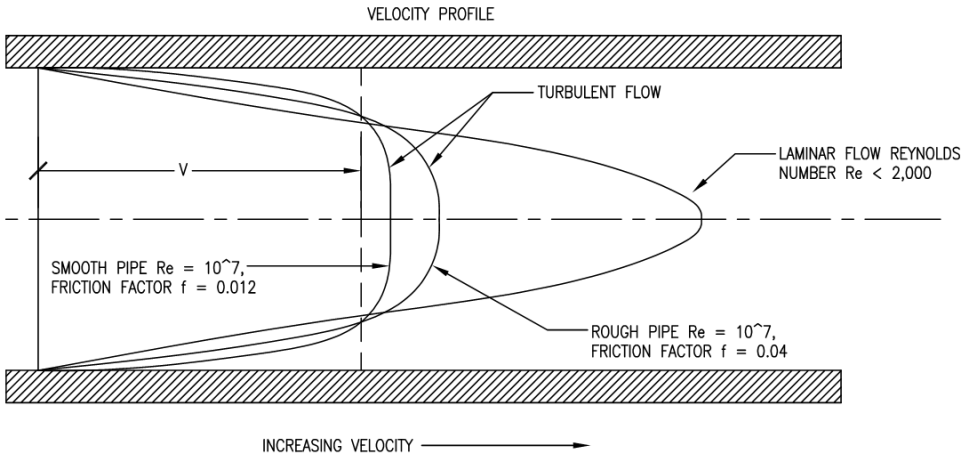

Figure 6.3: Velocity profile inside the pipe for laminar and turbulent flow. [64]

6.4.1 Friction in the tunnel – straight pipe

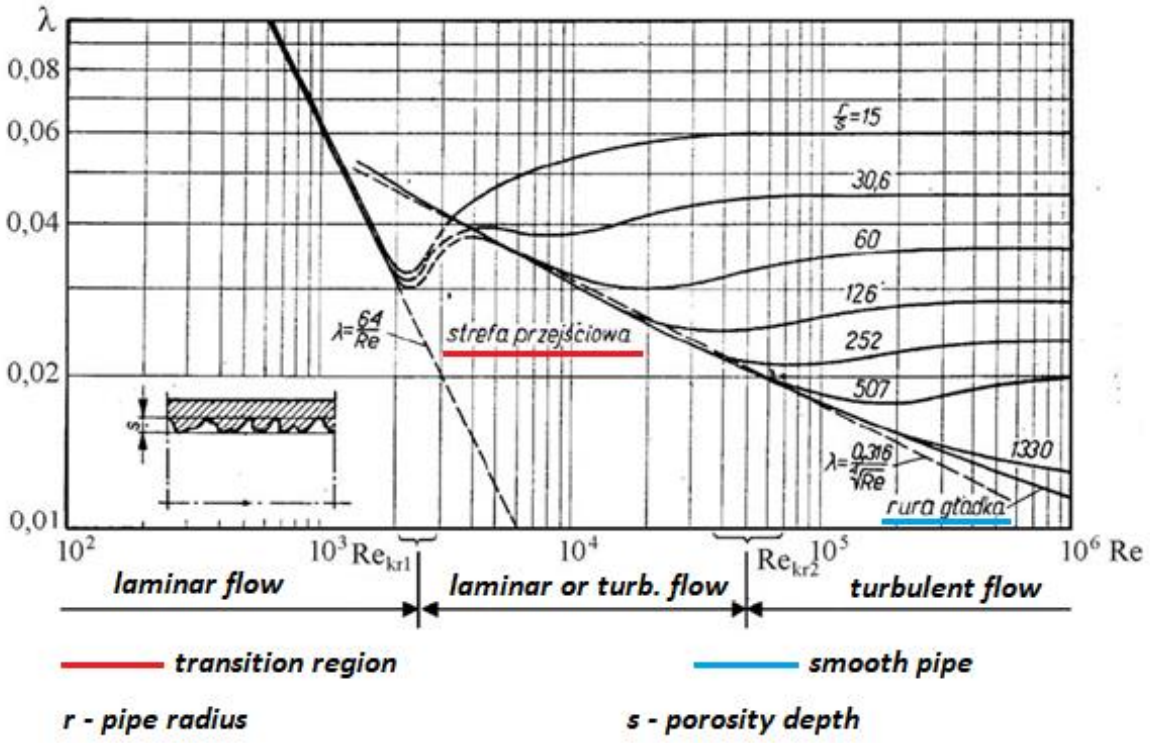

Figure 6.4: Nikuradse's chart - Linear drag friction coefficient λ for different porosity of pipe wall. [65]

For turbulent flow, and for pipes so called "technically smooth", linear drag friction coefficient can be obtained from empirically determined Blasius' formula [65] :

$$\lambda = \frac{0.316}{\sqrt[4]{R_e}} \quad [-]$$

6.5

[65] As much as convenient in everyday use are graphs, they all base on particular formulas. One of them is experimentally obtained equation by Mises:

$$\lambda = 0.0096 + \sqrt{\frac{K}{r}} + 1.2\sqrt{\frac{2}{R_e}} \quad [-]$$

6.6

where: r is pipe radius and K is pipe wall material dependent coefficient. The K coefficients were listed in the table below.

What is significant here, is rather wide range of the values for particular material. It suggests a lot of measurements taken on the one hand, but on the other, high accuracy should not be expected while using this formula.

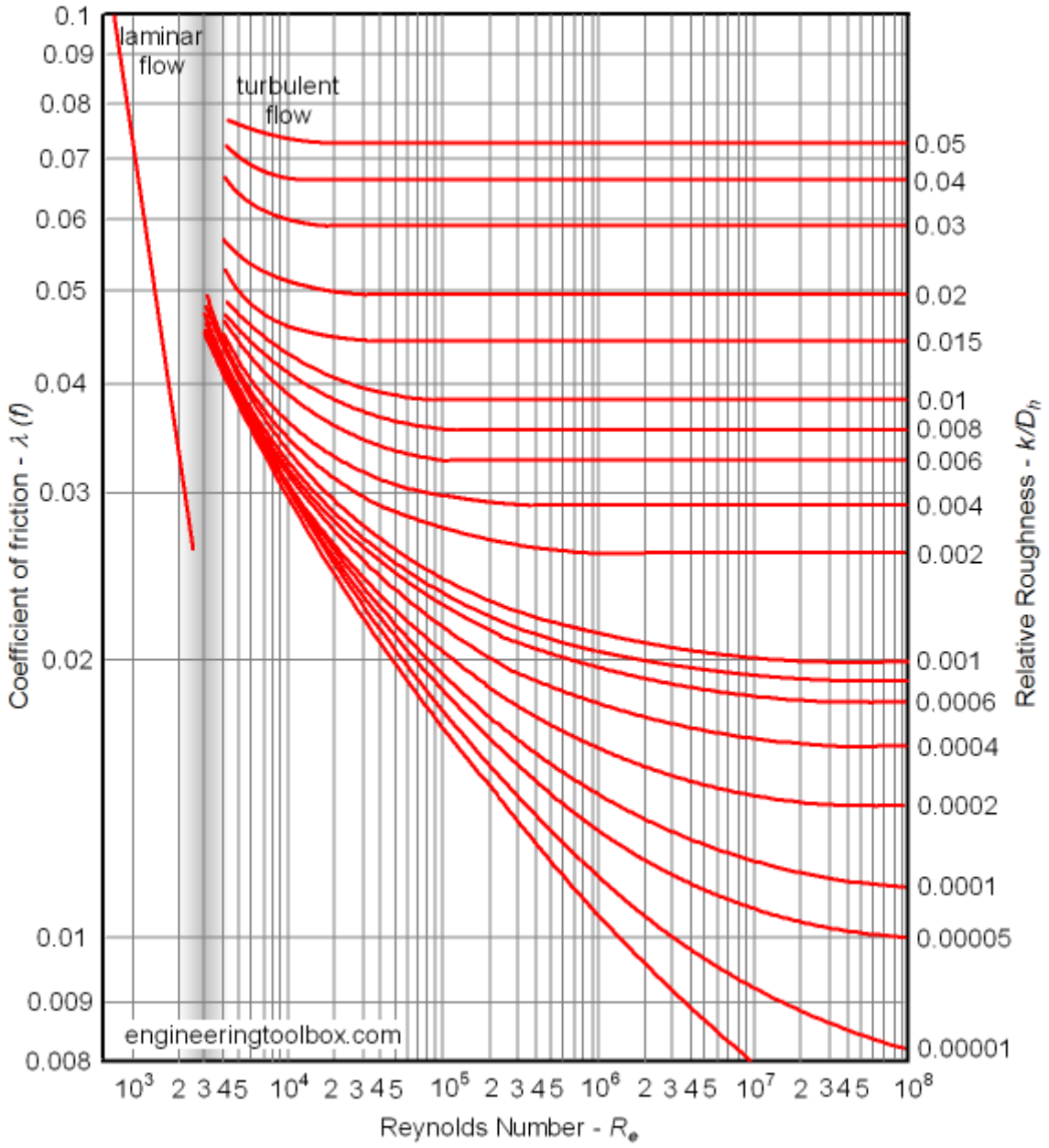

Figure 6.5: Linear drag friction coefficient λ for different Reynolds Numbers R_e and wall roughness. Where: k – pipe wall roughness [-], D_h – pipe hydraulic diameter [m]. [66]

Table 6.3: The K coefficients for different pipe wall material obtained experimentally by Mises.

no.	wall type	wall type dependent coefficient K [m]
1	glass pipe	$(0.2 \div 0.8) \cdot 10^{-8}$
2	brass pipe	$(0.2 \div 1.0) \cdot 10^{-8}$
3	steel pipe	$(2.0 \div 50) \cdot 10^{-8}$
4	cast iron pipe	$(100 \div 200) \cdot 10^{-8}$
5	corroded cast iron pipe	$(250 \div 500) \cdot 10^{-8}$

One of the most popular ways of determining coefficient λ for pipes with any wall roughness is Colebrooke's formula, which ensures accuracy within $\pm 15\%$:

$$\frac{1}{\sqrt{\lambda}} = -2.0 \cdot \log\left(\frac{S}{3.7 \cdot d} + \frac{2.51}{R_e \cdot \sqrt{\lambda}}\right) \quad [-]$$

6.7

for turbulent flows within Reynolds Number range:

$$4 \cdot 10^3 < R_e < 10^8$$

6.8

However, λ coefficient is in indirect form and needs to be calculated (determined) numerically with a use of iterative methods. Therefore, much easier is to use Moody's graph (Figure 6.5) which is in fact graphical representation of multiple solutions available for Colebrook's equation (6.7).

Another approach was proposed by Haaland in the eighties. This simpler formula delivers results within $\pm 2\%$ of complicated Colebrook's one.

$$\frac{1}{\sqrt{\lambda}} = -1.8 \cdot \log\left[\frac{6.9}{R_e} + \left(\frac{S}{3.7 \cdot d}\right)^{1.11}\right] \quad [-]$$

6.9

The problem with Nikuradse's formula and the graph based on it (Figure 6.4) is its low accuracy. The simplification of friction phenomena assumed by Nikuradse – based on equivalent friction $\frac{r}{s}$ $[-]$ – is not precise enough to be able to use it in practical use. It is rather convenient to make rough estimation than ultimate calculations. Real-life required accuracy can be obtained via empirically determined formulas and graphs. Undoubtedly, the best corelation with experimental results occurs in formulas based on physical quantities that can be clearly determined or measured (e.g., Colebrook, Moody, Haaland).

$$\lambda = a + \frac{b}{{R_e}^n} \quad [-]$$

6.10

Table 6.4: Linear drag friction coefficient components for formula above determined by different authors. Coefficients for smooth pipes and turbulent flow.

no.	equation by author	a	b	n	R_e
1	Blasius	0	0.3164	0.25	$5000 \div 10^5$ $2320 \div 10^5$
2	Generaux	0	0.16	0.16	$4000 \div 2 \cdot 10^7$
3	Jakob and Erik	0.00714	0.06104	0.35	$5000 \div 5 \cdot 10^5$
4	Herman and Schiller	0.0054	0.3968	0.3	$5000 \div 2 \cdot 10^6$ $2500 \div 2 \cdot 10^6$
5	Lang	0.015	1.7	0.5	$5000 \div 2 \cdot 10^6$
6	Nikuradse	0.0032	0.221	0.237	$10^5 \div 2 \cdot 10^6$
7	Rea	0	0.079	0.109	$8 \cdot 10^4 \div 10^6$
8	Koo	0.0056	0.5	0.32	$3000 \div 3 \cdot 10^6$

Linear loss coefficient for Reynolds number in range 4000-100000 is described by Blasius's empirical formula:

$$\lambda = 0.3164 \cdot R_e^{-0.25} \quad [-]$$

6.11

For Reynolds number value greater than 10^5 linear loss coefficient is defined by Prandtl – Karman's formula:

$$\frac{1}{\sqrt{\lambda}} = 2 \cdot log \frac{R_e \cdot \sqrt{\lambda}}{2.51}$$

6.12

Alternatively, Lees's formula can be utilized:

$$\lambda = 0.0072 + 0.06104 \cdot R_e^{-0.35} \quad [-]$$

6.13

In case of $\frac{k}{d} > 0.001$ then, Reynolds number located within $R_e \in \left(\frac{d}{k}, \frac{2000 \cdot d}{k}\right)$ determines so-called changeable hydraulic roughness zone [67]. Inside this zone flow energy losses are proportional to fluid velocity to the power 1.75÷2.0. While linear loss coefficient is calculated from Colebrook – White's formula [63] [68]:

$$\frac{1}{\sqrt{\lambda}} = -2 \cdot log \left(\frac{2.51}{R_e} \cdot \frac{1}{\sqrt{\lambda}} + \frac{k}{3.71 \cdot d}\right)$$

6.14

Or else, newer Lehman's formula:

$$\frac{1}{\sqrt{\lambda}} = -1.94 \cdot log \left[\left(\frac{4.26}{R_e} \cdot \frac{1}{\sqrt{\lambda}}\right)^{1.1} + \left(\frac{k}{3.71 \cdot d}\right)^{1.03}\right]$$

6.15

From the moment where Reynolds number exceeds $\frac{2000 \cdot d}{k}$ value, λ coefficient depends on pipe relative roughness *e* only [67]. The linear loss coefficient then is estimated from Nikuradse's formula:

$$\frac{1}{\sqrt{\lambda}} = 2 \cdot log \frac{3.71 \cdot d}{k}$$

6.16

The detailed description of flow in its different stages (depending on relative fluid velocity described by Reynolds number) results from difficulty of determining the flow energy losses precisely. The general behaviour of fluid in terms of roughness is well established. When

quotient k/d is a small value, then λ depends on R_e merely. For low Reynolds numbers, even if pipe relative wall roughness is at significant value, the energy losses are insignificant and flow can be considered as the flow through the smooth pipe. However, when R_e increases the flow becomes turbulent, through the transition phase. Within the transition zone, linear loss coefficient depends on both relative roughness *e* as well as Reynolds number. Finally, for the fully turbulent flow and high R_e values λ depends on k/d ratio only [69] .

For rough pipe flows there is also von Karman's formula experimentally verified by Nikuradse [69]:

$$\frac{1}{\sqrt{\lambda}} = 2 \cdot log \frac{d}{k} + 1.74$$

6.17

The formulas and equations listed above relate to plastic pipes. For pipes made from steel and cast-iron Walden's 6.18 or Altsul's 6.19 formulas are valid:

$$\frac{1}{\sqrt{\lambda}} = -2 \cdot log \left(\frac{6.1}{R_e^{0.915}} + \frac{0.268 \cdot k}{d} \right)$$

6.18

$$\lambda = 0.11 \cdot \left(\frac{68}{R_e} + \frac{k}{d} \right)^{0.25} \quad [-]$$

6.19

exemplary pipe absolute roughness coefficients [68]:

k=0.4 [mm] – the new steel and cast-iron pipes
k=0.05 [mm] – polyethylene pipes
k=0.043 [mm] – the new asbestos cement pipes
k=0.025 [mm] – hard PVC pipes

- While these values are not directly applicable in analysis of the waterjet performance, they indicate importance of manufacturing quality of the flow tunnel surface. For indicated range of the k coefficient λ values changes between 0.025 and 0.034 (100%, 170%). It means the tunnel internal surface should be as smooth as possible in order to minimise friction losses.

The formulas of the linear drag coefficient l described above refer to the flow inside the closed pipe with already stabilised and fully formed flow.

6.4.2 Linear losses of flow in the tunnel

[68] [70] [71] The tunnel of the waterjet propulsor transports impellent (water) from the inlet to the pump and further to the outlet nozzle. However, due to friction phenomenon occurring between water and duct's wall flow losses appears through the whole length of the

tunnel. In order to estimate their value, the following algorithm was employed for the base waterjet tunnel calculations. – A straight pipe model.

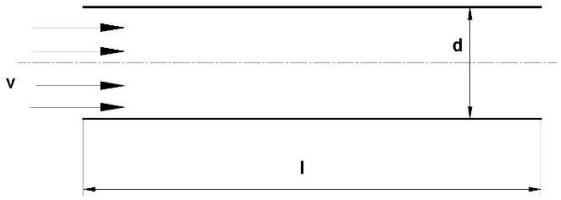

Figure 6.6: Flow velocity definition in a straight pipe without friction and with friction.

Darcy – Weisbach's formula describes straight pipe flow losses:

$$h_l = \lambda \cdot \frac{l}{d} \cdot \frac{v^2}{2 \cdot g} \quad [m]$$

6.20

Where losses coefficient takes from:

$$\zeta_l = \lambda \cdot \frac{l}{d} \quad [-]$$

6.21

Linear drag coefficient value depends on flow type determined by Reynolds number and pipe relative roughness. Thus:

$$\lambda = \lambda(R_e, e)$$

6.22

Where Reynolds number formula for pipes that defines flow character is:

$$R_e = \frac{v \cdot d}{\nu} \quad [-]$$

6.23

And the relative roughness is a relation between pipe absolute roughness and its diameter:

$$e = \frac{k}{d} \quad [-]$$

6.24

The linear drag coefficient λ varies depending on a flow type [72]. In analysed case the velocity is within the Reynolds Number range of $R_e \in \langle 4000, 100000 \rangle$, therefore the flow inside the tunnel is considered to be fully turbulent. For such flow conditions various formulas for the value of the λ coefficient were proposed. The formulas of the linear loss coefficient described refer to the flow inside a closed pipe with already established and fully developed flow. The

flow stabilization occurs at certain distance from the inlet and is called initial length. However, during technical considerations this phenomenon is usually ignored. – Such an approach was adopted for this work as well.

For the purpose of the semi-empirical calculation, in further part of this work the Lees' formula 6.25 was selected as the most appropriate for the values of Reynolds Number R_e close to 10^5 and easy to use in practice.

$$\lambda = 0.0072 + 0.6104 \cdot R_e^{-0.35} \quad [-]$$

6.25

6.4.3 Tunnel inlet

Usually, the tunnel inlet is a rectangular or oval opening in the vehicle's hull. The 21st ITTC [73] [62] recommends intake proportions at rate 1.3 : 1.0 (length about 30% greater than width) – see Figure 3.16 A and B – but other researches [20] indicates that changes within 20% in capture area proportions delivers only about 1% difference in the estimated power (thrust). Moreover, Van Terwisga [28] and Scherer et al. [74] concluded that there was no significant effect on power (thrust) losses or gains between rectangular and elliptical (Figure 3.16 C) intake shape. They have also found that variations of thrust are contained within 0.5% for the inlet proportions 1.3:1.0 and 1.5:1.0 (length:width ratio). Also, CFD analysis [74] of the inlet with a trapezoidal shape suggests that there is no necessity to determine inlet area precisely. Other researchers [62], [75], [22], indicates that this area is as important as the rest of the flow duct and cannot be neglected. It determines inflow character to the next stage and has substantial influence on drive efficiency. Therefore, it is recommended to analyse it precisely and conduct further scrutiny of this area [20]. The results of the author's investigations confirm these opinions in general.

6.4.4 Tunnel bend at the inlet

"The *Coandă effect* is the tendency of a fluid jet to be attracted to a nearby surface. The principle was named after Romanian aerodynamics pioneer Henri Coandă, who was the first to recognize the practical application of the phenomenon in aircraft development" [76].

In practice, the *Coandă effect* changes flow direction. If the surface curvature is smooth enough, it causes the fluid to stick to it and follows it until the surface ends sharply or the fluid stream is faced with some obstacle. In waterjet drive, the effect can be observed at the tunnel inlet where a part of the stream flowing around the vehicle's body is redirected to the duct. The obvious advantage of this phenomenon is that, at least partially, it leads to filling of the tunnel with water. This in turn reduces the amount of water needed to be sucked in and thus increases propulsion overall performance.

Unfortunately, the precise determination of the water stream flowing into the tunnel due to this natural phenomenon is very difficult. Hence, the losses estimations at this stage are only anticipations based on formulas related to sudden flow direction change or tunnel bend (described below).

6.4.5 Change of flow direction

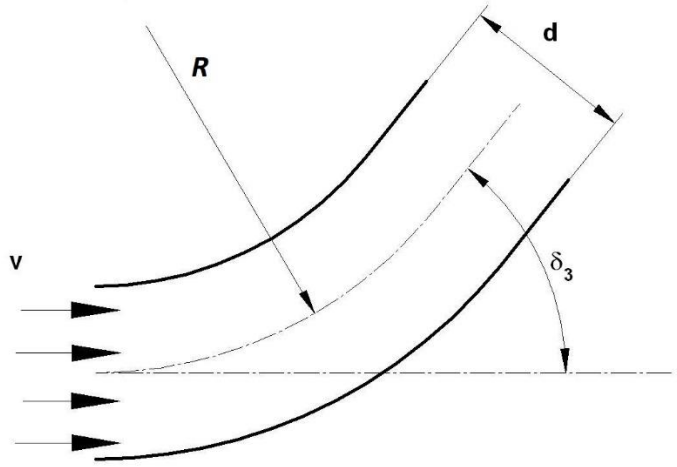

Figure 6.7: Change of fluid flow direction in bent pipe – smooth bend.

For the purpose of the semi-empirical calculation of the local flow losses in a bent pipe (Figure 6.7) the following formula (6.26) was selected and used further in this work:

$$h_o = \left\{\left[0.13 + 0.163 \cdot \left(\frac{d}{r}\right)^{3.5}\right] \cdot \frac{\delta}{90}\right\} \cdot \frac{v^2}{2 \cdot g} \quad [m] \tag{6.26}$$

6.4.6 Diffuser

The diffuser is introduced into the waterjet tunnel for three basic reasons:

- to increase the pump rotor diameter and therefore lower the velocity of the fluid. This leads to pressure increase in the pump and reduces cavitation problems in shallow depth applications.
- To compensate reduction of cross-section area of the tunnel due to presence of large dimeter of the rotor hub.
- To change the flow characteristic in the pump in order to achieve a mixed flow operation and reduce so-called unstable pressure head.

Local losses at the diffuser depends on its geometry (Figure 6.8).

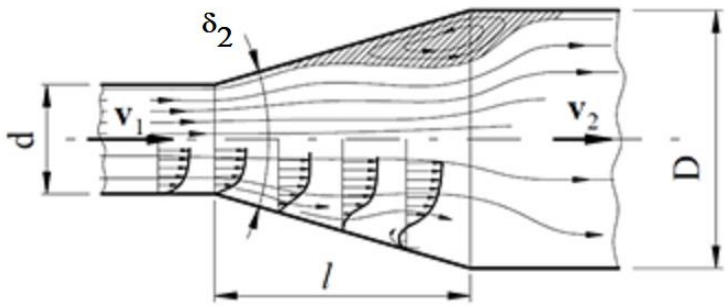

Figure 6.8: Fluid flow in a pipe with sudden cross-section area expansion (smooth).

The flow losses for local, sudden and smooth cross-area expansion are described by the following formula:

$$h_o = \frac{(v_1 - v_2)^2}{2 \cdot g} \cdot sin\,\delta_2 \quad [m]$$

6.27

Note: equation 6.27 is valid for angle $\delta_2 \leq 10^o$.

The equation above was used for semi-empirical calculation performed for the purposes of this work.

As local losses in the diffuser depend on the value of the flare angle δ it can be advised to extend the nozzle (diffuser) along the tunnel as far forward as possible.

6.4.7 Confusor (nozzle)

To determine flow losses in converging nozzle (Figure 6.9) Weisbach's formula (6.28) is used as it contains additional correction coefficient that represents flow throttling.

The $\left(\frac{1}{\chi} - 1\right)^2$ element stands for contract-broaden phenomenon occurring just behind pipe contraction point.

$$h_o = 0.04 + \left(\frac{1}{\chi} - 1\right)^2 \cdot \frac{v_2^2}{2 \cdot g} \quad [m]$$

6.28

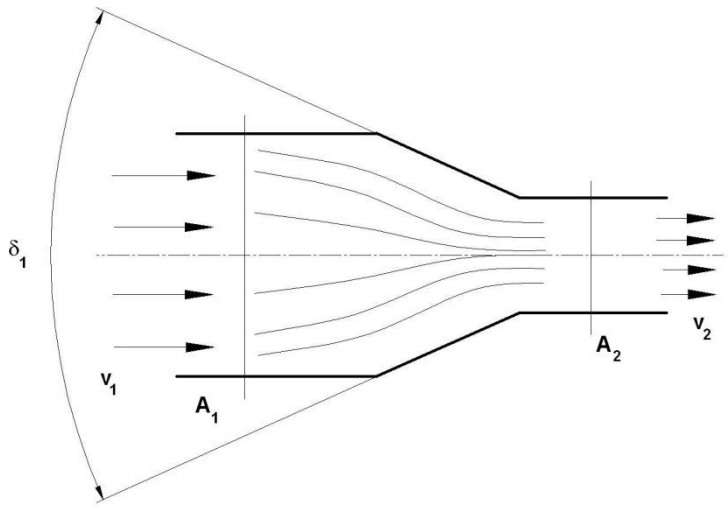

Figure 6.9: Fluid flow in a pipe with sudden cross-section area reduction (smooth).

The formula 6.28 was used for semi-empirical calculation performed for the purposes of this work.

Another approach to estimate flow loses in a confuser is experimentally proved formula proposed by Wędrychowicz et al. [77].

$$h_o = \frac{(v_2 - v_1)^2}{2 \cdot g} \cdot \sin\delta \quad [m]$$

6.29

Note: equation valid for angles $\delta_1 \leq 10^o$.

However, in practice Weisbach's formula is often used [78] :

$$h_o = \left(1 - \frac{A_1}{A_2}\right) \cdot \left(\frac{1}{\chi} - 1\right)^2 \cdot \frac{v_1^2}{2 \cdot g} \quad [m]$$

6.30

Where χ depends on edge type:

- sharp $\chi = 0.63$
- bended $\chi = 0.75$
- rounded $\chi = 0.90$
- nozzle $\chi = 0.89$

Another method to estimate loss coefficient is directly via pipe diameters. Then ζ is [79]:

$$\zeta = \frac{1 - \left(\frac{d_1}{d_2}\right)^2}{2} \quad [-]$$

6.31

Exemplary loss coefficient values:

$\delta_1 = 30° \rightarrow \zeta = 0.02$
$\delta_1 = 45° \rightarrow \zeta = 0.04$
$\delta_1 = 60° \rightarrow \zeta = 0.07$

6.4.8 Hydraulic head energy losses

The water physical lifting up phenomena in waterjet drives is due to water level difference between propulsion inlet and outlet. The *H* symbol stands for it in the official labelling and losses it generates are described as follows:

$$\zeta_4 = 2 \cdot \frac{N_{Loss4}}{m \cdot u^2} = 2 \cdot \frac{g \cdot H}{u^2} \cong 19.62 \frac{H}{u^2} \quad [-]$$

6.32

6.4.9 Hydraulic head of waterjet propulsion

The value of hydraulic head generated by waterjet propulsion is described by equation:

$$H = \frac{w_2^2 - u^2}{2 \cdot g} \quad [m]$$

6.33

6.5 Tunnel losses according to Albert Fliegner's method

[80] One of the first engineers who observed experimentally the chocking phenomenon was Albert Fliegner. Basing on his own work, he has proposed some improvements to the general models of the flow phenomena. Subsequently, specific models of local losses were developed for application in waterjets.

The summary energy losses in the waterjet duct are [19]:

$$N_{Loss} = N_{Loss1} + N_{Loss2} + N_{Loss3} + N_{Loss4} \quad [W]$$

6.34

6.5.1 Inlet nozzle energy losses (diffuser)

The equation formulated by A. Fliegner describes flow losses in diffuser:

$$\frac{N_{Loss1}}{m \cdot u^2} = \left\{ \frac{\lambda_t}{8\, sin\left(\frac{\delta_D}{2}\right)} \cdot \left[\left(\frac{A_{D2}}{A_{D1}}\right)^2 - 1 \right] + \left(\frac{A_{D2}}{A_{D1}} - 1\right)^2 \cdot sin\, \delta_D \right\} \cdot \frac{w_{D2}^2}{2 \cdot u^2}$$

6.35

Where non-dimensional loss coefficient for diffuser ζ_1 is:

$$\zeta_1 = 2 \frac{N_{Loss1}}{m \cdot u^2} \quad [-]$$

6.36

6.5.2 Tunnel bend energy losses

As mentioned earlier, diffuser bend should be a smooth arc and its "flare angle α should contain between 30 and 45 degrees" [19]. The tunnel bend radius *R* should meet following inequality:

$$\frac{R}{D_{PR}} > 4$$

6.37

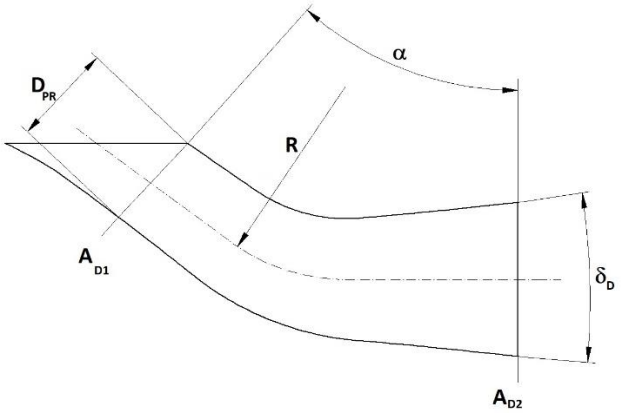

Figure 6.10: The diffuser notations for waterjet propulsor.

"Whereas diffuser divergence angle δ_D , according to the experimental results obtained during researches, should be kept between $7 \div 9°$ " [19]. The upper limit of its divergence is 10 degrees.

Therefore, taking all into account (diffuser bend and divergence angle, tunnel bend radius etc.) and assuming non-dimensional loss coefficient $\zeta \approx 0.08$, diffuser bend energy losses are described by:

$$\zeta_2 = 2 \cdot \frac{N_{Loss2}}{m \cdot u^2} = 2 \cdot \frac{0.08 \cdot w_{D2}^2}{2 \cdot u^2} = 0.08 \cdot \frac{w_{D2}^2}{u^2} \quad [-]$$

6.38

6.5.3 Outlet nozzle energy losses (confuser)

Another A. Fliegner's formula is used to describe the outlet nozzle losses:

$$\zeta_3 = 2 \cdot \frac{N_{Loss3}}{m \cdot u^2} = \frac{2 \cdot \lambda_t}{8\, sin\left(\frac{\delta_C}{2}\right)} \cdot \left[1 - \left(\frac{A_{C2}}{A_{C1}}\right)^2\right] \cdot \frac{w_{C2}^2}{2 \cdot u^2} \quad [-]$$

6.39

Where nozzle divergence angle is:

$$\delta_C = 2 \cdot arctg\left(\frac{D_1 - D_2}{2 \cdot l_C}\right) \quad [°]$$

6.40

6.6 The pump as element of the waterjet propulsor

As it can be seen in the Table 7.3 pump efficiency is the most important component of waterjet propulsor efficiency. It means that the pump efficiency must be known if the waterjet efficiency is evaluated using semi-empirical methods.

The total efficiency of a pump is defined as ratio between effective power and delivered power and it can by written as:

$$\eta = \frac{N_u}{N_d} \quad [\%]$$

6.41

Nowadays, large modern pumps reach performance of 90% efficiency level. While the average pump efficiency is 70-80% [81].

As already mentioned before, the rotor-stator part of the waterjet propulsor can be regarded as standard pump section. The most popular types of pumps used in jet drives are:

— axial pump
— diagonal (mixed-flow) pump
— helicoidal pump (in outboard motors)

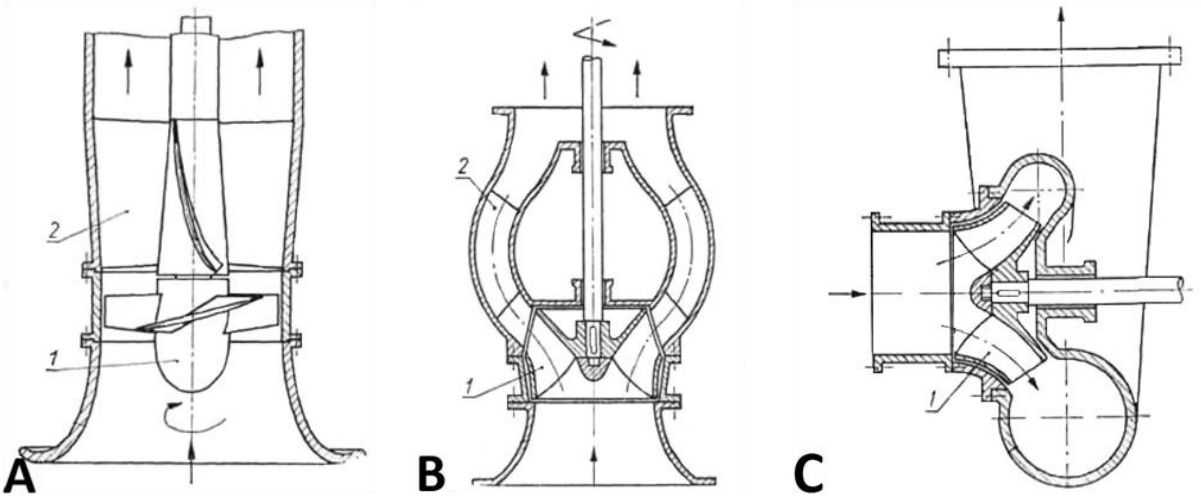

Figure 6.11: Cross-sections of exemplary pumps used in waterjet propulsions: A – axial pump, B – diagonal pump, C – helicoidal pump [81]. Notations: 1 – rotor, 2 – stator; straight arrows show flow direction.

According to well established knowledge, type of the pump needs to be selected basing on the speed index. The coefficient called pump kinematic speed index is defined by the formula 6.42. It depends on the relation between *Q*, *H* and *n*, that means it is closely related to pump geometry. The speed index allows for comparison of a pumps with identical dynamic characteristics but different geometry.

$$n_{sQ} = \frac{n \cdot Q^{1/2}}{H^{3/4}} = \frac{n}{\sqrt{H}} \cdot \sqrt{\frac{Q}{\sqrt{H}}} \quad [-]$$

6.42

The pump kinematic speed index is unique for each pump and operating point. Most sources present pumps characteristics in form of charts, as it is the most convenient way of showing this kind of information. The graphs in the Figure 6.12 show efficiency for wide range of pumps referenced to the velocity index.

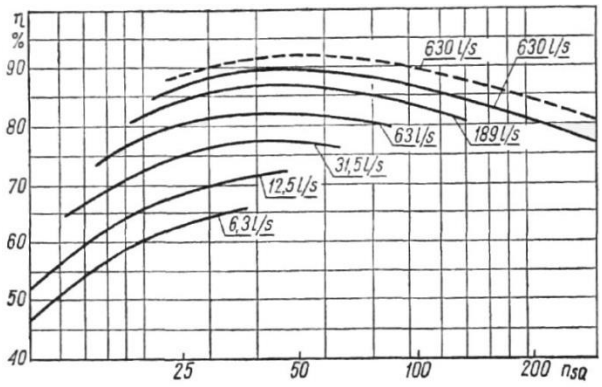

Figure 6.12: Pump performance curves based on pump kinematic speed index as given by Worthington [81].

According to the literature [82] "it is known that the highest attainable pump efficiencies are obtained with mixed-flow pumps in general. Both axial and centrifugal pump types do not reach this high level of more than 90% pump efficiency. However, for the development of a new axial-flow pump high efficiency level has been set as a constraint. Though this seems to be in contradiction with common experience, it is shown to be possible for waterjet."

The paper [82] conclusions were as follows:

- Though the geometry of the pump is similar to an axial-flow type, the top efficiency of a mixed-flow pump is still maintained.
- For a waterjet selection based on cavitation margins, a transom flange diameter reduction of 25% can be obtained with the axial pump. If the selection is based on maximum allowable power, which is applicable for high-speed applications (>60 kts), a reduction of about 8% can be achieved.
- The selection based on identical operating condition, e.g., power and RPM, results in an installation with a 17% smaller transom flange diameter. Moreover, the cavitation margins are improved significantly. A typical increase of about 6 knots at full power can be obtained. At lower speed, for example around the hump speed, an increase of thrust of more than 30% is found.
- Evaluation of the maximum allowable power based on mechanical strength criteria learns that the new axial pump can absorb about 16% more power for identical transom flange diameter.

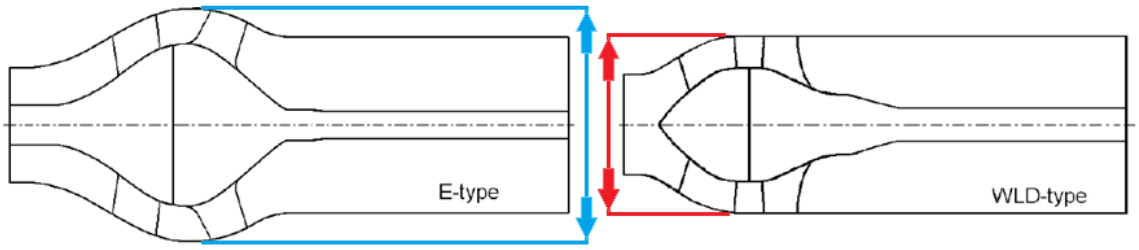

Figure 6.13: Comparison of transom flange diameter for identical cavitation performance: mixed-flow LJ160E (left) and axial-flow WLD-1570 (right) [82].

6.6.1 Efficiency of a small pump

One of the important issues, while considering pump for the analysed application, is very limited amount of data regarding pumps of the necessary size. According to literature, axial pumps with volumetric capacity of ~21 [m^3/h] (the flow volume in the discussed case) are very small and rarely optimized to reach high efficiency. However, there is still a possibility to compare pumps of different sizes and hence obtain essential input data for semi-empirical calculations. According to these data, for pump with assumed volumetric flow ~21 [m^3/h] and speed index of 200 [-] efficiency is about 63-65%.

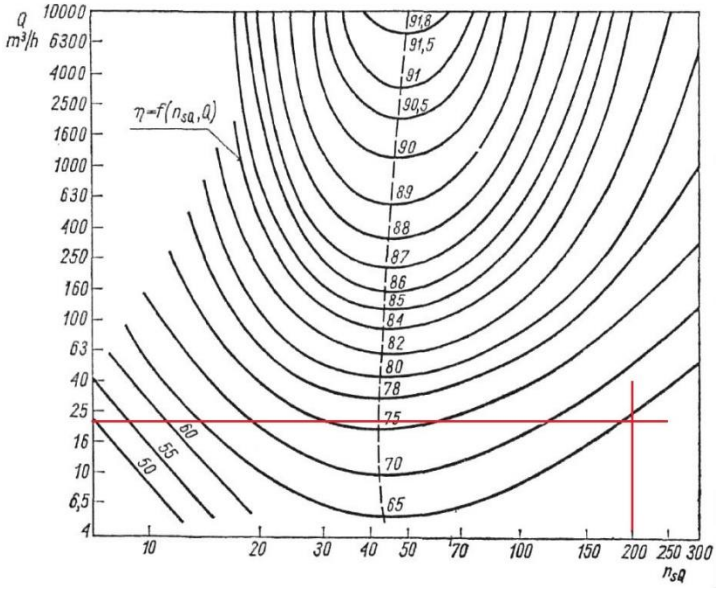

Figure 6.14: General performance curves of rotary pump based on pump kinematic speed index by Gradewald [81].

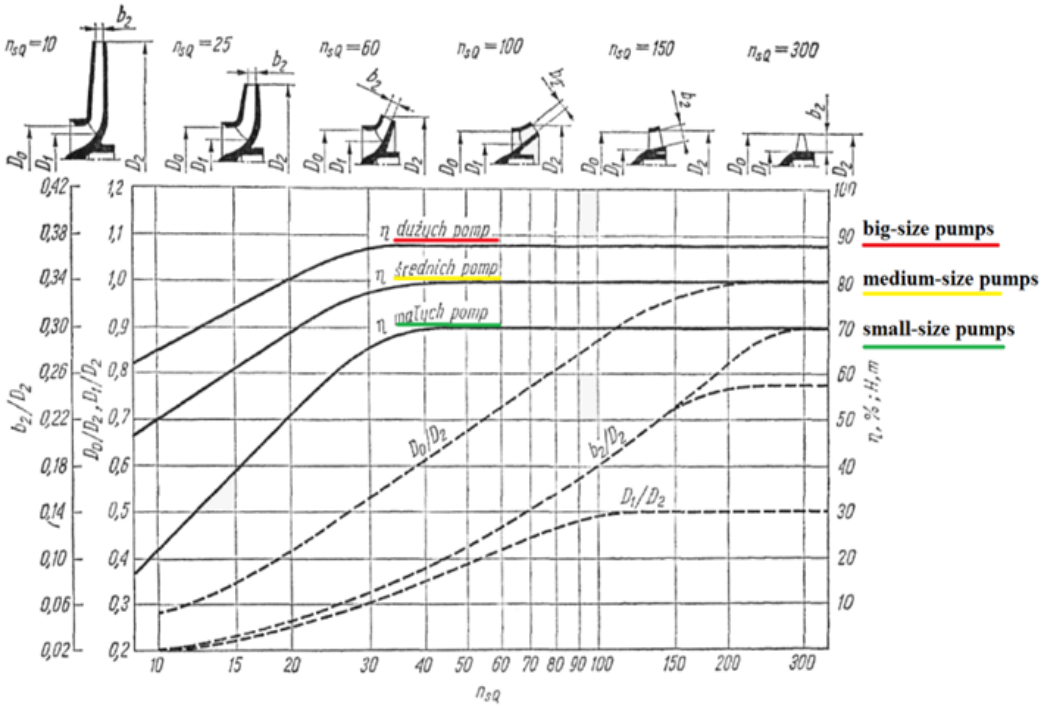

Figure 6.15: Pump performance curves and rotor shapes based on pump kinematic speed index by R. Neumaier [81].

In the analysed case, referring to notation in the graph above, the ratio between rotor outer diameter (D_2) and rotor hub (D_1) is:

$$\frac{D_1}{D_2} = \frac{0.02}{0.05} = 0.4 \quad [-]$$

6.43

and ration between rotor's blade height and rotor's outer diameter is:

$$\frac{b_2}{D_2} = \frac{0.015}{0.050} = 0.3 \quad [-]$$

6.44

The most popular formula used to determine total performance of a pump, based on model efficiency, is Moody's formula [81]:

$$\eta = 1 - (1 - \eta_m) \cdot \left(\frac{d_m}{d}\right)^{0.45} \cdot \left(\frac{n_m}{n}\right)^{0.2} \quad [\%]$$

6.45

The "*m*" index refers to model pump. The *d* and d_m are pumps rotor and the pump model rotor (reference) diameters respectively.

However, in case of lack of information regarding speed of the reference pump, simpler formula, developed by *Byron Jackson Pumps* (USA), can be used:

$$\frac{1-\eta}{1-\eta_m} = \left(\frac{d_m}{d}\right)^{0.165} \quad [\%]$$

6.46

Based on data published by top waterjets producers (such as HamiltonJet, Thrustmaster, Wärtsilä, ALAMARINE-JET, Marin Jet Power, Kongsberg etc.) – for the purpose of this work – it was assumed the reference pump have 1.0 [m] rotor diameter and 90% efficiency at the operating point. These values seem to be typical in case of large waterjet pumps. Hence, using Byron Jackson formula, for rotor with 50 [mm] diameter the calculated theoretical efficiency is over 83% and it drops slightly to 82% for smaller, 30 [mm] propeller – as shown in the Figure 6.16. This outcome is significantly higher (by about 15-20%) in comparison to what the graphs presented above indicate. They suggest, that maximum achievable efficiency for small-size pumps cannot cross 70%. And rotor-hub diameters ratio points to even lower values. On the one hand, the wide range of efficacy values, fluctuating approximately between 60% and 80%, gives theoretical support and justification for future pump efficiency improvements. On the other hand, it shows clearly, that analysed pump (waterjet drive) is too small to relay merely on available theory and this particular case needs individual approach.

For further considerations in this work, less optimistic efficiencies were arbitrarily assumed. The adopted values for various diameters are presented in the table and figure below.

Table 6.5 Assumed efficiencies of the pumps used in waterjet propulsors depending on the rotor diameter as adopted to semi empirical calculations

no.	parameter				
1	rotor diameter [mm]	30	40	50	60
2	efficiency	60%	63%	65%	67%

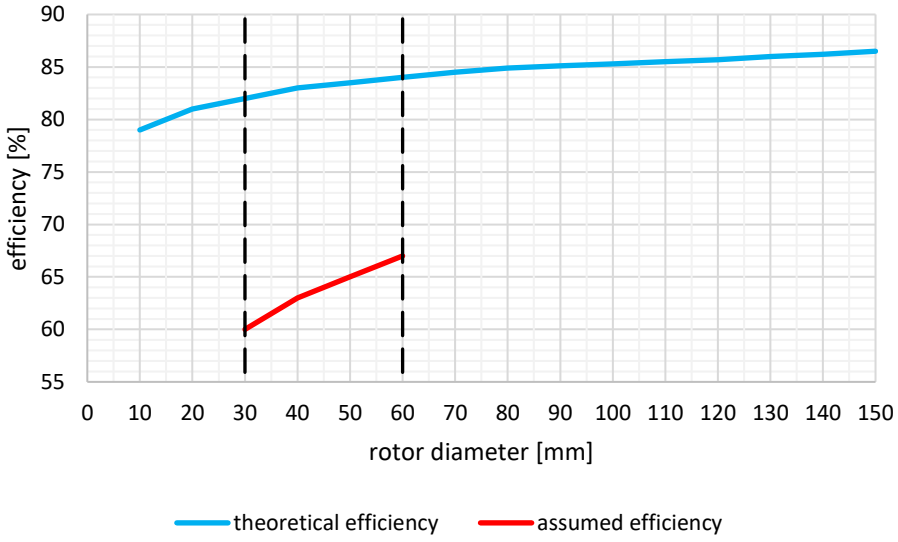

Figure 6.16: Theoretical small pump efficiency calculated with a use of Byron Jackson Pumps formula 6.46, as well as efficiency value assumed for the semi-empirical calculations of the waterjet propulsors.

6.6.2 Influence of the wake

The water that is ingested into the inlet of the waterjet tunnel partially originates from the hull's boundary layer. The mass-averaged velocity of the ingested water (v_{in}) is lower than the ship speed due to this boundary layer. The velocity deficit is expressed as the momentum wake fraction (w) and is defined as:

$$w = 1 - \frac{w_1}{u} \quad [-]$$

6.47

The thrust force can be expressed by the following expression:

$$F_u = m \cdot (w_2 - w_1) \quad [N]$$

6.48

Where effective propulsion power is a product of thrust and vessel velocity:

$$N_u = F \cdot u = m \cdot (w_2 - w_1) \cdot u \quad [W]$$

6.49

Determination of the wake fraction (w) is rather complex, since the cross-sectional shape of the stream tube is not defined at this consideration.

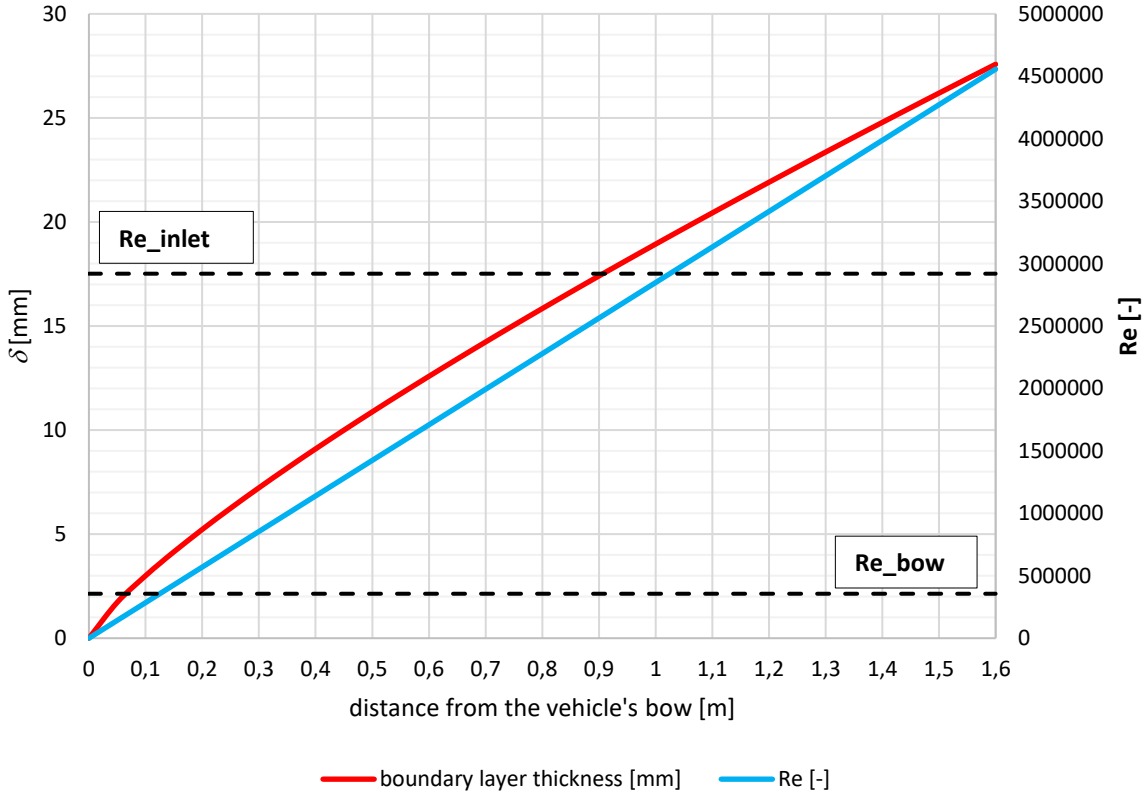

Figure 6.17: Reynolds Number along the hull of analysed vehicle and the boundary layer thickness for a flat plate (for the water temperature of 15 [deg C]), that represents boundary layer forming on hull's cylindrical segment. "Re_bow" refers to the point, where the bow turns into cylindrical hull. "Re_inlet" stands for Reynolds Number at waterjet inlet.

However, for a given volumetric flow rate through the waterjet, the length of an inlet can be calculated, once the velocity distribution in the boundary layer is known. To obtain first indication of the velocity distribution, standard theory for a flat plate boundary layer – described in several textbooks [83] [84] – can be used. It is also convenient to use a power-law velocity profile for the boundary layer velocity distribution:

$$\frac{v}{U_\infty} = \frac{z}{\delta} > \frac{1}{n} \quad [-]$$

6.50

where *v* refers to the local velocity in the boundary layer at a distance *z* normal to the wall; U_∞ denotes the velocity of undisturbed stream; δ stands for the local boundary layer height and *n* is the power-law index.

According to basic expression 6.51 [83], the thickness of the turbulent layer *δ(x)* at flat plate develops as shown in the Figure 6.17 and at the propulsor inlet (1039 [mm] measuring from the bow) should reach around 19-20 [mm]. It corresponds well with CFD simulations suggestions, where the boundary layer height at the propulsor inlet is about 20 [mm].

$$\delta(x) \approx 0.37 \frac{x}{{Re_x}^{1/5}} \quad [m]$$

6.51

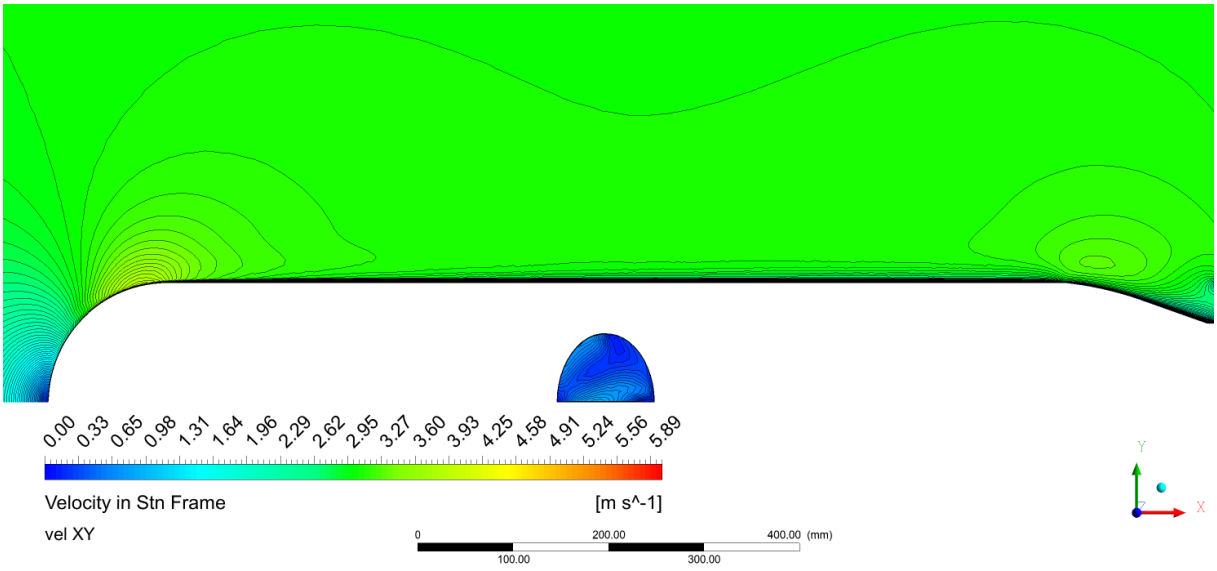

Figure 6.18: Boundary Layer formation on vehicle's hull for operational velocity 3.0 [m/s] and rotors velocity of 4500 [rpm]. Clear, visible Boundary Layer reduction can be notice right at the propulsor's inlet. It is due to propulsor's suction.

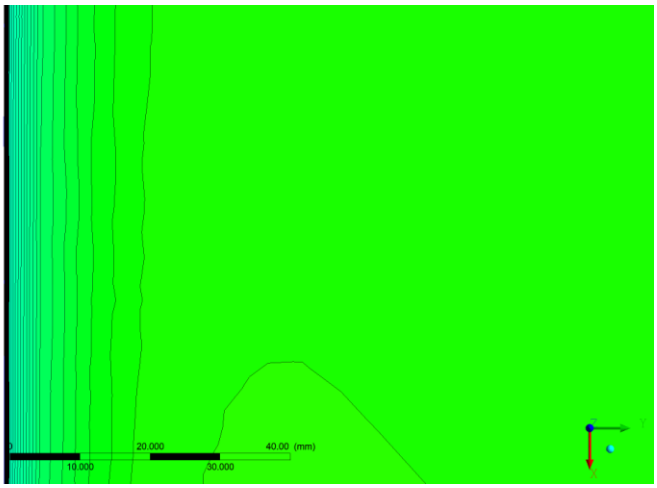

Figure 6.19: Boundary Layer height near the inlet – fragment of the picture above rotated 90 degrees right. In comparison to flat plate, here the Boundary Layer height is cut down by propulsor's suction.

Following Odd M. Faltinsen the wake fraction "may vary between 0 and 0.4 for a displacement vessel, depending on the hull form" [62]. And for instance: "A typical value for a wake fraction *w* is 0.10 to 0.14 for a fast ferry." [52].

6.7 Propeller shaft in the tunnel

The propeller's shaft is real and hard to avoid obstruction located just before the pump and disturbing the inflow to the rotor. In order to minimize shaft's influence on pumps efficiency three solutions can be taken into account:

- the first option is to avoid shaft sleeve and improve water inflow by rotating shaft
- the other possibility is to streamline the shaft along the flow direction
- the third approach can base on rim-driven, shaftless rotor.

7 Performance calculation of the submersible waterjet propulsor using semiempirical description

7.1 Initial design of a waterjet propulsor

Given the expected thrust force generated by the waterjet propulsor at the operational velocity of the vehicle, the design process needs to be initiated by determination of selected parameters:

- estimation of the optimum diameter of the waterjet pump
- estimation of optimum speed of the waterjet pump
- estimation of the geometry of the waterjet tunnel
- estimation of the optimum dimensions of the outlet nozzle

7.2 Calculation algorithm

The calculation procedure used to determine the propulsor's parameters is based on expressions described in the chapter 6. The calculation algorithm used to estimate basic parameters of the waterjet propulsor assumes some simplification – constant tunnel diameter between stations no. 2 and 4 (see the Figure 6.1). Therefore, the inflow to the pump section and the pump region itself is regarded as uniform. The pump is assumed to be of an axial type. Whereas the outlet nozzle – originally fitted with stator that increases pump efficiency – in this consideration is regarded as simple confuser.

The entire propulsor was divided into sections:

- bend (inlet)
- bend (inlet to rotor section)
- diffuser (rotor section)
- confuser (outlet)
- straight pipe (tunnel length in general)

Further, at this stage it was assumed that the water inflows the propulsor with the velocity equal to the velocity of the vehicle itself. The rotor is expected to generate pressure required to move assumed amount of water through the tunnel and then eject it through the outlet nozzle. The water leaving the pump section enters the stator-equipped outlet nozzle where it is accelerated to the velocity required to achieve expected (operational) thrust.

7.3 Waterjet propulsor's basic parameters evaluation for assumed operational conditions

Geometric limitations are an important factor while considering replacement for the open propellers by means of the waterjet propulsors. To preserve propulsion and manoeuvring capabilities of the existing vehicle, it was decided to keep current configuration – it means four waterjet propulsors built into flow stabilizing fins in X arrangement. To make everything fit and to assure undisturbed flow around the fins, the pump's rotor diameter has to be possibly

small. According to [85] initial diameter of the pump's rotor for the waterjet propulsor can be calculated using the expression below. The same formula is also recommended as initial step in defining diameter for a propeller ducted in the Kort nozzle. Further, the author suggests to take rotor's diameter even greater than maximum allowed by geometry of the vehicle. In considered case, it was found, that rotor's diameter has to be smaller than 60 [mm].

The rotational speed of the pump's rotor is parameter that has to be assumed.

$$D_{opt} = 1.45 \cdot \sqrt[4]{\frac{T}{\rho \cdot n^2}} \quad [m] \tag{7.1}$$

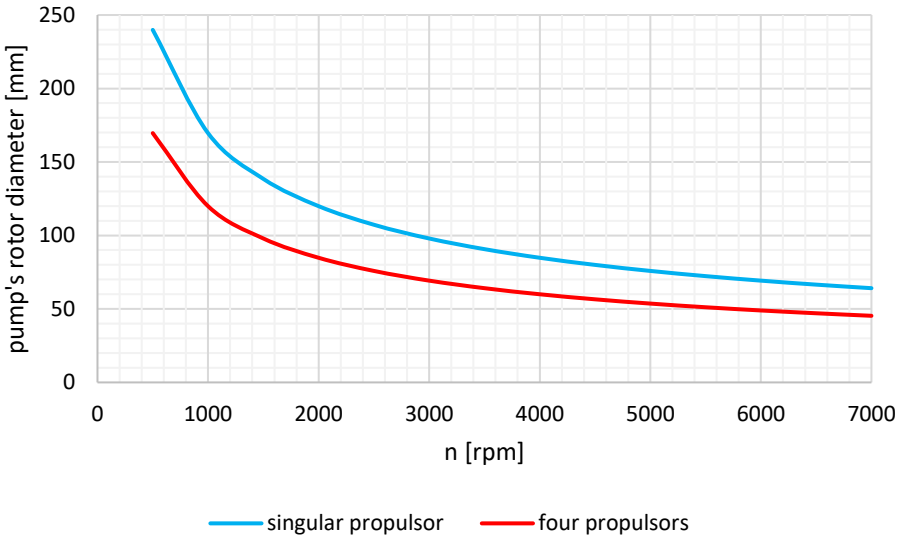

Figure 7.1: Optimum pump's rotor diameter calculated with a use of expression 7.1. The results stand for vehicle's operating point in two configurations: vehicle propelled by a single waterjet propulsor (thrust of 56 [N]) and four propulsors (with 14 [N] of thrust each).

The formulas from chapter 5 can be used to determine outlet nozzle diameter and after simple transformation direct equation appears:

$$D = \sqrt{\frac{4F_u}{\pi \cdot \rho \cdot \left(\frac{u^2}{\mu^2} - \frac{u^2}{\mu}\right)}} \quad [m] \tag{7.2}$$

The range of possible nozzle sizes is presented in the chart below.

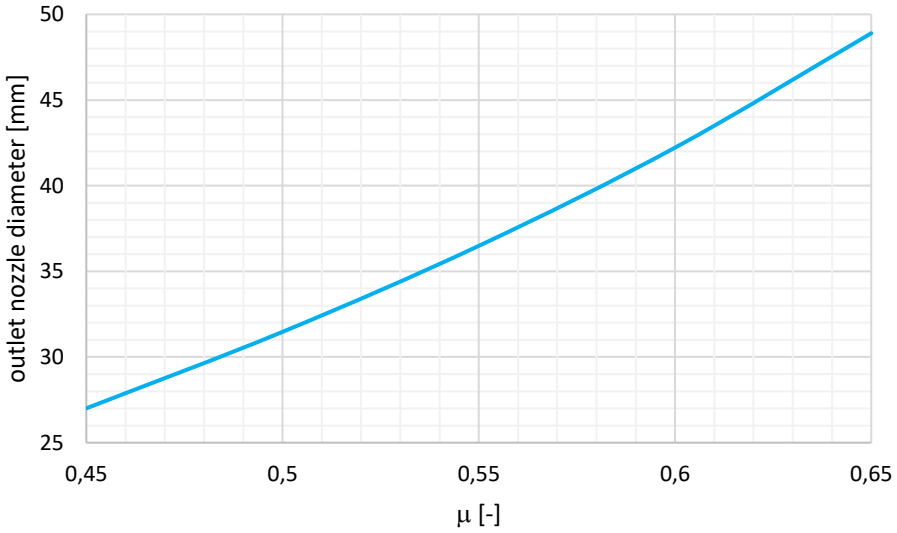

Figure 7.2: The outlet nozzle of a single waterjet propulsor in reference to relative velocity of an outlet jet. The range of velocity index μ for vehicle's operational velocity of 3 [m/s].

Table 7.1 Waterjet propulsor parameters for various rotor diameters and 14 [N] of thrust force.

no.	parameter	symbol	Unit	rotor 30 [mm]	rotor 40 [mm]	rotor 50 [mm]	rotor 60 [mm]
1	vehicle velocity	u	[m/s]	3.00	3.00	3.00	3.00
2	velocity at station no. 6	w_2	[m/s]	9.61	6.71	5.38	4.65
3	velocity index $\mu=u/w_2$	μ	[-]	0.31	0.45	0.56	0.65
4	velocity increase	$c_2=w_2-u$	[m/s]	6.61	3.71	2.38	1.65
5	**pump propeller diameter**	**D**	**[cm]**	**3.00**	**4.00**	**5.00**	**6.00**
6	propeller cross-sec. area	S_p	[cm^2]	7.07	12.56	19.63	28.26
7	mass flow	m	[kg/s]	2.12	3.77	5.89	8.48
8	volumetric flow	Q	[m^3/h]	7.63	13.56	21.20	30.52
9	water kinem. visco. at 10ºC (10e-6)	ν	[m^2/s]	1.35	1.35	1.35	1.35
10	outlet nozzle cross-sec. area	S_n	[cm^2]	2.21	5.62	10.94	18.23
11	nozzle surface / tunnel surface	S_n/S_p	[-]	0.31	0.45	0.56	0.65
12	outlet nozzle diameter	d	[cm]	1.68	2.67	3.73	4.82
13	outlet nozzle length	L	[cm]	4.00	4.00	4.00	4.00
14	vehicle propulsion power	$N_{u\text{-}vehicle}$	[W]	42.03	41.94	42.04	41.97
15	**waterjet trust**	**F_u**	**[N]**	**14.01**	**13.98**	**14.01**	**13.99**
16	carry over losses (power)	N_{carry}	[W]	46.30	25.93	16.67	11.54
17	R_e inside the tunnel	$R_{e\text{-}tunnel}$	[-]	66667	88889	111111	133333
18	channel friction coefficient	λ_{tunnel}	[-]	0.08	0.08	0.08	0.08
19	tunnel length	l	[cm]	15.00	15.00	15.00	15.00
20	tunnel slenderness	l/D	[-]	5.00	3.75	3.00	2.50
21	tunnel friction loss coefficient	ζ_f	[-]	0.42	0.31	0.25	0.20
22	loss at inlet	ζ_i	[-]	0.10	0.10	0.10	0.10
23	tunnel bend angle 1	α_1	[deg]	21.00	21.00	21.00	21.00
24	tunnel bend radius 1	R_1	[cm]	35.00	35.00	35.00	35.00
25	tunnel bend loss coef. 1	ζ_{b1}	[-]	0.06	0.06	0.06	0.06
26	tunnel bend angle 2	α_2	[deg]	21.00	21.00	21.00	21.00
27	tunnel bend radius 2	R_2	[cm]	7.50	7.50	7.50	7.50
28	tunnel bend loss coef. 2	ζ_{b2}	[-]	0.08	0.12	0.20	0.32
29	diffuser loss coefficient	ζ_d	[-]	0.10	0.10	0.10	0.10
30	$^1/_2$ outlet nozzle flare angle	$\delta_c/2$	[rad]	0.16	0.16	0.16	0.15
31	$^1/_2$ outlet nozzle flare angle	$\delta_c/2$	[deg]	9.40	9.41	9.00	8.40
32	out-nozzle loss coef. (in ref. to w_2)	$\zeta_{H\_out\text{-}nozzle\_w}$	[-]	0.15	0.10	0.06	0.04
33	out-nozzle loss coef. (in ref. to u)	$\zeta_{H\_out\text{-}nozzle\_u}$	[-]	1.56	0.49	0.19	0.09
34	outlet nozzle pressure loss	$H_{loss\_out\text{-}nozzle}$	[m]	0.27	0.11	0.07	0.04
35	head of outlet nozzle height	$H_{loss\_out\text{-}nozzle}$	[m]	0.00	0.00	0.00	0.00
36	sum of coefficients of losses	$\Sigma\zeta$	[-]	2.32	1.18	0.90	0.87
37	head of losses (m)	ΣH_{loss}	[m]	1.07	0.54	0.41	0.40
38	head of losses (Pa)	ΣH_{loss}	[Pa]	10653	5426	4109	4002
39	power losses	N_{loss}	[W]	22.15	20.06	23.73	33.28
40	head of carry over losses	H_{carry}	[m]	2.23	0.70	0.29	0.14
41	propulsion head	H_{prop}	[m]	2.02	1.13	0.73	0.50
42	pump head	H_{pump}	[m]	5.31	2.38	1.43	1.04
43	$\mathbf{N_p \cdot \eta_p = N_{u\text{-}vehicle} + N_{carry} + N_{loss}}$		**[W]**	**110.48**	**87.92**	**82.44**	**86.79**
44	waterjet efficiency	η_{wj}	[-]	0.23	0.30	0.33	0.32
45	motor output power	N_{motor}	[W]	184.14	139.56	126.83	129.53
46	motor and controller efficiency	η_{z+s}	[-]	0.70	0.70	0.70	0.70
47	power drain of motor controller	N_s	[W]	263.05	199.38	181.19	185.05
48	total propulsion efficiency	η	[-]	0.16	0.21	0.23	0.23
49	pump velocity per second	n	[rps]	125	94	75	63
50	pump velocity per minute	n	[rpm]	7500	5625	4500	3750
51	pump kinematic speed index	n_{sQ}	[-]	99	180	264	334

Note: some indexes used in the tables above may not refer directly to the ones listed at the beginning of this thesis. The units differ as well. The reason for this is a large number of parameters used in the calculations. However, all of them were shortly described in order to make it easier to identify.

Table 7.2: Waterjet propulsor parameters for rotor diameter of 50 [mm] as a function of the jet stream outlet velocity. The thrust force of 14 [N] is required to propel the vehicle at 3.0 [m/s].

no.	parameter	symbol	unit	jet stream outlet velocity w_2 at station no. 6 [m/s]				
				5.00	5.25	5.50	6.00	6.50
1	vehicle's velocity	u	[m/s]	3.00	3.00	3.00	3.00	3.00
2	velocity index $\mu=u/w_2$	μ	[-]	0.60	0.57	0.55	0.50	0.46
3	velocity increase	$c_2=w_2-u$	[m/s]	2.00	2.25	2.50	3.00	3.50
4	pump propeller diameter	D	[cm]	5.00	5.00	5.00	5.00	5.00
5	propeller cross-sec. area	S_p	[cm^2]	19.63	19.63	19.63	19.63	19.63
6	mass flow	m	[kg/s]	5.89	5.89	5.89	5.89	5.89
7	volumetric flow	Q	[m^3/h]	21.20	21.20	21.20	21.20	21.20
8	water kinem. visco. at 10ºC (10e-6)	ν	[m^2/s]	1.35	1.35	1.35	1.35	1.35
9	outlet nozzle cross-sec. area	S_n	[cm^2]	11.78	11.21	10.70	9.81	9.06
10	nozzle surface / tunnel surface	S_n/S_p	[-]	0.60	0.57	0.55	0.50	0.46
11	outlet nozzle diameter	d	[cm]	3.87	3.78	3.69	3.54	3.40
12	outlet nozzle length	L	[cm]	4.00	4.00	4.00	4.00	4.00
13	**waterjet trust**	**F_u**	**[N]**	**11.78**	**13.25**	**14.72**	**17.66**	**20.61**
14	vehicle propulsion power	$N_{u\text{-}vehicle}$	[W]	35.33	39.74	44.16	52.99	61.82
15	carry over losses (power)	N_{carry}	[W]	11.78	14.90	18.40	26.49	36.06
16	R_e inside the tunnel	$R_{e\text{-}tunnel}$	[-]	111111	111111	111111	111111	111111
17	tunnel friction coefficient	λ_{tunnel}	[-]	0.08	0.08	0.08	0.08	0.08
18	tunnel length	l	[cm]	15.00	15.00	15.00	15.00	15.00
19	tunnel slenderness	l/D	[-]	3.00	3.00	3.00	3.00	3.00
20	tunnel friction loss coefficient	ζ_f	[-]	0.25	0.25	0.25	0.25	0.25
21	loss at inlet	ζ_i	[-]	0.10	0.10	0.10	0.10	0.10
22	tunnel bend angle 1	α_1	[deg]	21.00	21.00	21.00	21.00	21.00
23	tunnel bend radius 1	R_1	[cm]	35.00	35.00	35.00	35.00	35.00
24	tunnel bend loss coef. 1	ζ_{b1}	[-]	0.03	0.03	0.03	0.03	0.03
25	tunnel bend angle 2	α_2	[deg]	21.00	21.00	21.00	21.00	21.00
26	tunnel bend radius 2	R_2	[cm]	7.50	7.50	7.50	7.50	7.50
27	tunnel bend loss coef. 2	ζ_{b2}	[-]	0.04	0.04	0.04	0.04	0.04
28	diffuser loss coefficient	ζ_d	[-]	0.10	0.10	0.10	0.10	0.10
29	$^1/_2$ outlet nozzle flare angle	$\delta_c/2$	[rad]	0.14	0.15	0.16	0.18	0.20
30	$^1/_2$ outlet nozzle flare angle	$\delta_c/2$	[deg]	8.02	8.67	9.28	10.37	11.33
31	out-nozzle loss coef. (in ref. to w_2)	$\zeta_{H\_out\text{-}nozzle\_w}$	[-]	0.04	0.05	0.07	0.09	0.11
32	out-nozzle loss coef. (in ref. to u)	$\zeta_{H\_out\text{-}nozzle\_u}$	[-]	0.12	0.17	0.22	0.35	0.52
33	outlet nozzle pressure loss	$H_{loss\_out\text{-}nozzle}$	[m]	0.06	0.06	0.07	0.08	0.09
34	head of outlet nozzle height	$H_{loss\_out\text{-}nozzle}$	[m]	0.00	0.00	0.00	0.00	0.00
35	sum of coefficients of losses	$\Sigma\zeta$	[-]	0.64	0.69	0.74	0.87	1.04
36	head of losses (m)	ΣH_{loss}	[m]	0.29	0.31	0.34	0.40	0.48
37	head of losses (Pa)	ΣH_{loss}	[Pa]	2936	3142	3387	3998	4779
38	power losses	N_{loss}	[W]	16.96	18.15	19.56	23.09	27.60
39	head of carry over losses	H_{carry}	[m]	0.20	0.26	0.32	0.46	0.62
40	propulsion head	H_{prop}	[m]	0.61	0.69	0.76	0.92	1.07
41	pump head	H_{pump}	[m]	1.11	1.26	1.42	1.78	2.17
42	pump efficiency	η_p	[-]	0.65	0.65	0.65	0.65	0.65
43	$\mathbf{N_p \cdot \eta_p = N_{u\text{-}vehicle} + N_{carry} + N_{loss}}$		**[W]**	**64.06**	**72.79**	**82.12**	**102.57**	**125.48**
44	waterjet efficiency	η_{wj}	[-]	0.36	0.35	0.35	0.34	0.32
45	motor output power	N_{motor}	[W]	98.55	111.99	126.33	157.80	193.05
46	motor and controller efficiency	η_{z+s}	[-]	0.70	0.70	0.70	0.70	0.70
47	power drain of motor controller	N_s	[W]	140.79	159.98	180.48	225.43	275.78
48	total propulsion efficiency	η	[-]	0.25	0.25	0.24	0.24	0.22
49	pump velocity per second	n	[rps]	75	75	75	75	75
50	pump velocity per minute	n	[rpm]	4500	4500	4500	4500	4500
51	pump kinematic speed index	n_{sQ}	[-]	319	290	265	224	193

Note: some indexes used in the tables above may not refer directly to the ones listed at the beginning of this thesis. The units differ as well. The reason for this is a large number of parameters used in the calculations. However, all of them were shortly described in order to make it easier to identify.

The results of the calculations presented in the Table 7.1 and Table 7.2 are summarized in the Table 7.3.

Different propulsion types or different propellers / rotors can be compared with a use of the propeller load factor ζ_T. It is simple formula based on thrust generated by the propeller *T*, its size S_{PROP} and velocity it generates *v*.

$$\zeta_T = \frac{2 \cdot T}{\rho \cdot v^2 \cdot S_{PROP}} \quad [-]$$

7.3

The Table 7.3 below indicates the influence of the various features on the overall performance of the waterjet. The calculation results can be summarized as follows:

- dominating influence of the pump efficiency
- limited influence of the propulsion's tunnel parameters
- increasing influence of the tunnel losses (particularly due to friction losses) with increasing tunnel diameter (assuming constant tunnel length)
- the carry over losses drops significantly with increasing tunnel and pump diameter; however, it is negatively compensated by rapidly increasing tunnel losses
- for assumed vehicle's velocity and corresponding drag, the optimum diameter of the pump rotor is 50 [mm]. This value can be compared with the values calculated using expression 7.1 and shown in the Figure 7.1.

Table 7.3: Comparison of the relative parameters of waterjet propulsors with various pump rotor diameters for assumed thrust of 14 [N].

no.	parameter	symbol	unit	pump rotor diameter [mm]			
				30	40	50	60
1	velocity of the vehicle	u	[m/s]	3.00	3.00	3.00	3.00
2	velocity at station no. 6	w_2	[m/s]	9.61	6.71	5.38	4.65
3	velocity index $\mu=u/w_2$	μ	[-]	0.31	0.45	0.56	0.65
4	waterjet trust	F_u	[N]	14.01	13.98	14.01	13.99
5	motor output power required	N_m	[W]	184.14	139.56	126.83	129.53
6	ship prop. power - waterjet efficiency		[%]	22.83	30.05	33.14	32.40
7	carry over relative loss		[%]	25.15	18.58	13.15	8.91
8	pump relative loss		[%]	40.00	37.00	35.00	33.00
9	**sum of tunnel relative losses**		**[%]**	**12.03**	**14.37**	**18.71**	**25.69**
10	tunnel friction relative losses		[%]	2.19	3.80	5.17	6.02
11	inlet relative loss		[%]	0.52	1.21	2.09	2.95
12	bend 1 relative loss		[%]	0.57	1.02	1.60	2.33
13	bend 2 relative loss		[%]	0.41	1.47	4.12	9.51
14	diffuser relative losses		[%]	0.52	1.21	2.09	2.95
15	outlet nozzle relative loss		[%]	8.10	5.99	4.06	2.57

Note: some indexes used in the tables above may not refer directly to the ones listed at the beginning of this thesis. The units differ as well. The reason for this is a large number of parameters used in the calculations. However, all of them were shortly described in order to make it easier to identify.

It can be seen that operating parameters of the pump define the value of the velocity index around 300 [-]. This value allows for application of an axial pump that is simpler to design and manufacture than mixed flow pump. It is also easier to install such pump within the space available inside the vehicle's aft (rear end flow stabilizers).

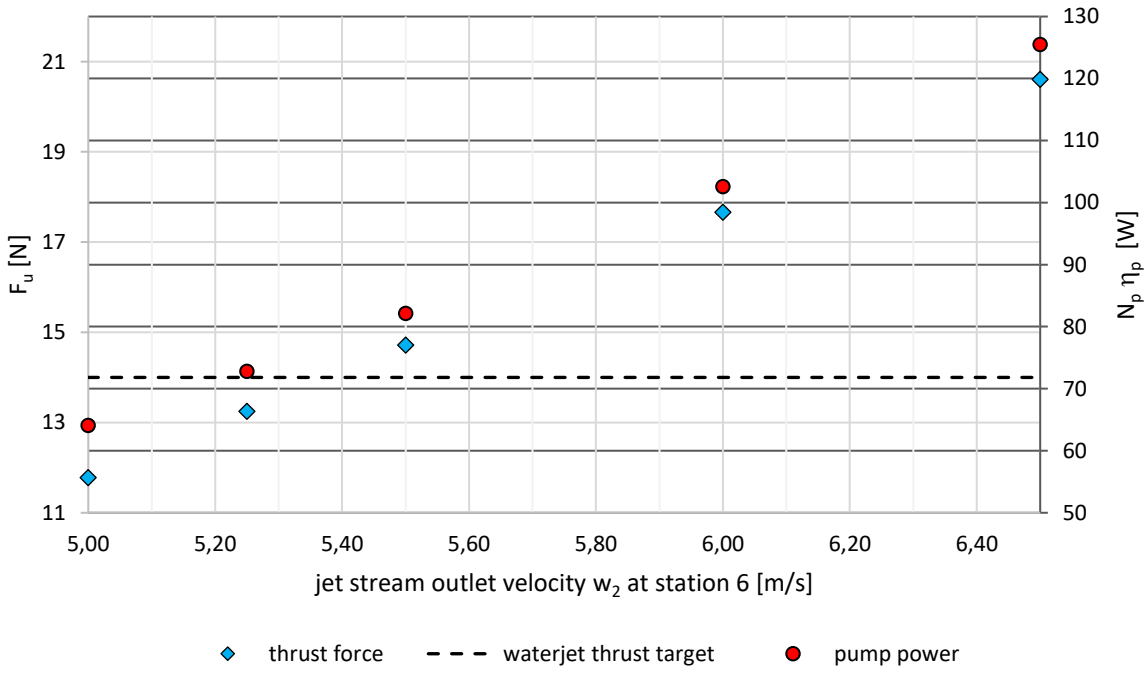

Figure 7.3: Graphical representation of analytical calculation for waterjet propulsor equipped with 50 [mm] rotor (rows 13 and 43 in the Table 7.2).

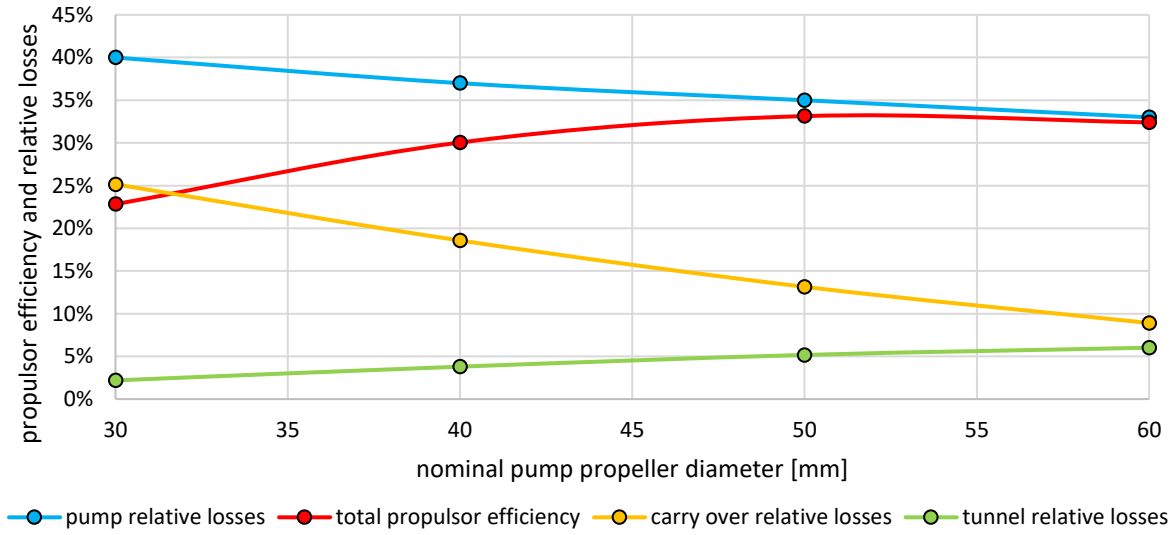

Figure 7.4: Graphical comparison of calculated relative losses and propulsion efficiencies for different pump propeller diameters (Table 7.3Table 4.1).

8 Investigation of possible improvements of the waterjet propulsion efficiency with a use of CFD methods

The current CFD methods give the possibility of predicting numerous different quantities. In this particular case, forces acting on the vehicle and flow separation play the key role. Therefore, the ability to obtain credible numerical results is very important and can help indicate areas of possible improvements. However, it must be kept in mind, the potential increase of the propulsor efficiency using this method requires separate extensive experimental research. A wide range of different geometries configurations for both propulsion and the vehicle are necessary.

The reason for introducing CFD in the design process is possible costs and time reduction normally required by the real vehicle experiments. However, it is questionable if the current CFD codes are accurate and reliable enough to simulate the phenomena in the studied flow.

8.1 CFD studies on selected waterjet elements and their influence on overall propulsion performance

8.1.1 Introduction

Both tests results and theoretical considerations suggest that application of a waterjet in the investigated vehicle can be justified solution. However, despite promising, off-the-shelf propulsion-kits were far from being perfect and the new drive had to be optimised to meet operating point's requirements. That is why, from the very beginning, all of analyses described above were in a matter of fact a prelude to self-designed waterjet propulsor. Pump pundit and computational fluid dynamics simulations aided the design process.

A pump-design specialist was responsible for rotor-stator pair, whereas the author focused on development of the tunnel. The design started on waterjet theory described in chapter 6 and followed by long series of CFD simulations. The experience gained during previous projects gave the author self-confidence strong enough to base on it regardless of the initial results. Though being drag prediction analyses mainly, they were accurate enough to build the trust to the general flow characteristic – even if the values themselves do not match the references ones precisely (e.g., [86]). Such approach is a good starting point – especially when the designer heads into the unknown. Therefore, the first target was set at the velocity field inside the propulsion's tunnel. The aim was to get as smooth and uniform flow distribution as it was possible.

The very first assumption was, that the "problem" is circularly symmetric and the case was limited to a single propulsor (see the Figure 8.28). The sonar canopy and transponder were ignored deliberately because, at this stage, their importance was considered as minor – it affects the vertical propeller inflow the most – not the top horizontal ones – so it could have been simplified this way. The vehicle's hull, however, was deployed mainly to build the boundary layer before propulsion inlet. Therefore, one of the bottom quarters was taken into account and

placed into the domain dimensions certainly represent vehicle's operating environment – a high sea.

At this point, the author would like to emphasize, in his opinion, very important matters while performing these types of simulations: the domain size, problem complexity and an approach to the solution.

Actually, in nearly all the cases studied while preparing to perform these simulations scientists / engineers limited their analyses in one way or another. These simplifications can be grouped as follows:

- A heavy domain reduction, where only small part of the pump or propeller is taken into analysis. In other words, rotational periodicity is deployed, rotor-stator pair is cut into sections and only a fraction of the whole pump or propulsion is analysed – see an example in the Figure 8.1. [87] [88] [89] [90] [91] [92] [93] A very common modelling method used in pump design and performance optimisation process.
- The full geometry of rotor and stator is kept, but fluid domain is limited again. This time, it often starts right before pump inlet and ends shortly after it. [49] [94] [95] [96] [97] It is not a bad idea for problems such as blood pumps [98] [99], where flow inside the pipe (vain) is linked directly with pump efficiency. It is also crucial in unsteady state simulations. It allows to analyse the flow character inside the pump without severe simplifications maintaining reasonable number of mesh elements and relatively short calculation time. What is more, it is accurate enough to investigate the whole device in terms of phenomena such as cavitation or flow damping and flow breakdowns. [48]
- A bare propeller investigated inside a big domain. This type of analysis is directed to wind turbine rather than waterjet drives or vessels' propellers researches. [100] [101] [102] It represents solitude standing wind turbine quite well, but it omits hull – propeller interaction phenomenon.
- A virtual, rotating disc put instead of full rotor (and stator) geometry. It is a good simplification and facility regarding investigation of flow inside waterjet propulsion's tunnel or around the vessel's hull. In terms of velocity and pressure fields or overall flow character, it can deliver valuable results. In addition, compared to full geometry analysis rotor's absence reduces number of mesh elements significantly and hence speeds up simulations. [22] [103] [58]
- The analyses based on the whole geometry. The most sophisticated simulations including complete geometry and often more than one phenomenon is taken into consideration. [104] [105] Moreover, given the very recent software development also hull – propulsion coupled analyses become possible. [106]
- Sometimes it is also possible to perform CFD analysis in very tight domain. However, it must be borne in mind that it works in particular cases only. [107] [108] For instance, when the principal aim of analysis is to research only a part of investigated design [109]; compare and contrast different mathematical models describing phenomena we are interested in; the very first comparison of different rotor's blade geometries etc. In other cases, when precise result is required, exceptional carefulness is advised.

So, given only this brief list and rough classification it can be seen there are few possibilities to perform CFD simulations of newly designed jet drive. In this case it was decided to do it as full hull–propulsor interaction. Though it was impossible to translate thrust force from rotor's blades via shaft to vehicle's hull in order to move it, still a complex analysis was feasible. In other words, it was expected to achieve reliable results using Fluid Structure Interaction approach with minimum model simplifications possible. Personally, the author sees very little opportunities for achieving good outcomes with a use of all but this method among the ones mentioned above. In his opinion correlation between jet's outflow and water flowing around the vehicle's aft canopy is the key element here. Of course, from the very beginning, it was obvious that, given the size of the vehicle, forces to be measured and unpredictability of test environment it would be very difficult or even impossible to obtain satisfying convergence between numerical and experimental results. That is the reason why it was decided to focus on operating point only.

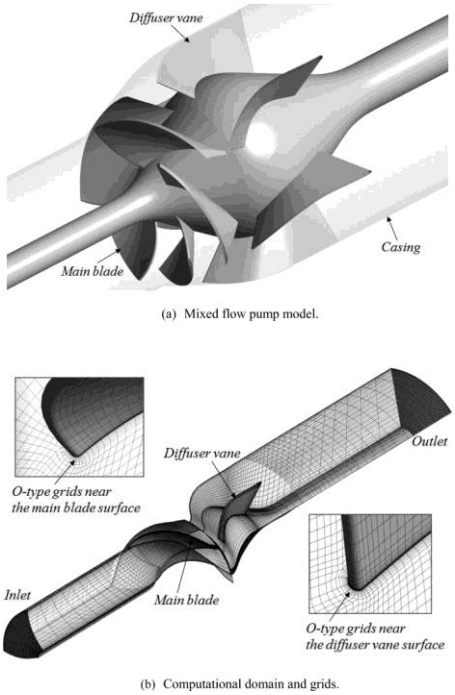

Figure 8.1: A domain division example for common turbine CFD analysis and / or optimisation. Because of its periodicity around rotor's axis-of-revolution, pump internal volume was cut into identical sections. It results in lower total number of mesh elements and shortens calculation time. [110]

8.1.2 Mathematical model of turbulence

All CFD analyses performed for this thesis were based on Reynolds-Averaged Navier-Stokes (RANS) equations, that describe both types of flow: laminar and turbulent. It must be remembered however they cover wide range of turbulence length and time scales – including the slightest ones. It means there is a group of turbulence scales, which are smaller than the smallest finite volume cell in analysed domain. To make it possible to simulate two different flow regimes (laminar and turbulent) within one simulation run and without recourse to excessive mesh density or direct numerical simulations, the turbulence models were developed and one of them – *Shear Stress Transport* – was used in this case.

In terms of results, it is extremely important to determine the transition point between laminar sublayer and turbulent layer as accurately as it is possible for appropriate flow. Moreover, in case of investigated vehicle, its hull-protruding elements (sonar canopy, launch handles and transponder), vertical propulsion tunnel and jet drive rotors complicate simulation additionally. Hence the importance of adequate turbulence model choice.

The *Shear Stress Transport* is two-equation model based on $k-\omega$ one. Its main advantages are high stability and boundary layer solution approach. The SST does not resolve (calculate) near the wall velocity profile, but predicts it with a use of a wall function. It allows to perform analyses using lower density meshes and still obtain precise solution.

The wall function operates in two main ways. The first function, called "scalable", does not require precise first layer height for boundary layer. As the name suggests points necessary to build the velocity profile are obtained from rescaled mesh. It is very useful feature in case providing appropriate mesh in boundary layer is difficult or even impossible. However, in considered problem, where flow separation plays very important role, the second wall function model is more suitable. It is called "automatic", which means it switches between laminar and turbulent boundary layer model automatically. It is, in author's opinion, the key feature given the places such as rotors blades, stator blades backside and space underneath the shaft or fin's run-off areas. All these regions are places, where the flow separation, flow damping or flow breakdown occurs or may occur.

It must be kept in mind, that unlike the previous model, where reaching good results convergence is possible even if y^+ factor goes down to about 1 (one), here it plays the major role. Hence, the y^+ factor was the mesh parameters determinant.

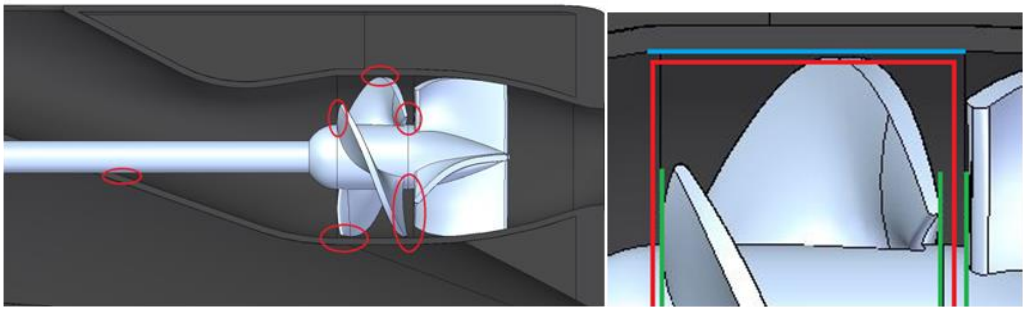

Figure 8.2: Places where "automatic" wall function is expected to gain the upper hand.

Due to peculiar shape and small space available, the places presented in the Figure 8.2 were expected to cause problems during the meshing process:

- the transition between propulsion tunnel wall and shaft casing – the bottom part – because of sharp edge and heavily bend surfaces intersecting each other
- the gap between rotor's blade tip and the tunnel wall – because of insufficient room for mesh necessary to meet the y^+ requirements
- the space among rotor and stator
- the fin's sharp edge combined with small, flat surface at the tunnel outlet

Although the SST model is based on $k-\omega$ one, it is in a matter of fact a combination of merits of $k-\varepsilon$ (especially its RNG form) and $k-\omega$ models. It is not only better in delivering accurate solution (e.g., [111]), but also more stable and less sensitive to lower quality meshes.

All the simulations were performed in *Ansys CFX*, which SST model is based on Wilcox's $k-\omega$ one [112] [113]. The solver resolves two transport equations: *k* for the turbulent kinetic energy and ω for turbulent frequency.

k – equation

$$\frac{\partial k}{\partial t}+U_j\frac{\partial k}{\partial x_j}=\tau_{ij}\frac{\partial U_i}{\partial x_j}-0.09k\omega+\frac{\partial}{\partial x_j}\left[\left(\nu+0.5\frac{k}{\omega}\right)\frac{\partial k}{\partial x_j}\right] \quad \textbf{8.1}$$

ω – equation

$$\frac{\partial \omega}{\partial t}+U_j\frac{\partial \omega}{\partial x_j}=\frac{5}{9}\frac{\omega}{k}\tau_{ij}\frac{\partial U_i}{\partial x_j}-\frac{3}{40}\omega^2+\frac{\partial}{\partial x_j}\left[\left(\nu+0.5\frac{k}{\omega}\right)\frac{\partial \omega}{\partial x_j}\right] \quad \textbf{8.2}$$

The basic notations of Wilcox's equations, with all coefficients already applied, makes the recognition of particular ingredients easier. Therefore, *U* stands for water velocity, τ is molecular stress tensor (includes both normal as well as shear components of the stress), ν represents water kinematic viscosity coefficient and *x* is an element location. Of course, depending on the software, the formulas can take various forms, but do not differ much from each other.

8.1.3 Flow around the investigated vehicle's body

Initial phase of the calculations was devoted to simulate flow around the body of the vehicle. This allowed to find the basic settings of CFD simulation for further studies of working waterjet propulsors. It was possible to verify the results of these calculations using results of the measurements of the resistance of the real vehicles in the same configurations.

- 4 x standard 100 [mm] propellers
- 4 x standard 100 [mm] propellers with mesh-guard
- 4 x waterjet propulsors with 39 [mm] diameter of the pump rotor
- 4 x waterjet propulsors with 50 [mm] diameter of the pump rotor

The numerical outcomes combined with experimental data gathered in later tests are presented below. Verified results of the CFD simulations are good background for further investigation of the propulsors operating with influence of the flow around the body.

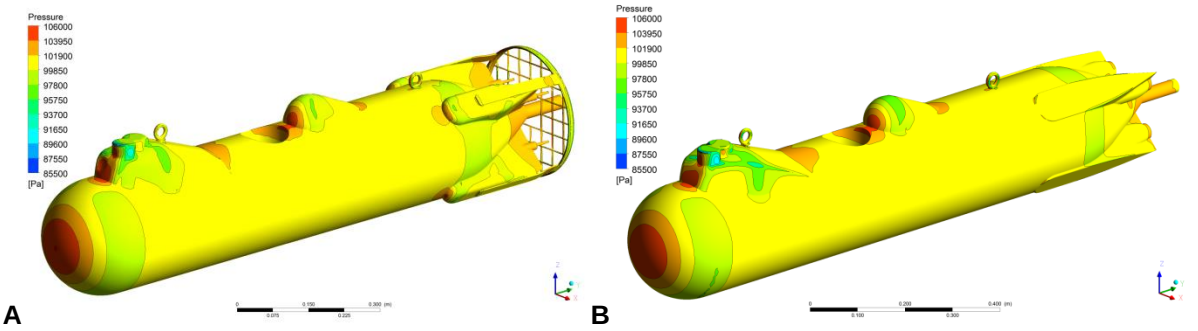

Figure 8.3: Pressure distribution on vehicle's hull – standard, mesh-guarded propellers (A) and waterjet drive (B).

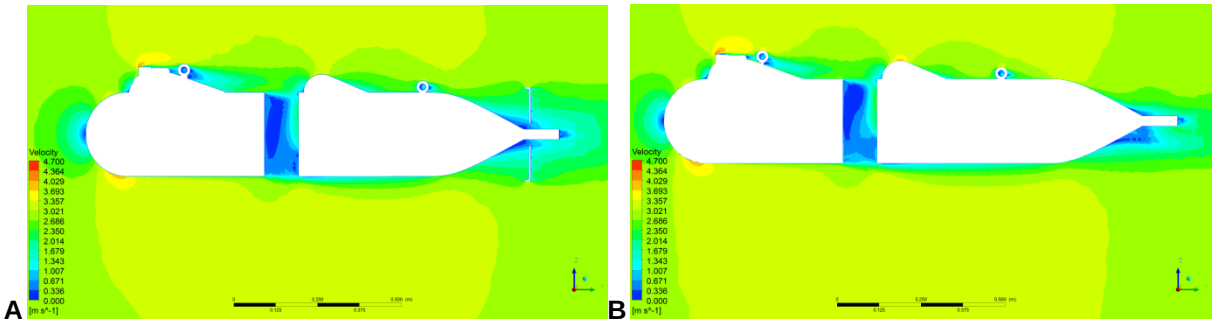

Figure 8.4: Velocity field on longitudinal section plane – standard, mesh-guarded propellers (A) and waterjet drive (B).

The CFD-obtained outcomes seem to correspond very well to the experimental data (Table 8.1). The operating point at 3.0 [m/s] and its vicinity match within 6% for all analysed configurations – lower velocities were not relevant to the study hence, in some cases, poor convergence was not a concern. It led to the conclusion, the method and settings used in the simulations, at this stage, proved their value.

Table 8.1: Prediction of the vehicle drag for different configurations, compared to experimental results.

		SP			SP+G			WJ39G			WJ50		
no.	**v**	**R_{exp}**	**R_{CFD}**	**Δ_R**	**R_{exp}**	**R_{CFD}**	**Δ_R**	**R_{exp}**	**R_{CFD}**	**Δ_R**	**R_{exp}**	**R_{CFD}**	**Δ_R**
	[m/s]	**[N]**	**[N]**	**[%]**	**[N]**	**[N]**	**[%]**	**[N]**	**[N]**	**[%]**	**[N]**	**[N]**	**[%]**
1	0.5	1.00	1.68	68.0	2.75	2.69	-2.2	1.25	1.60	28.0	2.00	2.39	19.5
2	1.0	5.10	6.05	18.6	9.75	10.27	5.3	5.25	5.50	4.8	7.00	7.70	10.0
3	1.5	12.50	13.21	5.7	20.00	19.51	-2.4	11.50	11.79	2.5	15.00	15.98	6.5
4	2.0	22.75	23.12	1.6	36.00	33.76	-6.2	20.50	20.28	-1.1	25.75	23.50	-8.7
5	2.5	36.50	38.48	5.4	54.00	52.26	-3.2	32.00	30.12	-5.9	38.50	36.07	-6.3
6	3.0	53.50	55.12	3.0	75.00	74.55	-0.6	46.00	43.28	-5.9	52.00	51.19	-1.6

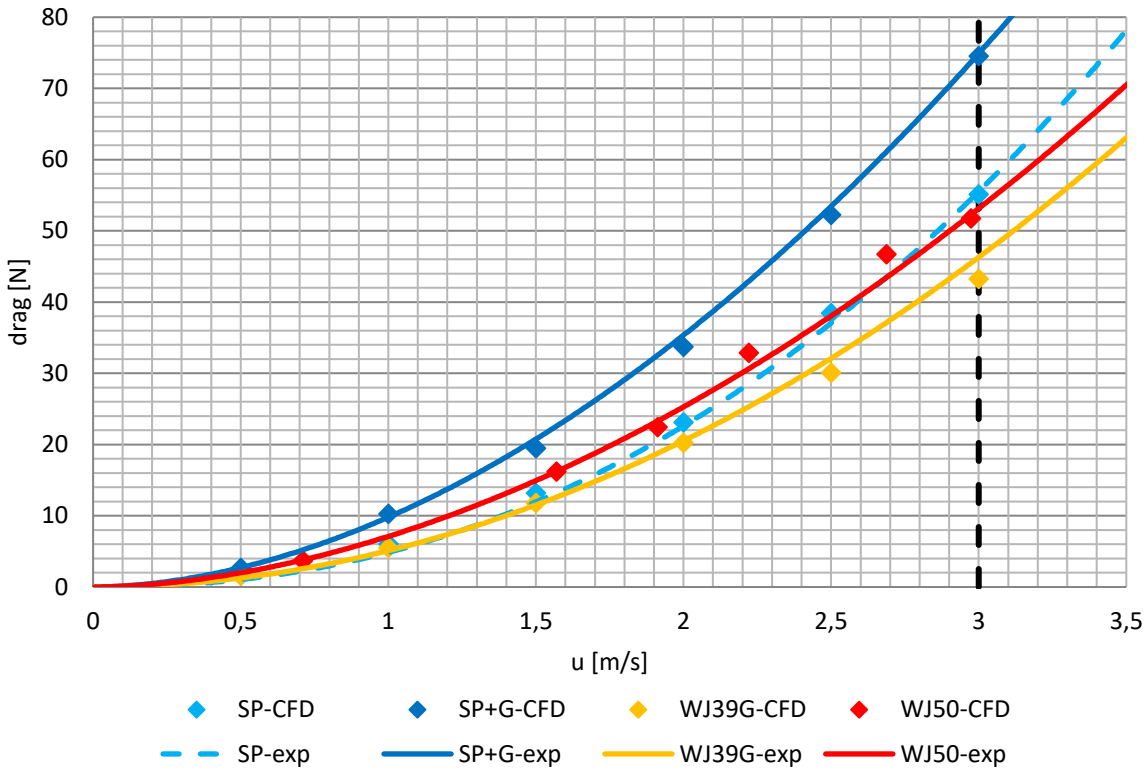

Figure 8.5: Vehicle's drag curves – experimental results and CFD predictions comparison.

8.2 Development of the dedicated waterjet propulsor

8.2.1 Inlet shape performance analysis

As mentioned earlier (subsection 6.4.3), independent studies of other naval scientists proved minor influence of inlet area shape on jet drive overall performance. However, this area still requires very careful approach.

The analysis covered four basic shapes:

— elliptical (recommended by Alexander and Terwisga [114])
— elliptical-rectangular
— rectangular
— rectangular-elliptical

All the geometries share the same inlet area at station 2 (see Figure 6.1 and Figure 8.9 inlet throat) and have common tunnel generating line. The domain dimensions were set to represent vehicle's ones. The tunnel outflow was set at the pump inlet and was equivalent to expected mass flow rate at 5.89 [kg/s]. The overall velocity in the domain refers to vehicle's operating point at 3.0 [m/s].

Very important thing must be written and kept in mind at this point. Providing optimum results for each inlet shape would require further work over tunnel shape, because relation between intake and the tunnel is very strong. Therefore, if exceptionally precise and accurate

results were needed the separate study over this subject is required. In this case, however, the focus was put on basic shape changes and their influence on the ultimate outcome.

According to Alexander's et al. [20] recommendation, the elliptical intake should provide the most uniform velocity field. In four analysed cases, the greatest difference between results is just above 3%. Therefore, it seems to confirm previous findings in this matter, that this area is flexible and leaves wide range of possibilities to the designer.

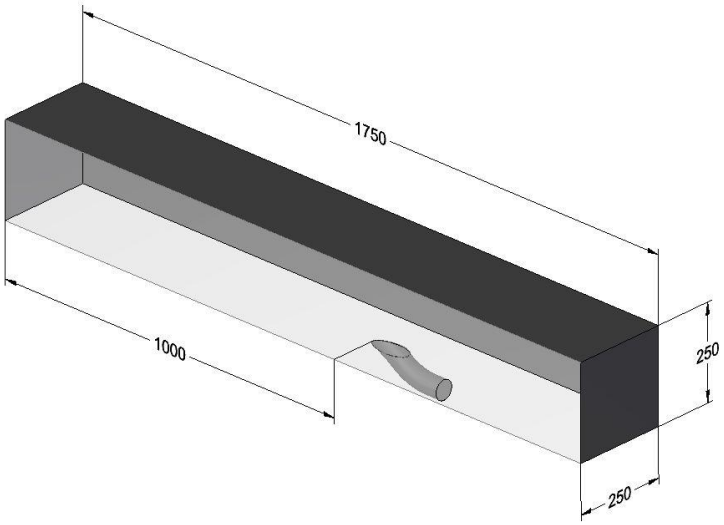

Figure 8.6: Inlet shape studies – the domain dimensions [mm].

Table 8.2: Water velocities at different areas of the tunnel for investigated intake shapes.

		water velocity [m/s]		
no.	**shape**	**inlet**	**inlet throat**	**outlet**
1	elliptical	3.19	2.98	2.91
2	elliptical-rectangular	3.09	3.00	2.92
3	rectangular	3.10	3.00	2.94
4	rectangular-elliptical	3.06	3.01	2.93

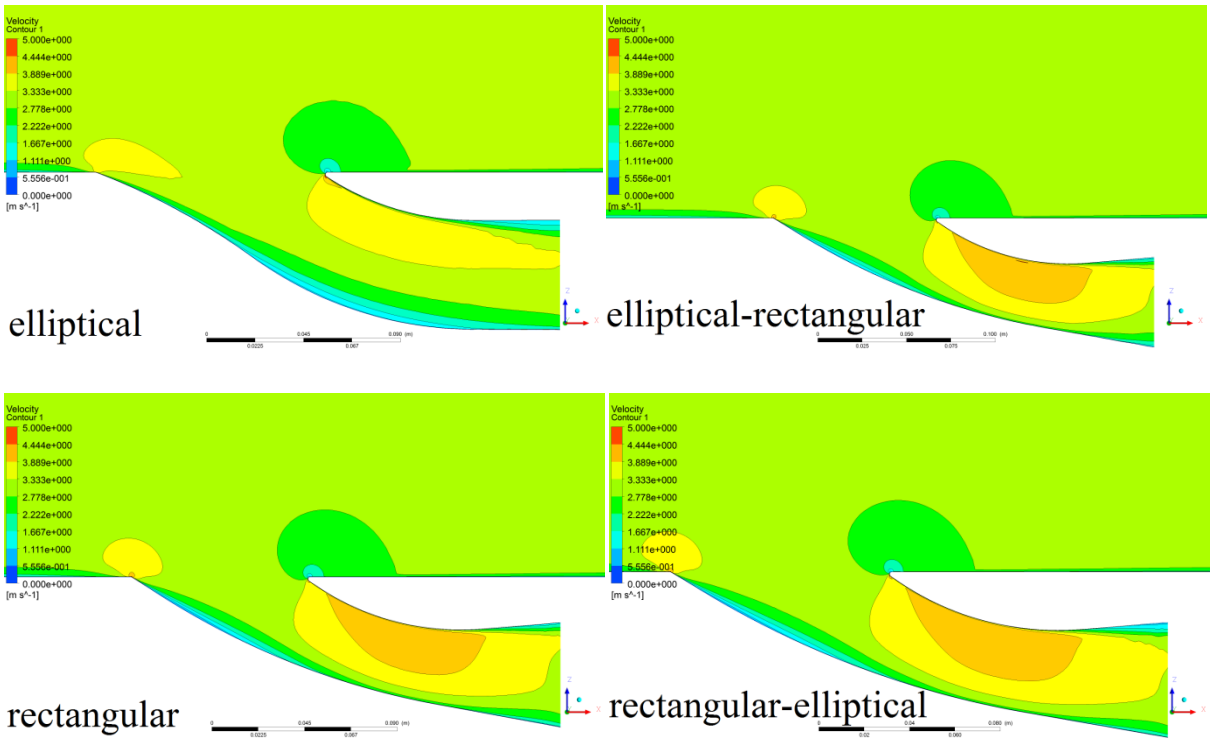

Figure 8.7: The velocity fields inside the tunnel for four inlet shapes.

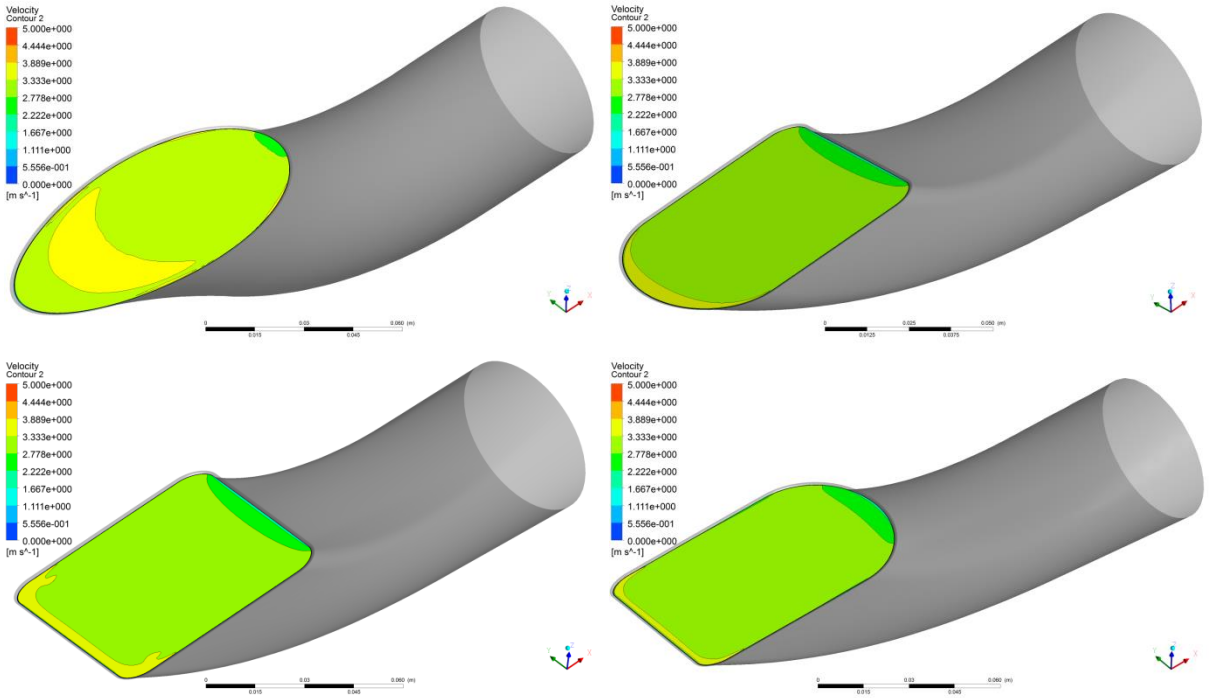

Figure 8.8: The velocity fields at the INLET area.

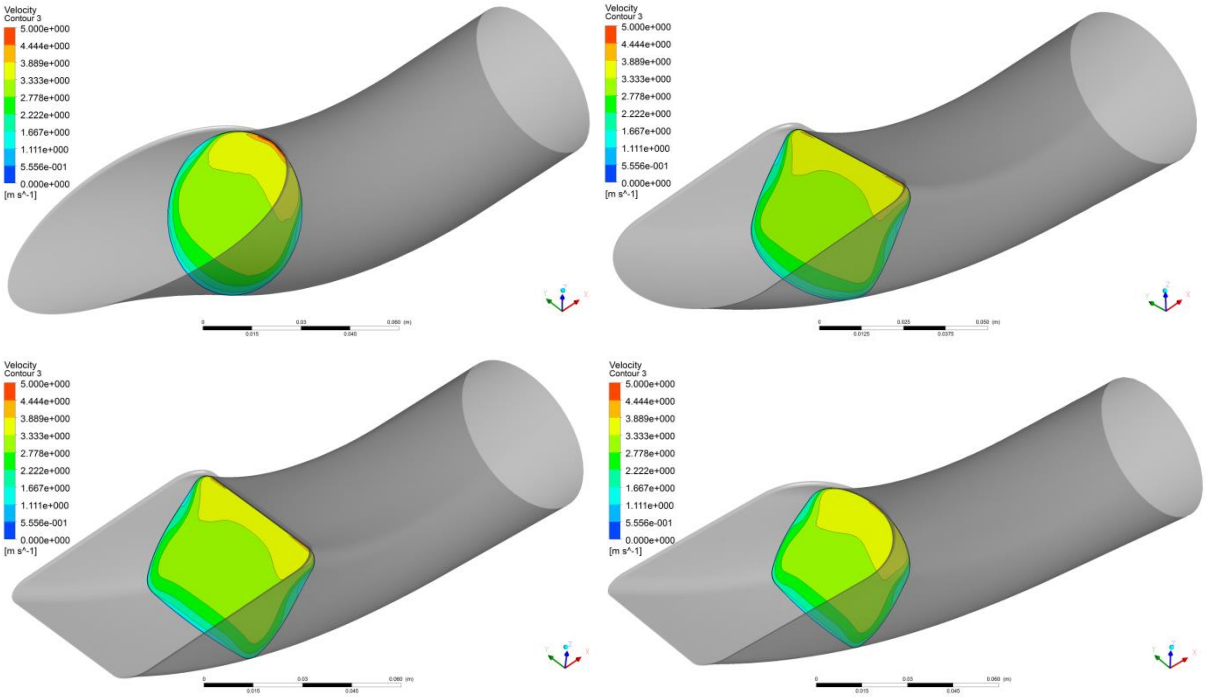

Figure 8.9: The velocity fields at the INLET THROAT.

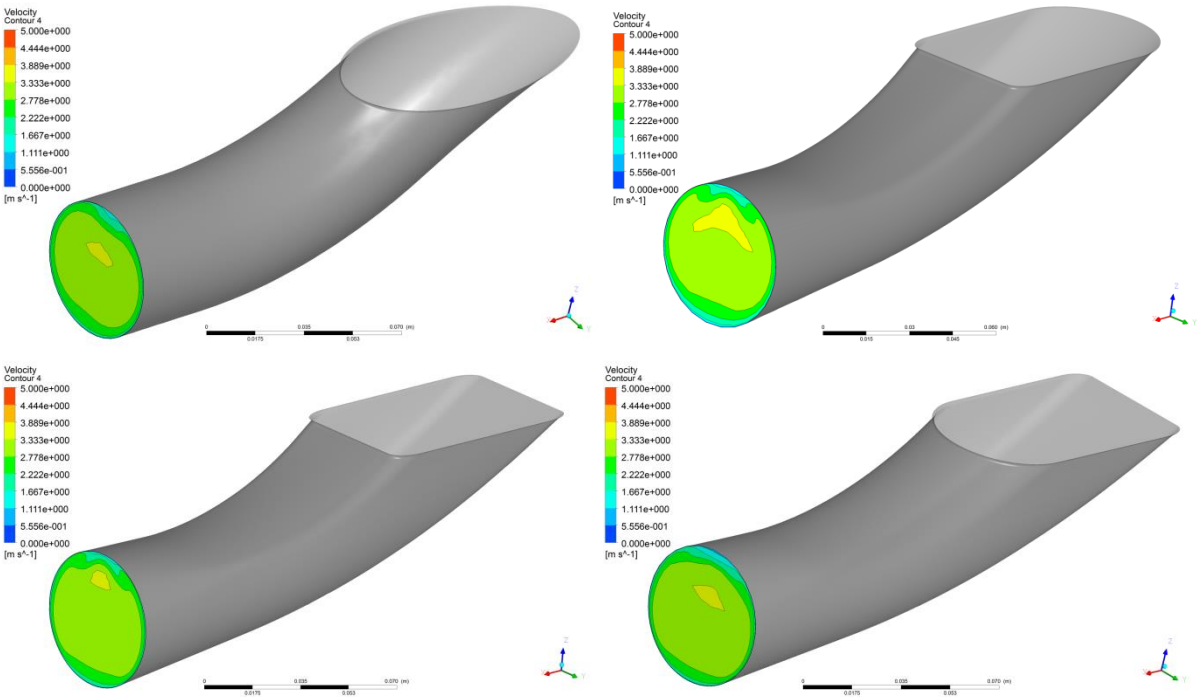

Figure 8.10: The velocity fields at the pump inlet (domain OUTLET in this particular case).

8.2.2 Analysis of the inlet flow separation on the propulsor's performance

The next stage of the waterjet propulsor analyses referred to potential improvements at inlet separation edge. The fundamental question was whether there was a possibility to improve the water inflow to the tunnel and thus propulsion's overall performance. The idea was to

introduce the solution similar to the one used in jet fighters, where jet engine inlet is placed at some distance from airplane's hull.

Figure 8.11: F-16 B jet fighter – clearly visible gap between airframe and the engine inlet [115] .

Theoretically, the gap should be big enough to ensure cut-off of the whole boundary layer at maximum speed. The analysis was performed with a use of tunnel shape and waterjet propulsor developed especially for this project (WJ50). The tunnel development was described in the next subsection. The solution, however, was found to have significant negative influence on the vehicle's drag. The CFD research (Figure 8.12) suggests 30-40% drag increase for selected designs when compared to the flush type intake – to see the difference between flush and ram intake see the Figure 3.15.

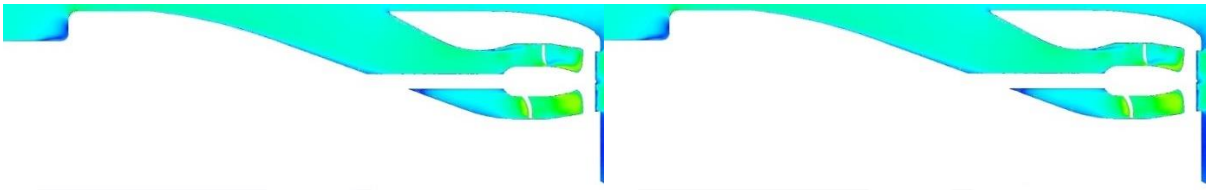

H **F16**

Figure 8.12: The velocity fields at the intake and inside the waterjet tunnel developed for minimum losses. Versions H and F16 with the separated intake flow.

8.2.3 Development of the tunnel geometry for the best performance

The collection of pictures below presents tunnel investigation process – the way it was driven and problems encountered. All pictures show velocity fields in the longitudinal symmetry plane. Sometimes stator's blades disturb the view, hence all these irregular and peculiar cut-offs presence. Naturally, the main aim was to minimise the flow losses for assumed operating parameters, which meant to develop the smoothest velocity layout possible. In this case, the precise velocity values are unimportant, that is why the legend is absent. However, as usual the colder colour the lower velocity, which means deep blue represents zero. The numbers and letters refer to consecutive tunnel versions. There were plenty of different shapes analysed, but the ones that had not brought anything new or simply had failed in developing expected results were put aside – the predicted thrust force was measured (calculated) always in the same way – a product of absolute outlet velocity and mass flow rate at the tunnel outlet. It was also

decided to keep the order, even though some of them were just theoretical or concept investigations never planned to be used.

For reminder, the main reason the researches were started for was an urgent need for a solution to the problem with regularly tangling tether. It is a very serious matter in everyday use and many times hampered test schedule or complicated the work performed. Therefore, having chosen jet drive, where rotor is fully covered by the tunnel, focus was put on other potential sources of problems. The obvious place is the tunnel inlet, where still some debris can be sucked in. The very first, initial shape was based on Fliegner's theory (number 1 at the Figure 8.13). Then, the modification process of inlet size and form started (versions from 2 to 6a). Any reference to other engineers' work is a little bit confusing. Some claim there is no big difference whether inlet should be rectangular or elliptically shaped [28] [74] or even precise size does not matter as it makes no big difference to the ultimate outcome [20]. The author cannot agree with these opinions fully. Even if there is no need in pinpointing the intake area, the velocity fields and clearly visible flow detachments in versions 2 to 6a leave no doubts about an importance of the inlet shape.

Another matter, in terms of overall efficiency, is whether it is better to have:

- small inlet area in order to prevent debris being sucked in – however, it means greater velocity at the tunnel inlet, which in turn leads to higher pressure needed to be generated by the rotor
- big inlet area – smaller inlet velocity, but at the same time the risk of flow throttling and breakdown if the velocity at the inlet to the tunnel was too small.

Logic suggests the inlet size should equalise both velocities or provide inlet velocity a fraction greater than vehicle's one – naturally, all these considerations refer to operating point only. The investigations followed this way and looking at pre-tests' simulations for versions 10 and higher, where inner and outer velocities were nearly the same, it looks it was the right decision.

Tunnel versions 10, 10a, 10b and 11a refer to the concept of rim-driven rotor. The idea, however, turned out to be infeasible and had to be abandoned. Nevertheless, it is a good example of shaft influence on internal flow character though.

The two versions labelled as *H* and *F16* refer to separate analysis investigating a possibility of using a jet-plane-like inlet (mentioned earlier) in order to improve overall performance. The main purpose was to deliver the best possible inflow conditions for more than one operating point. It could be useful for independent (autonomous) vehicle operating at the high seas. The first series of simulations performed on few initial shapes suggest it may be an acceptable solution. However, widened operating velocity range would have to be compromised by drag increase, so a balance between those two quantities still has to be found.

In conclusion, despite the fact that no.13 seems to develop slightly better, a little bit more uniform velocity distribution, the version 14ae was chosen as the ultimate one. The series of CFD simulations suggested significantly greater thrust force. Moreover, according to the pump

designer, the outcome of pressure and velocity fields in particular places were within the expected range in about ± 10%. The tunnel 14ae also includes the final version of rotor – stator pair. Furthermore, the disparity in velocity fields between tunnels 13 and 14ae is due to visibly different rotor location – the latter is rotated with respect to the previous.

All tunnels discussed above, in numbering order, are presented in the pictures below.

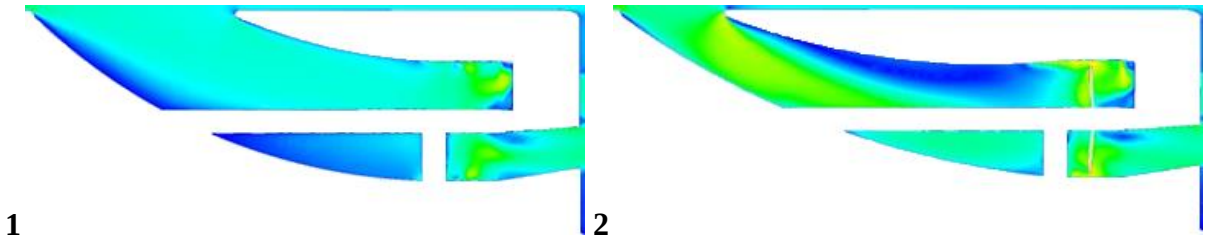

Figure 8.13: The velocity fields inside the waterjet propulsor tunnel – versions 1 and 2.

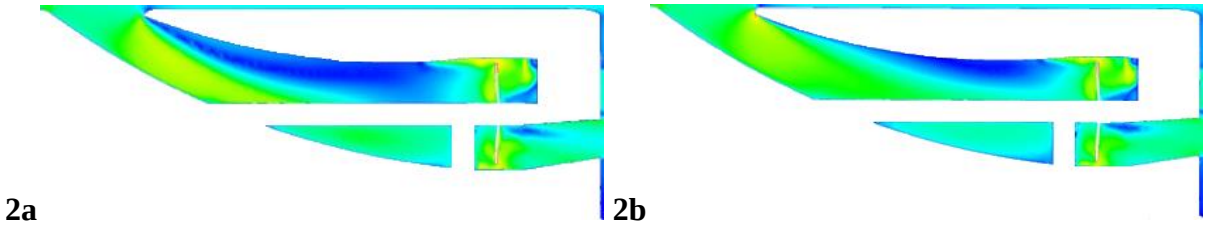

Figure 8.14: The velocity fields inside the waterjet propulsor tunnel – versions 2a and 2b.

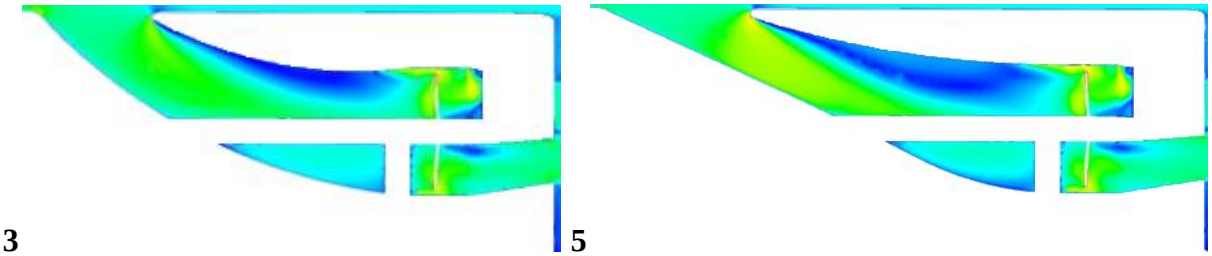

Figure 8.15: The velocity fields inside the waterjet propulsor tunnel – versions 3 and 5.

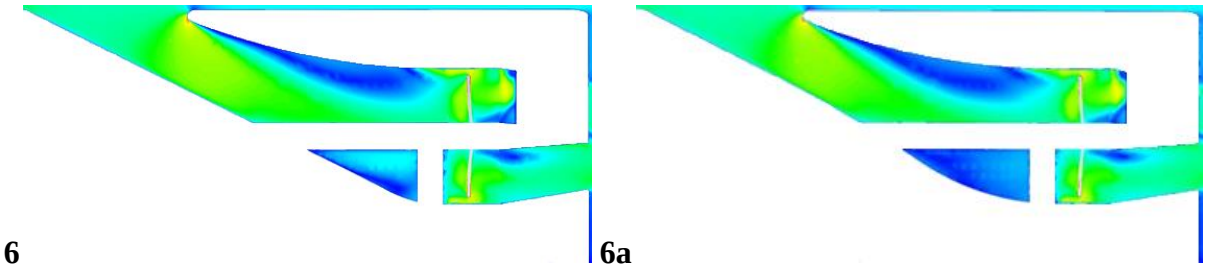

Figure 8.16: The velocity fields inside the waterjet propulsor tunnel – versions 6 and 6a.

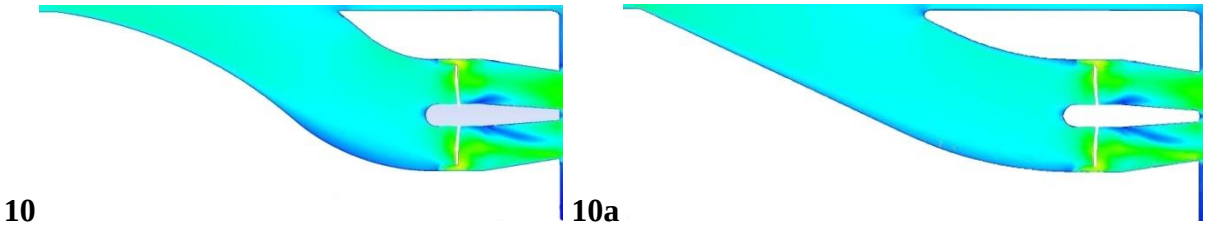

Figure 8.17: The velocity fields inside the waterjet propulsor tunnel – versions 10 and 10a.

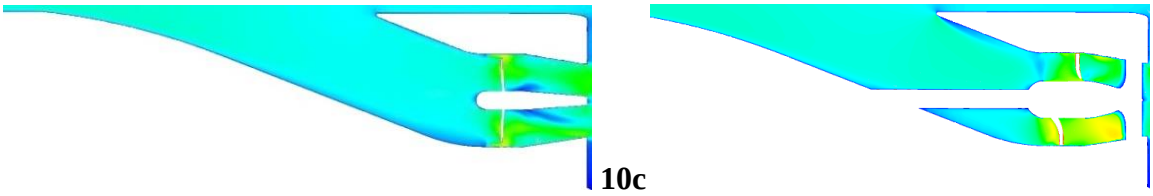

10b **10c**

Figure 8.18: The velocity fields inside the waterjet propulsor tunnel – versions 10b and 10c.

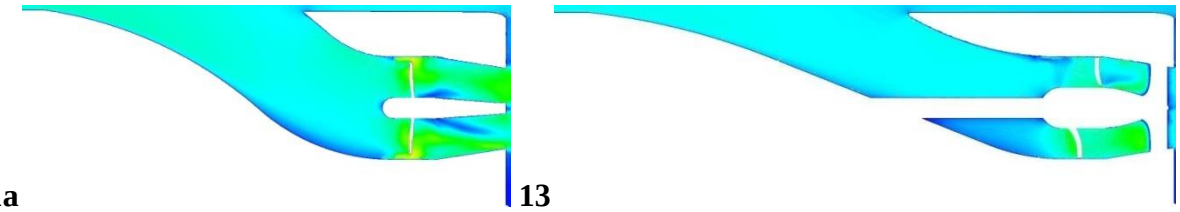

11a **13**

Figure 8.19: The velocity fields inside the waterjet propulsor tunnel – versions 11a and 13.

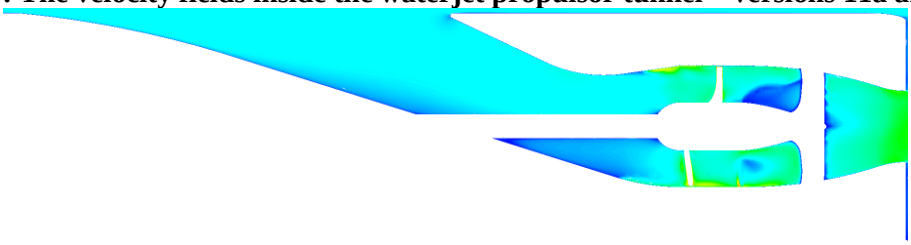

14ae

Figure 8.20: The velocity fields inside the waterjet propulsor tunnel – version 14 ae. This shape was ultimately accepted for real vehicle investigations.

8.2.4 Outlet nozzle shape analysis

The last part included in potential gains in performance analyses covered outlet nozzle shape.

As previously, the geometry was detached from the rest of the propulsion and only space inside the nozzle was investigated. The nozzle inlet diameter corresponds to tunnel diameter at rotor's outflow area (station 4 at the Figure 6.1). The outlet one is a result of vehicle's velocity, rotors revolution and thrust force expected – in this case, it was set to 30 [mm] and it refers to station 6 at the Figure 6.1. The variables able to operate with were: the nozzle length (the nozzle taper angle) and the wall shape. Among all the shapes analysed, four were chosen to present the development process.

Interestingly, the shapes presented below delivered nearly the same outcomes and proved outside wall influence on ultimate result was next to nothing. The differences between values of velocities and pressures at the outlet are well within 1%. Therefore, in author's opinion, the precise wall shape may be regarded as negligible.

Table 8.3: The outlet velocities for four different nozzle shapes.

no.	shape	outlet velocity [m/s]
1	A	8.728
2	B	8.674
3	C	8.679
4	D	8.704

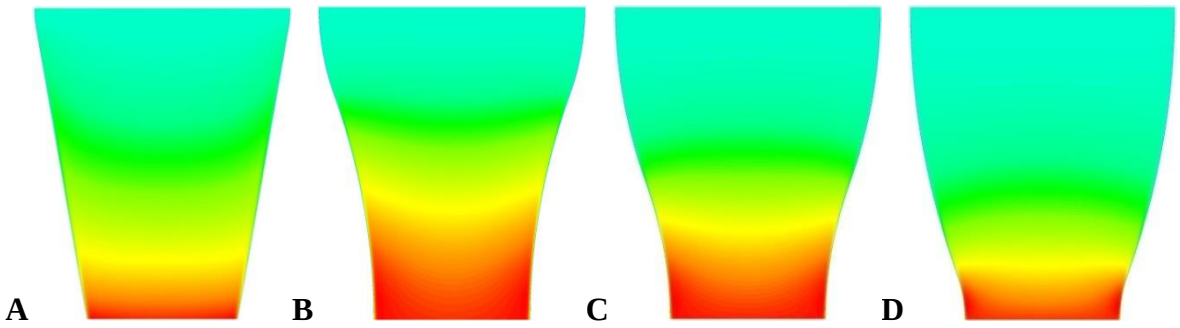

Figure 8.21: The velocity fields inside selected outlet nozzle shapes.

Given tiny divergences in results, shape **D** was accepted as the ultimate one. The advantage of this form is that it provides smooth outlet stream without "vena contracta". It increases operating outlet area as well as makes it easier to measure velocity and flow rate values in CFD.

8.2.5 Design of the pump

The operating point for the designed pump was set at 4500 [rpm]. It was based on both theoretical and experimental research. The outcomes from WJ49G experiments clearly suggest it should be the destination point for examined problem.

8.2.5.1 The pump designed with a use of pump design methods

A small axial-pump will be used to power waterjet propulsion and it will be built into properly shaped tunnel. The main design assumptions are presented in the table below.

Table 8.4: The main assumptions for newly designed waterjet propulsion (WJ50).

no.	name	symbol	value	unit
1	impeller diameter	D	50	[mm]
2	outlet nozzle diameter	D_{out}	30-40	[mm]
3	pump hydraulic head	H	1.3	[m]
4	pump hydraulic pressure	P_H	13	[kPa]
5	pump mass flow	Q	60	[cm/s]
6	Revolutions	n	3600-4500	[rpm]

The size of the pump made it impossible to make any references to other axial-pumps. Because of very limited (or even lack of) data in the literature for such a small pump, all the necessary calculations were done with a use of two methods:

- so called one-dimensional method
- aerodynamics method of Wozniesienski and Pekin

The inflow to the pump was assumed to be straight, without an initial swirl. The whirl behind the rotor is compensated by the stator placed right after the impeller. The rotor-stator pair was designed for chosen tunnel (version 14ae in the Figure 8.20). And with these

parameters, the pump should generate more than 5 [m/s] outlet velocity, which combined with assumed mass flow rate was expected to deliver required thrust force of 13-14 [N] (52-56 [N] in total for four propellers).

The result geometry is presented in the figure below. The propulsor is designated to be manufactured with a use of "Rapid Prototyping" method (3D print).

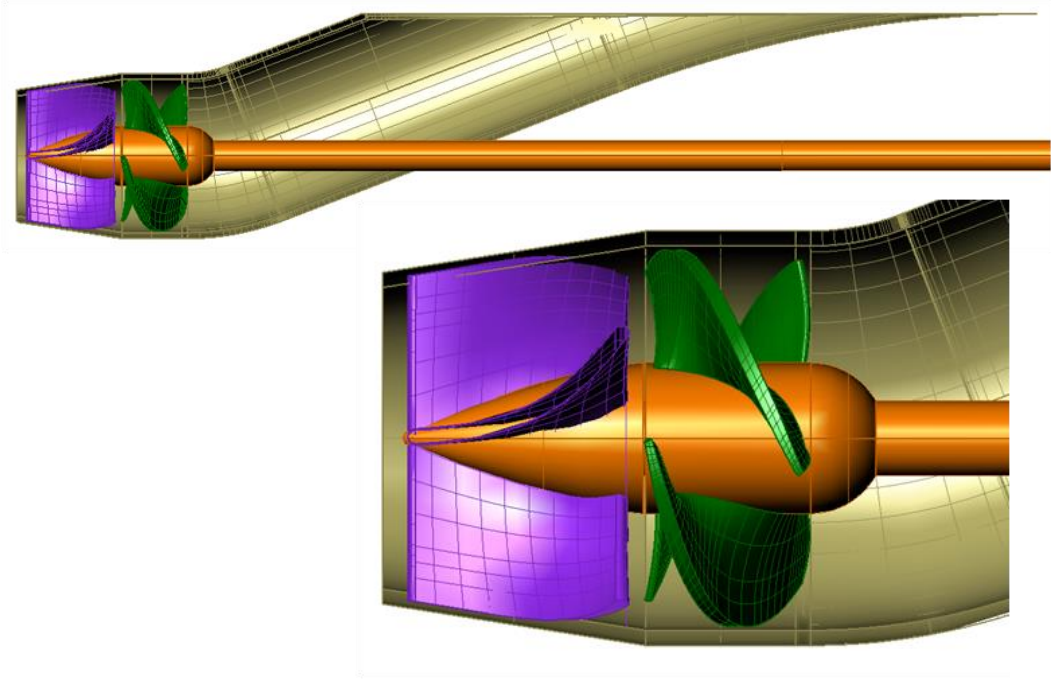

Figure 8.22: Geometry delivered by the pump designer – newly designed small pump for analysed waterjet propulsor placed inside the tunnel. Impeller diameter 50 [mm], hub diameter 20 [mm], shaft diameter 10 [mm].

8.2.5.2 Pump analysis with a use of CFD

The separate analysis was done just for the newly designed pump itself. The simulation covered calculated and expected operating point – water velocity 3.0 [m/s] and rotor's revolutions at 4500 [rpm]. The pictures below present pressure distribution on rotor and stator as well as pressure and velocity fields at the symmetry plane.

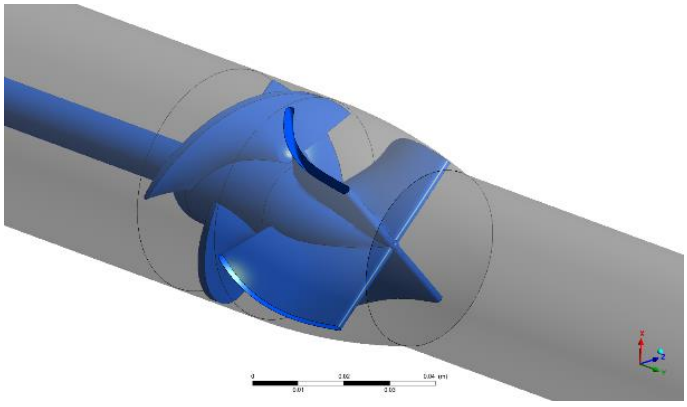

Figure 8.23: Newly designed pump geometry without propulsion tunnel inside the domain used in the analysis.

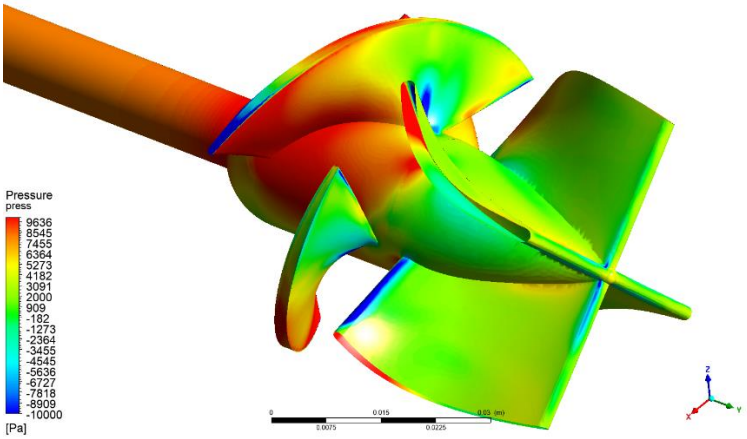

Figure 8.24: Pressure distribution on rotor and stator – outlet view.

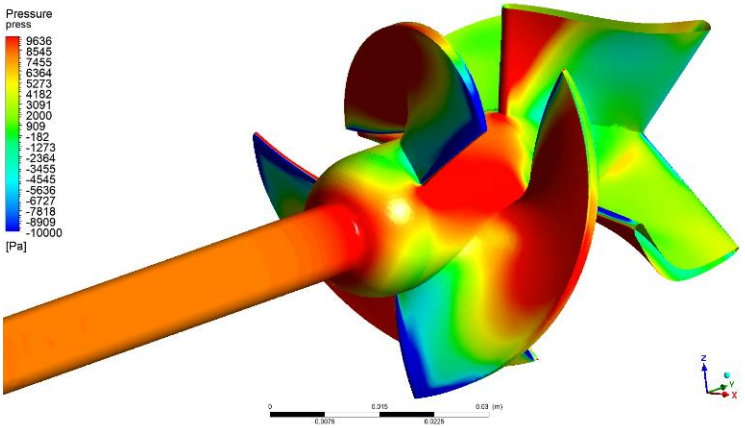

Figure 8.25: Pressure distribution on rotor and stator – inlet view.

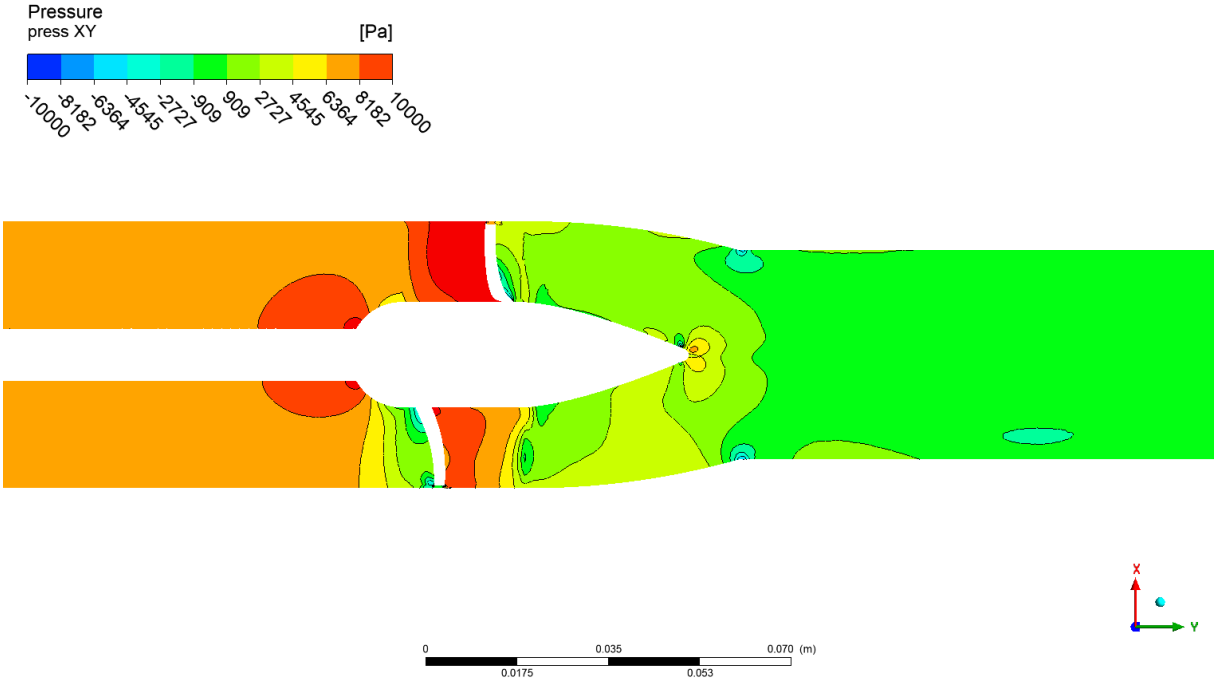

Figure 8.26: Pressure field at the symmetry plane.

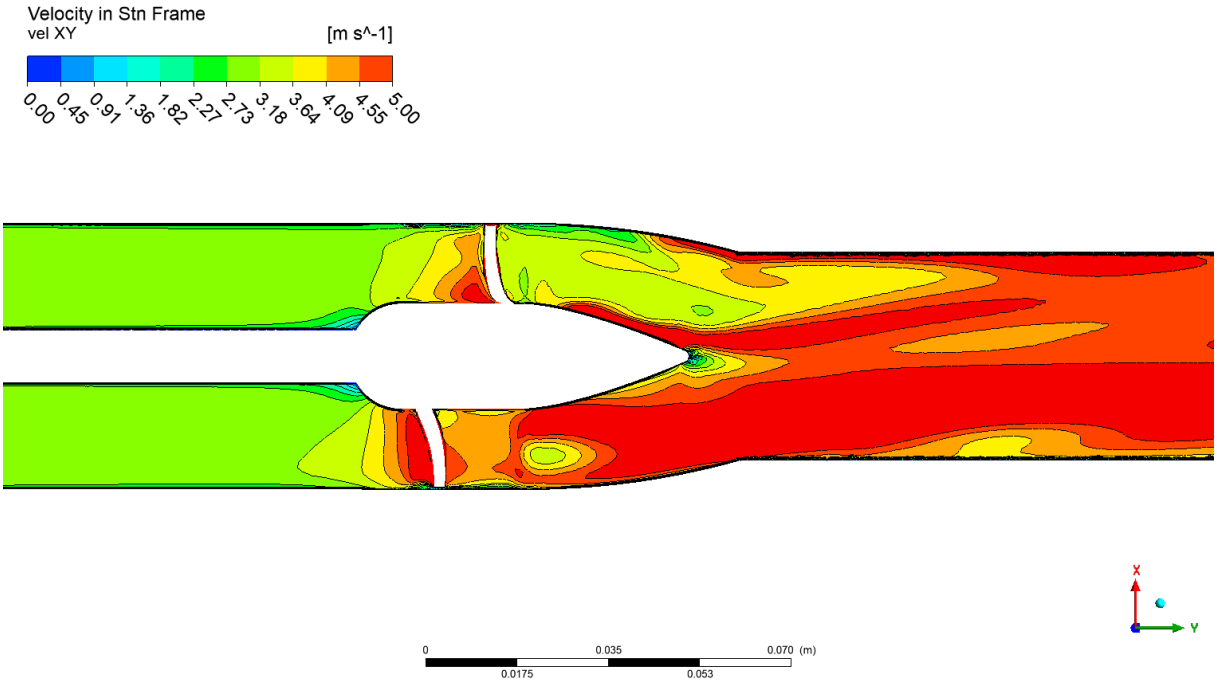

Figure 8.27: Velocity field at the symmetry plane.

As it can be seen in the pictures above, pressure distributions on rotor and stator surfaces are far from being perfect. The thrust of the propulsor is lower than expected too. This phenomenon will be confirmed in further investigations described in the next subsections.

Table 8.5: The results for the newly designed pump at its operating point.

no.	parameter	unit	
1	water velocity	[m/s]	3.000
2	outlet velocity	[m/s]	4.805
3	velocity Δ	[m/s]	1.805
4	mass flow at outlet	[kg/s]	5.875
5	thrust	[N]	10.60

8.3 CFD analysis of the integrated waterjet propulsor and propulsion-hull interaction

The analysis was performed with a use of four models:

— 90^0 model (quarter of the vehicle)
— 180^0 model (half of the vehicle)
— full vehicle's model
— full vehicle's model affixed to the test station

The aim was to compare and contrast simplifications' influence on ultimate result of the waterjet propulsion. All the simulations were run in exact the same way, hence only one was described.

8.3.1 90^0 model – bare hull

Mentioned earlier drag prediction analyses were performed the same way the further simulations. The full body vehicle was placed in two-size domains. The difference between them was the outside diameter that multiplied vehicle's hull diameter by 20 and 10 respectively. The outcomes for both matched each other therefore the smaller one was in use in subsequent investigations.

The first-step simulations for waterjet were carried on in the bigger domain though. In addition, the geometry was simplified and beside the propulsor itself, it contained vehicle's bare hull only. All protruding elements were taken away, the vertical propulsion tunnel discarded. – The hull then was just to build boundary layer height at the propulsion's tunnel inlet. Moreover, keeping in mind previous problems in some regions [116] significant improvement in mesh generation process was expected.

Naturally, the domain was to represent vehicle's operating environment – the high seas. Then, given the vehicle's cylindrical shape, it was decided to use a cylinder that dimensions were as presented in the picture below.

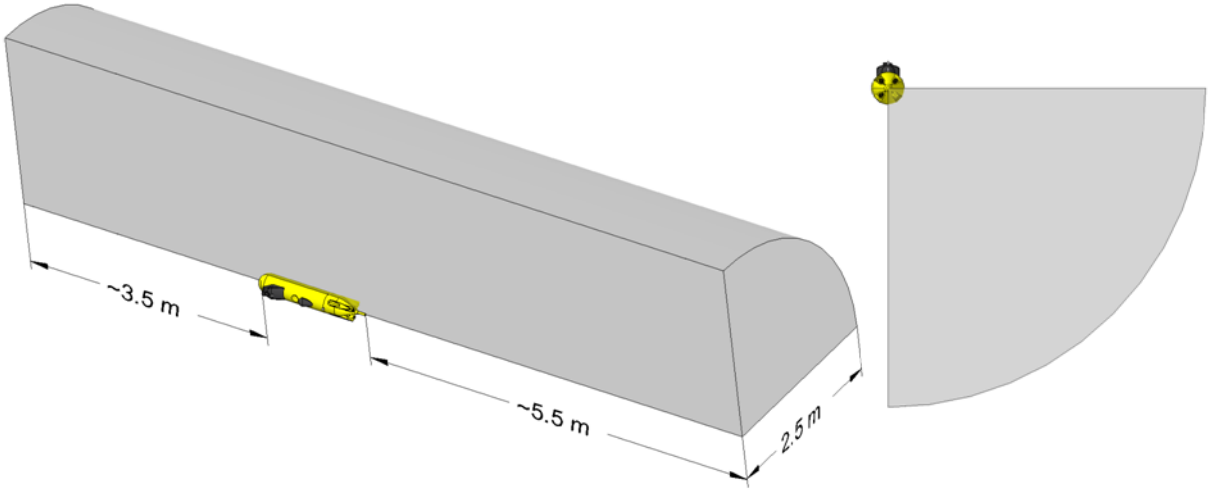

Figure 8.28: The overall view and main dimensions of the domain used in the CFD jet drive analyses.

Due to requirements of Ansys CFX solver, the model was divided into two separate domains with interface surfaces between them:

- WATER DOMAIN included vehicle's hull, propulsion tunnel and stator. This domain was static.
- ROTOR DOMAIN included the rotor. This domain (domains in latter simulations) was rotating.

8.3.1.1 Boundary conditions

Each numerical simulation requires following matters determination:

BOUNDARY CONDITIONS – describe the roles each surface plays in the simulation.

The Figure 8.29 presents overall view of WATER DOMAIN used in 90º model analyses. The faded black surface (black arrows) stands for domain inlet, the blue one for domain outlet (blue arrows) modelled as bidirectional unrestricted flow. Next, the yellow surfaces mark out the vehicle's profile. Finally, the light gray surfaces were defined as frictionless walls.

Furthermore, the picture Figure 8.31 shows ROTOR DOMAIN, where blue surfaces were defined as default-roughness rotating walls and the grey ones outline domain boundaries (and they are simultaneously the interface surfaces).

INITIAL CONDITIONS – determine a point where simulation starts from.

The only initial conditions applied were static relative pressure set at 0 [atm] and inlet velocity set at 3.0 [m/s].

RUNNING CONDITIONS – guide solver toward destination point.

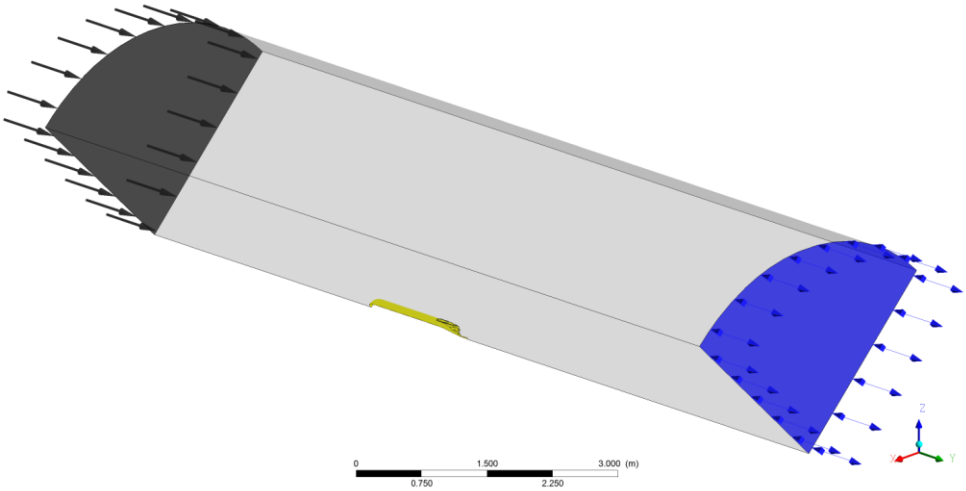

Figure 8.29: WATER DOMAIN used in waterjet 90º model simulations. Y-axis points flow direction.

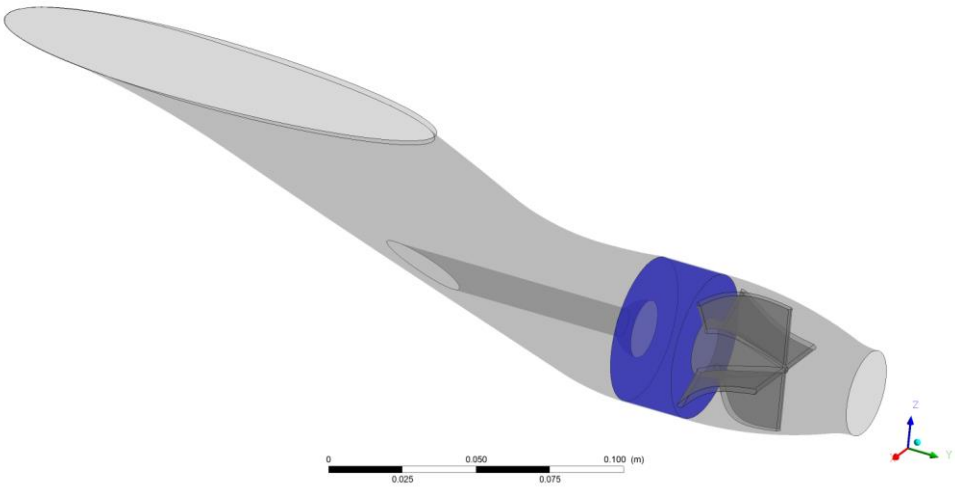

Figure 8.30: Close-up of tunnel interior. The blue colours represent domain interface surfaces.

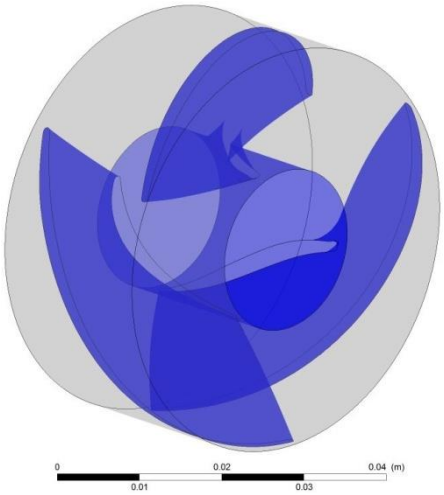

Figure 8.31: ROTOR DOMAIN used in all waterjet simulations. The grey colour outlines domain boundaries and interface surfaces.

8.3.2 180^0 model

Because of noticeable asymmetry in sonar and camera canopy, it was decided to split the domain in half into upper and lower sections rather than left and right ones. The modelling simulations' settings were exact the same as previously in the 90^o model.

The domains' overall view for vehicle's model is presented in the pictures below.

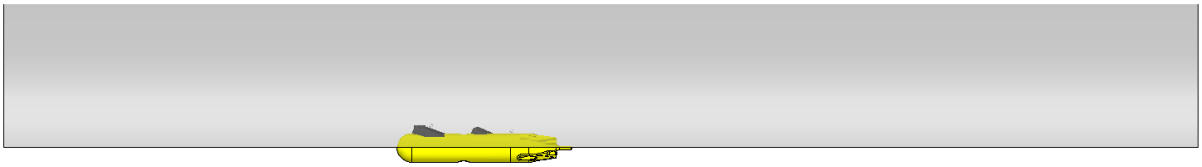

Figure 8.32: The upper domain for 180^0 model simulations.

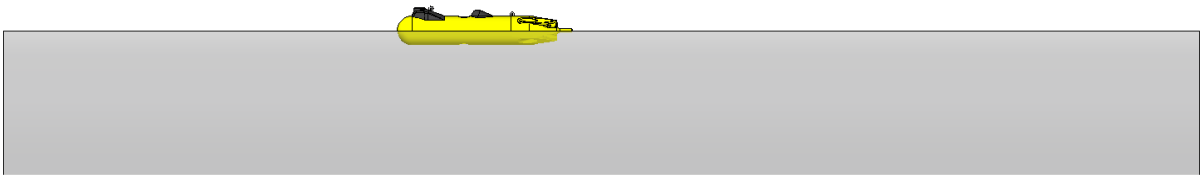

Figure 8.33: The lower domain for 180^0 model simulations.

8.3.3 Full vehicle

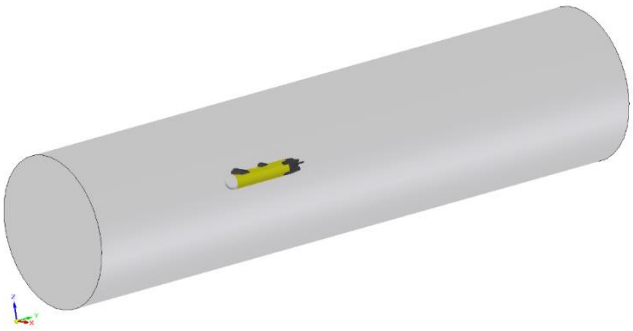

Figure 8.34: The full vehicle model in the domain for CFD simulations.

8.3.4 Conclusion

All four approaches delivered similar result, therefore only one are presented. The table shows outcomes for all four jet propulsors of one particular case: vehicle's velocity 2.929 [m/s] and revolutions 4203 [rpm].

Table 8.6: Simulation predictions and experimental results comparison for selected case of newly designed waterjet propulsion (WJ50).

no.	parameter	unit	propulsion				
			BOTTOM right	**BOTTOM left**	**TOP right**	**TOP left**	**average**
1	revolutions	[rpm]	4203	4203	4203	4203	4203
2	vel. vehicle	[m/s]	5.379	5.415	5.391	5.365	5.388
3	vel. outlet relative	[m/s]	2.929	2.929	2.929	2.929	2.929
4	vel. outlet absolute	[m/s]	2.450	2.486	2.462	2.436	2.459
5	mass flow rate	[kg/s]	3.610	3.638	3.616	3.594	3.615
6	thrust CFD	[N]	*8.84*	*9.04*	*8.90*	*8.75*	*8.89*
7	thrust experiment	[N]	6.95	6.95	6.95	6.95	6.95
8	thrust Δ	[-]	27.3%	30.1%	28.1%	26.0%	27.9%
9	drag CFD	[N]	66.80	66.80	66.80	66.80	66.80
10	drag experiment	[N]	52.00	52.00	52.00	52.00	52.00
11	drag Δ	[-]	28.5%	28.5%	28.5%	28.5%	28.5%
12	final outcome Δ	[-]	-1.2%	1.7%	-0.4%	-2.5%	-0.6%

As usual, propulsion analysis delivered higher vehicle's drag force value. Therefore, percentage difference between this result and the experimental one was calculated. Similar disparity was calculated for jet drive propulsion. Further, both percentage differences were subtracted from each other to determine the ultimate simulation error.

The following pictures show the differences in the water inflow to the particular propulsion tunnels. In both cases, the independent vehicle and the one affixed to the test station (pipe), upper propulsors experience more difficult operating conditions than their lower counterparts do. Moreover, the streamlines indicate uneven flow distribution around the upper part of vehicle's hull. This seems to prove pre-simulation anticipations and back up the way, the domain was split for 180^0 model.

Further, the vertical propulsion tunnel has rather marginal influence and it is just a confirmation of regularly experienced phenomenon. During tests, when the vehicle runs at full speed, the operator is unable to move it vertically using vertical propeller – the ROV simply does not respond at all.

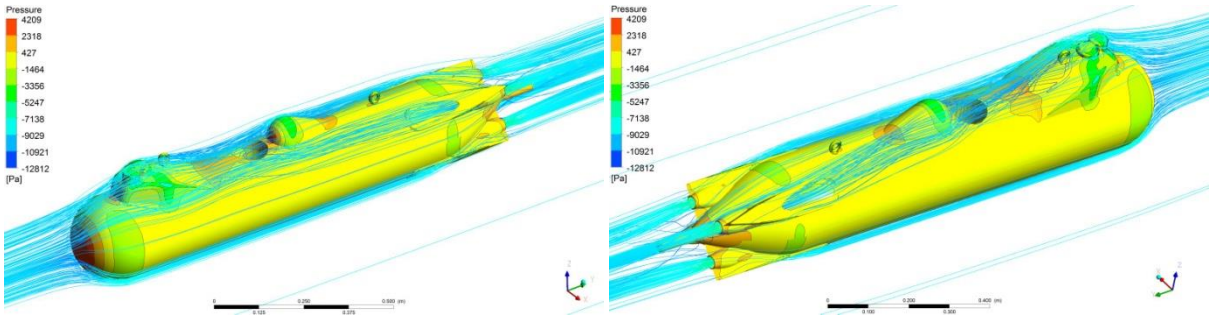

Figure 8.35: The pressure distribution and streamlines around the vehicle's body – independent vehicle.

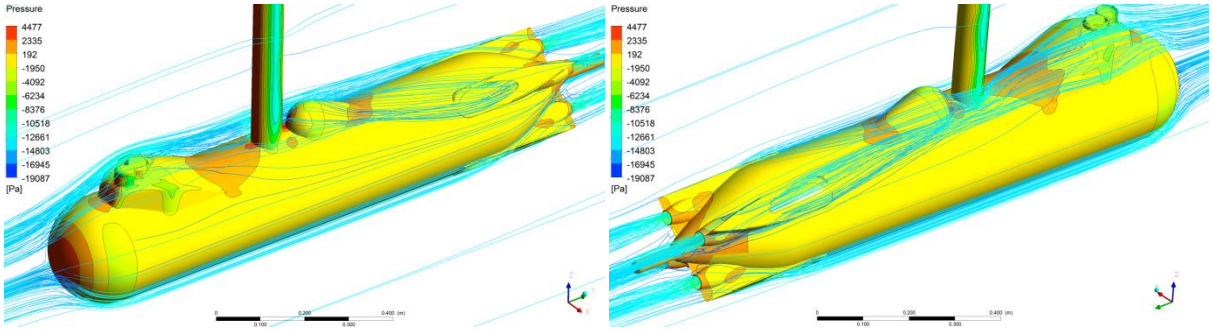

Figure 8.36: The pressure distribution and streamlines around the vehicle's body – vehicle during tests.

The direct comparison between top and bottom view illustrates the disturbances generated by sonar canopy and transponder from a slightly different perspective.

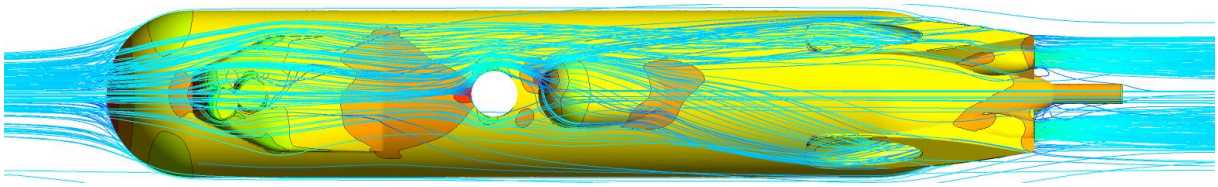

Figure 8.37: Streamlines around the vehicle – top view – vehicle during tests.

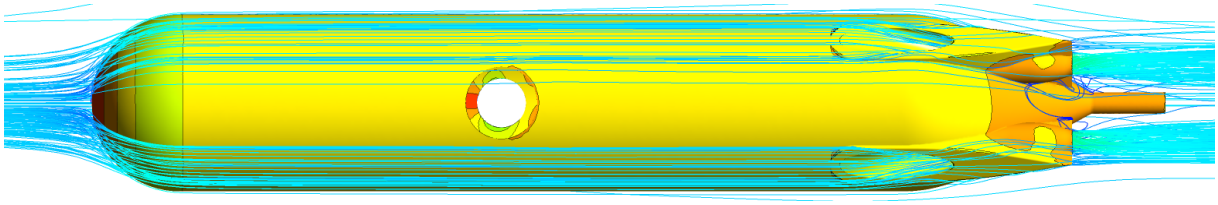

Figure 8.38: Streamlines around the vehicle – bottom view – vehicle during tests.

In conclusion, there is no significant difference between analysed models and all three approaches (quarter-, half- and full body model) can be used at equal measures.

8.4 Velocity field inside the tunnel of the working propulsor

As it was mentioned at the beginning, heading into the unknown and having no reference but theoretical estimations, the goal was set to develop as smooth as possible velocity field inside the propulsion tunnel. Therefore, the focus was on experiments with tunnel inlet region and overall profile – the two elements bonded up with each other. And instantly, the idea of minimum inlet area turned out to be infeasible. The pictures presented in the subsection 8.2.1

show that the inlet size has crucial influence on flow character inside the duct and inflow to the impeller.

Another issue that could influence propulsor efficiency is the region underneath the shaft. There were several attempts to minimise its disturbance modifying tunnel wall in different ways. One of them was a resignation from diffuser right before rotor's section. It resulted in very good velocity distribution (version 10c in the Figure 8.18), but did not deliver expected thrust force. Further modifications improved the thrust outcome, however, at the same time deteriorated the flow. The 13th version of the tunnel (Figure 8.19) seems to be better than the ultimate one, but according to the prediction, it generated less thrust force than *14ae* one.

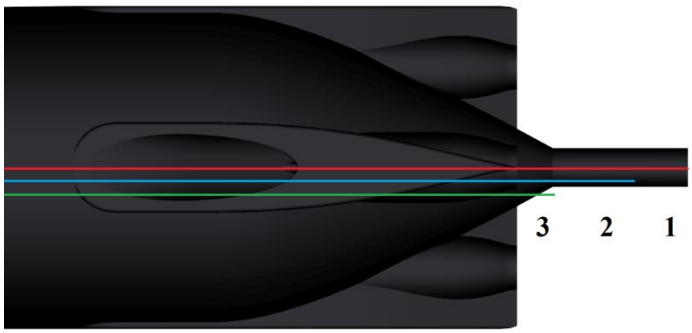

Figure 8.39: Cross-section planes placement for velocity field inside the WJ50 propulsor.

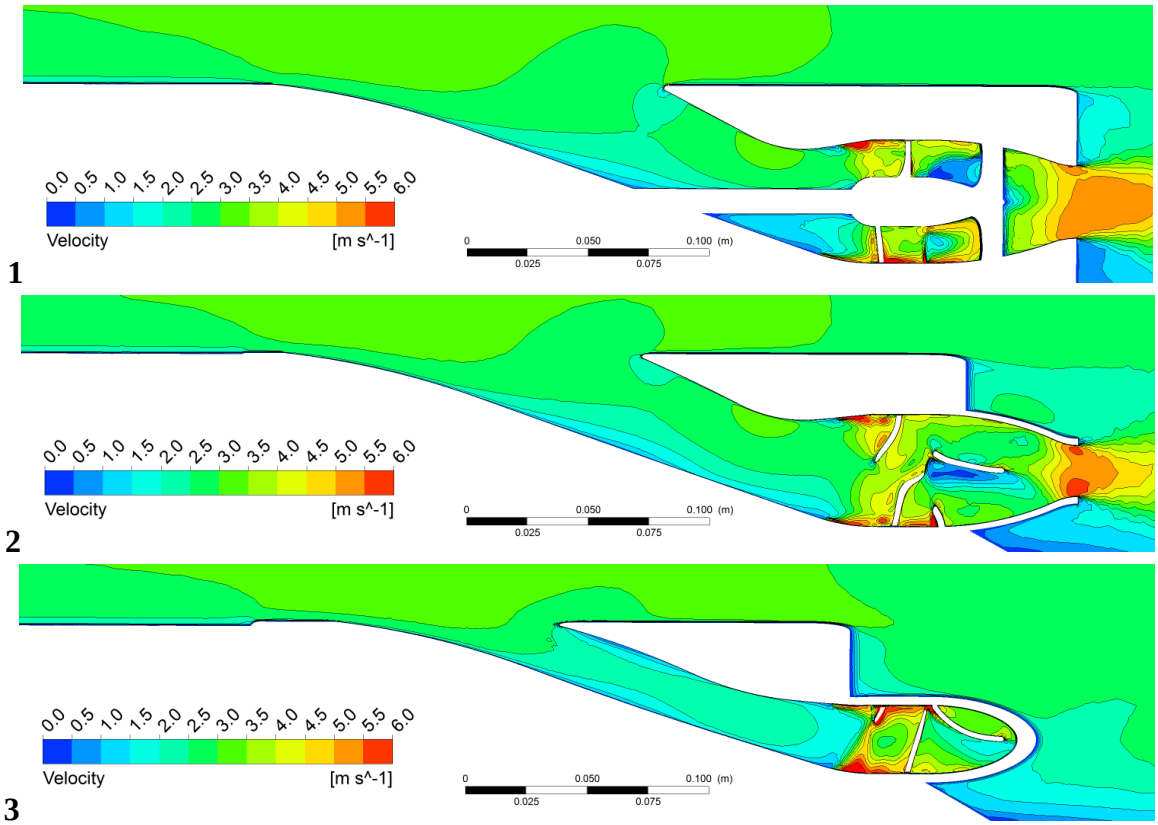

Figure 8.40: The velocity field inside the WJ50 propulsion.

Above, the predicted velocity profiles in three longitudinal sections are presented. The first one at the symmetry plane and two further moved aside 10 and 20 [mm] respectively.

8.5 Influence of the nozzle diameter on WJ50 propulsor performance

Despite the diameter of the outlet nozzle was defined at 40 [mm], it was decided to investigate smaller diameters too – hence the 3D-printed propulsor had had the outlet nozzle diameter lowered to 30 [mm]. It allowed to examine four different sizes of the nozzle simply by cutting it.

For the smallest nozzle diameter two series of simulations were run – for still water and 1.5 [m/s] water velocity and the variety of rotor's revolutions. The parameters values were chosen deliberately, so as to have the possibility to verify the simulations experimentally in the controlled environment of the flow tank (12.2.1).

8.5.1 Calculations for water velocity 0.0 [m/s] (static thrust)

The calculations for zero velocity ware done with a simplified model and different approach. Simulations were used to determine forces acting on individual parts of the propulsion and then all the forces were summarized. This is a common method for bare propellers and – in this case – can be used to compare and contrast different operating conditions for the same geometry model.

$$T_{v=0[\frac{m}{s}]} = \sum F_i \quad [N] \tag{8.3}$$

Table 8.7: CFD predictions for water velocity v=0.0 [m/s].

no.	parameter	unit	rotor's revolutions [rpm]			
1			**2000**	**3000**	**4000**	**5000**
2	F_{rotor}	[N]	-3.9	-8.8	-15.8	-24.9
3	F_{stator}	[N]	-0.9	-2.0	-3.5	-5.6
4	F_{shaft}	[N]	-0.3	-0.6	-1.0	-1.7
5	F_{tunnel}	[N]	2.1	4.9	8.6	13.4
6	F_{hull}	[N]	0.0	0.1	0.1	0.2
7	thrust	[N]	3.0	6.4	11.6	18.6

8.5.2 Calculations for water velocity v=1.5 [m/s]

The calculations for 1.5 [m/s] water velocity were performed in exact the same way as the ones for still water.

The table below presents CFD prediction's values and the graph that follows it compares results for both analysed water velocities.

$$T_{v=1.5[\frac{m}{s}]} = \sum F_i - (F_{tunnel} + F_{hull})_{n=0\ [rpm]} \quad [N] \tag{8.4}$$

Table 8.8: CFD predictions for water velocity v=1.5 [m/s].

no.	parameter	unit	rotor's revolutions [rpm]				
1			**0**	**2000**	**3000**	**4000**	**5000**
2	F_{rotor}	[N]	0.0	-3.7	-8.5	-15.3	-24.0
3	F_{stator}	[N]	0.0	-1.0	-2.2	-3.9	-6.0
4	F_{shaft}	[N]	0.0	-0.1	-0.3	-0.6	-1.1
5	F_{tunnel}	[N]	0.5	3.2	6.2	10.3	15.5
6	F_{hull}	[N]	2.8	2.6	2.7	2.8	3.0
7	thrust	[N]	0.0	2.3	5.4	10.0	15.9

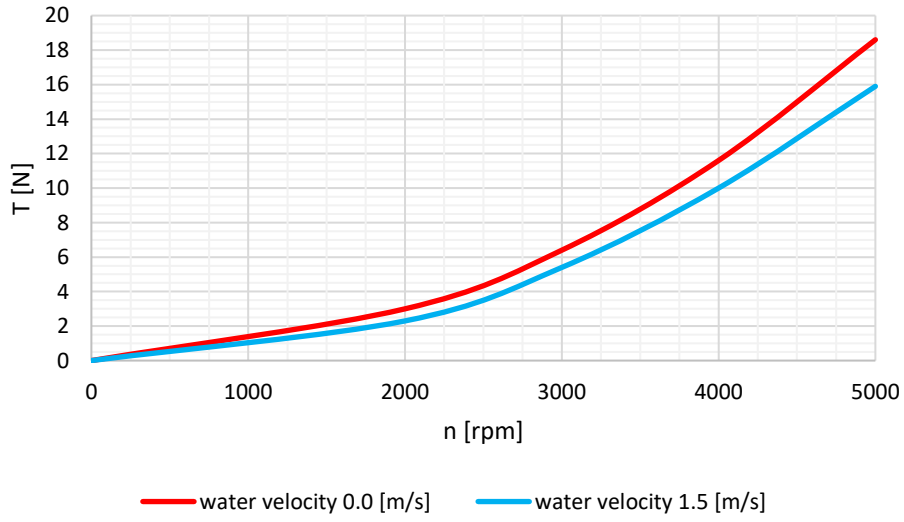

Figure 8.41: Propulsion thrust in function of rotor speed for two water velocities.

8.5.3 Calculations for increasing outlet nozzle diameter

The series of simulations were performed for the outlet nozzle shortened in a few steps. It started with 30 [mm] diameter and then, the nozzle was cut by a steady step of 1.0 [cm]. It resulted in four different diameters.

All of the simulations were run for the same operating conditions:

— rotor's revolutions 3000 [rpm]
— water velocity 1.5 [m/s]

The thrust forces were determined the same way as previously. However, this time propulsion's efficiency was estimated too.

$$\eta = \frac{P_{received}}{P_{delivered}} = \frac{T \cdot v}{n \cdot M} \quad [\%]$$

8.5

Table 8.9: CFD predictions for different outlet nozzle diameters.

no.	parameter	unit	outlet nozzle diameter [mm]			
1			**30**	**33**	**40**	**45**
2	F_{rotor}	[N]	-8.5	-7.9	-5.5	-4.3
3	F_{stator}	[N]	-2.2	-2.0	-0.7	-0.8
4	F_{shaft}	[N]	-0.3	-0.2	-0.5	-0.1
5	F_{tunnel}	[N]	2.7	2.9	1.7	4.8
6	F_{hull}	[N]	6.2	5.0	3.2	-0.7
7	$P_{delivered}$	[W]	31.0	30.0	25.0	22.0
8	thrust	[N]	5.4	5.5	5.1	4.4
9	η	[-]	26.1%	27.5%	30.6%	30.0%

The graphical representation of simulations' results is presented in the graphs below.

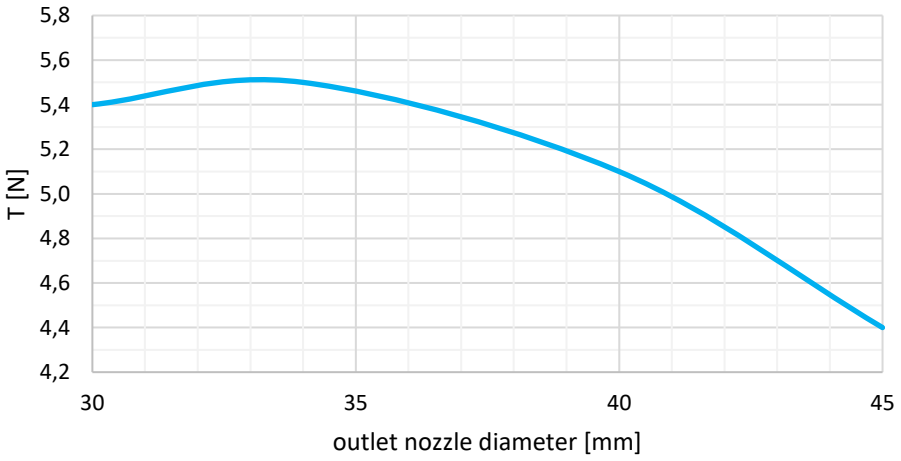

Figure 8.42: Propulsion's thrust in function of the outlet nozzle diameter.

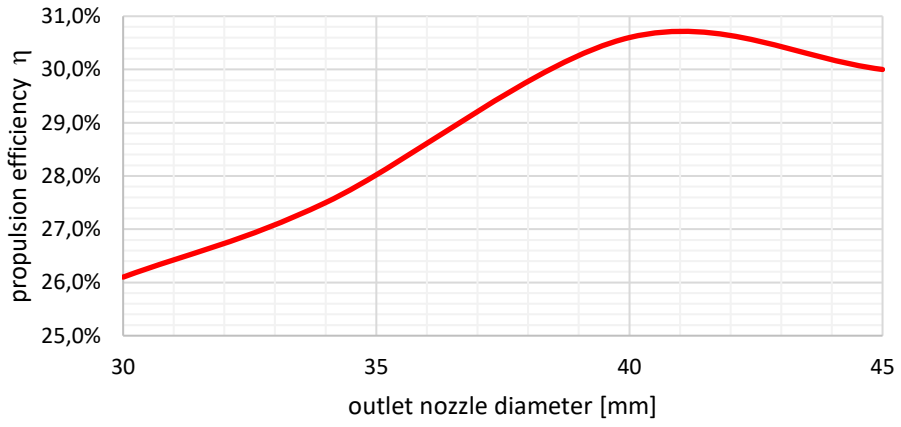

Figure 8.43: Propulsion's efficiency in function of the outlet nozzle diameter.

The pictures below present pressure distribution at the symmetry plane for four different outlet nozzle diameters.

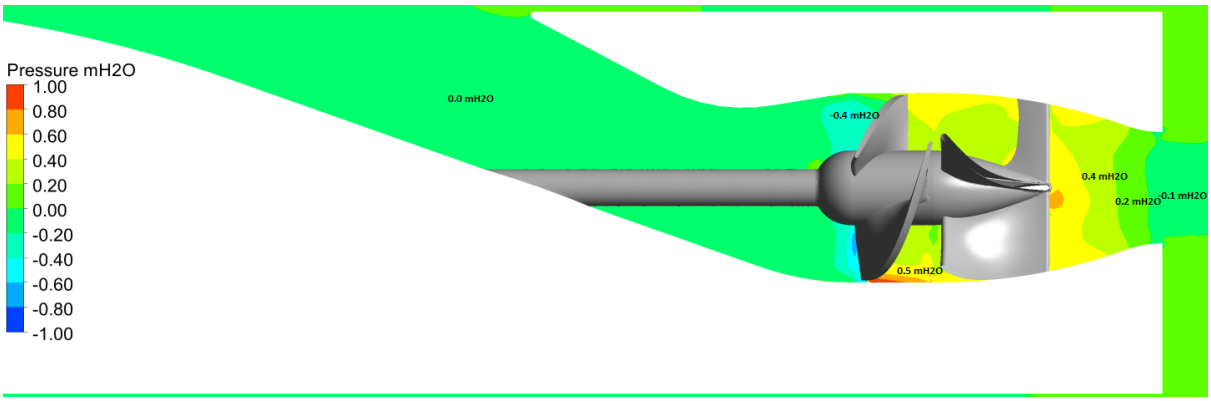

Figure 8.44: Pressure field at the symmetry plane – outlet nozzle diameter 30 [mm].

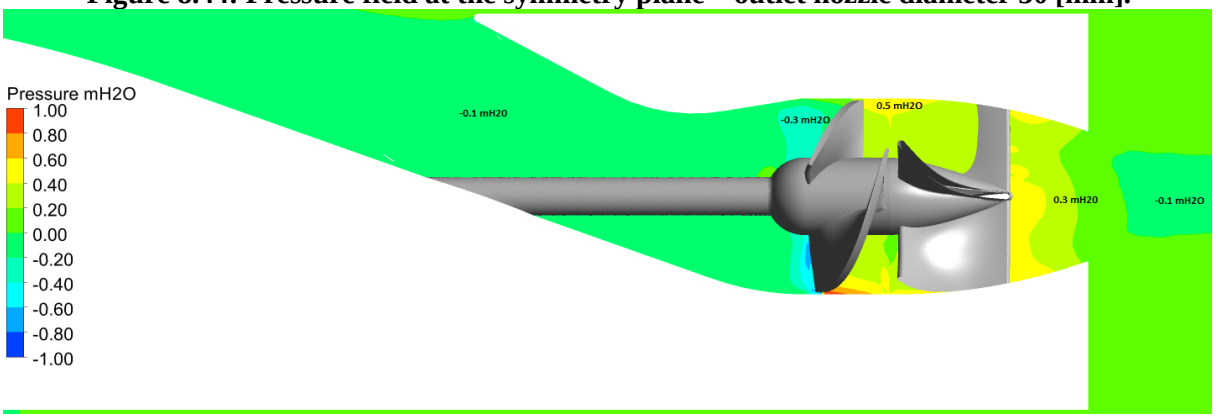

Figure 8.45: Pressure field at the symmetry plane – outlet nozzle diameter 33 [mm].

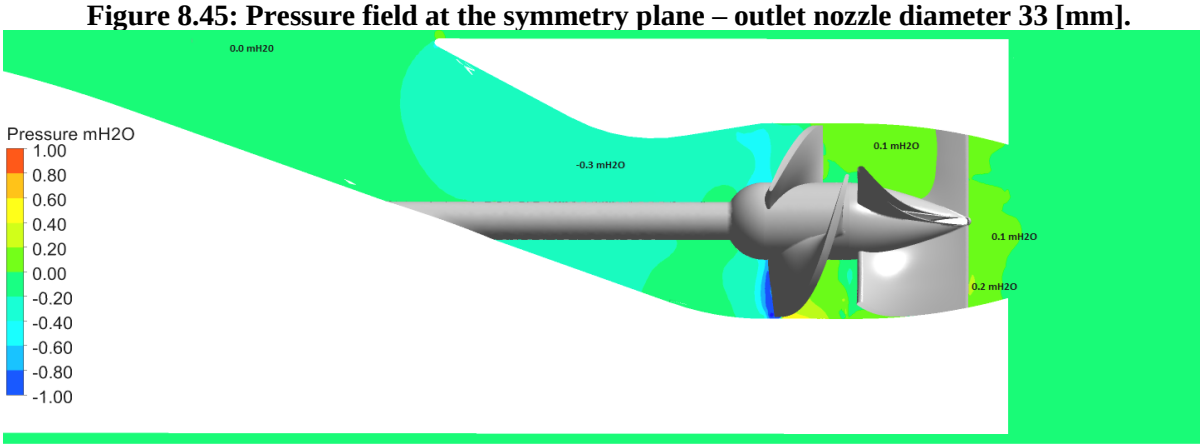

Figure 8.46: Pressure field at the symmetry plane – outlet nozzle diameter 40 [mm].

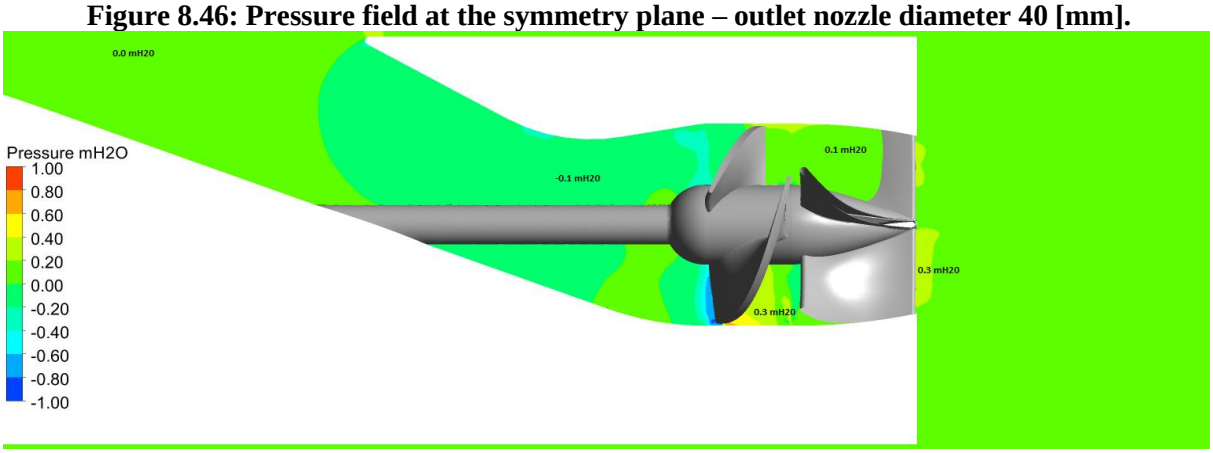

Figure 8.47: Pressure field at the symmetry plane – outlet nozzle diameter 45 [mm].

8.5.4 Calculations for water velocity 3.0 [m/s]

Finally, the table below compare and contrast pressure levels at selected propulsion stations for two nozzle diameters. The analysis was done for operating point 3.0 [m/s] of water velocity.

Table 8.10: Pressures and thrust forces prediction for two sizes of outlet nozzle. Numbers in the brackets refer to propulsion stations – see Figure 6.1.

no.	parameter	unit	outlet nozzle diameter [mm]					
1			30			40		
2	rotor's revolutions	[rpm]	4200	5000	7000	4200	5000	7000
3	pressures							
4	in domain (0)	[Pa]	-5556	-8667	-27222	-556	1556	1111
5	at propulsion inlet (2)	[Pa]	-8444	-13889	-37778	-4444	-3556	-6667
6	at rotor inlet (3)	[Pa]	-11333	-24333	-48333	-4444	-8667	-6667
7	average at stator outlet (5)	[Pa]	222	1778	4444	7222	6667	8889
8	max at stator outlet	[Pa]	3111	7000	4444	7222	6667	16667
9	hydraulic head at rotor inlet (3)	[mH_2O]	-1.16	-2.48	-4.93	-0.45	-0.88	-0.68
10	hydraulic head at stator outlet (5)	[mH_2O]	0.59	1.07	3.23	0.79	0.52	0.79
11	force at rotor's blades	[N]	15.47	23.08	45.65	10.11	15.12	33.31
12	thrust	[N]	3.00	2.74	9.15	7.07	13.40	38.22

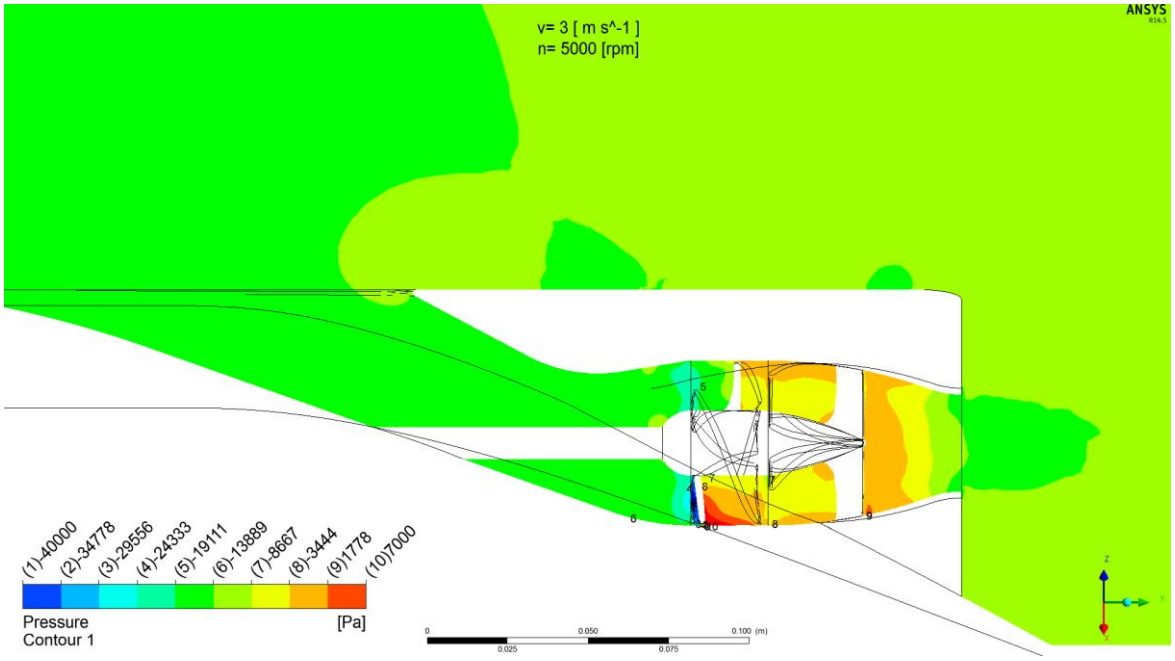

Figure 8.48: Pressure field at the symmetry plane for outlet nozzle diameter 30 [mm].

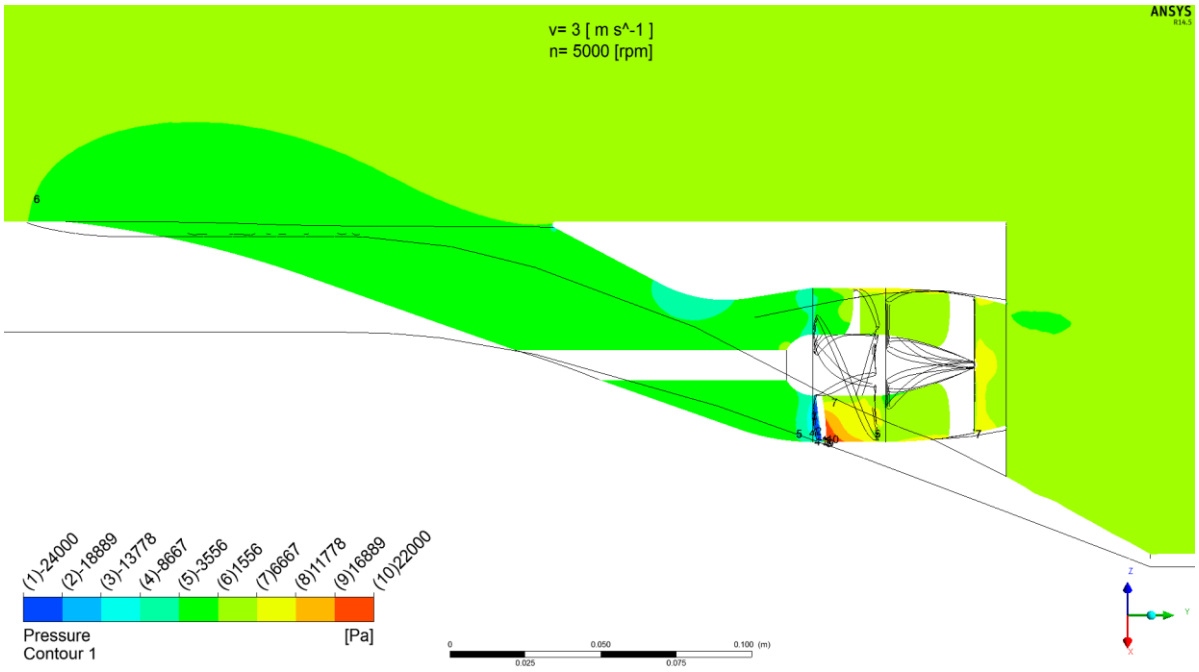

Figure 8.49: Pressure field at the symmetry plane for outlet nozzle 40 [mm].

8.6 Refining the propulsor's geometry

Every change of the flow parameters generates some energy losses. Therefore, it is desirable to analyse pressure and velocity changes along the tunnel to identify potential problematic regions.

Application of semi empirical calculations and CFD simulations gives general propulsor performance data. Data regarding local flow parameters are available too. However, they are difficult to analyze in numerical form. Graphical representation of these data seems to be a convenient tool in process of refining geometry of the propulsor tunnel.

The graphs describing changes of pressure and velocity along the tunnel of the WJ50 propulsor are presented in the figure on the next page. The graphs of velocity (v), pressure drop due to friction (p_friction) and total pressure averaged (p_total) were build using the data presented in the Table 7.1 and the Table 7.2 and were calculated using semi-empirical method. Curves between discrete points are interpolated linearly. The graph of average pressure (p_CFD) represent data obtained from CFD simulation for assumed operating point.

While analysing the graphs it is apparent that in many parts of the tunnel its local geometry influences flow parameters without a reason:

1. Between station 1 and station 2 the parameters cannot be influenced except for increasing tunnel's bent radius. Closed tunnel begins at station 2 and according to initial assumption its cross-section area is kept constant to the pump (station 3). However, to improve the flow inside the tunnel the local radius of the ceiling of the tunnel was decreased. This move has hanged cross-section of the tunnel in this point. As a result, a choking point appeared. This increased water velocity between station 2 and station 3

and reduced the velocity in the diffuser after station 3. The value of the pressure varies accordingly. Furthermore, friction losses rose at the throttle area.

While increase of the pressure at the pump's inlet is positive factor for operating conditions of the pump it seems to be good solution to initiate diffuser at the inlet (station 2).

2. In considered design, the flow approaches the pump at station 3 were diameter of the rotor's shaft sharply increases to form the rotor's hub.

   It is another area of possible improvement. Therefore, it is recommended to equalize the shaft's diameter to the one of the propeller in order to decrease sharp increase of the flow velocity.
3. At station 4 the flow leaves the rotor's space and enters the nozzle/stator part. In the considered design rapid drop of water velocity is visible. It is a consequence of application of the shape of the nozzle marked D (see Figure 8.21) and short conical continuation of the rotor's hub.

   To avoid this phenomenon the nozzle between 300 and 310 mm of the tunnel length (right at the nozzle outlet), needs to be more conical than proposed in the design.

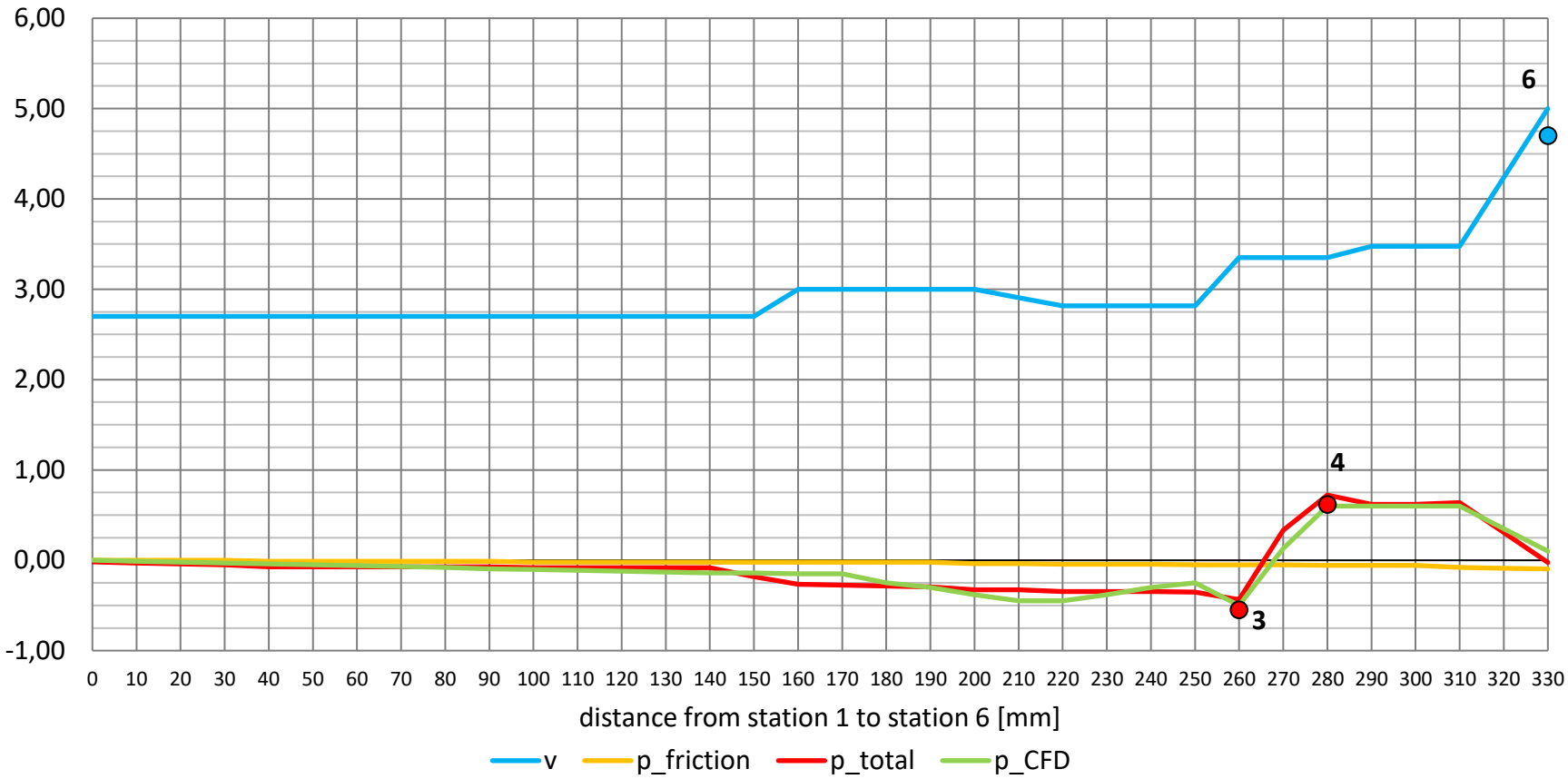

Figure 8.50: Property variations though WJ50 propulsor calculated using: CFD simulation (p_CFD) and semi-empirical method (v, p_friction, p_total). Points refer to stations and measuring points (see the Figure 6.1 and the Figure 9.7).

Notation:

v – velocity inside the propulsion tunnel [m/s]

p_friction – pressure loss due to friction [mH_2O]

p_total – total pressure inside the tunnel [mH_2O]

p_CFD – pressure simulated with a use of CFD [mH_2O]

9 The experimental evaluation of waterjet propulsion system theoretical investigation

Figure 9.1: The Gluptak vehicle with standard screw propellers – SP configuration.

Figure 9.2: The Gluptak vehicle with standard propellers and propellers' guard – SP+G configuration.

Figure 9.3: The Gluptak vehicle equipped with four G39 [39mm] waterjet propulsors.

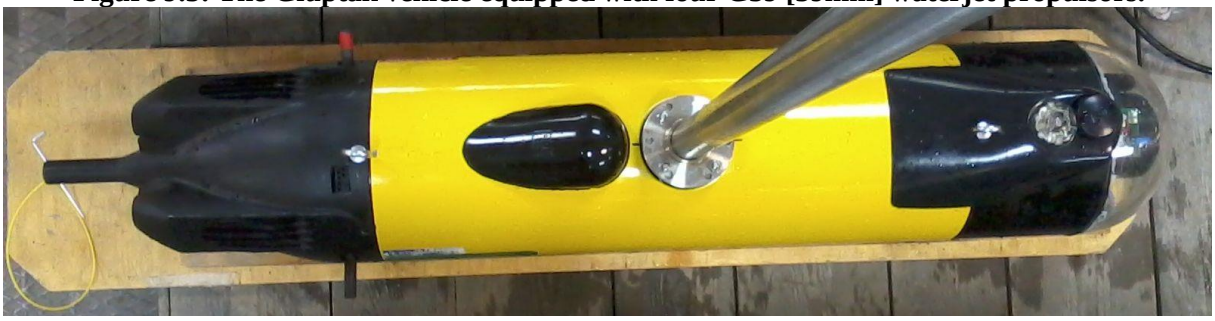

Figure 9.4: The Gluptak vehicle equipped with four G49 [49mm] waterjet propulsors.

Figure 9.5: The Gluptak vehicle equipped with four WJ50 [50mm] waterjet propulsors.

The initial, theoretical analysis indicated that application of the waterjet drives in the submersible propulsion system can be justified. Therefore, the author decided to prove theoretical results of semi empirical and CFD calculations in a series of experiments using real object of study that was described in the Chapter 4 . The experiments were conducted at both limited and unlimited water areas. Laboratory tests were run in the flow tank were water velocities of 1.5 [m/s] are achievable. Higher velocities, up to 3.5 [m/s] were available at the lake laboratory facility.

All the versions of the propulsion's configuration of the Gluptak vehicle that were tested for the purpose of this work are shown in the photographs below. The Figure 9.1 shows the base configuration propelled by the open screw propellers. In the Figure 9.2 the base configuration is supplemented with protection grill that is a kind of remedy against possibility of entanglement of the control cable by operating propellers. The Figure 9.3, Figure 9.4 and Figure 9.5 show three versions of vehicle with the waterjets investigated as an alternative to an open screw propeller.

9.1 Vehicle with waterjet propulsors

For initial practical experiments commercially available waterjet propulsors were selected. All of them were designed for boat models and manufactured by the *Graupner* company to unknown specification. The details regarding their geometry are also unknown. All the propulsors with basic data are listed in table below.

The smallest 29 millimetres propulsor was utilized to evaluate general image of operating small device. I was also utilized to find differences in thrust, power consumption and efficiency for loomed and immersed nozzle propulsion. The three larger propulsors were built into the aft canopies of the tested vehicles.

Due to various revolution ranges the standard propellers and the jet drives operate in, it was necessary to use electric motors with two different specifications. Bare screws were powered by motor S-4000 (where the number refers to its maximum revolutions at no load conditions), the waterjet propulsors were equipped with the S-10000 motors. Efficiency curves for relevant load conditions are presented in the appendixes 12.3 and 12.4. They allow to calculate power consumption of the propulsors, basing on total power drained at test conditions.

Table 9.1: List of the waterjet propulsors used in the experiments.

no.	test designation	inlet shape	pump rotor diameter [mm]	number of rotor blades	manufacturer designation
1	G29	rectangular	29	2	Jet Antrieb 2 Booster (no.2345)
2	G39	rectangular	39	2	Jet Antrieb (no. 2340)
3	G49	rectangular	49	6	Jet Antrieb 5 (no. 2347)
4	WJ50	elliptic	50	3	

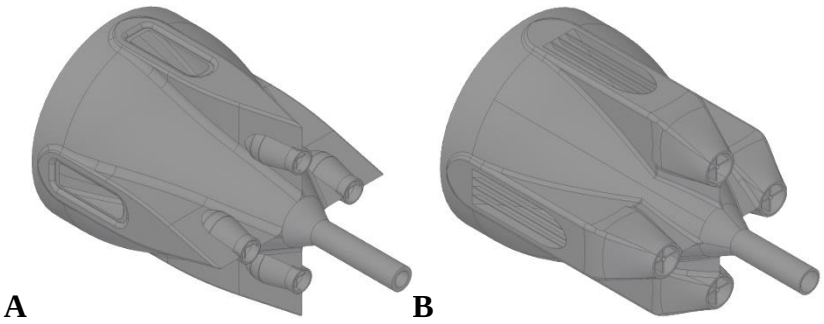

Figure 9.6: Vehicle's aft sections with waterjet drive 39 [mm] (A) and 49 [mm] (B).

9.2 Test methods, test stations and measurement equipment

Test facilities and equipment used for measurements are described in details in the Appendix II – Test conditions and measurement equipment.

In a nutshell, propulsion tests were performed using body of the real vehicle with all four propulsors installed. This assured operation of the propulsors in their real conditions. It is particularly important if flow character and boundary layer development is considered. Further, application and simultaneous operation of 4 propulsors increases total value of forces that need to be measured. This increases accuracy of measurements especially in the case of tests performed in natural environment conditions.

In the flow tank conditions both forward and backword thrust were measured.

The parameters measured during tests of all configurations of the propulsors are listed in the Table 9.2.

Finally, a series of tests was performed to investigate influence of the outlet nozzle diameter on the propulsor performance.

During all experiments, the vehicle was equipped with *AMTI* multi-axis 3D force sensor (Figure 12.8). The force sensor was affixed in place of vertical thruster in the middle of the body of the vehicle. It assured direct measurement of forces and moments acting on the vehicle's body close to its origin. – See Figure 12.3 (vehicle in the flow tank) and two photographs above Figure 9.4 and Figure 9.5 (vehicle prepared for tests equipped with force sensor).

Further, during all experiments the following measurement scheme was adopted:

1. Increase relative water velocity in 0.0–3.5 [m/s] range with 0.5 [m/s] steps.
2. Stabilize relative water velocity.
3. Compensate drag force with thrust of the propulsors.
4. Record values of the listed parameters during a period of 30 seconds.

Multisensor pressure measurement tool

In order to measure the pressure in three selected points – see the Figure 9.7 – a special device was built. The pressure was measured by membrane sensors operating within a range of -0.02 [MPa] to +0.02 [MPa], which equals to -2 [mH_20] to +2 [mH_2O]. Sensors' accuracy was 0.1% (2.0 [mm]). The whole unit consisted of 5 STS ATM 120049 sensors. The tubes connecting investigated points with the sensors were 3.0 [mm] in diameter – it was enough to assure low pressure damping.

One of the sensors was responsible for measuring the depth of the propulsion and was used as a reference point for the remaining sensors.

The results obtained during performed experiments allow to verify theoretical, semi-empirical and simulation methods.

Table 9.2: List of parameters measured during tests of investigated propulsors.

no.	parameter	unit	relative accuracy
1	water relative velocity	[m/s]	Ott velocity Meter, ADV meter
2	bottom relative velocity	[m/s]	Explorer DVL
3	X force (drag)	[N]	0.20%
4	Y force	[N]	0.20%
5	Z force	[N]	0.20%
6	voltage supplied from source	[V]	0.05%
7	current drained from the source	[A]	0.05%
8	motor current 1	[A]	0.05%
9	motor speed 1	[A]	0.20%
10	motor current 2	[A]	0.05%
11	motor speed 2	[A]	0.20%
12	motor current 3	[A]	0.05%
13	motor speed 3	[A]	0.20%
14	motor current 4	[A]	0.05%
15	motor speed 4	[A]	0.20%

9.3 Performance evaluation of separated waterjet propulsor

In order to determine real influence of the outlet nozzle diameter on propulsor's thrust a series of experiments were performed. Additionally, in selected regions pressure inside the propulsion's tunnel was measured. The table below presents results for five nozzle diameters and a range of six rotor's velocities for each diameter.

The experiments regarding the outlet nozzle were run according to the same schedule – gradual increase of rotor speed from 0 [rpm] to maximum 5400 [rpm]. The cut-off points were maximum revolutions or current threshold of 9 [A] – which is an equivalent of 210 [W] (maximum power available).

The measurements were taken for both, forward and backward operation.

The cone-shaped outlet nozzle was shortened (cut-off) in steps of 5 [mm] each. It allowed to study nozzle's diameter within 30.0-42.6 [mm] range. The 42% diameter change resulted in just over 100% cross-section area increase.

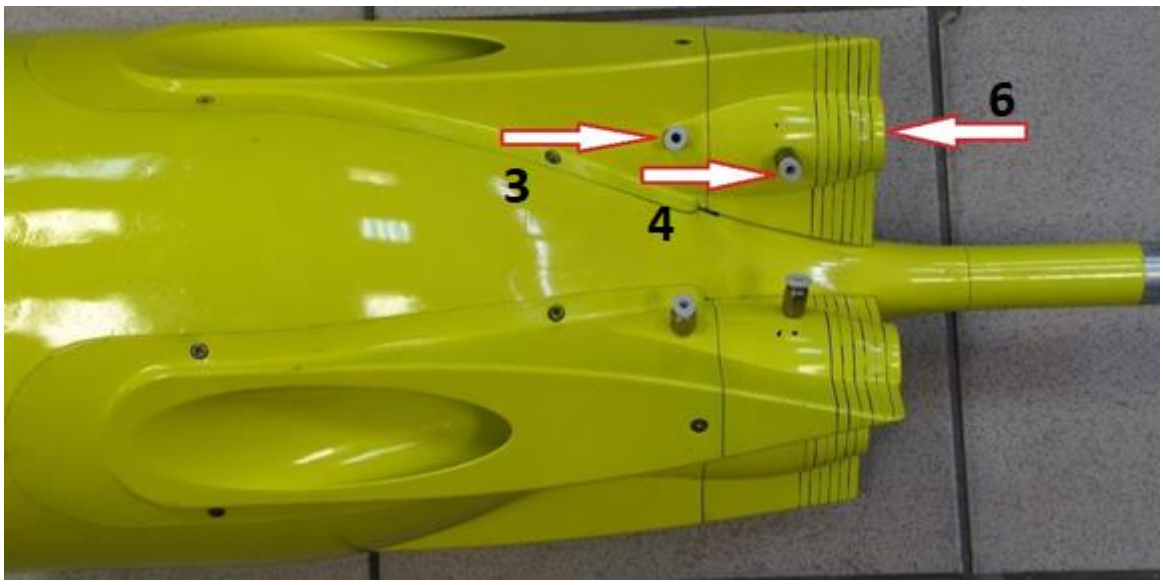

Figure 9.7: The investigated WJ50 propulsor. The arrows indicate points where pressure was measured. The points refer to stations: 3 (in front of the rotor), 4 (behind the rotor) and 6 (right at the outlet of the outlet nozzle) – see the Figure 6.1. Black lines show nozzle's cut-off steps.

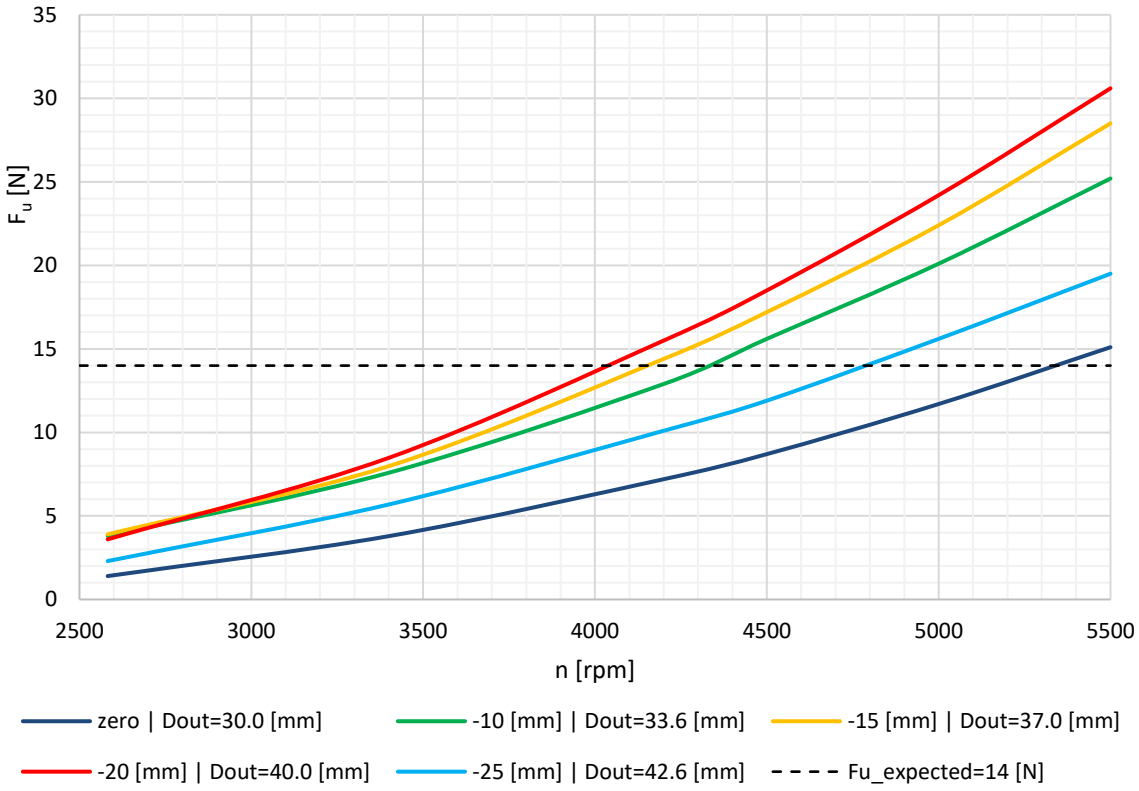

Figure 9.8: The CFD predictions for the WJ50 propulsion's thrust for different outlet nozzle diameters. The water velocity 3.0 [m/s].

Table 9.3: The CFD prediction for the WJ50 thrust for different outlet nozzle diameter as well as different rotor speed. The water velocity 3.0 [m/s].

				n [rpm]					
on.	cut-off [mm]	D_{out} [mm]	A_{out} [m^2]	2582	3403	4200	4500	5000	5500
1	zero	30.0	0.00071	1.4	3.8	7.2	8.7	11.7	15.1
2	-10	33.6	0.00089	3.8	7.6	12.9	15.6	20.1	25.2
3	-15	37.0	0.00108	3.9	8.0	14.4	17.2	22.4	28.5
4	-20	40.0	0.00126	3.6	8.5	15.5	18.5	24.2	30.6
5	-25	42.6	0.00143	2.3	5.7	10.1	11.9	15.6	19.5

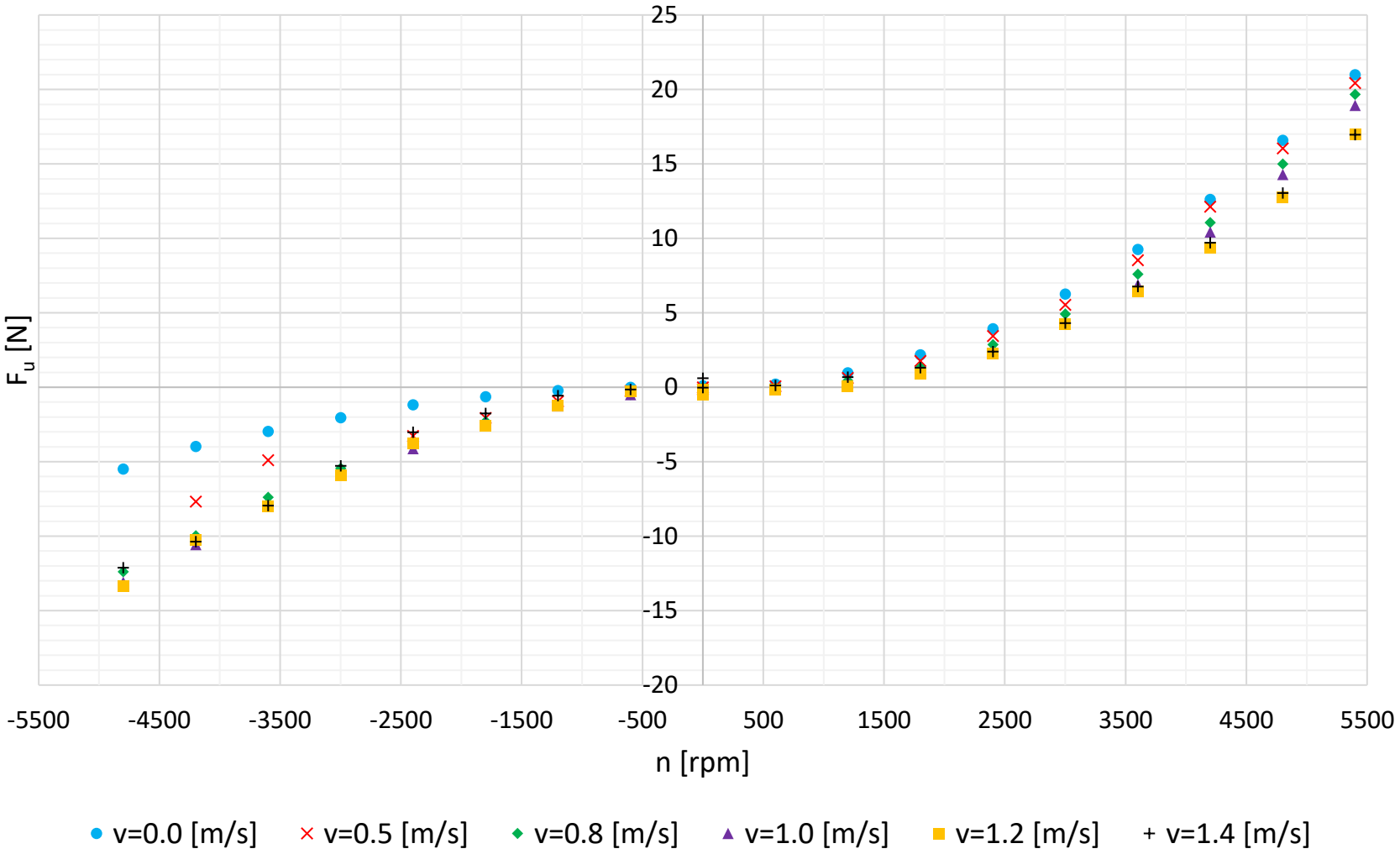

Figure 9.9: Thrust as a function of motor revolutions for different water velocities. Positive values represent propulsion operating "forward", negative ones refer to propulsion operating "backwards". Investigated WJ50 with outlet nozzle diameter 40 [mm].

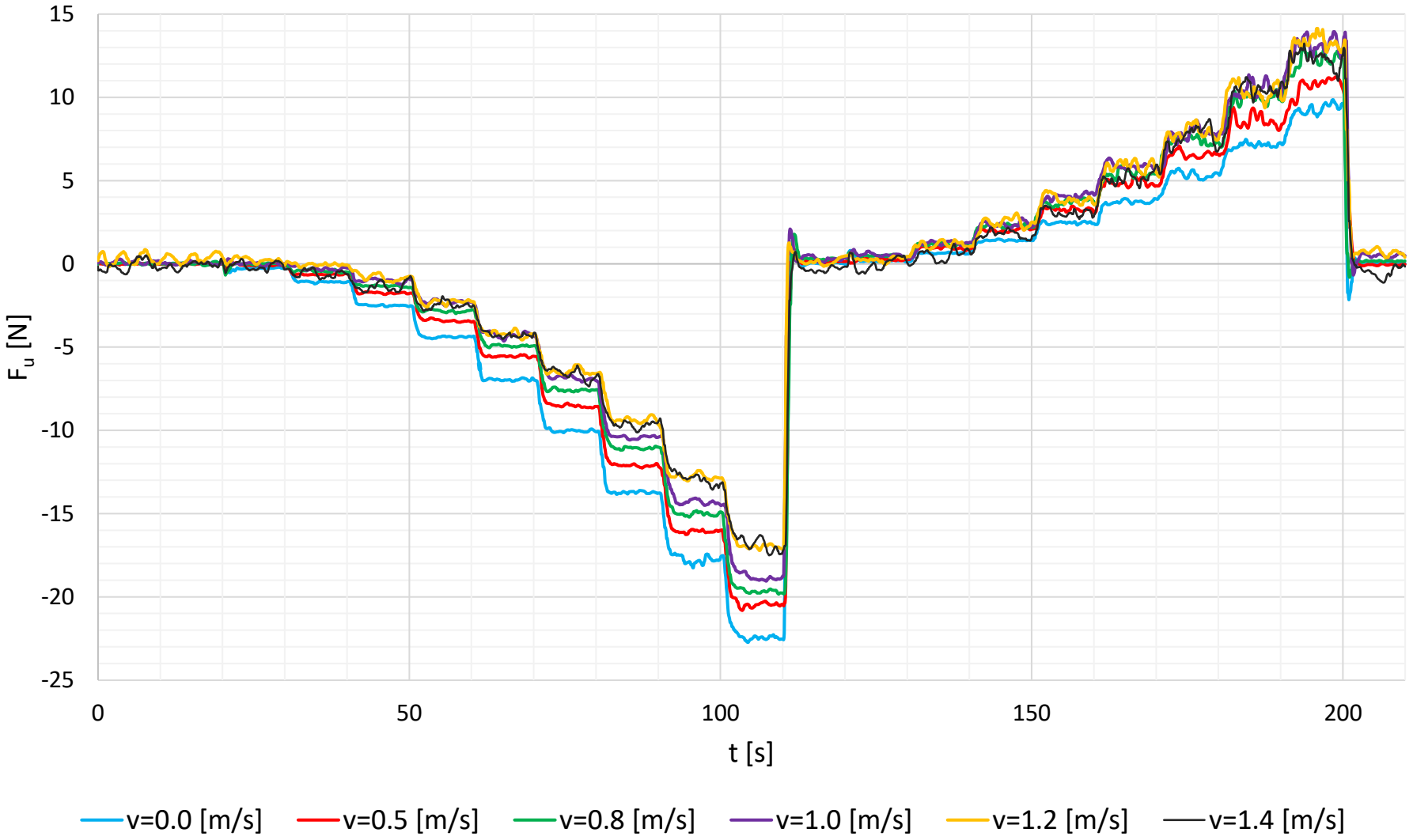

Figure 9.10: Thrust force change as a function of time for different water velocities. Negative values represent propulsion operating "forward", positive ones refer to propulsion operating "backwards". Investigated WJ50 with outlet nozzle diameter 40 [mm].

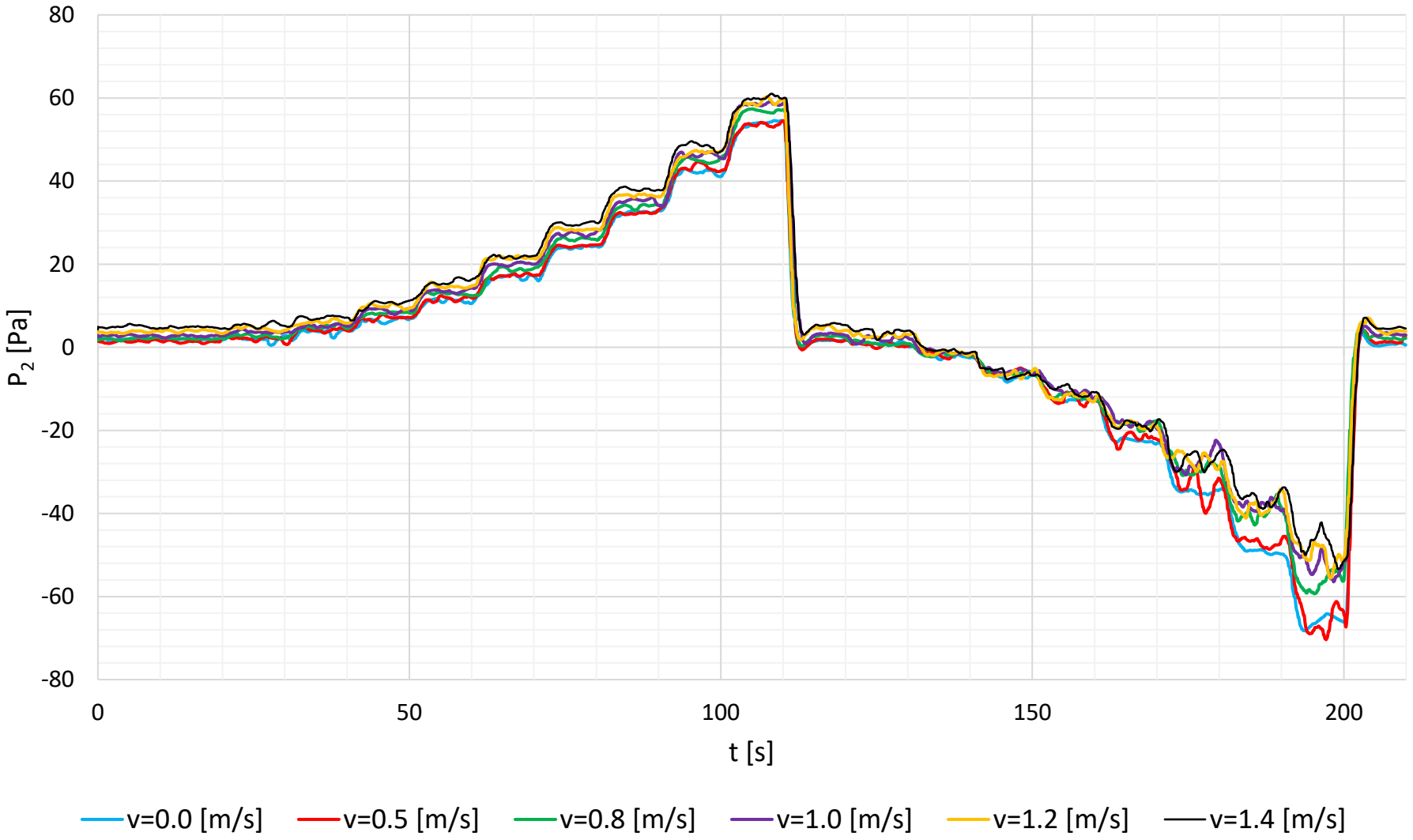

Figure 9.11: Pressure behind rotor change as a function of time for different water velocities. Positive values represent propulsion operating "forward", negative ones refer to propulsion operating "backwards". Investigated WJ50 with outlet nozzle diameter 40 [mm].

9.4 The experimental results for different outlet nozzle diameters

Table 9.4: The experimental results for different outlet nozzle diameters obtained in the flow tank. Rotor's speed 5400 [rpm], water velocity 1.4 [m/s].

				pressure [cmH_2O]				
no.	**cut-off [mm]**	**Dout [mm]**	**Fu [N]**	**in front of the rotor**	**behind the rotor**	**at the nozzle's outlet**	**outlet velocity [m/s]**	**Δp [cmH_2O]**
1	0	30.0	16	-50	75	160	6.00	125
2	-5	32.0	13	-55	80	160	5.75	135
3	-10	33.6	14	-75	50	160	5.50	125
4	-15	37.0	17	-95	10	140	5.25	105
5	-20	40.0	15	-110	-10	110	4.75	100
6	-20	40.0	15	-110	60	110	4.75	170

Δp – pressure increase inside the propulsion's pump

Note: positions 5 and 6 in the table above refer to the same propulsor's configuration, but the measurement point at stage 4 (behind the rotor) was moved into different location. All the remaining nozzle sizes were analysed using sensor's new position. This was explained in the results discussion chapter.

10 The experimental results discussion

First and foremost, the new drive has not met the expectations in terms of vehicle's operating point.

The experimental outcomes for all analysed jet drives are very peculiar and it is difficult to form short and simple conclusion.

10.1 The initial flow tank tests

The first comparative tests performed in the flow tank suggested all waterjet propulsors can compete with standard propellers. Given the static water thrust (zero velocity), the WJ39G (smaller Graupner) matched standard bare propellers (SP), whereas the WJ49G (bigger Graupner) was near standard propellers with grill (SP+G). The newly designed WJ50 however, seemed to be slightly better (~15%) in terms of thrust-power ratio (see the Figure 10.1).

The next comparison is yet again based on flow tank test, but this time for water velocity of 0.7 m/s]. And again, Graupner jet drives seem to be competitive to standard propellers. The WJ50 however, outperforms standard screws, but only to some point. The turning point is right before 14 [N] (thrust force value expected) and for higher F_u, every Newton costs more Watts than in case of standard guarded propellers.

The overall efficiency seems to be much higher for WJ50 in flow tank conditions – 44% (WJ50) to 28% (SP) and 25% (SP+G). However, it must be remembered, that this comparison refers to vehicle's velocity of 0.7 [m/s], where standard propellers operate at very low speed – hence this big difference in efficacy. (Graphs in the Figure 12.33 and Figure 12.36).

10.2 Design error location

For reminder, the regular problems with vehicle's drive system and its propellers frequently tangled with debris were the lead motivation for this research. Also, from the very beginning, it was clear the potential solution, introduced and implemented to the vehicle with its existing design, would have to be compromised. And because of changes already planned, it was decided to interfere with the whole aft canopy. It gave the possibility to build-in and test the jet drives. However, still some constraints had to be set.

The prepared changes did not include the battery pack replacement or any redesigns in the main part. Therefore, the vehicle's new propulsion had to ensure it was still able to perform its tasks without a risk of a failure – it was expected to run for at least 12 minutes at the operating speed of 3.0 [m/s]. In practice, it means that if the new propulsion was able to deliver sufficient thrust force and at the same time its energy consumption did not exceed maximum available from the batteries, then regardless of its efficiency, it would be accepted as a counterpart.

Information above was reminded because of two reasons. Firstly, right from the start it was expected that the real jet drive efficiency would be rather lower than the one predicted by the theory. The outdoor trials results for WJ49G were very optimistic and suggested the

propulsion efficiency at the operating point might have been as much as the half of the one for standard bare propellers or even more. However, the main concern in this matter was the lack of experience in similar designs.

Secondly, even the pump pundit admitted that planned rotor size was beyond any pump chart (nomogram) available. That is why it was assumed the overall performance of newly designed drive would be lower than the value indicated by the theory. However, the prospective efficiency drop was expected to be covered by significant vehicle's drag reduction.

The propulsor (and the pump) size was determined by the vehicle's fin dimensions, that imposed the maximum possible rotor size and defined the start point of further calculations. Further, the WJ49G outcomes suggested that 4200-4500 [rpm] rotor's speed range should be enough to deliver sufficient thrust. Obviously, additional assumption was the new drive would be, at least slightly, better than the old one too.

Now, given the jet drive tunnel main dimensions and assuming the first step efficiency at 100% (pure theoretical assumption to obtain starting point for further calculations), the propulsion should deliver around 13.5 [N] of thrust at about 2400 [rpm]. The thrust however, is a product of mass flow rate and outlet absolute velocity. Hence, the same force value can be obtained via different combination of those two variables. Now, if we set the velocity index μ at $0.50 \div 0.55$, which means about 6.0 [m/s] at the tunnel outlet, and calculate the non-dimensional losses inside the tunnel at $0.05 \div 0.10$, than, according to Fliegner's theory (see the chart at page 35), the overall propulsion efficiency should be about $60 \div 65\%$. Moreover, the axial pump performance itself can reach 90%. Therefore, the ultimate jet drive efficiency should be expected at about 60%. Obviously, considering propulsion ultimate performance, the thrust would drop. Nevertheless, it would be compensated by a rise of revolutions number. We must also remember, these were basic, theoretical calculations and of course, as it can be seen in the table below, some safety margin was left. For instance, the revolution number was simply divided by propulsion performance value – what is more it matches to the previous conclusion made after WJ49G tests. In fact, the thrust rise is not linear and follows quadratic curve, then it should be greater.

10.3 Comparison of the waterjet propulsors

At the end, a comparison of all five vehicle's drive configurations using different coefficient was done. It will use flow tank investigations results, because only there it was possible to secure the same and stable operating conditions as well as the velocity during all measurements.

The drawback of this comparison is that it could be done for 0.0 and 0.7 [m/s] velocities only. Nonetheless, it is still valuable analysis.

All three different coefficients base on ratio between thrust generated by the propeller and its size. In the tables presented in the Appendix V – Coefficients, all five drive configurations were confronted at the same level of motor revolutions as well as at the maximum revolution

measured. Additionally, the coefficient of propeller's excellence includes power delivered to the propeller. The coefficients are as follows:

— coefficient of excellence [61]

$$\zeta_{P0} = \frac{T}{2 \cdot 75 \cdot N_d} \cdot \sqrt{\frac{2 \cdot T}{\rho \cdot S}} \quad [–] \tag{10.1}$$

— von Karman's coefficient (yield coefficient) [60]

$$C_k = \sqrt{\frac{T^3}{\rho \cdot S \cdot n^2}} \quad [–] \tag{10.2}$$

— Bondeman's coefficient (a static thrust coefficient) [60]

$$C_b = \frac{T}{\sqrt[3]{2 \cdot \rho \cdot S \cdot n^2}} \quad [–] \tag{10.3}$$

It was no surprise that at the same level of revolutions standard propellers had performed better than waterjets. Bondeman's and von Karman's coefficients indicate SP as much better solution and outclasses the jet drives. On the other hand, given the maximum values measured during flow tank tests, coefficient of propeller's excellence hints these different propulsion types can be comparable in particular operating points.

Therefore, based on outdoor experiments' outcomes, the results were normalized, so that they referred to vehicle's operating point. During the conversions, everything possible was done to keep the highest accuracy possible, that is why the velocity is not the 3.0 [m/s] precisely. It allowed to compare and contrast the real power requirements and thrust delivery for each investigated drive types – for reminder, four propulsions power the vehicle hence its drag force was divided into four.

Table 10.1: Coefficients of excellence for points close to vehicle's operating point.

no.	**drive**	**S_{PROP}**	**u**	**¼ drag**	**Thrust**	**n**	**N_d**	**ζ_{P0}**
1	*SP+G*	0.00785	2.650	15.50	15.75	2469	100.1	0.0021
2	*SP+G*	0.00785	3.330	22.50	22.63	2831	124.2	0.0029
3	*WJ39G*	0.00119	2.950	11.25	11.62	5848	206.3	0.0017
4	*WJ49G*	0.00189	2.860	11.25	11.25	3811	107.0	0.0024
5	*WJ50*	0.00196	2.929	12.95	13.00	5700	135.0	0.0023

There was also a possibility to compare three drives tested in the same conditions in the real environment – at the lake. The table below presents power consumption comparison for standard bare propellers (SP), standard propellers covered by protection grill (SP+G) and one of Graupner's off-the-shelf waterjet drives WJ49G.

The addition of propellers' guard has entailed about 40% of drag increase and nearly 47% of power requirement. The overall performance for the propulsion in this setup was 57% and 39% respectively. While, the waterjet drive efficiency is 31%. However, the change in the drive type resulted in a large drag force decrease. The vehicle in WJ49G specification produced only about 58% of drag generated by the configuration with guarded screw propellers.

Table 10.2: Comparison of propulsion performance and power consumption for three different setups measured in the same conditions.

no.	propulsion type	R [N]	$T_{per\ propeller}$ [N]	n [rpm]	η	N_d [W]
1	SP	53.50	13.38	2400	57%	75
2	SP+G	75.00	18.75	2700	39%	110
3	WJ49G	43.25	10.81	3800	31%	110

As mentioned earlier, waterjet drive's efficiency drop had been expected to be compromised by significant vehicle's drag reduction. It would allow to run the vehicle with currently used power unit. Now, if we take a look at the Table 10.1, we can see that bigger jet drives can be competitive not only in terms of a coefficient alone, but also in terms of power requirements. If we round the values, we can say Graupner WJ49G needs just about 5% power more to meet the operating point than standard propeller equipped with propellers' mesh guard. It is satisfying result, despite the new drive turned out to perform worse than the off-the-shelf Graupner.

Finally, all drive types comparison is presented in a chart form in the Appendix III – Results of the tests of the investigated propulsion systems.

The last and probably the simplest question about the differences between analysed propulsions is: what is the thrust to power ratio? To answer it, two charts were prepared. The graphs below show the cost of a single Newton (and consecutive ones) in terms of power in Watts.

The lines were extrapolated forward in order to obtain the intersection points.

As the first chart for ratios at zero velocity is rather demonstrative one, the second is much more interesting. It visualises the jet drives potential if they are designed and used properly.

Taking into account configuration where standard propellers are covered by mesh guard (blue solid line), it can be seen quite a big range where thrust generated by WJ50 (red solid line) costs less power. What is more, it can be said, that both Graupners stay competitive throughout the whole chart range.

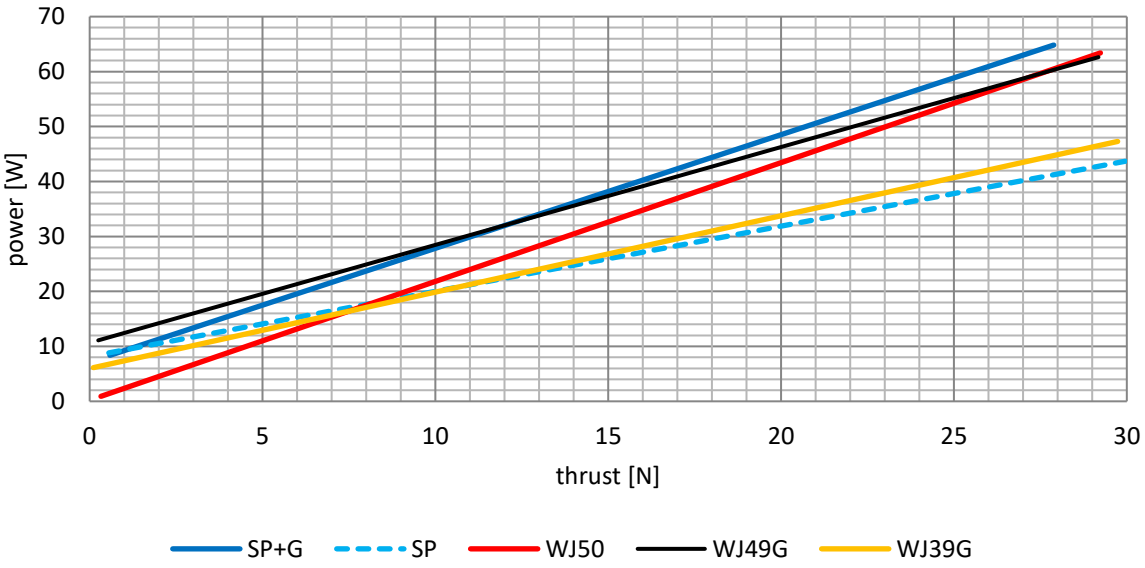

Figure 10.1: Thrust-power ratio for investigated propulsions – flow tank experiments at zero speed.

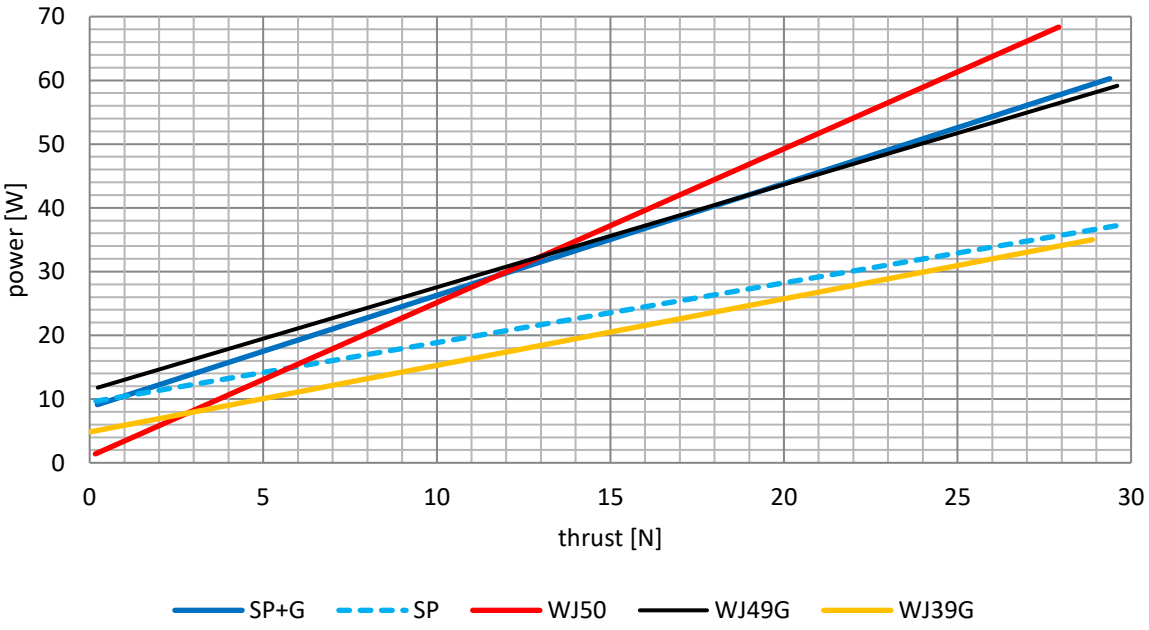

Figure 10.2: Thrust-power ratio for investigated propulsions – flow tank experiments at speed 0.700 [m/s].

11 Conclusion

11.1 Semi-empirical method as a tool for modelling of a waterjet propulsor

As it can be seen from cited results the semi-empirical method gives good agreement with measurement results. It allows for quick study of influence of basic components on total performance of the propulsor composed of several components:

- The theory describing the waterjet drives formulated by Albert Fliegner was confirmed by experimental results. The ultimate result is slightly underestimated, but it can be regarded as positive.
- The general theory about flow losses inside the pipe, surprisingly, turned out to be representative, however exceptional carefulness in tunnel division is advised performing these calculations.

Negative features of the semi empirical method in application to considered class of objects are as follows:

- It is not possible to define position of the station or geometric feature precisely.
- Only averaged values of the parameters are available. Type of flow inside the tunnel needs to be estimated.
- Influence of the shape of the local geometries of the tunnel on the local flow parameters cannot be studied.

11.2 CFD method as a tool for modeling of a water jet propulsor

- Despite complexity, Fluid Structure Interaction method used in CFD analyses that aided the new drive design process seems to be correct. The divergences between experimental outcomes and the ones predicted by CFD simulations are caused by propulsion's poor workmanship not modelling errors.
- The first attempt with a very simple model, where only the pump was analysed was wrong given a complex flow character around the vehicle's body. The boundary layer and all protruding elements proved to disturb the inflow to the tunnel enough, not to be neglected in similar simulations in the future.
- It is very important too, to remember about interaction between propulsion and the vehicle’s hull. Pure drag prediction around an operating point proved to deliver very good results with accuracy within a few percent. However, the same prediction with operating propulsor tends to significantly overestimate drag value. The percentage difference strongly corelates with difference between simulation outcomes and experimental ones.
- Summarizing forces at particular parts of the model to obtain thrust force – standard method for bare propeller – turned out to be wrong for waterjet propulsor. It might be good enough for direct comparison between different simulations, but has regular tendency to underestimate the results. Hence, it is advised to calculate the thrust force

by multiplying absolute velocity and mass flow at the outlet nozzle outlet and then correct it by mentioned above percentage difference in drag force.

11.3 Areas of future investigation

— The most promising area for further research in terms of propulsor's efficiency is the pump. Because of its significant influence on total efficiency, increase of the pump efficiency from 60% level to 80% level (relative 33% increase) can give the waterjet propulsor efficiency of 56% – close to the one of the free screw propeller. Of course, given that the limitations assumed for propulsion suite of the underwater vehicle are still valid.

— From practical point of view, another important matter for this problem is reversing the propulsor's thrusts. It is required to achieve adequate manoeuvring performance of the vehicle, particularly at low speed. It can be achieved in traditional way using external jet directing devices. More advanced seems to be application articulated components of the propulsor. The latter solution is far more complicated, but promises more compact arrangement. In both the cases substantial re-thinking of the propulsor configuration is required. Basing on results of this work it seems that CFD methods can be used to study a number of possible solutions in details to reduce range of real experiments.

11.4 Practical application of the results

Summarizing, results of the experiments described in this thesis suggest clearly that waterjet propulsors can be competitive and hence a counterpart to standard propellers considering described limitations of both arrangements. The key factor is to design them properly.

Bibliography

[1] „Propulsor - definition," 2014.09.22. [Online]. Available: http://en.wikipedia.org/wiki/Propulsor.

[2] „Propulsor - exemplary picture," 2014.09.22. [Online]. Available: http://en.wikipedia.org/wiki/File:Propulsor_MK50.jpg.

[3] „Propeller - definition," 2014.09.22. [Online]. Available: http://en.wikipedia.org/wiki/Propeller.

[4] „Propeller - exemplary picture," 2014.09.22. [Online]. Available: http://en.wikipedia.org/wiki/File:Ship-propeller.jpg.

[5] „First ROV," 2013.09.02. [Online]. Available: http://sandacom.wordpress.com/2010/07/08/remotely-operated-vehicles-history-waldos-howard-hughes/.

[6] „Deepwater ROV 1," 2013.09.02. [Online]. Available: http://johnsmyth.ie/blog/wp-content/uploads/2009/05/marine-rov-1.jpg?w=840.

[7] „Small ROV - VideoRay 1," 2013.09.02. [Online]. Available: http://filemaker2-server.cbl.umces.edu/sensorimages/7606-explorerx3.gif.

[8] „Small ROV - VideoRay 2," 2013.09.02. [Online]. Available: http://www.upstreampipeline.co.uk/photos/rov1.jpg.

[9] „AUV 1," 2013.09.02. [Online]. Available: http://www.usm.edu/news/archives/older/cms/images/stories/August/auv%20publicity%20shot-2006%20(2).jpg.

[10] „AUV 2," 2013.09.02. [Online]. Available: http://upload.wikimedia.org/wikipedia/en/4/49/SAMS-AUV-prototype.jpg.

[11] „AUV 3," 2013.09.02. [Online]. Available: http://www.ysisystems.com/media/products/EcoMapper-easy-deploy.jpg.

[12] „DPV 1," 2013.09.02. [Online]. Available: http://aquaviews.net/wp-content/uploads/2011/02/SDOSE.jpg.

[13] „DPV 2," 2013.09.02. [Online]. Available: http://stiddmil.com/wp-content/uploads/2012/08/DPD-main-image1.jpg.

[14] „Pump-jet," 2014.09.25. [Online]. Available: http://en.wikipedia.org/wiki/Pump-jet.

[15] Z. L. W. Z. J. C. J. L. Yuanxing Dai, „CFD_FEM analysis of flow-induced vibrations in waterjet propulsion unit," *Journal of Marine Science and Engineering*, 27 July 2022.

[16] „ALROSA submarine pump jet 1," 2013.01.19). [Online]. Available: http://3.bp.blogspot.com/-rsUb1vjwE8A/Tlf-Yvze2cI/AAAAAAAABMk/Zef0r0-LXuQ/s1600/Pump-jet+of+the+Kilo-II+class+pumpjet+submarine+propeller+water+aquatic+turbine.jpg.

[17] „ALROSA submarine pump jet 2,” 2014.10.17. [Online]. Available: http://i59.fastpic.ru/big/2013/1029/c9/5def82b5d55729e3f0c89e9a25572cc9.jpg.

[18] „Blue Shark Torpedo - Pump Jet,” 2013.01.19. [Online]. Available: http://upload.wikimedia.org/wikipedia/commons/thumb/f/fe/Blue_Shark_Hafif_Torpido.JPG/800px-Blue_Shark_Hafif_Torpido.JPG.

[19] W. d. h. i. p. n. P. Próchnicki, „Analiza możliwości napędu strumieniowego statku,” Gdańsk, 2001.

[20] 23rd International Towing Tank Conference, „The Specialist Committee on Validation of Waterjet Test Procedures, Volume II, p.387-415,” Venice, 2002.

[21] A. Eslamdoost, L. Larsson i R. Bensow, „A pressure jump method for modeling waterjet/hull interaction,” *Ocean Engineering 88,* pp. 120-130, 10 July 2014.

[22] T. Hino i K. Ohashi, „Numerical Simulation of Flow around a Waterjet Propelled Ship,” w *First International Symposium on Maritime Propulsors*, Trondheim, Norway, June 2009.

[23] G. D. D. D. A. D. M. Riccardo Broglia, „Simulation of turning circle by CFD: Analysis of different propeller models and their effect on manoeuvring prediction,” *Applied Ocean Research,* nr 39, 2012.

[24] J. D. S. C. A. R. M. Yuting Jin, „DTMB 5415M dynamic manoeuvres with URANS computation using body-force and discretised propeller models,” *Ocean Engineering,* nr 182, pp. 305-317, 2019.

[25] Z. L. A. Y. Yong Zhang, „Numerical analysis on self-propulsion of a waterjet-propelled ship with different propulsion models,” *Applied Sciences,* nr 12, 2022.

[26] A. Eslamdoost, „Investigations of waterjet/hull interaction effects,” Chalmers University of Technology, Department of Shipping and Marine Technology, Gothenburg, Sweden, 2012.

[27] A. Eslamdoost, „The hydrodynamics of waterjet/hull interaction (Phd Thesis),” Chalmers University of Technology, Department of Shipping and Marine Technology, Gothenburg, Sweden, 2014.

[28] T. van Terwisga, „Waterjet-hull interaction,” 1996.

[29] J. G. C. W. T.-c. W. K.-w. S. Jie Gong, „Analysis of waterjet-hull interaction and its impact on the propulsion performance of a four-waterjet-propelled ship,” *Ocean Engineering 180,* pp. 211-222, 2019.

[30] J. Z. Y. S. G. D. W. C. Lei Zhang, „A practical approach to the assesment of waterjet propulsion performance: the case of a waterjet-propelled trimaran,” *Polish Maritime Research 4 (104),* pp. 27-38, 2019.

[31] Scherer, Mutnick i Lanni, „Procedure for conducting a towing tank test of a waterjet propelled craft using Laser Doppler velocimetry to determine the momentum and energy flux,” w *26th ATTC,* Glen Cove, USA, 2001.

[32] W. Jiao, L. Cheng, D. Zhang, B. Zhang, Y. Su i C. Wang, „Optimal design of inlet passage for waterjet propulsion system based on flow and geometric parameters,” *Hindawi, Advances in Materials Science and Engineering,* p. 21, 24 October 2019.

[33] I. H. Lewis Mununga, „Waterjet intake flow improvement using boundary layer blowing and vortex generators," *Transactions,* tom 26, nr 1, pp. 1-6, 1999.

[34] „www.cloudfront.net," 2013.11.01. [Online]. Available: http://d2n4wb9orp1vta.cloudfront.net/resources/images/cdn/cms/0908hpc-patrol2.jpg.

[35] „www.gcaptain.com," 2013.11.01. [Online]. Available: http://gcaptain.com/wp-content/uploads/2009/02/sealth-ship-jet-propulsion.jpg.

[36] „Waterjet Rolls Royce - Kamewa FF series," 2009.06.29. [Online]. Available: http://www.liveyachting.com/wp-content/uploads/2009/06/rolls-royce-waterjet-ffseries.jpg.

[37] X. Chen, L. Cheng, C. Wang i C. Luo, „Influence of inlet duct length on the hydraulic performance of the waterjet propulsion device," *Hindawi, Shock and Vibration,* p. 13, 29 May 2021.

[38] D. R. Lavis, B. G. Forstell i J. G. Purnell, „Compact waterjets for high-speed ships," w *5th International Conference on High Performance Marine Vehicles*, Sydney, 2006.

[39] Y. Shen, P. Hu i S. J. et.al., „Design of novel shaftless pump-jet propulsor for multi-purpose long-range and high-speed autonomous underwater vehicle," *IEEE Transactions on Magnetics,* tom 52, nr 7, July 2016.

[40] A. W. Hughes, „Investigation of tip-driven thruster and waterjet propulsion system (PhD Thesis)," University of Southampton, Faculty of Applied Science and Engineering, Southampton, UK, 2000.

[41] W.-G. Park, J. H. Jang, H. H. Chun i M. C. Kim, „Numerical flow and performance analysis of water jet propulsion system," *Ocean Engineering 32,* nr 32, pp. 2107-2120, October 2005.

[42] J. Wu, L. Cheng, C. Luo i C. Wang, „Influence of external jet on hydraulic performance and flow field characteristics of water jet propulsion pump device," *Hindawi, Shock and Vibration,* p. 15, 24 May 2021.

[43] „www.wikimedia.org," 2013.11.01. [Online]. Available: http://upload.wikimedia.org/wikipedia/commons/4/4b/Waterjet.jpg.

[44] „www.pmcgroup.se," 2013.11.01. [Online]. Available: http://www.pmcgroup.se/Global/Solutions/Offshore-Marine/Images/PMC-Solutions-Offshore-Marine-Hydraulic-Cylinders-Waterjet-576x401.jpg.

[45] „www.huntdesigns.com," 2013.11.01. [Online]. Available: http://www.huntdesigns.com/images/pages/waterjets-jet.png.

[46] „Intelli Jet Marine Inc.," 2014.10.19. [Online]. Available: http://www.iijet.com/index.html.

[47] J. Allison, „Marine Waterjet Propulsion," *SNAME Transactions,* tom 101, pp. 275-335, 1993.

[48] S. S. e. al., „Toward Predicting Performance of an Axial Flow Waterjet Including the Effects of Cavitation and Thrust Breakdown," w *First International Symposium on Marine Propulsors*, Trondheim, Norway, June 2009.

[49] M. K. e. al., „Comparison of waterjet performance in tracked vehicles by impeller diameter," *Ocean Engineering,* nr 36, pp. 1438-1445, 2009.

[50] S. G. E. M. F. S. Manivannan Kandasamy, „Numerical and Experimental Evaluation of Waterjet Propelled Delft Catamarans,” w *11th International Conference on Fast Sea Transportation*, Honolulu, Hawaii, USA, September 2011.

[51] N. B. D C Murrin, „Waterjet propulsion system tested in a wind tunnel and compared with numerical simulation,” *International Journal of Small Craft Technology,* 2006.

[52] N. Bulten, "Numerical Analysis of a Waterjet Propulsion System" (PhD), 2006.

[53] U. A. Korde, „Study of a jet-propulsion method for an underwater vehicle,” *Ocean Engineering 31,* nr 31, pp. 1205-1218, July 2004.

[54] M.-C. Kim i H.-H. Chun, „Experimental investigation into the performance of the axial-flow-type water jet according to the variation of impeller tip clearance,” *Ocean Engineering 34,* nr 34, pp. 275-283, February 2007.

[55] S. Sharkh, „ROV with waterjet propulsion (case study),” 30 01 2012. [Online]. Available: http://www.southampton.ac.uk/~suleiman/projects/rov/rov/report/report.PDF.

[56] M. N. Burtness, „Pressure distribution and losses in a waterjet propulsion system,” Davidson Laboratory, New Jersey, 1987.

[57] N. Fujisawa, „Measurements of Basic Performance for Waterjet Propulsion System in Water Tunnel,” *International Journal of Rotating Machnery,* tom 2, nr 1, pp. 43-50, 1995.

[58] T. Dinham-Peren, „CFD and submerged waterjets,” *The Naval Architect RINA,* pp. 33-36, July/August 2010.

[59] K. Koushan, „A Preliminary Design and Off-Design Prediction Method for Waterjet Propulsion Systems,” w *International Conference on Waterjet Propulsion*, Amsterdam, 1998.

[60] L. Rowiński, Pojazdy głębinowe. Budowa i wyposażenie, Gdańsk: Wydawnictwo prywatne WiB, 2008.

[61] J. Staliński, Teoria okrętu, I red., Gdynia: Wydawnictwo Morskie, 1961.

[62] O. M. Faltinsen, "Hydrodynamics of High-Speed Maritime Vehicles", I red., Cambridge University Press, 2005.

[63] N. Mioczyńska, „Modelowanie matematyczne opróżniania rurociągów przesyłowych,” Kraków, 2006.

[64] Bim4tips.com, „How to calculate pressure loss through a duct,” 24 12 2019. [Online]. Available: https://www.bim4tips.com/updates/how-autodesk-revit-calculates-pressure-loss-through-duct-csbd6-euzls-rz9zz-fofju-xkphc. [Data uzyskania dostępu: 16 08 2022].

[65] H. S. Krystyna Jeżowiecka-Kabsch, Mechanika płynów, Wrocław: Oficyna Wydawnicza Politechniki Wrocławskiej, 2001.

[66] EngineeringToolBox.com, „Laminar Flow - Friction Coefficients,” 2008. [Online]. Available: https://www.engineeringtoolbox.com/laminar-friction-coefficient-d_1032.html. [Data uzyskania dostępu: 16 08 2022].

[67] J. W. Adolf Jarosz, "Hydraulika", Warszawa: Państwowe Wydawnictwo Rolnicze i Leśne, 1970.

[68] M. R. J. T. Zbigniew Heidrich, "Wodociągi i kanalizacja, część I", I red., Warszawa: Wydawnictwa Szkolne i Pedagogiczne, 1980.

[69] B. K. Achanta Ramakrishna Rao, „"Friction factor for turbulent pipe flow",” 01 2013. [Online]. Available: http://eprints.iisc.ernet.in/9587/1/Friction_Factor_for_Turbulent_Pipe_Flow.pdf.

[70] R. M. i. inni, "Poradnik-Wodociągi i Kanalizacja", Warszawa: Wydawnictwo Arkady, 1991.

[71] A. Tuszko, "Hydraulika i wodociągi", Warszawa: Wydawnictwa Geologiczne, 1971.

[72] J. Klugiewicz, "Hydraulika", II red., Bydgoszcz: Akademia Techniczno-Rolnicza - Wydawnictwo Uczelniane, 1993.

[73] 2. I. T. T. Conference, „Report of the Waterjets Group”.

[74] O. M. I. L. F. Scherer, „Procedure for conducting a towing tank test of a waterjet propelled craft using Laser Doppler velocimetry to determine the momentum and energy flux,” Glen Cove, NY, USA, 2001.

[75] A. T. S. Hughes, „Computational Fluid Dynamic Investigation of Hull-Waterjet Flow Interaction,” 1997.

[76] „Coanda effect definition,” 2014.09.25. [Online]. Available: http://en.wikipedia.org/wiki/Coandă_effect#cite_note-1.

[77] W. W. i. inni, „Zależność współczynnika strat miejscowych od liczby Reynoldsa podczas przepływu wody przez nagłe zwężenie rury,” *Ochrona Środowiska,* tom 28, nr 3, pp. 51-54, 2006.

[78] E. S. Hermann Recknagel, "Ogrzewanie i klimatyzacja. Poradnik", Warszawa: Wydawnictwo Arkady, 1976.

[79] C. Grabarczyk, "Przepływy cieczy w przewodach: metody obliczeniowe", Poznań: Wydawnictwo Envirotech sp. z o. o., 1997.

[80] G. Bar-Meir, Fundamentals of Compressible Fluid Mechanics, Chicago, November 2013 (version 0.4.9.8).

[81] M. Stępniewski, "Pompy", II red., Warszawa: Wydawnictwo Naukowo-Techniczne, 1985.

[82] N. Bulten, „A Breakthrough in Waterjet Propulsion Systems,” w *Proceedings of the International Maritime Defence Exhibition and Conference*, Doha, Quatar, 2008.

[83] H. Schlichting, "Boundary-Layer Theory", 7th red., 1979.

[84] F. M. White, "Fluid Mechanics", 4th red., University of Rhode Island.

[85] Г. В. В. П. В.Н. АНФИМОВ, Судовые тяговые расчеты, Москва: ТРАНСПОРТ, 1978.

[86] O. Lewis, "Aerodynamics analysis of a 2-man bobsleigh" MSc Thesis, Deflt: Delft University of Technology, 2006.

[87] S. Ivanell, „Hydrodynamic simulation of a torpedo with pump jet propulsion system," Stockholm, 2001.

[88] W. N. D. J D Denton, „Computational fluid dynamics for turbomachinery design," *Journal of Mechanical Engineering Science,* tom 213, nr Part C, pp. 107-124, 1999.

[89] K. T. Marzena Banaszek, „Rotor blade geometry optimization in Kaplan turbine," *TASK QUARTERLY,* tom 14, nr 3, pp. 209-225, 2010.

[90] T. T. T. e. al., *"Fluid dynamics simulation for propeller".*

[91] A. A. Y. e. al., *"Investigation of flow inside an axial-flow pump of GV-IMP type".*

[92] J. W. L. e. al., *"Modeling of Cavitating Flow through Waterjet Propulsors".*

[93] H. W. OH, „Application of Computational Fluid Dynamics to Practical Design and Performance Analysis of Turbomachinery," w *Computational Fluid Dynamics*, INTECH, January 2010, p. 420.

[94] I. S. J. e. al., „Shape optimization of impeller blades for a bidirectional axial flow pump using Polynomial Surrogate <odel," *World Academy of Science, Engineering and Technology,* nr 66, pp. 775-781, 2012.

[95] H. M. E. Lisowski, „CFD modelling of a jet pump with circumferential nozzles for large flow rates," *Archives of Foundry Engineering,* tom 10, nr Special Issue 3/2010, pp. 69-72, 2010.

[96] R. L. T. H. F.R. Menter, „CFD simulation of turbomachinery flows - verification, validation and modelling," w *European Congress on Computational Methods in Applied Science and Engineering*, Jyvaskyla, 24-28 July 2004.

[97] X. L. e. al., „Comparison of TurbulenceModels for Simulating Flow in Waterjets," w *11th International Conference on Fast Sea Transport*, Honolulu, Hawaii, USA, September 2011.

[98] Z. W. X. L. Huachun Wu, „Design and simulation of axial flow Maglev Blood Pump," *Modern Education and Computer Science, I.J. Information Engineering and Electronic Business,* nr 2, pp. 42-48, March 2011.

[99] Y. Z. e. al., „Design optimization of an axial blood pump with computational fluid dynamics," *American Society of Artificial Internal Organs,* pp. 150-155, 2008.

[100] A. H. David Hartwanger, „3D modelling of a wind turbine using CFD," w *NAFEMS Conference*, United Kingdom, 2008.

[101] L. N. L. Nilay Sezer-Uzol, „3-D Time-accurate CFD simulations of wind turbine rotor flow fields," *American Institute of Aeronautics and Astronautics, Pensylvania State University,* nr 0394, pp. 1-23, 2006.

[102] C. K. e. al., „A CFD study of wind turbine aerodynamics," w *American Society for Engineering Education, 2012 ASEE North Central Section Conference*, Grand Valley State University, Michigan, USA, 2012.

[103] M. Kraskowski, „Raport techniczny z obliczeń CFD do pojazdu podwodnego," Gdańsk, 2009.

[104] M. K. e. al., „Design and testing of underwater thruster for SHRIMP ROV-ITB," *Indian Journal of Maritime Science,* tom 38, nr 3, pp. 338-345, September 2009.

[105] M. K. e. al., „Design of SHRIMP ROV for surveillance and mine sweeper," *Indian Journal of Maritime Science,* tom 38, nr 3, pp. 332-337, September 2009.

[106] Y. L. Y. e. al., „Numerical Investigation of the Impact of SES-Waterjet Interaction and Flow Non-uniformity on Pump Performance," w *11th International Conference on Fast Sea Transportation*, Honolulu, Hawaii, USA, September 2011.

[107] R. A. V. e. al., „Modeling and simulation of an underwater ROV for surveillance and inspection of port facilities using CFD tools," w *27th International Conference on Offshore Mechanics and Arctic Engineering*, Estoril, Portugal, June 15-20th 2008.

[108] G. E. K. Xian Luo, *"Fast 3D Flow Simulations of a Waterjet Propulsion System"*.

[109] A. G. e. al., *"Multiobjective Design OPTIMISATION of a Water_Jet Inlet: A Numerical approach and experimental validation"*.

[110] K.-Y. K. Jin-Hyuk Kim, „Analysis and Optimization of a Vaned Diffuser in a Mixed Flow Pump to Improve Hydrodynamic Performance," *Journal of Fluid Engineering,* tom 134, nr 7, June 2012.

[111] J. C.-F. e. al., *"Advanced CFD Analysis of Aerodynamics Using CFX",* 2001.

[112] D. Wilcox, „Multiscale model for turbulent flows," w *24th Aerospace Science Meeting, American Institute of Aeronautics and Astronautics*, AIAA Journal 1986.

[113] D. Wilcox, „Re-assessment of the scale-determining equation for advanced turbulence models," w *AIAA Journal vol. 26, no. 11*, 1988.

[114] K. A. a. T. V. Terwisga, *"Recent work on waterjet-hull interactions effects",* 1993.

[115] „F-16 engine inlet," 2014.10.15. [Online]. Available: http://www.f-16.net/f-16-news-article2217.html.

[116] J. J. Maciej Kaczmarczyk, „Unmanned mine-cleaning underwater vehicle numerical drag prediction," *Journal of KONBiN,* nr 1 (21), 2012.

[117] E. T. K.J. Rawson, "Basic Ship Theory vol. 2", V red., Butterworth-Heinemann, 2001.

[118] J. Dudziak, "Teoria okrętu", I red., Gdańsk: Wydawnictwo Morskie, 1988.

[119] H. Kallingalthodi, „Cavitation detection in a water jet propulsion unit," Christchurch, 2009.

[120] „Tip cavitation," 2013.03.27. [Online]. Available: http://www.fluidlab.sys.t.u-tokyo.ac.jp/Research/CavPictures/large/Tip.sb.jpg.

[121] „Sheet cavitation," 2013.03.27. [Online]. Available: http://www.fluidlab.sys.t.u-tokyo.ac.jp/Research/CavPictures/large/Sheet.birdseye.jpg.

[122] „Bubble cavitation," 2013.03.27. [Online]. Available: http://authors.library.caltech.edu/25017/4/figs/fig706.jpg.

[123] P. A. John P. Breslin, "Hydrodynamics of ship propellers", I red., Cambridge: Cambridge University Press, 1996.

[124] EngineeringToolBox.com, „Water - Dynamic (Absolute) and Kinematic Viscosity vs. Temperature and Pressure," 2004. [Online]. Available: https://www.engineeringtoolbox.com/water-dynamic-kinematic-viscosity-d_596.html. [Data uzyskania dostępu: 27 06 2022].

[125] „AMTI force sensors," 2013.05.04. [Online]. Available: www.amti.biz.

[126] „Ott velocity meter," 2013.10.03. [Online]. Available: http://www.ott.com/web/ott_de.nsf/id/pa_c31_e.html.

[127] „DVL Explorer," [Online]. Available: http://www.rdinstruments.com/explorer.aspx.

[128] „SonTek Inc. ADV - principle of operation," 2014.10.01. [Online]. Available: http://www.sontek.com/productsdetail.php?16-MHz-MicroADV-3.

[129] P. zbiorowa, "Mały poradnik mechanika", XI red., Warszawa: Wydawnictwa Naukowo-Techniczne, 1969.

[130] J. Bukowski, "Mechanika płynów", V red., Warszawa: Wydawnictwo Naukowe PWN, 1976.

[131] A. T. Troskolański, "Hydromechanika", III red., Warszawa: Wydawnictwa Naukowo-Techniczne, 1967.

[132] K. J.-K. Katarzyna Strzelecka, „Rzeczywiste wartości współczynnika oporów miejscowych podczas przepływu wody przez skokowe rozszerzenie rury," *Ochrona Środowiska,* tom 30, nr 2, pp. 29-33, 2008.

[133] K. S. Krystyna Jeżowiecka-Kabsch, „Wpływ nagłego rozszerzenia rury na wartość współczynnika strat miejscowych," *Ochrona Środowiska,* tom 28, nr 2, pp. 53-56, 2006.

[134] K. Tesch, "Mechanika płynów", Gdańsk: Wydawnictwo Politechniki Gdańskiej, 2008.

[135] ANSYS, „CFX - Solver Theory Guide R14," November 2011.

[136] P. Pajączkowski, *"Simulation of transient states in large hydrodynamic thrust bearings",* 2010.

[137] J. S. Geisbert, *"Hydrodynamic modeling for Autonomous Underwater Vehicles using computational and semi-empirical methods",* 2007.

[138] ANSYS, „CFX - Solver Modeling Guide R14," November 2011.

[139] „Jet engine scheme," 2011.07.04. [Online]. Available: http://upload.wikimedia.org/wikipedia/commons/4/4c/Jet_engine.svg.

[140] „Outboard motor Evinrude - Pump Jet," 2013.01.19. [Online]. Available: http://blog.boats.com/files/evinrude55mfejet-3733.jpg.

[141] „www.outboardsjet.com," 2013.12.01. [Online]. Available: http://outboardsjet.com/wp-content/uploads/2011/04/OptimaxJet110.jpg.

[142] „Deepwater ROV 2,” 2013.09.02. [Online]. Available: http://www.thecqi.org/Global/Images/community/North_of_Scotland/FS_technips1.jpg.

[143] „EMAX CF2822,” 2013.09.09. [Online]. Available: http://i01.i.aliimg.com/wsphoto/v0/375935757/-font-b-EMAX-b-font-CF2822-1200KV-Outrunner-Motor-for-Airplane-ACNU-free-shipping-fee.jpg.

[144] „www.flopromarine.com,” 2013.11.01. [Online]. Available: http://www.flopromarine.com/img/screwBulletImpeller640x320.jpg.

[145] „www.nauticalweb.com,” 2013.11.01. [Online]. Available: http://www.nauticalweb.com/superyacht/501/rollsroyce/kamewa1.jpg.

[146] „www.yachtforums.com,” 2013.11.01. [Online]. Available: http://www.yachtforums.com/forums/attachments/technical-discussion/14374d1156235108-jet-drive-vs-prop-jet-pump-inducer-jpg.

[147] „www.mercurymarine.com,” 2013.12.01. [Online]. Available: http://www.mercurymarine.com/media/mercury/images/engines/jets/optimax-jet-inset.jpg.

[148] M. S. W. A. W. Josef Kestin, „Viscosity of luquid water in the range of -8 deg C to 150 deg C,” *Journal of Physics and Chemical References,* tom Data 7, nr 941, 1978.

[149] L. L. R. B. Arash Eslamdoost, „A pressure jump method for modeling waterjet/hull interaction,” *Ocean Engineering,* pp. 120-130, 10 July 2014.

[150] K. Koushan, „A preliminary design and off-design prediction method for waterjet propulsion systems,” w *International Conference on Waterjet Propulsion,* Amsterdam, 1998.

12 Appendixes

12.1 Appendix I – Cavitation in waterjet propulsor

[61] [117] [87] [118] [119] The propeller efficiency depends on ratio between thrust and torque (which is related directly with power delivered to the rotor shaft). The greater thrust value and the lesser torque the better efficiency – and vice versa. These two values are generated by rotor lift and drag forces respectively. Therefore, in this context, rotor blade can be divided into two main sections: high-pressure area (push side) and low-pressure area (suction side). The proportion between both sides depends on propeller geometry and revolution speed. Moreover, with increasing revolution speed divergence between them rises too. It means that pressure on the suction side falls lower and lower and finally reaches the point where cavitation occurs.

The cavitation phenomenon is a serious threat for high speed and high blade skew [117] propellers especially. The state, in which water evaporates due to low absolute pressure, hampers propulsion efficiency (throttling) and causes mechanical damage to the rotor. It occurs in the areas, where total absolute pressure drops below saturated vapour pressure – the transition point differs depending on a type of fluid and its temperature.

Because of its character, cavitation can be divided into three different types:

— tip cavitation
— sheet / face cavitation
— bubble cavitation
— mixed cavitation

A 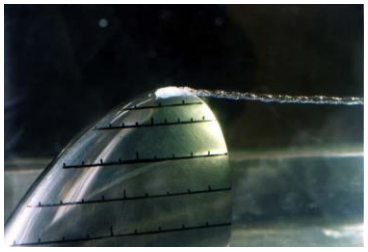 **B** 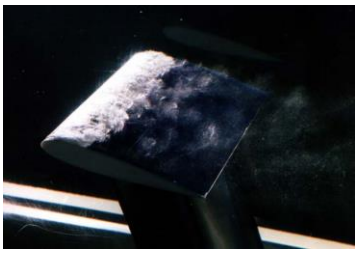 **C** 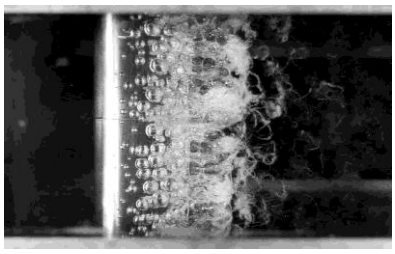

Figure 12.1: Exemplary cavitation visualizations: A – tip [120], B – sheet [121] and C – bubble [122].

The cavitation occurrence probability can be estimated based on cavitation number. The formula describing the coefficient is defined as follows:

$$\sigma_v = \frac{p - p_v}{\frac{1}{2} \cdot \rho \cdot U_\infty^2} \quad [-]$$

12.1

Note: all symbols according to ITTC Standard Symbols (1976).

Where total pressure p is:

$$p = p_{atm} + p_{water} = p_{atm} + \rho g h \quad [Pa]$$

12.2

In other words, cavitation number "is a measure of the tendency of the moving fluid to cavitate. When σ_v is large, cavitation is unlikely; when σ_v is small the likelihood of the cavitation is high." [123] And since the phenomenon itself is related to rotor geometry and load at specific operating conditions, it is possible to use Euler (minimum) pressure coefficient to determine the inception point of cavitation.

$$C_{p\,min} = \frac{p_{min} - p}{\frac{1}{2}\rho U_\infty^2} \quad [-]$$

12.3

Therefore, the nominal value of cavitation number for cavitation inception can be described as:

$$\sigma_{vi} = \left|C_{p\,min}\right| = \frac{p_{atm} + \rho g h - p_v}{\frac{1}{2}\rho U_i^2} \quad [-]$$

12.4

The mean value of $C_{p\min}$ is taken because negative value occurs in 12.3. Moreover, "it has been observed that the pressure within the cavity… is usually a little higher than the vapour pressure" [123] thus, it should be treated as an approximate point for cavitation inception rather than exact one. Therefore, in short it can be written as:

$$\sigma_v < \left|C_{p\,min}\right| \Leftrightarrow p_{min} < p_v \longrightarrow cavitation$$
$$\sigma_v > \left|C_{p\,min}\right| \Leftrightarrow p_{min} > p_v \longrightarrow no\ cavitation$$

12.5

Where $p_{\min}$ refers to minimum pressure value at investigated surface (area).

Notice: it should also be mentioned that cavitation number increases with water depth, hence the cavitation occurrence probability decreases. It is important from the analysed problem point of view.

12.2 Appendix II – Test conditions and measurement equipment

12.2.1 Flow tank

12.2.1.1 General description

In all indoor experiments, the department's flow tank was used. It is closed container with a flow powered by an axial pump. Its measuring area is about 4.7 [m] long and 1 [m] wide and deep, which allowed to investigate the full-size vehicle and avoid scale divergences. What is more, tank dimensions gave the possibility to use the same vehicle's draught during indoors and outdoors tests. Practice also proved that the near wall effect plays no matter for low-velocity measurements and there are no concerns about its reliability.

The maximum flow velocity capable to obtain exceeds 1.5 [m/s], however tens of years of experiments proved results to be valuable for velocities not exceeding one meter per second. Therefore, it was decided to run two velocities: zero and 0.7 [m/s]. The first one was to show each propulsion sheer thrust, the second was enough to demonstrate the thrust drop for moving vehicle.

The tank overall view is presented in the Figure 12.2 below:

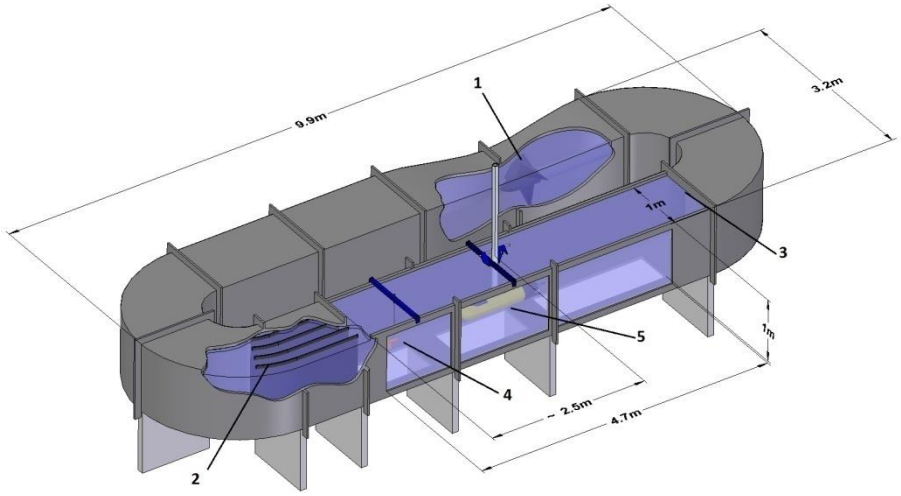

Figure 12.2: The flow tank scheme: 1 – axial pump, 2 – stators, 3 – wave damper, 4 – water velocity meter, 5 – investigated object.

12.2.1.2 Advantages

- isolated environment
- relatively steady flow with minimum disturbances
- high measurements' accuracy
- no weather influence over results
- no time limits

12.2.1.3 Disadvantages

— maximum velocity for reliable measurements up to only 1.5 [m/s]
— fractional but still present tank's walls influence
— limited space inside the tank

12.2.1.4 Measurement scheme:

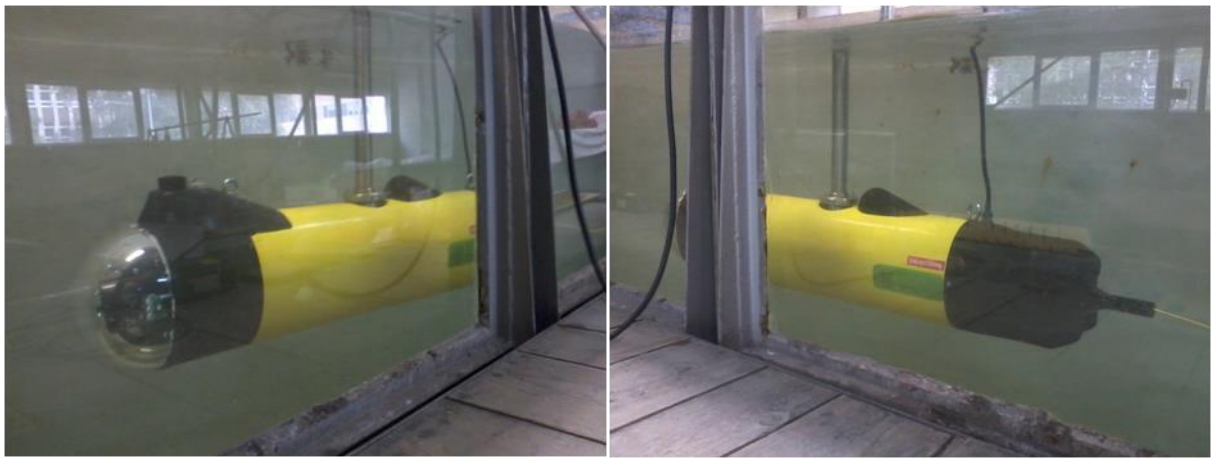

Figure 12.3: ROV during flow tank tests – configuration 4 X WJ49G.

Unless stated otherwise for particular part of the experiment, all tests were carried out according to the same schedule. Each revolution increase was followed by about 60 [s] gap. The time was long enough to stabilise the system and then to take the measurement. Each measurement was taken three times and is an average value of at least 30 [s] period. It was because there were relatively small force values expected. The outcomes steadily oscillated within few percentages, what was regarded as satisfying. The differences depended directly on water flow disturbance left by previous measurements, but it did not affect the final effect at all.

12.2.2 Tests in natural environment

12.2.2.1 General description

The experiments were performed at Jeziorak Lake.

During tests, University's floating research station was used (Figure 12.4). It is a special purpose vessel; a catamaran designed and built to carry out such investigations. It provides maximum measurement velocity of 5 [m/s].

The investigated vehicle was fixed between hulls at a depth of half a meter. I it was approximately the same depth as the one used during flow tank tests.

Despite of many years of catamaran utilization in tests, it was impossible to cover exactly the same range of velocities. Nonetheless, a special care was taken to ensure similar velocities steps as much as it was possible.

Taking into account vehicle's operating point (set at [3.0 m/s]) the outdoor, lake trials provide the best conditions for scheduled measurements in spite of the natural interferences such as water current, wind and boats passing nearby. All these influences may cause serious results errors.

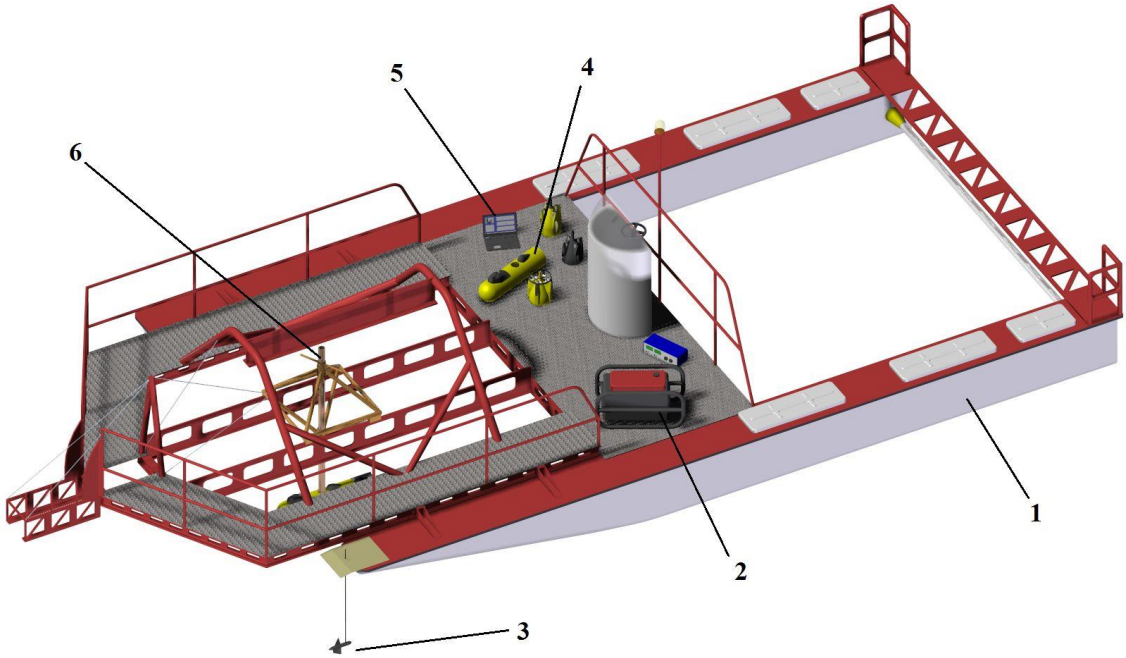

Figure 12.4: The floating research station overall view. 1 – catamaran, 2 – investigated vehicle's power supply, 3 – velocity meter, 4 – investigated vehicle, 5 – control and data gathering station, 6 – vehicle-holder.

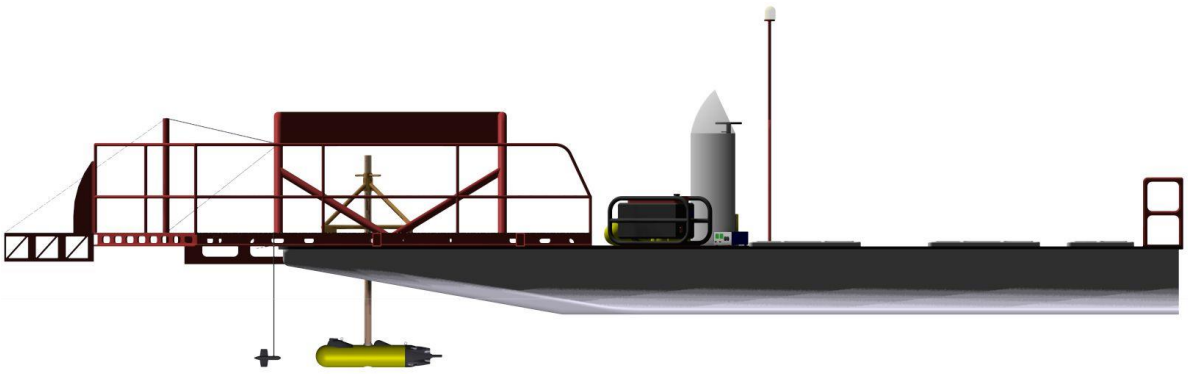

Figure 12.5: The floating research station side view. The transition line between dark and light hull refers to the water table.

12.2.2.2 Advantages

— in relation to the vehicle's size, it may be considered as unlimited space
— the lake surroundings of high banks and dense forests provide some protection against wind

— peculiar shape of the Jeziorak Lake allows up to 4 [km] of straight runs in advantageous conditions

12.2.2.3 Disadvantages

— outdoor tests depend on weather conditions and require calm, windless weather; even light wind generates side drift that influences measurement results
— lake's other users (yachts, motorboats, jet skis etc.)
— logistically demanding because of its remote location
— impossible winter tests
— fluid viscosity depends on its temperature

12.2.2.4 Measurement scheme:

The measurements were based on principle of compensation of the vehicle's drag by means of working propulsors. The measuring catamaran was run at several different velocities. When selected velocity stabilized within 0.1 [m/s], the vehicle's drag was measured. Then, the speed of the propellers or the pump rotors was increased in order to obtain thrust equalization to the vehicle's drag. This state was indicated by zeroing of the force along x-axis measured by the force sensor. During this phase the following parameters were recorded in 30 [s] periods to allow data filtering and averaging:

— forces along axes: *x* (longitudinal), *y* (lateral) and *z* (vertical)
— catamaran speed along axes *x* and *y*
— moments around axes *x*, *y*, and *z*
— current drain from power supply
— supply voltage
— speed of the propellers or pump rotors

Furthermore, looking for every possible convenience it was decided to run both types of propulsors using the same configuration of the vehicle. In practice, it meant changes of aft canopies only, which allowed saving plenty of time. It was executed in two ways:

— the vehicle running with single propeller / waterjet propulsor
— the vehicle running with four propellers / waterjet propulsors

In case of a single propeller, such approach resulted in vast conversion of the existing ROV. In fact, it turned out to be an extreme simplification (see the Figure 12.6). All unnecessary components such as onboard computers, batteries, the warhead, camera etc. were removed. Instead, a simple construction consisting of an electric motor, torque-meter, revolution counter and data-transferring computer was introduced (Figure 12.7). Moreover, so far maximum time for a single run was limited by batteries capacity. This time, however, using an external power supply from onboard generator opened a possibility to perform much longer tests.

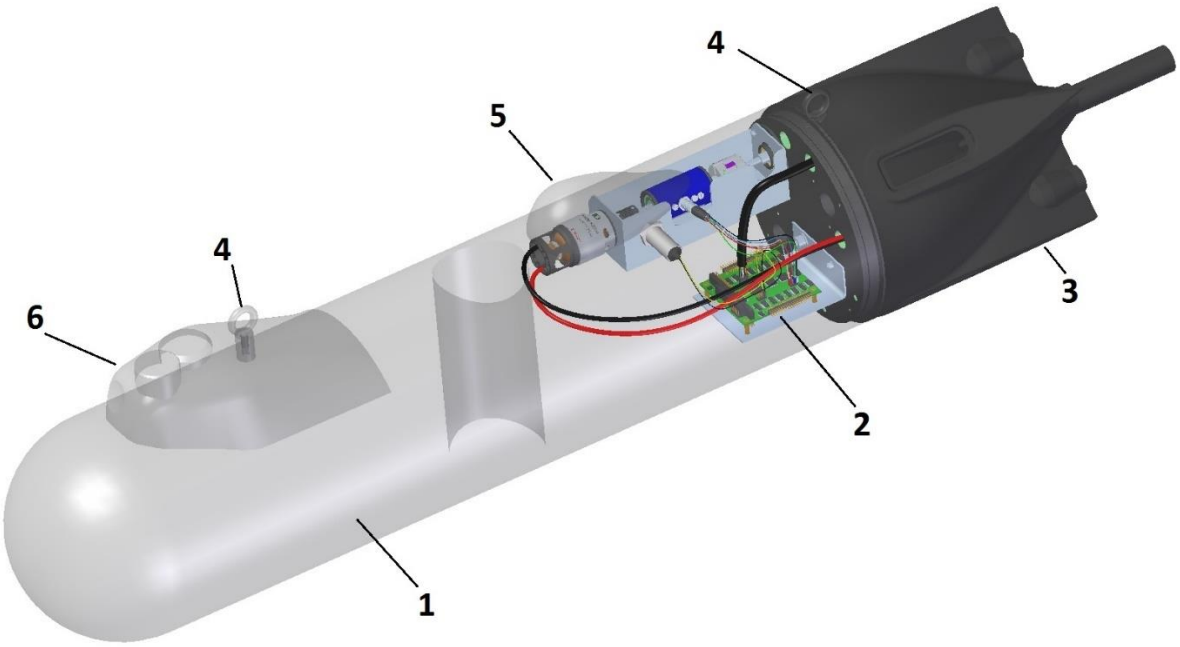

Figure 12.6: ROV converted into test vehicle. 1- hull, 2 – power and measure devices, 3 – aft canopy (waterjet), 4 – handlings, 5 – transponder, 6 – sonar and camera canopy.

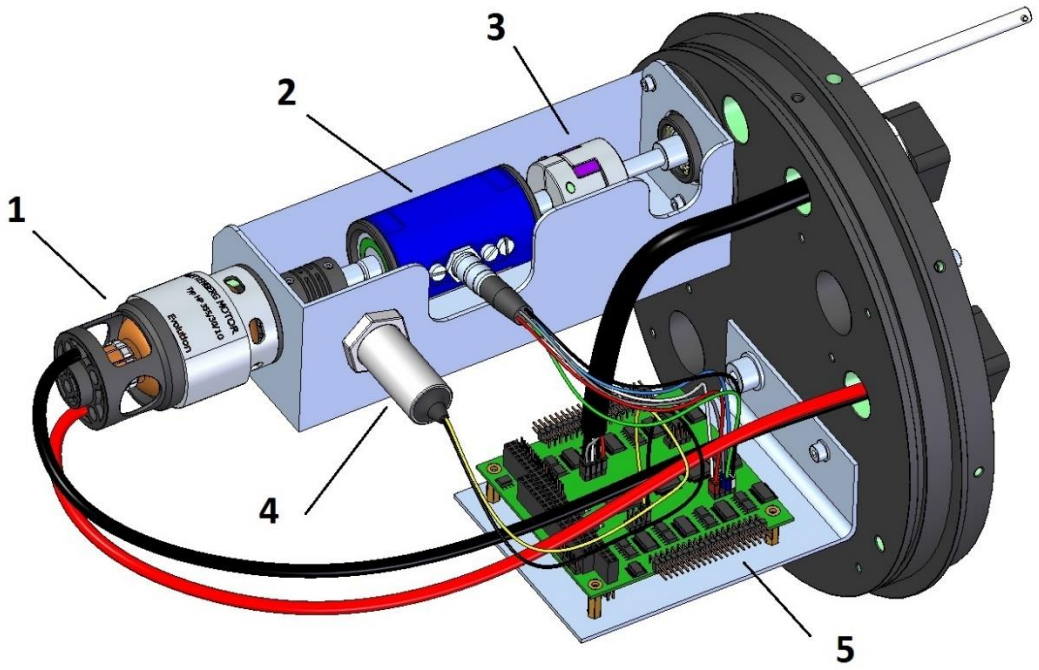

Figure 12.7: The test station interior. 1 – an electric motor, 2 – torque-meter, 3 – coupling, 4 – revolution counter, 5 – computer.

12.2.3 Measurement equipment and software

12.2.3.1 Water temperature meter

During all tests, the water temperature was not measured on regular basis. However, given the time of the year and conditions the experiments were performed in, in both cases the fluid temperature was quite stable and stayed in range of 15÷18 degrees of Celsius. Nonetheless, it has to be remembered, that temperature variation of this magnitude influences water kinematic viscosity. In this case, it differs between $1.0533 \cdot 10^{-6} \div 1.1384 \cdot 10^{-6} \quad \left[\frac{m^2}{s}\right]$ [124], which gives just over 8% variation.

Water viscosity change influences Reynolds Number and variations correspond to percentages fluctuations.

$$R_e = \frac{v \cdot L}{\nu} \quad [-]$$

12.6

Fortunately, temperature, Reynolds Number and water kinematic viscosity fluctuations have marginal influence on waterjet propulsor performance, as they change friction coefficient values in a very little way.

$$\lambda = 0.072 + 0.6104 \cdot R_e^{-0.35} \quad [-]$$

12.7

Table 12.1: Friction coefficient for extreme values of water temperature the tests were run in.

no.	parameter	symbol	unit		
1	water temperature	T	[deg C]	18	15
2	vehicle's velocity	v	[m/s]	3.00	3.00
3	vehicle's length	L	[m]	1.55	1.55
4	water kinematic viscosity	ν	[m^2/s]	1.0533E-06	1.1384E-06
5	Reynolds Number	Re	[-]	4414697	4084680
6	friction coefficient	λ	[-]	0.074883362	0.074962847
7	difference	Δλ	[-]	-0.11%	

12.2.3.2 Force sensor

The researches were based on vehicle's drag compensation. Therefore, for drag / thrust forces measurements, two types of *AMTI* multi-axis force sensors were used:

— AMTI MC3A-1000 for small forces
— AMTI UDW3-1000 for large forces (waterproof meter)

The relative accuracy for both sensors is $\pm 0.2\%$.

A **B**

Figure 12.8: The force sensors used during the experiments. *AMTI* model MC3A-1000 (A) and model UDW3-1000 (B). [125]

12.2.3.3 Water velocity meters

The Ott velocity meter

The water velocity was measured in two ways. In all the cases, the Ott type mechanical velocity meter model C31 equipped with propeller no.1-23969 was the basic sensor. It allows measuring velocities up to 7.0 [m/s] with declared accuracy $\pm 0.7\%$. Many years of usage proved its value in considered measurement conditions. Nonetheless, the device is regularly calibrated and certificated by Ship Hydrodynamics Division of Ship Design and Research Centre in Gdańsk.

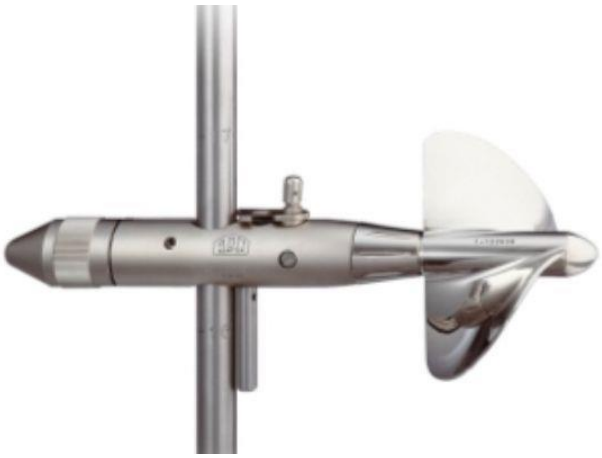

Figure 12.9: Ott velocity meter used in propulsion tests. [126]

Doppler velocity meter for the catamaran velocity measurements

The Teledyne RD Instruments DVL Explorer was used to measure vehicle's velocity with reference to the lake bottom during outdoor tests. It was decided to do so, because of constant natural environment interferences, and relatively low force values expected to be measured. It is valuable supplement to the Ott velocity meter.

— maximum depth / altitude: 75 [m]

— minimum depth / altitude: 0.5 [m]
— velocity range: ± 5.0 [m/s]
— long term accuracy: ± 0.4% = ± 0.2 [cm/s]
— precision: ± 1.2 [cm/s] at velocity 1.0 [m/s]
— resolution: 0.1 [cm/s]
— ping rate: 7 [Hz]

Figure 12.10: Transducer of the Teledyne RD Instruments Doppler Velocity Log used during lake tests. [127]

Doppler velocity meter for the local water velocity measurements

The Acoustic Doppler Velocimeter (ADV) was used to measure the water flow velocity in the flow tank. The *SonTek Inc.* ADV is a three-axis sensor the manner of which is shown in the Figure 12.11. The sensor is capable of taking the measurement in arbitrary point set in the fluid volume.

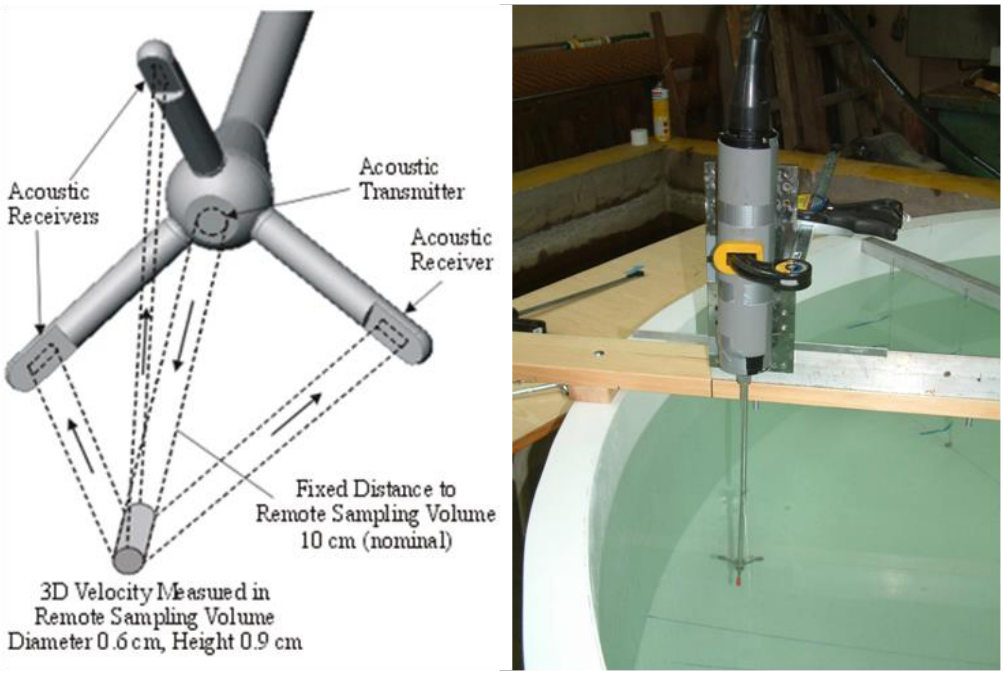

Figure 12.11: The *SonTek Inc*. ADV sensor - the principle of operation and the measurement volume. [128] The sensor installed in the tank model.

According to the manufacturer, the distance from the sensor to the sampled volume is 100 [mm]. The velocity measurement resolution is 0.1 [mm/s] with declared accuracy of ±1% for measured velocity (up to 2.5 [mm/s]). The internal temperature sensor accuracy, used for compensation, is 0.1 degree of Celsius and the maximum operational depth is 60 [m].

12.2.3.4 Electrical sensors in the vehicle

All the electrical parameters, as well as rotational speed of the propellers or rotors, were measured by the sensors normally utilized by the control system of the vehicle.

The intensity of the current used to supply the propulsors was measured in two ways: individually for each motor and for the whole vehicle.

Current meters are built using the current sensor ACS775 manufactured by *Allegro MicroSystems Inc*. It offers accuracy of the 14-bit, that corresponds to 0.005 [A] or 0.05% of the full scale.

Voltage meter

The measurement accuracy is 0.3 [mV] (0.05%).

Motor speed meter

The motor revolutions were measured by the motor controller. The accuracy was ±10 [rpm] (0.2%), at range up to 6000 [rpm].

12.2.3.5 Motor calibration facility

The motor calibration facility, composed of motor and motor power supply, was used to measure of all the necessary parameters of the drive system. It allowed to determine drive system's detailed characteristics. Such approach gives a possibility for indirect evaluation of propeller / pump rotor: torque demand, rotational speed, voltage supply, current consumption.

The main parameters of the calibration facility are as follows:

— voltage meter range: up to 30 [V], accuracy 1%
— current meter range: up to 10 [A], accuracy 1%
— torque meter range: 2.5÷500 [Nm], accuracy ±0.1%
— motor speed range: up to 5000 [rpm], accuracy 20 [rpm]

The torque was measured by *Megatron* meter DFM22-2.5.

The motor speed was measured by means of the *Telemecanique* RPM-meter model *XS1NO8PA349* for a vehicle running with single propeller / waterjet propulsor. This was a proximity sensor with operating range up to 5000 [rpm] and measurement error of 20 [rpm] (0.4% of the top speed)

The picture below presents overall view as well as the main components of the facility.

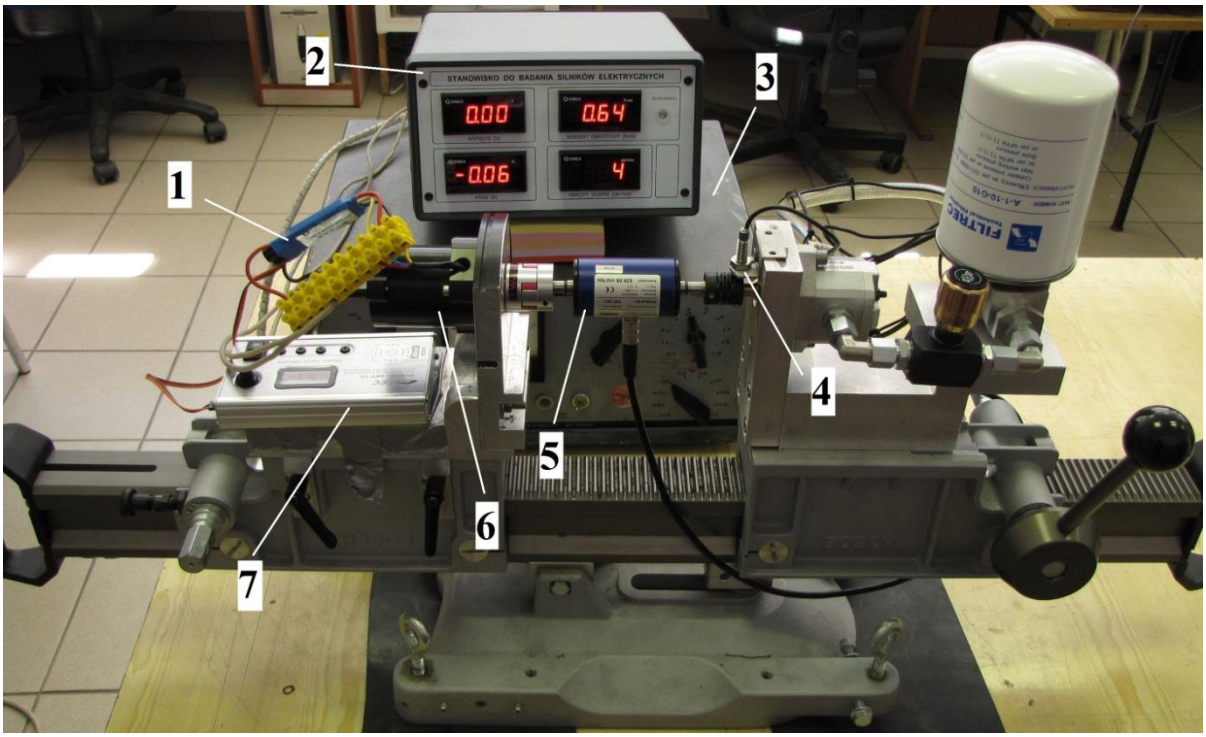

Figure 12.12: Overall view of the motor calibration facility. The numbers in the picture refer to 1 – motor controller, 2 – measuring device (current, voltage, speed, torque), 3 – power supply, 4 – revolution counter, 5 – torque meter, 6 – investigated motor, 7 – speed controller.

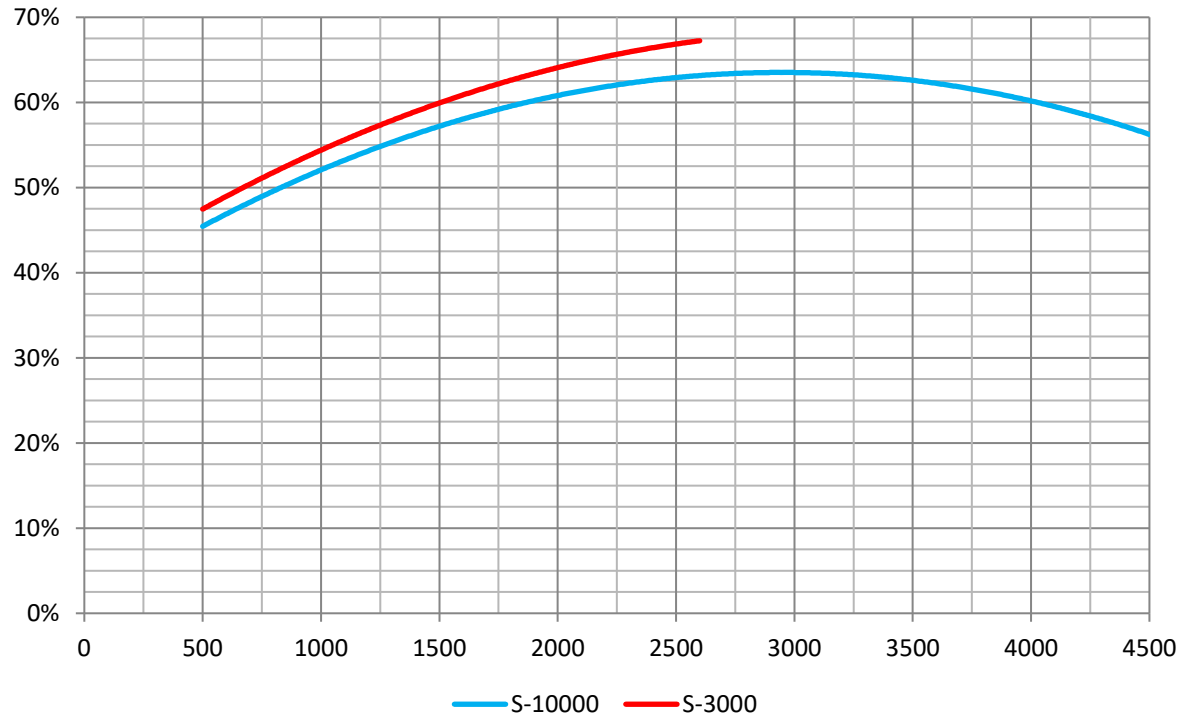

Figure 12.13: Efficiency curves of the drive systems composed of electric motors and power supply units used during tests. Results include BLDC motor controller efficiency (standard range 85-90%).

12.3 Appendix III – Results of the tests of the investigated propulsion systems – LAKE EXPERIMENTS

12.3.1 The propulsion system composed of four 100 [mm] diameter propellers

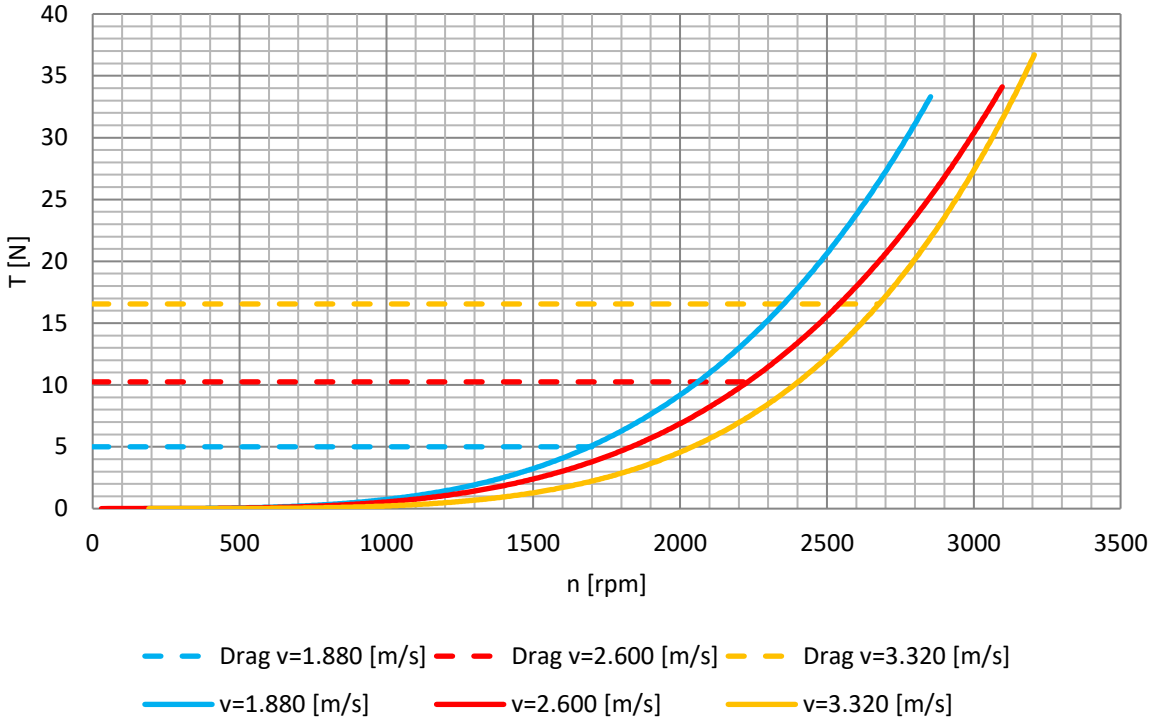

Figure 12.14: SP – Standard, bare propeller thrust curves for a single propeller.

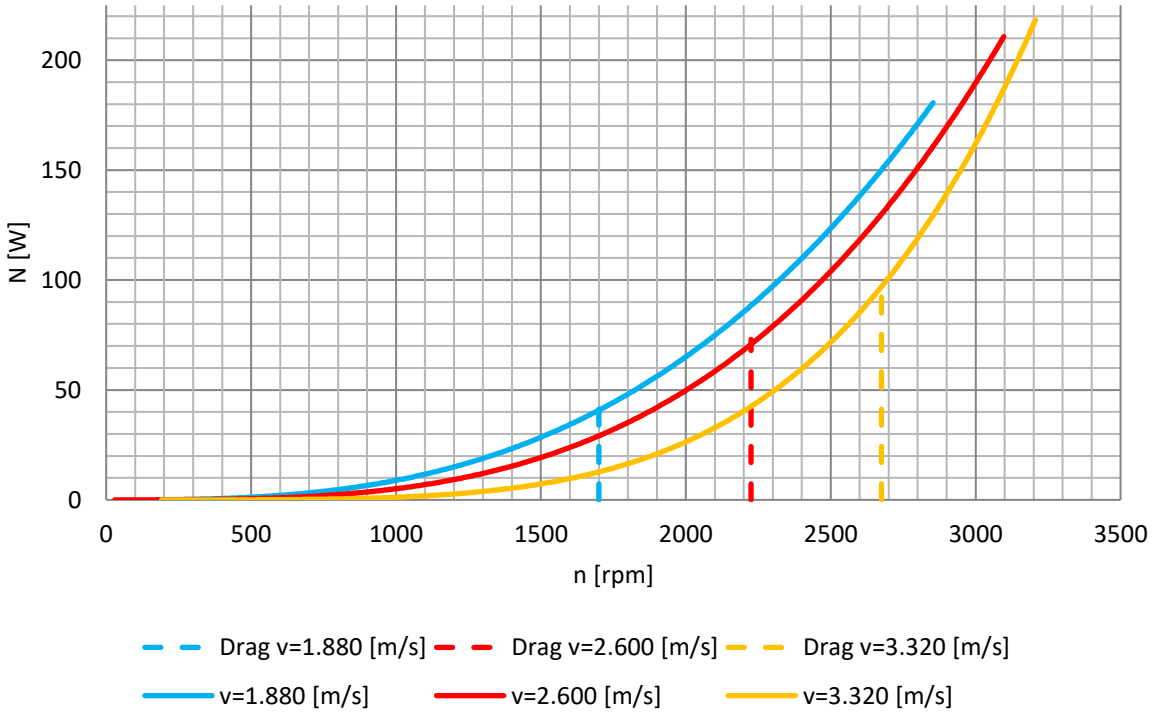

Figure 12.15: SP – Standard, bare propeller power curves for a single propeller.

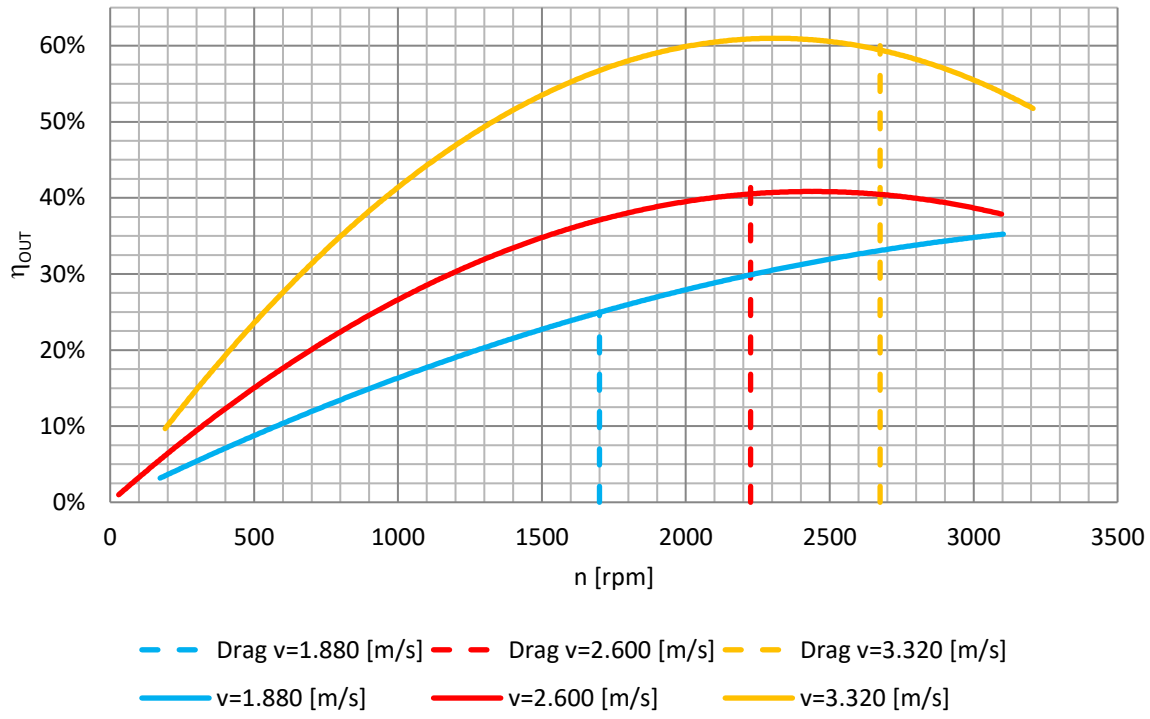

Figure 12.16: SP – Standard, bare propeller performance curves for a single propeller.

12.3.2 The propulsion system composed of a single G29 waterjet propulsor

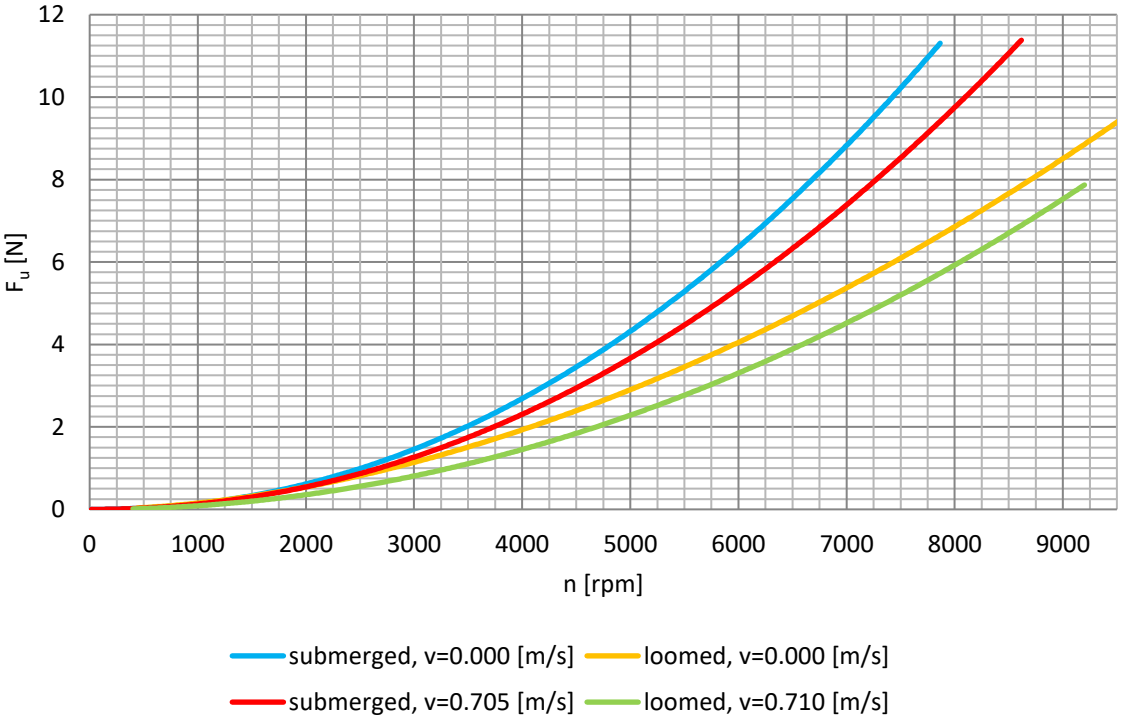

Figure 12.17: Comparison of the thrust curves of the G29 (29 [mm]) waterjet propulsor with air and water discharge for a single propeller.

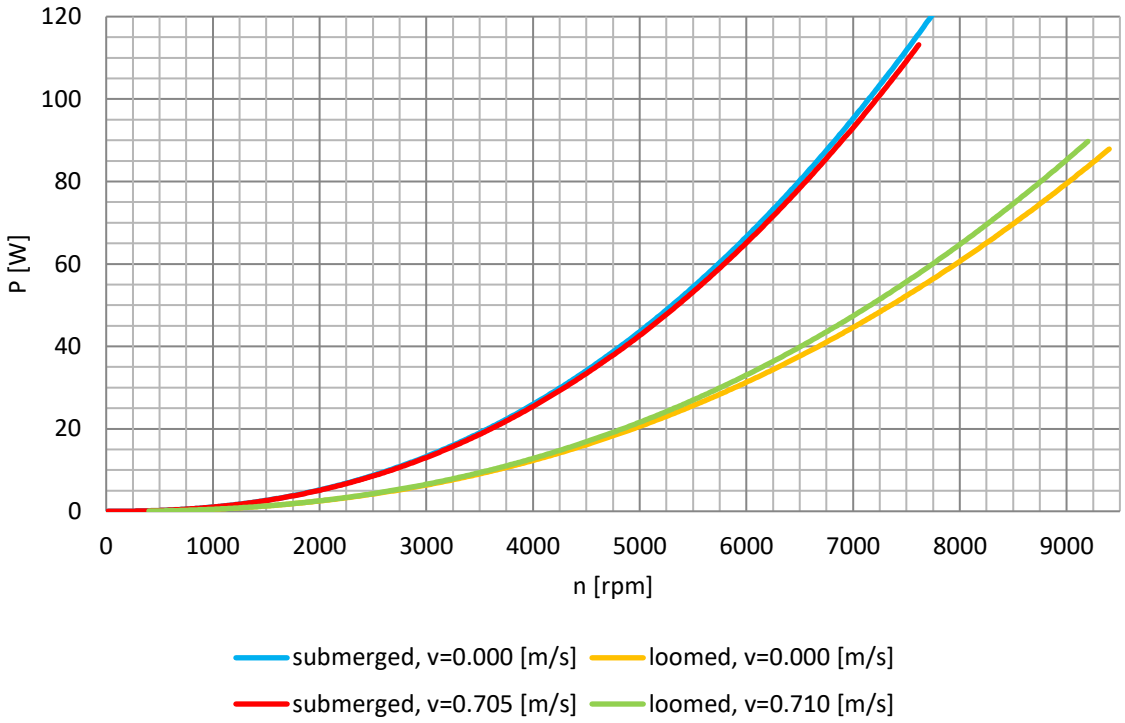

Figure 12.18: Comparison of the power curves of the G29 (29 [mm]) waterjet propulsor with air and water discharge for a single propeller.

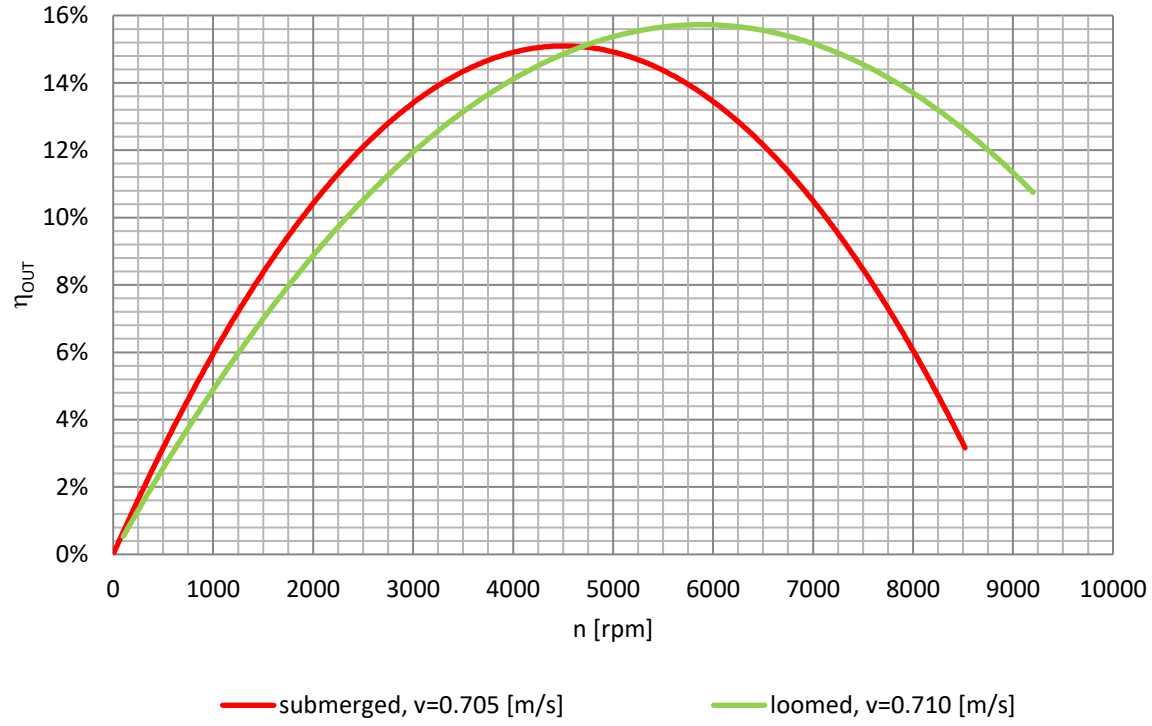

Figure 12.19 Comparison of the efficiency curves of the G29 (29 [mm]) waterjet propulsor with air and water discharge for a single propeller.

12.3.3 The propulsion system composed of four G39 waterjet propulsors

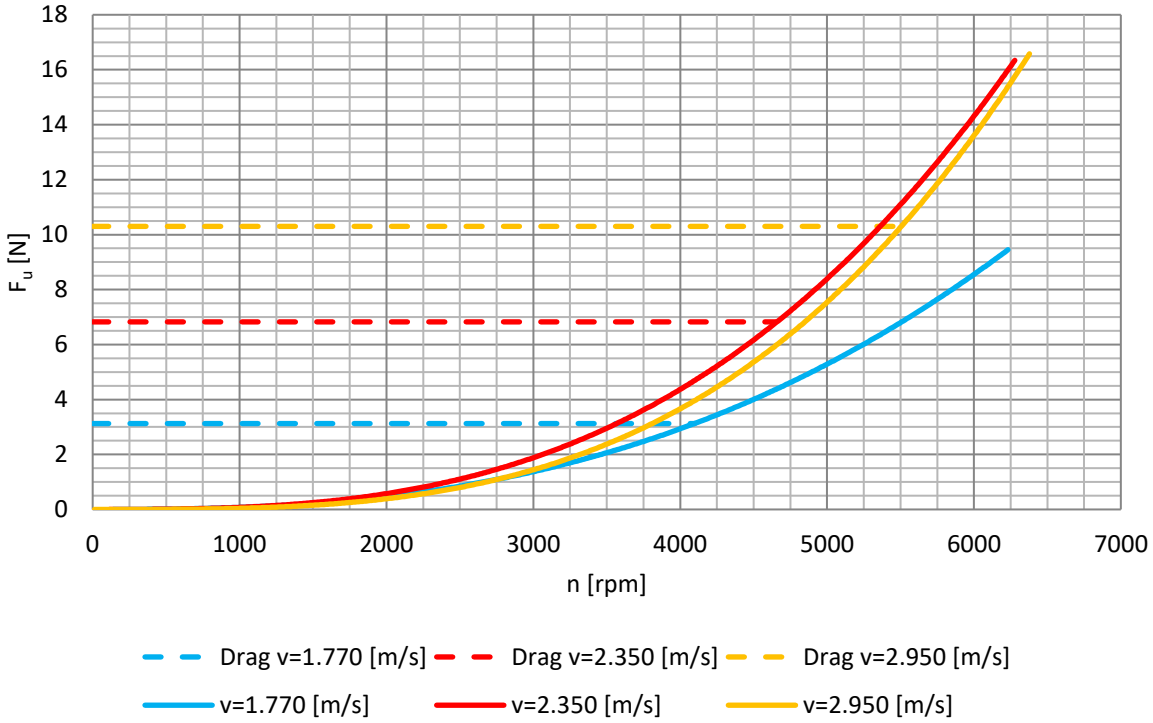

Figure 12.20: WJ39G – Graupner waterjet drive 39 [mm] thrust curves for a single propeller.

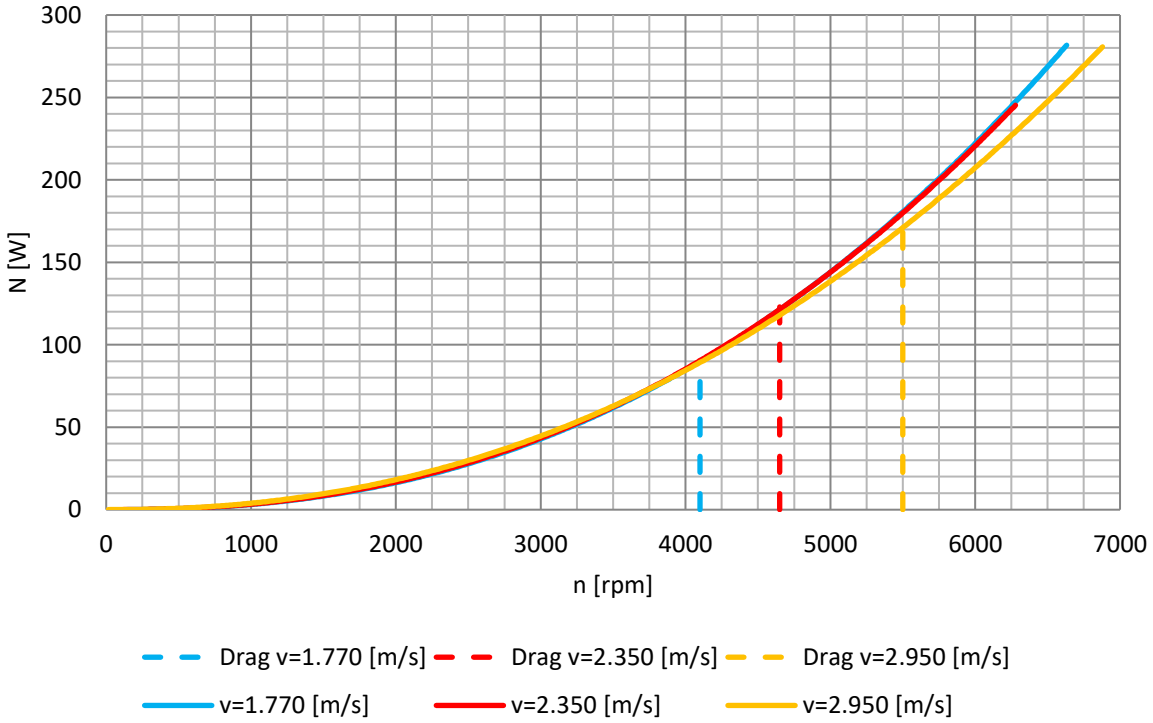

Figure 12.21: WJ39G – Graupner waterjet drive 39 [mm] power curves for a single propeller.

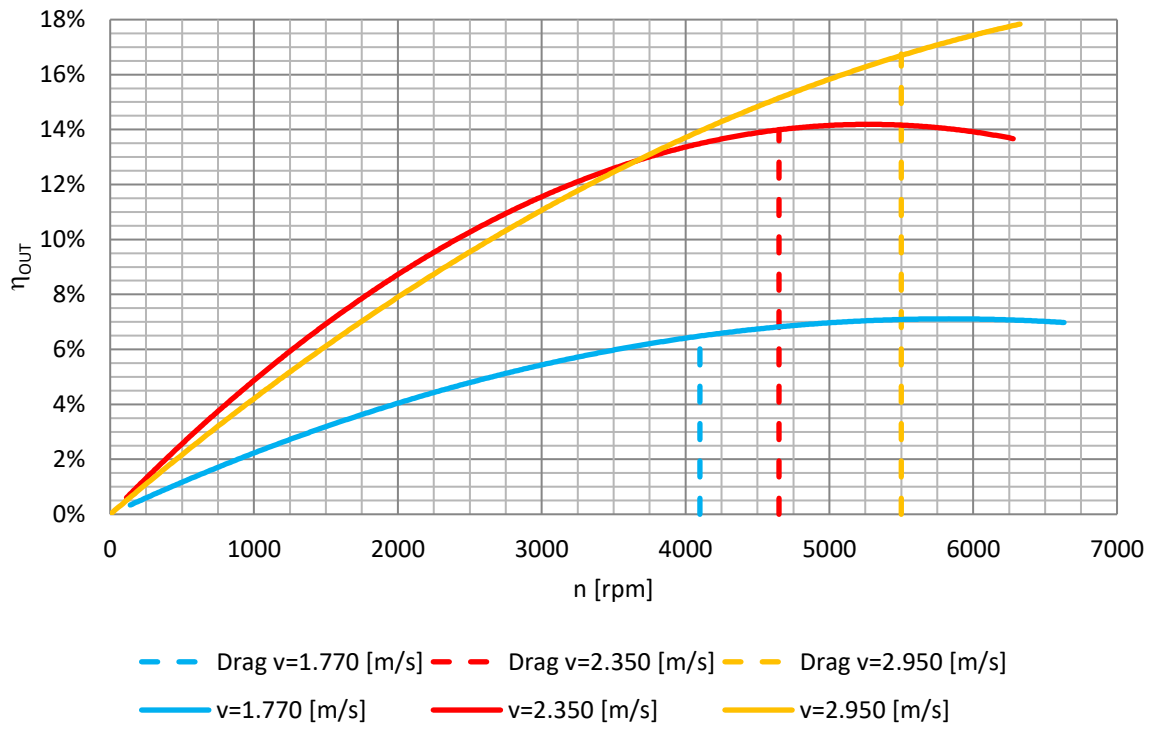

Figure 12.22: WJ39G – Graupner waterjet drive 39 [mm] performance curves for a single propeller.

12.3.4 The propulsion system composed of four G49 waterjet propulsors

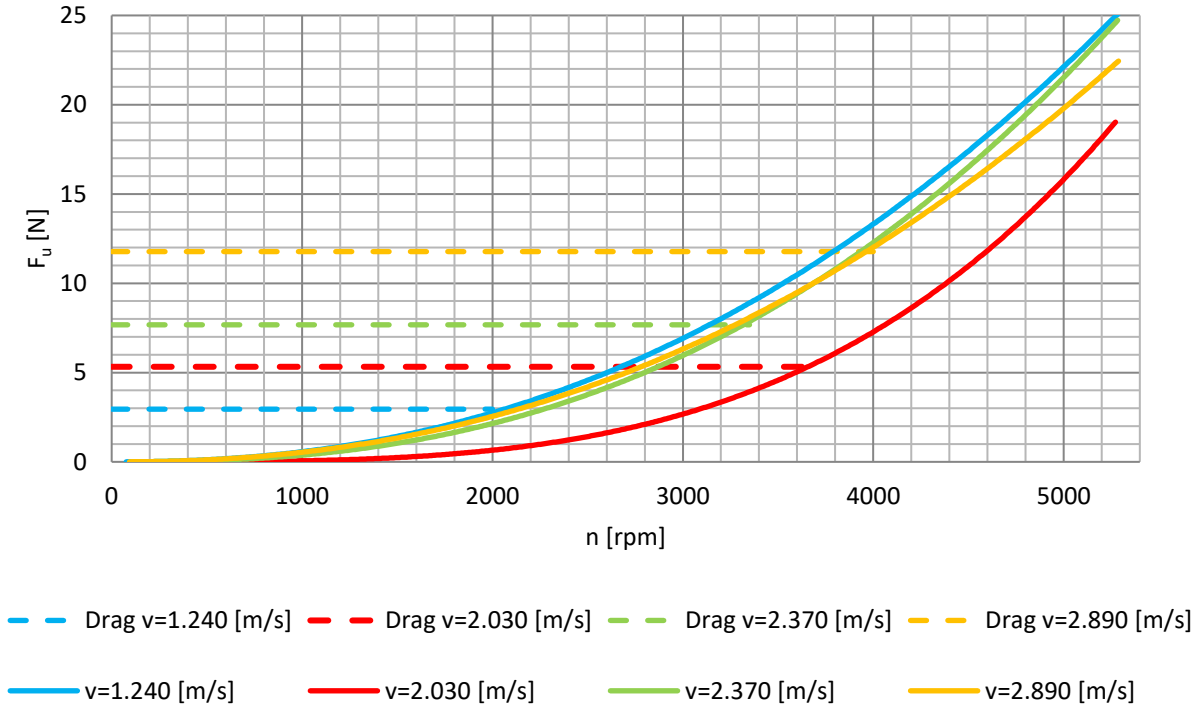

Figure 12.23: WJ49G – Graupner waterjet drive 49 [mm] thrust curves for a single propeller.

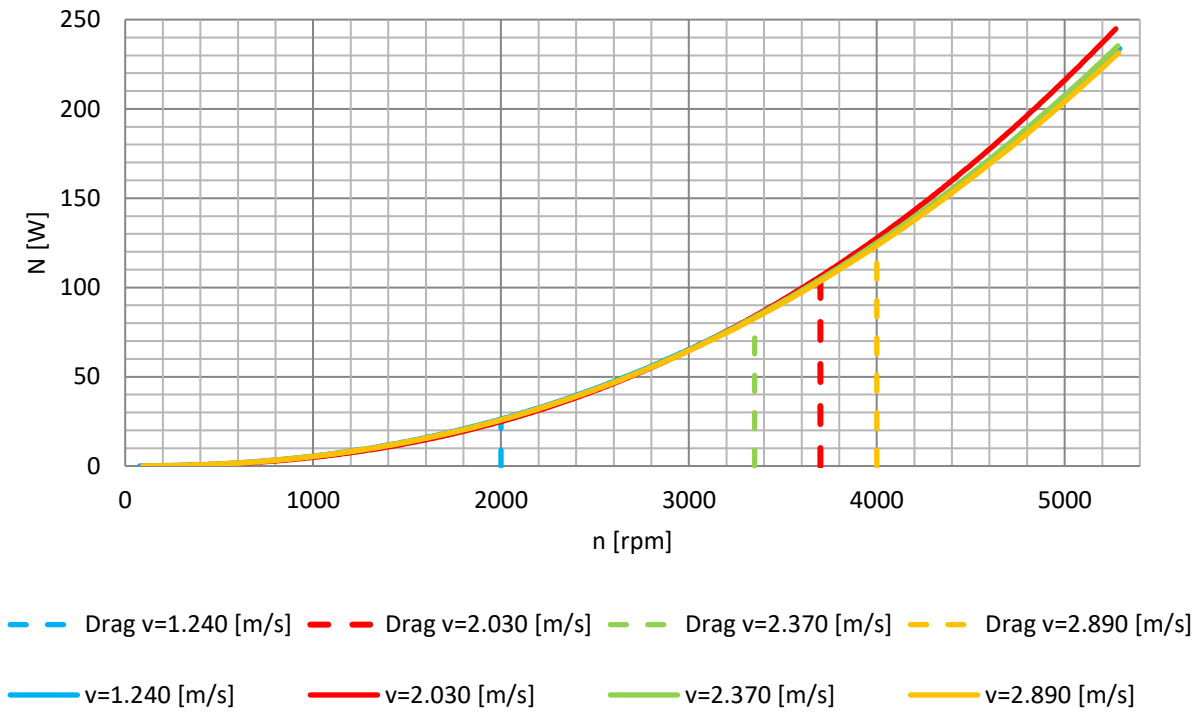

Figure 12.24: WJ49G – Graupner waterjet drive 49 [mm] power curves for a single propeller.

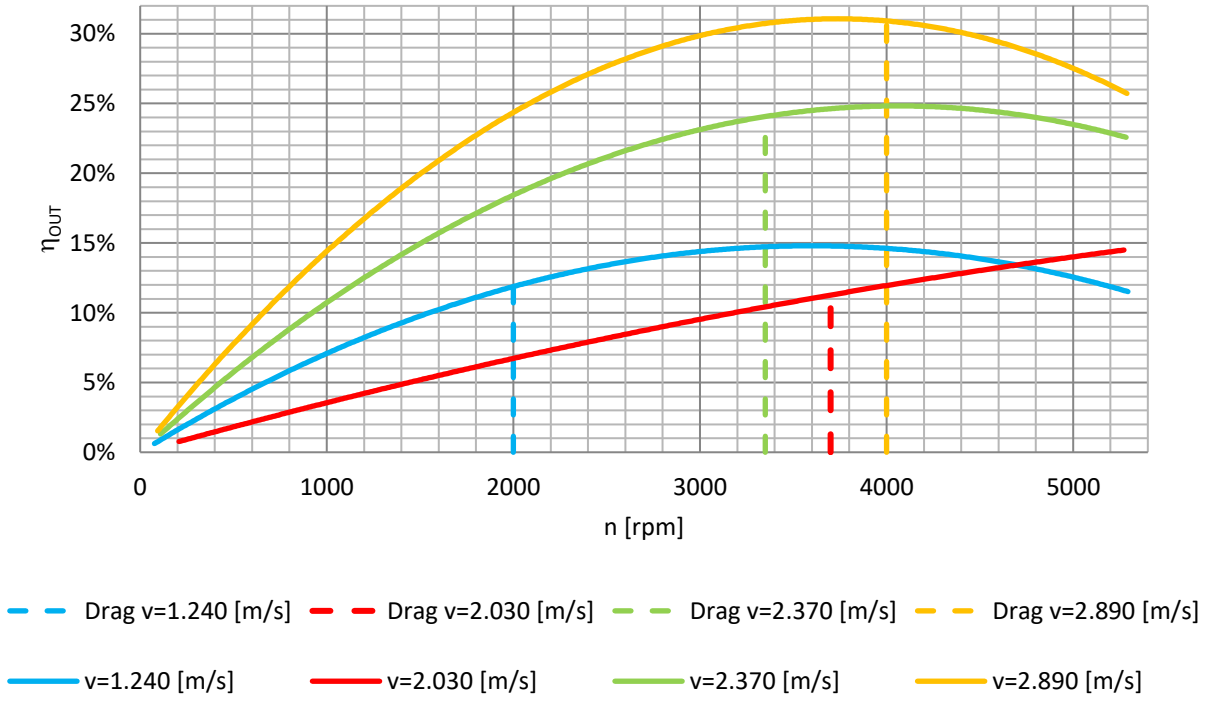

Figure 12.25: WJ49G – Graupner waterjet drive 49 [mm] performance curves for a single propeller.

12.3.5 The propulsion system composed of four WJ50 waterjet propulsors

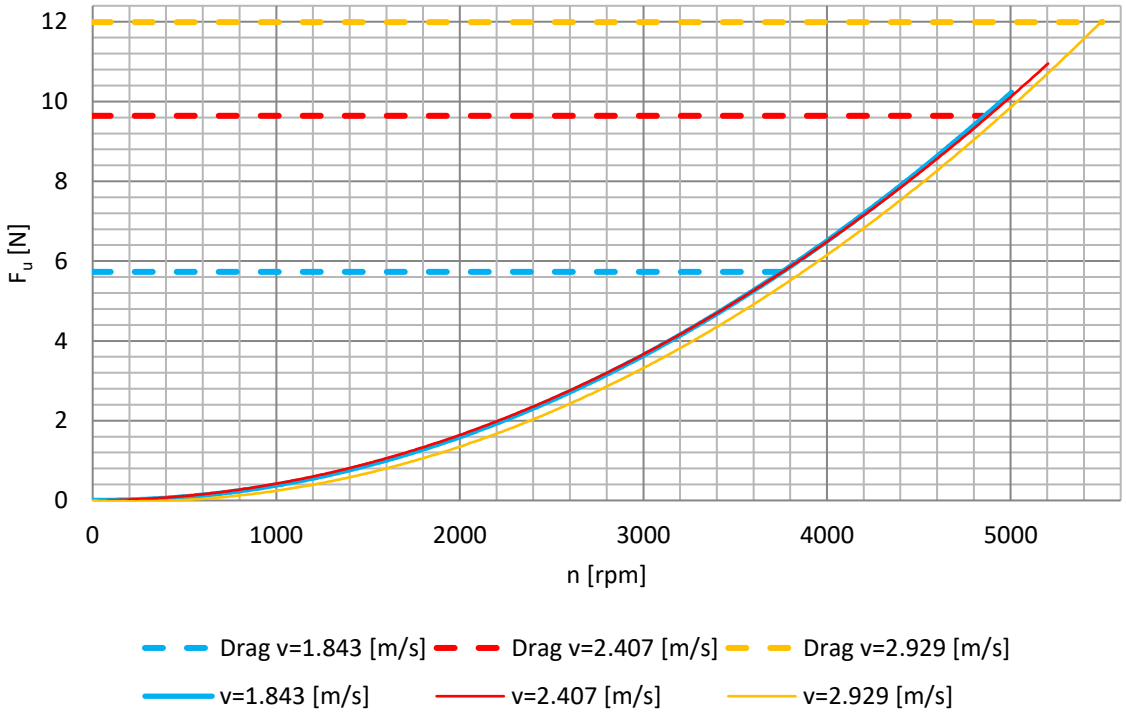

Figure 12.26: WJ50 thrust curves for a single propeller.

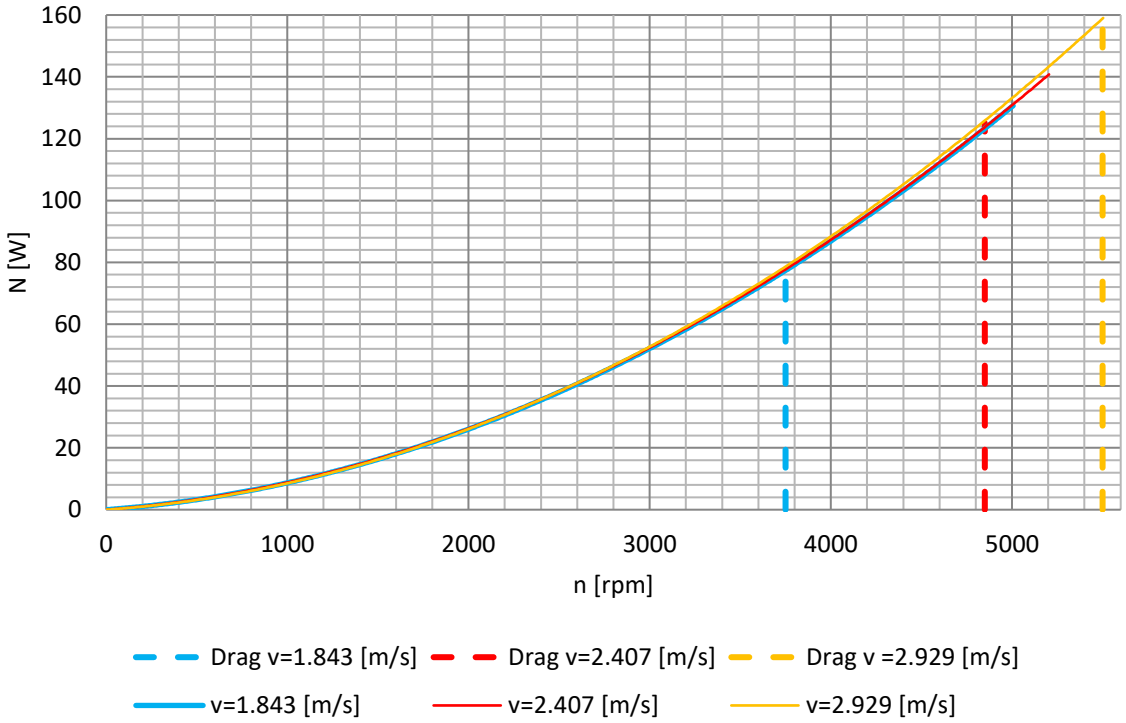

Figure 12.27: WJ50 power curves for a single propeller.

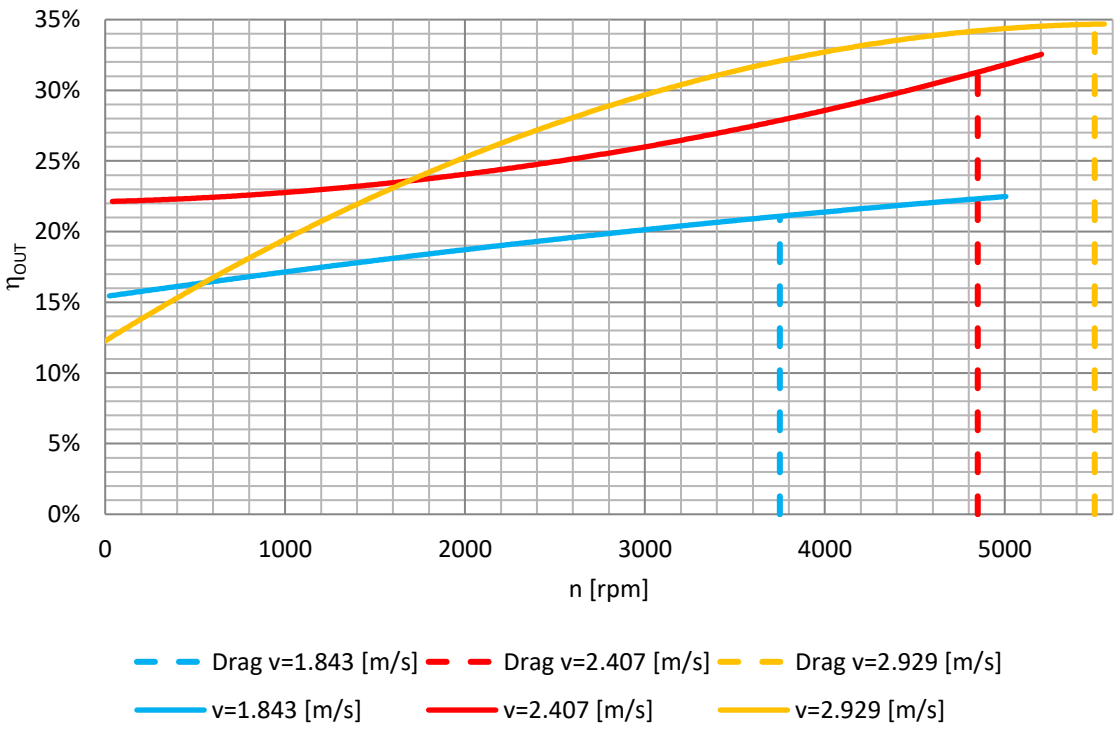

Figure 12.28: WJ50 performance curves for a single propeller.

12.4 Appendix IV – Results of the experiments with real models of the Gluptak vehicle in the FLOW TANK

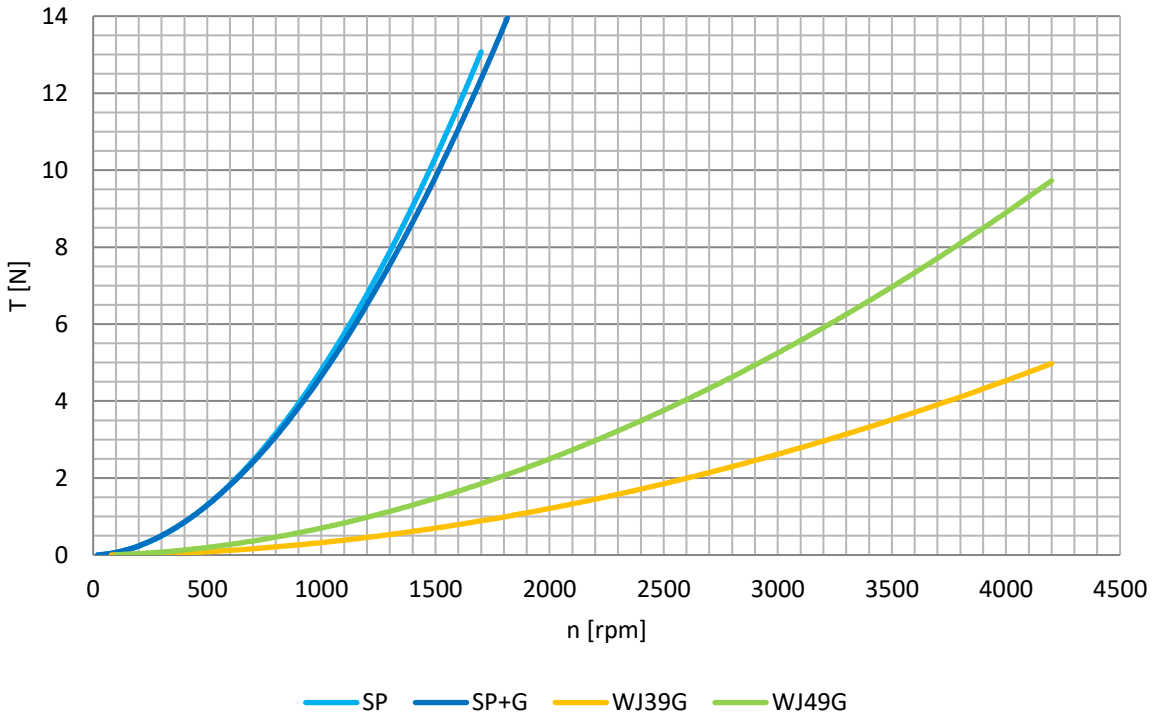

Figure 12.29: Thrust curves for analysed propulsions at 0.000 [m/s] – flow tank experiments for a single propeller.

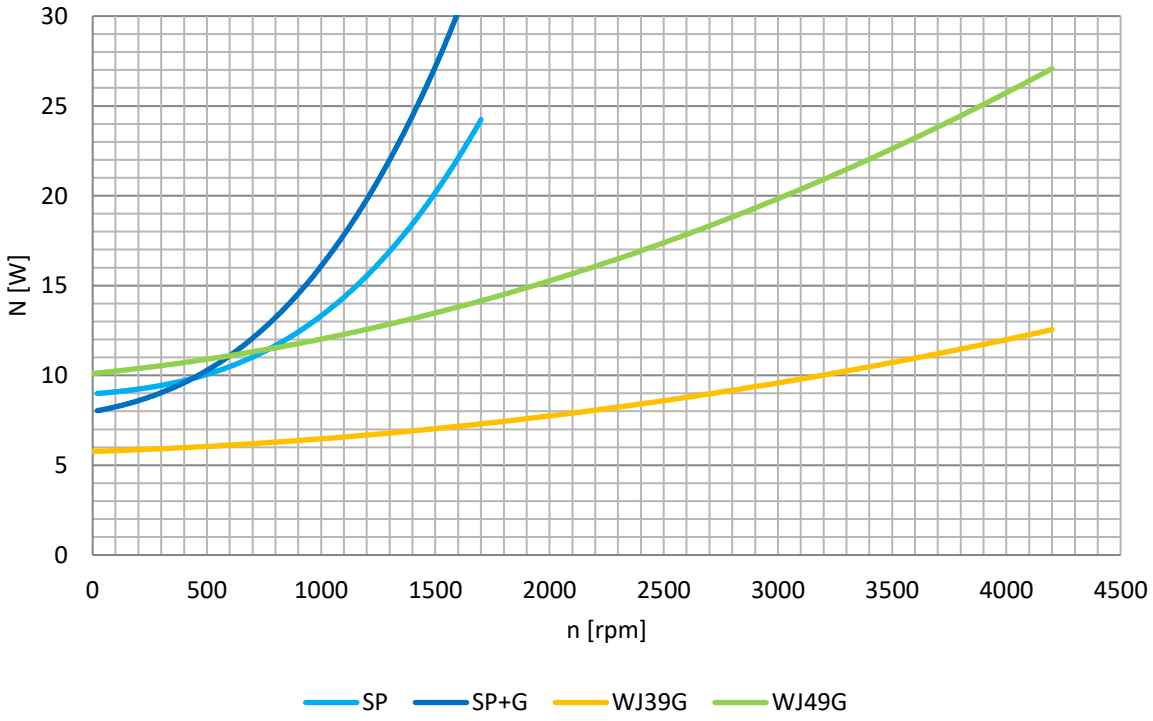

Figure 12.30: Power consumption curves for analysed propulsions at 0.000 [m/s] – flow tank experiments for a single propeller.

Note: *Drag SP* notation (and successive) refer to vehicle's drag at flow tank investigations operating point set for 0.700 [m/s].

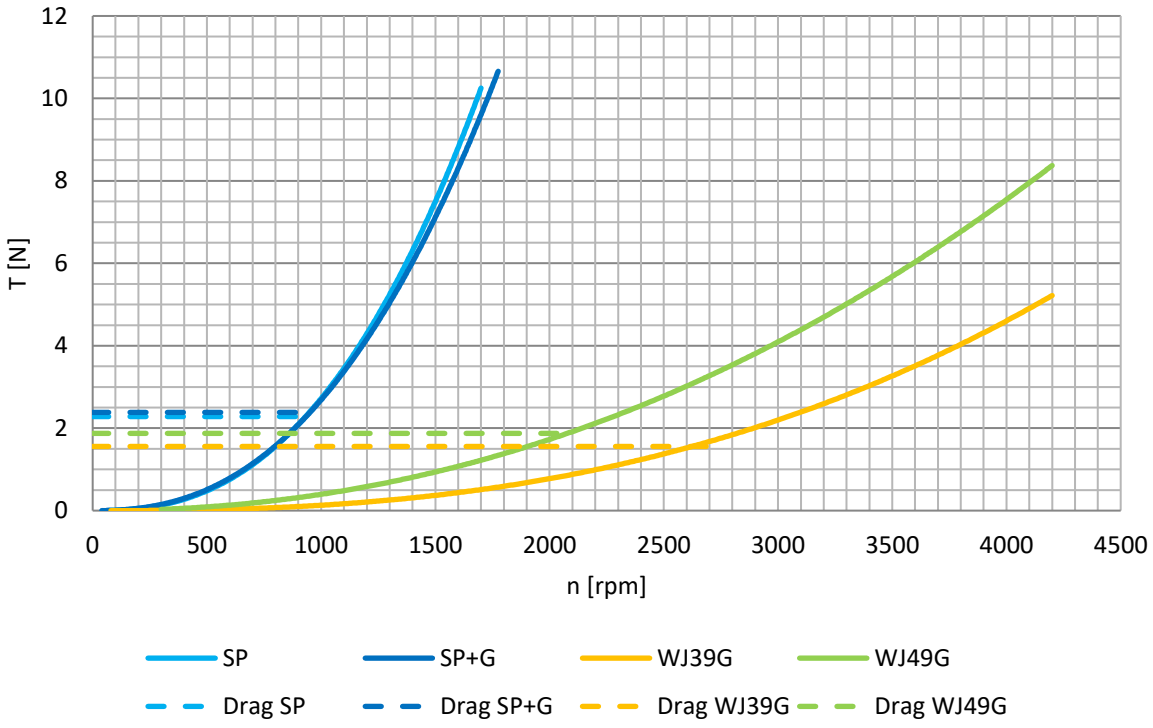

Figure 12.31: Thrust curves for analysed propulsions at 0.700 [m/s] – flow tank experiments for a single propeller.

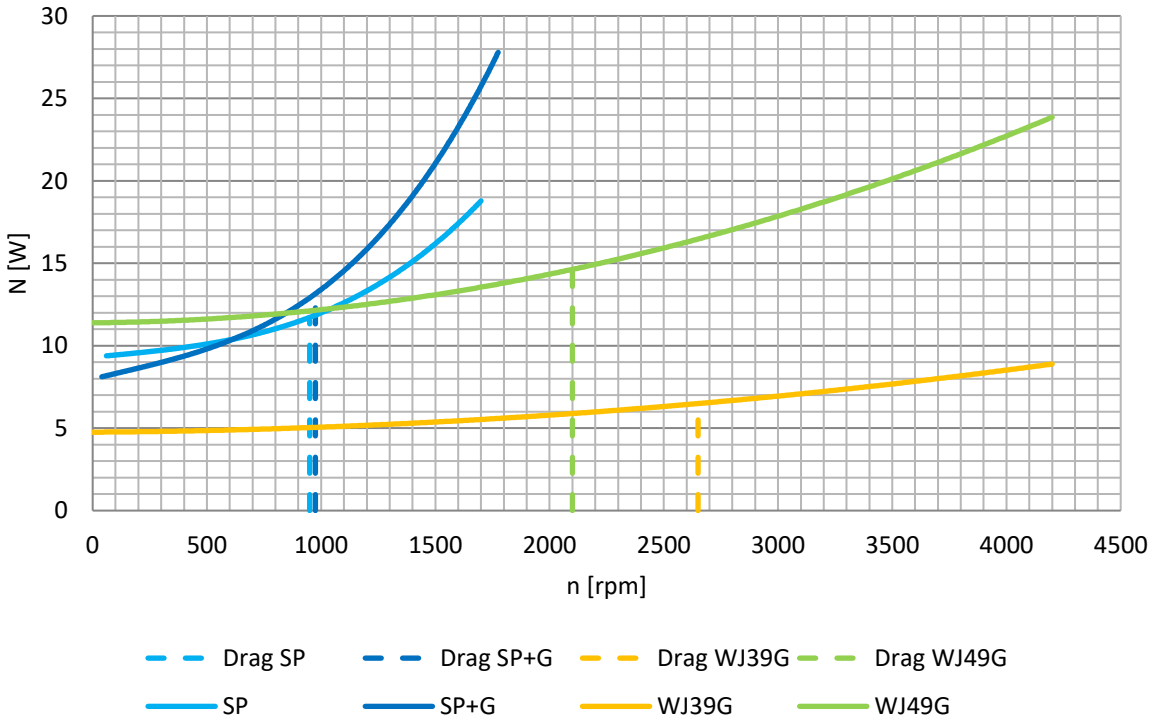

Figure 12.32: Power consumption curves for analysed propulsions at 0.700 [m/s] – flow tank experiments for a single propeller.

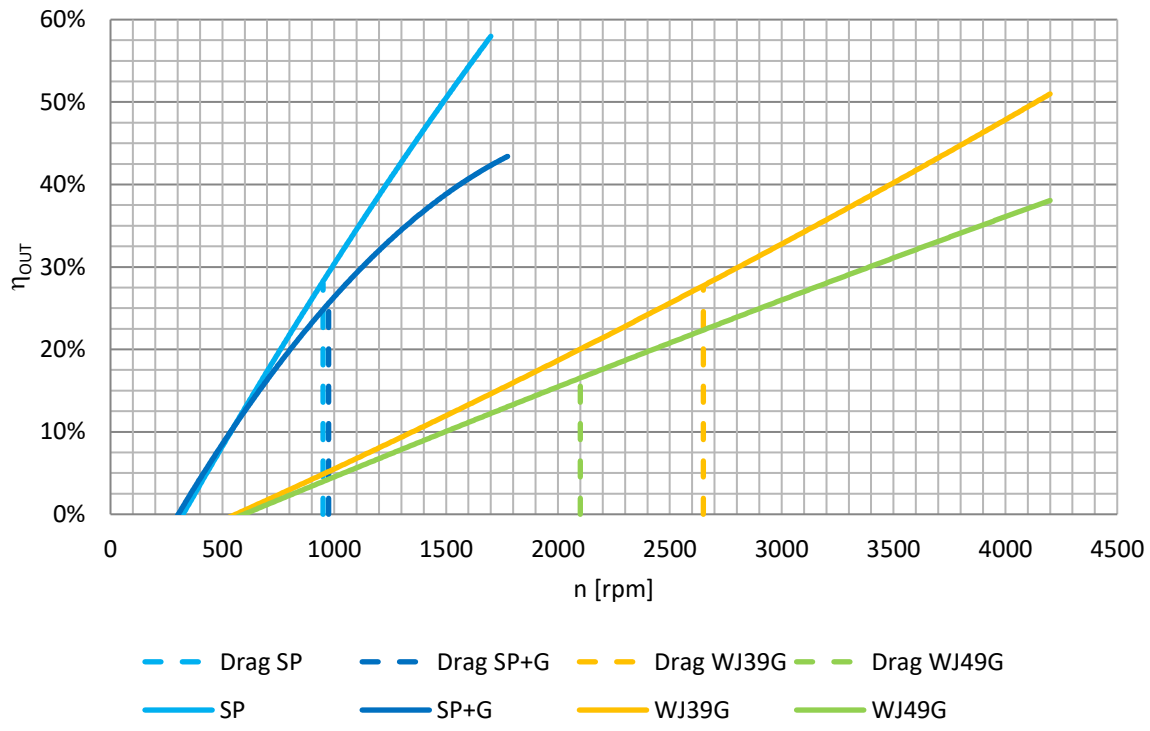

Figure 12.33: Efficiency curves for analysed propulsions at 0.700 [m/s] – flow tank experiments for a single propeller.

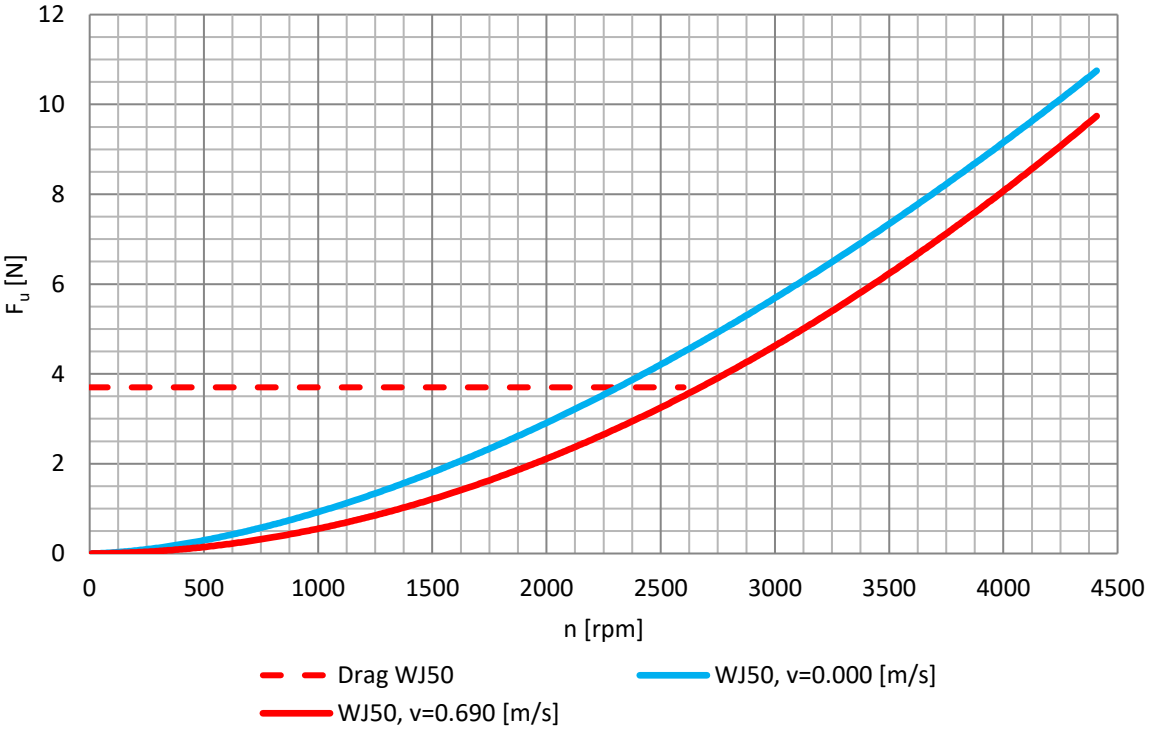

Figure 12.34: Thrust curves for WJ50 propulsion – flow tank experiments for a single propeller.

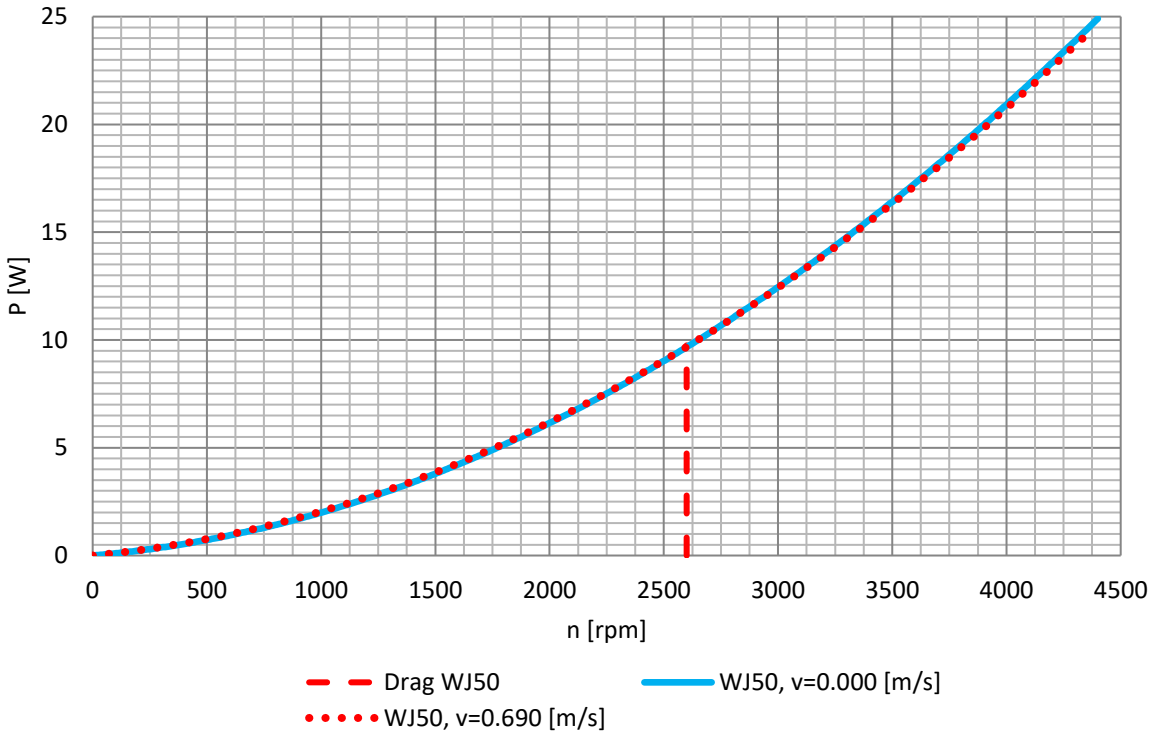

Figure 12.35: Power consumption curves for WJ50 propulsion – flow tank experiments for a single propeller.

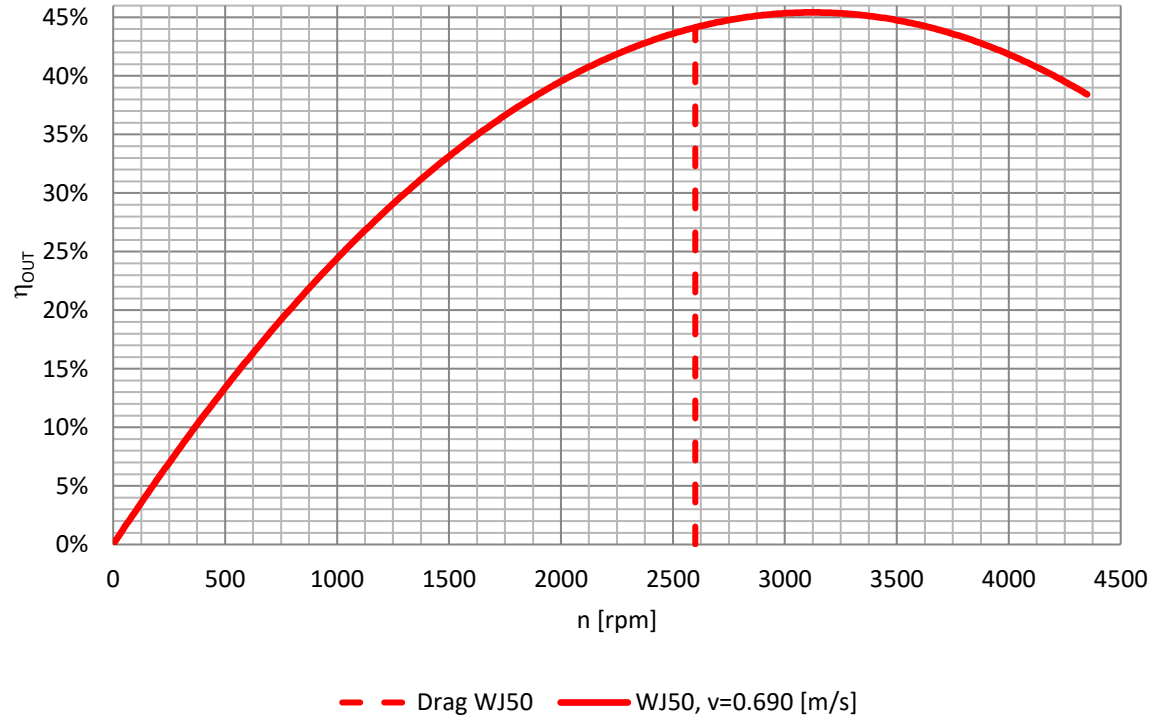

Figure 12.36: Efficiency curve for WJ50 propulsion at 0.690 [m/s] – flow tank experiments for a single propeller.

12.5 Appendix V – Coefficients

The variables with index $_{MAX}$ refer to maximum values measured.

Table 12.2: Coefficients of propeller's excellence for flow tank experiments at zero speed.

no.	drive	S_{PROP}	Thrust	$Thrust_{MAX}$	n	n_{MAX}	N_d	N_{dMAX}	ζ_{P0}	ζ_{P0MAX}
1	*SP*	0.00785	10.13	12.80	1500	1700	20.2	24.2	0.0054	0.0064
2	*SP+G*	0.00785	9.96	12.89	1500	1740	27.3	34.9	0.0039	0.0045
3	*WJ39G*	0.00119	0.76	4.74	1500	4200	7.2	12.6	0.0008	0.0070
4	*WJ49G*	0.00189	1.66	9.18	1580	4200	13.8	27.2	0.0011	0.0070
5	*WJ50*	0.00196	1.70	10.24	1500	4200	3.9	23.2	0.0038	0.0095

Table 12.3: Coefficients of propeller's excellence for flow tank experiments at speed 0.700 [m/s].

no.	drive	S_{PROP}	Thrust	$Thrust_{MAX}$	n	n_{MAX}	N_d	N_{dMAX}	ζ_{P0}	ζ_{P0MAX}
1	*SP*	0.00785	7.47	9.57	1500	1700	16.3	18.7	0.0042	0.0053
2	*SP+G*	0.00785	7.23	9.38	1500	1740	21.0	25.8	0.0031	0.0037
3	*WJ39G*	0.00119	0.49	3.89	1500	4200	5.4	9.0	0.0006	0.0074
4	*WJ49G*	0.00189	1.09	7.60	1580	4200	13.2	24.0	0.0006	0.0060
5	*WJ50*	0.00196	1.14	8.91	1500	4200	3.9	23.1	0.0021	0.0077

Table 12.4: Von Karman's coefficients (yield coefficients) for flow tank experiments at zero speed.

no.	drive	S_{PROP}	Thrust	$Thrust_{MAX}$	n	n_{MAX}	C_k	C_{kMAX}
1	*SP*	0.00785	10.13	12.80	1500	1700	0.0077	0.0096
2	*SP+G*	0.00785	9.96	12.89	1500	1740	0.0075	0.0095
3	*WJ39G*	0.00119	0.76	4.74	1500	4200	0.0004	0.0022
4	*WJ49G*	0.00189	1.66	9.18	1580	4200	0.0010	0.0048
5	*WJ50*	0.00196	1.70	10.24	1500	4200	0.0011	0.0056

Table 12.5: Von Karman's coefficients (yield coefficients) for flow tank experiments at speed 0.700 [m/s].

no.	drive	S_{PROP}	Thrust	$Thrust_{MAX}$	n	n_{MAX}	C_k	C_{kMAX}
1	*SP*	0.00785	7.47	9.57	1500	1700	0.0049	0.0062
2	*SP+G*	0.00785	7.23	9.38	1500	1740	0.0046	0.0059
3	*WJ39G*	0.00119	0.49	3.89	1500	4200	0.0002	0.0017
4	*WJ49G*	0.00189	1.09	7.60	1580	4200	0.0005	0.0036
5	*WJ50*	0.00196	1.14	8.91	1500	4200	0.0006	0.0045

Table 12.6: Bondeman's coefficient of propeller's static thrust for flow tank experiments.

no.	drive	S_{PROP}	Thrust	$Thrust_{MAX}$	n	n_{MAX}	C_b	C_{bMAX}
1	*SP*	0.00785	10.13	12.80	1500	1700	0.0309	0.0359
2	*SP+G*	0.00785	9.96	12.89	1500	1740	0.0303	0.0356
3	*WJ39G*	0.00119	0.76	4.74	1500	4200	0.0043	0.0136
4	*WJ49G*	0.00189	1.66	9.18	1580	4200	0.0078	0.0227
5	*WJ50*	0.00196	1.70	10.24	1500	4200	0.0082	0.0249